THE ENERGY SPECTRUM OF COSMIC RAY WITH ENERGY ABOVE 1 EEV

XINGZHI ZHANG

submitted in partial fulfillment of

the requirements for the degree of

Doctor of Philosophy

in the Graduate School of Arts and Science,

COLUMBIA UNIVERSITY

2001

Abstract

THE ENERGY SPECTRUM OF COSMIC RAY ABOVE 1 EEV

XINGZHI ZHANG

The energy spectrum of Ultra High Energy cosmic rays above 1 EeV is measured by High Resolution Fly's Eye experiment (HiRes) in the monocular mode. The atmosphere is calibrated by using laser shots. The multiply scattering effect of light propagation is studied for Scintillation detector for the first time. A new global reconstruction method was developed to analysis the data. This method gives less than 20% energy resolution for cosmic ray above 6 EeV. Resolution and systematics are also studied. The measured spectrum is consistent with Fly's Eye stereo result [3] within statistic errors under similar weather conditions. It is significantly different from AGASA experiment results[4]. One event above 100 Eev has been detected. The spectrum appears highly compressed above Greisen-Zatsepin-Kuz'min cutoff. It is consistent with existence of GZK cut off.

Contents

List of Tables

List of Figures

Acknowledgements

I would like to thank my advisor Prof. Wonyong Lee for his full support and guiding throughout this work. His friendship and encouragement is also very important for me to finish this work. Thanks also go to Prof. Pierre Sokolsky in University of Utah for his help in physics and providing great working environment for me when I was staying in Utah for the last 3 years.

I want to thank all members of HiRes collaboration. They spent so much time in detector building and date collecting. I would specialy thank Dr. John Mathews, Mr. Stan Thomas, Prof. Charles Jui for detector calibration and all the detector hardware information; Dr. Lawrence Wiencke and Prof. John M. Mathews for providing laser shots and help in atmosphere analysis; Mr. C. Song and Dr. T. Abu-Zayyad's help in detector Mont Carlo; Dr. Z. Cao and Dr. Y. Ho's help in the data analysis issues.

My graduate studies separate me from my family for a long time. I wish to express my sincere appreciation for my parents and their love, and my deepest regret for can not be with them for so long time.

The least but not the last, I would like to thank all friends in the youth fellowship of Salt Lake City Chinese Christian Church. Their friendship and love from Christ are great support for me when I was staying in Utah.

This research is funded by National Science Foundation through Nevis Laboratory of Columbia University. CHPC of University of Utah provided the huge CPU time for data analysis.

dedicated to XXX

Chapter 1

Introduction

1.1 Motivation

Cosmic rays are energetic particles arriving from space. They cover a huge range of energies - from below 10^9eV up to 10^{20}eV. The spectrum is steeply falling (see Figure 2.1) and follows a roughly E^{-3} power law. Below 10^{14} eV, balloon and satellite experiments are able to directly measure the cosmic ray. So the energy, composition, and direction can be well understood.

Above 10^{15}eV, because the flux is too low that direct measurement is no longer possible. In this case, the detection methods include ground arrays, atmospheric fluorescence detection, and air Cherenkov detection. Each of these techniques measures some aspect of the Extensive Air Shower(EAS), which results from the impact of the primary particle with the atmosphere. Ground arrays of scintillation detector, muon detector or air Cherenkov detector spread out over a large area on the ground, by measuring the lateral charge distribution or Cherenkov light distribution of EAS on

the ground, the primary energy, and direction can be reconstructed. The atmosphere fluorescence detector observes the fluorescence light emitted by atmospheric Nitrogen molecules in response to the passage of charged particles of the shower, and measures the longitudinal profile of EAS. This technique can measure the energy very well. With stereo setup, the arrival direction of the primary can also be measured very well. Fluorescence light is emitted isotropically from EAS, allowing for detection of showers at large distance. This makes a very big aperture.

The Ultra high energy (UHE) cosmic ray protons or nucleus will interact with 2.7°K cosmic microwave background if the sources are far enough. This interaction causes a cutoff in the energy spectrum near 5×10^{19}eV, which is called GZK cutoff [1]. What is the highest energy of cosmic rays which can reach us, where they come from, what they are, these are the most important questions to be answered in cosmic ray physics. Detection of cosmic rays with energy above 10^{20}eV [3, 4] has given rise to much discussion regarding their origin. Many models have been proposed as source candidates of such high energy cosmic rays (see [5, 6, 7] for review). To understand the origin, acceleration and propagation of UHE cosmic rays, three basic things should be well measured: energy spectrum, composition, and anisotropy.

1.2 This Report

The High Resolution Fly's Eye(HiRes) is a fluorescence detector, it is dedicated to study the spectrum, composition and anisotropy of cosmic ray with energy above 3×10^{18}eV. The detector includes two sites separated by 12.6 km distance. This allows for stereo observation of a single EAS, and makes a better shower reconstruction and better understanding on the systematics. HiRes-I has been collecting data ever since

1997. HiRes-II site was under construction until the end of 1999, only recently began full time data taking. This dissertation reports the monocular observation results by HiRes-I site. Even through stereo mode is the preferred mode of operation, this dissertation will address how well we can do on the monocular mode to understand the properties of UHE cosmic ray, mainly I will focus on the energy spectrum and the GZK cutoff.

Chapter 2

Cosmic Ray Physics

The first hints that cosmic rays exist came in the late 1800s when it was observed that gold-leaf electro-scopes slowly discharged, and no explanation could be found. Faraday postulated the existence of ionizing radiation. In 1901 natural radioactivity had been discovered, these particles capable of causing ionization of air and discharged electroscopes. But a charged electroscopes kept away from natural radioactivity source would still discharge was a major mystery. In 1913 Victor Hess made a series of balloon flights and determined that the ionization rate increased with altitude above 1.5 km. and proved the cosmic origin of the radiation.

In 1938 Pierre Auger *et al*[8] found that the radiation reaching the ground was correlated over large distances and short time scales. From this they inferred that they were seeing the secondary particles due to cascading effects caused by the interaction of a highly energetic primary particle high in atmosphere. They discovered extensive air shower(EAS).

Until the advent of high-energy accelerators in 1950s, experiments at the high-

energy were leaded by cosmic rays. The muon, pion and kaon were all discovered in cosmic ray experiments. Even after most high-energy experiment moved to accelerators, cosmic ray experiments continue. Now at the end of century, after 50 years of accelerator experiments, cosmic ray experiments are becoming fashionable again. Because they could be used to study particle interactions at energies far above those available at terrestrial accelerators.

2.1 Cosmic Ray Spectrum

The ultimate questions of cosmic ray physics are the cosmic ray origin and acceleration mechanism. To answer these questions, people try to detect cosmic ray and identify the energy, composition, arrival direction, and general anisotropy.

The most distinctive feature of cosmic ray physics is that the flux of cosmic rays follows a power law in energy:

$$N(E)dE \propto E^{-\gamma}dE \tag{2.1}$$

where γ is the spectrum index. As shown in Figure 2.1, the spectrum breaks and the index changes from 2.7 to 3.0 between 10^{15}eV and 10^{16}eV. The breaking point is called "knee". The existence of "knee" has been interpreted as the point when cosmic ray no longer be trapped by the magnetic field within our galaxy and leak out of it [9], or at the point when acceleration process changes [10].

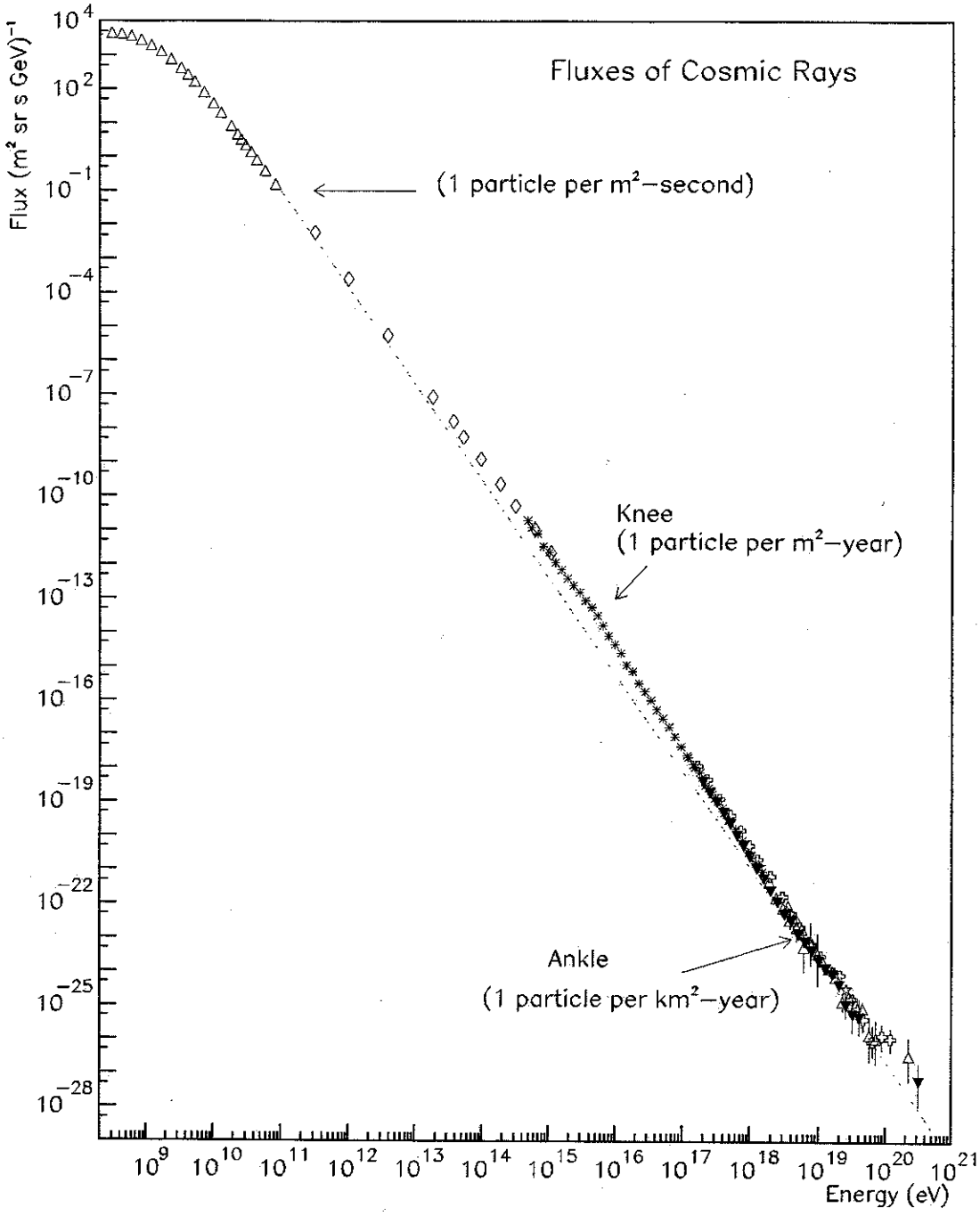

Figure 2.1: *The differential energy spectrum of cosmic rays. The dotted line shows* E^{-3} *power law for comparison.* 10^{14} *eV is the region between balloon/satellite direct measurement and ground based indirect data.*

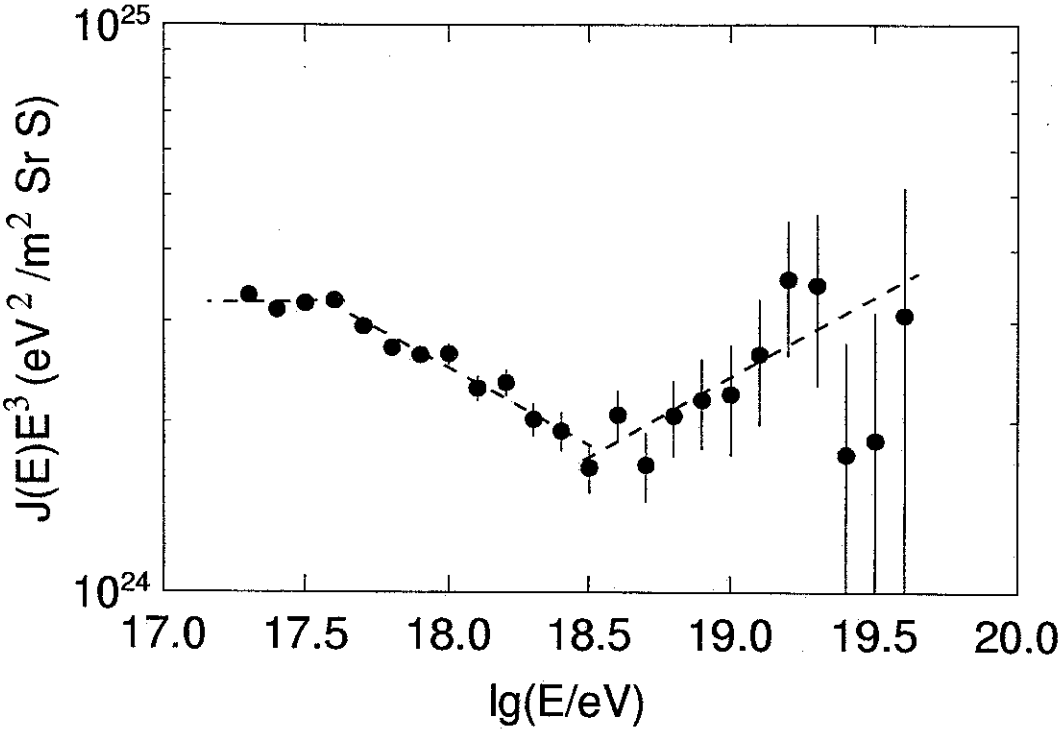

Figure 2.2: *The differential energy spectrum of cosmic ray by stereo Fly's Eye experiment*

The second break called "ankle" is around 3×10^{18}eV. According to Fly's Eye stereo results[11] (see Figure 2.2 the spectrum index drop from 3.27 to 2.71 at 3×10^{18} eV (3EeV). The most resent result from AGASA[4] as shown in Figure 2.3 also shows a break at 10 EeV, and the index changes from 3.16 to 2.78. Both experiments observe a break point at different energies.

The most important AGASA result is that there are significant number of events above GZK cutoff. At the time of the publication, they had observed a total of six events above 100 EeV. After that, they saw another two more events[2]. One of the main topic of this thesis is to measure the spectrum above 10^{18}eV, and see if there are events above 10^{20} eV.

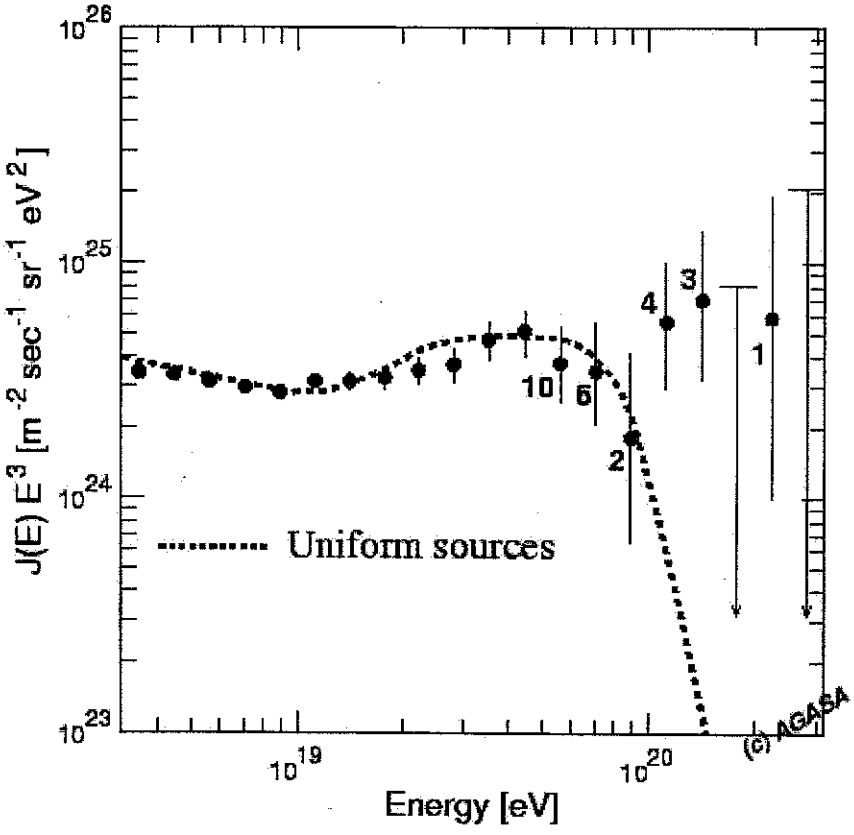

Figure 2.3: *Energy spectrum observed by AGASA. The number attached show the number of events in each energy bin. The dashed curve represents the spectrum expected for extra-galactic sources distributed uniformly in the Universe.*

2.2 Cosmic Ray Composition

The composition is well understood by directly measured nuclei up to 10^{14}eV by balloon or satellite experiments. For cosmic rays below 10^{10}eV, some come from solar flares and winds, but the existence of extra-solar component has also been possible. From 10^{10} to 10^{14} eV, cosmic rays are less affected by solar wind. the composition of these cosmic rays is similar to matter in the solar system[12].

Above 10^{14}eV, because the low flux of cosmic ray, indirect experiment based on measurement of EAS becomes necessary. So the composition measurement becomes indirectly and has large statistical fluctuations.

The first issue is to distinguish γ ray showers from hadron induced cosmic ray showers. This can be done by measuring muon content or lateral correlation of the Cherenkov light[13]. At EHE range, the distinguish between γ ray from hadron ray can be inferred from the shower X_{max} measurement, and also from south-north flux asymmetry induced by LPM[14] effect, and earth magnetic field effect[15].

The second issue is to find the atomic weight of cosmic rays if they are hadron. If the superposition model is correct. the first interaction of proton should be deeper than iron with same primary energy, which makes the X_{max} of proton initialized shower deeper than that of iron. For the same reason, the fluctuation of X_{max} from proton initialized showers is bigger than that of iron. The elaborate Mont Carlo calculation of these pictures are given in CORSIKA[16].

The first clue of the hadron composition is the elongation rate, which is defined as

$$\Gamma_{el} = \frac{dX_{max}}{dlog_{10}E} \tag{2.2}$$

By comparing the experiment elongation rate to the pure proton and iron elongation rate based on the Mont Carlo calculation. It will tell you what the composition is.

Another way to determine the composition is by measuring the muon component in a shower. Based on MC simulation, the muon component is more in an iron initialized shower than that in a proton shower. The composition can also be determined by comparing with MC.

AGASA[17] used muon component, and Fly's Eye[18] (as shown in Figure 2.4) used elongation rate to measure the composition. If they use same Hadronic model in the MC calculation, they both see the change of composition from proton to iron from 10^{17}eV to 10^{18}eV[19]. Fly's Eye detector can detect X_{max} directly, at this point, they have more advantage. The most resent result from HiRes Prototype combined with Mia muon ground array experiments[20] also has this change between 10^{17} to 10^{18} eV as shown in Figure 2.5. This experiment is a hybrid detector used both muon ground array and fluorescence techniques. The advantage is very clear. But due to the small statistics and aperture, It could not measure above 10^{18}eV.

For the hadron composition measurement talked above, the interpretation of the result strongly depend on the hadronic interaction model used in the EAS Mont Carlo calculation. Same measurement can draw different conclusion based on different models[19]. HiRes-Mia hybrid experiment shows [20] the muon density predicted from MC is too small comparing with the experiment for hadron above 10^{17} eV.

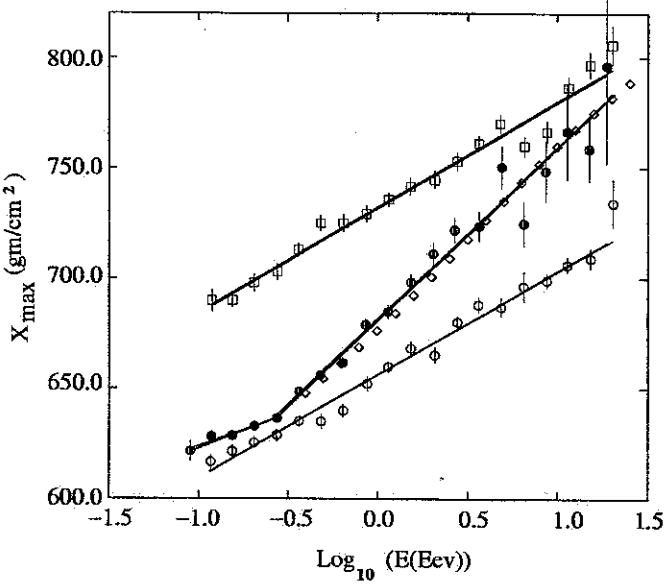

Figure 2.4: *The X_{max} distribution of Fly's Eye experiment. The data are shown in solid dot. The iron simulation data are shown as circle. The proton simulation data are shown in square. Two component fit are shown in diamonds.*

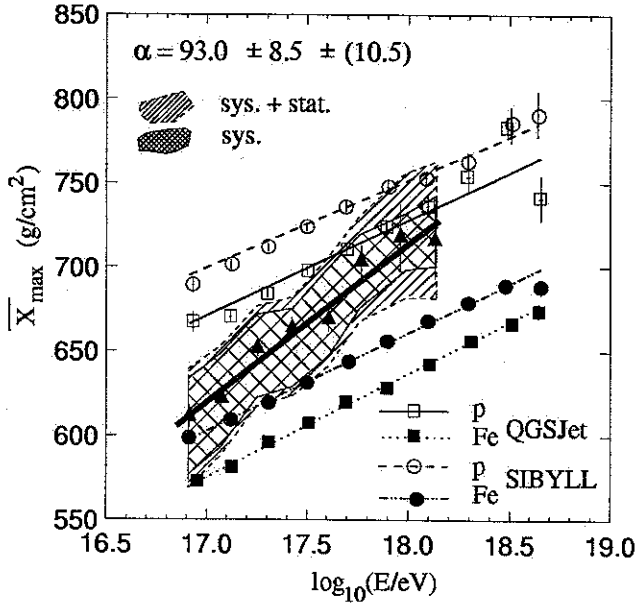

Figure 2.5: *The X_{max} distribution vs Energy from HiRes-Mia hybrid experiment. The data is shown as closed triangles. The circles, squares refer to simulation results for proton and iron with different hadronic interaction model and different.*

2.3 Anisotropy

The exact origin of cosmic rays remains a mystery. Because most cosmic rays are charged nuclei, which will interact with the galactic magnetic fields, and the trajectories are bent and lost the original direction. From simply magnetism we can get the gyro-radius:

$$R_g = \frac{\gamma m v sin\vartheta}{zeB} \approx 1.1 \frac{E_{18}}{zB_\mu}(kpc) \tag{2.3}$$

in which E_{18} is the energy in EeV (10^{18}eV), B_μ is the magnetic field in unit micro-gauss μG (10^{-6} gauss). z is the charge number.

Measurements for the average galactic magnetic field yield values of $1 - 10\mu G$ [12]. Protons with energy up to EeV coming from galactic sources $\sim 10kpc$ away has R_g about 1 kpc, and then lost the source direction information. When energy $>$ 50EeV, the bending angle is less than 1 rad , therefor , it is possible to see clustering of cosmic rays around source.

If the cosmic rays come from extra-galactic source, with intergalactic field about $10^{-3}\mu G$, and distance about 10Mpc, for high than 50EeV proton, it is still possible to see clustering of cosmic rays around source.

When cosmic ray is heavier than proton, then the angular deflection will become stronger. From this point, the energy dependence of the anisotropy will also provides a consistency check on assumptions about compositions.

The GZK cut off cosmic ray has energy about 100 EeV, if we apply the same calculation as above, the bending angle is about a few degrees. so we can trace back to the source.

Because it is difficult to observe point sources, large scale anisotropy will give

information about the source. Consider a simple model, the galactic magnetic field is basically perpendicular to the galactic plane, the cosmic rays come from galaxy will confined in the galactic plane, this will enhance the anisotropy. Same argument works for extra-galactic source. But the most recent study by Teshima[21] and Huang[22] did not find any anisotropy beyond 3σ. Unfortunately, these study are based on limited data set. The giant detector like Auger, which will setup at both south and and north hemispheres, it will have more advantage to answer this question.

2.4 Acceleration Mechanism and GZK Cutoff

One of the ultimate question of cosmic ray physics is the acceleration mechanism, especially if the source is galactic sources. When the source is extra-galactic or universal source, the cosmic ray will interact with cosmic microwave background. And has a so called GZK cutoff on the energy spectrum. In this section, I will generally discuss them, especially the GZK mechanism. Since we are most interested in answering whether GZK cutoff exist or not.

2.4.1 Fermi Acceleration Mechanism

Twenty-five years after the discovery of cosmic rays, Fermi gave the first possible mechanism to explain the cosmic acceleration [24, 12]. The simply picture of this mechanism is that, the plasma clouds in the interstellar medium act as magnetic mirrors and reflect charged particles. The particle can gain energy if the cloud is moving toward it, on the other way, if the cloud is moving away, the particle will loss energy. But on average, there are more collision when cloud and particle are moving

toward each other, which leads to a energy gain to the particle. This is so called second-order Fermi acceleration. But this nergy gaining process is slow.

Applying this idea to shock front, comes the so called first-order Fermi acceleration[25, 26]. In the rest frame of the shock, material both upstream and downstream of the shock moves toward the shock. So a charged particle trapped between the upstream and downstream will gain energy every time it crosses the shock front. In this process there is on energy loss comparing to the second-order Fermi acceleration, and the acceleration time is only limited by the lifetime of the shock[26]. So the particle can be accelerate to very high energy. Apply this mechanism to supernova explosion, a proton can be accelerate up to 10TeV[26]. Shocks are common in the universe, they may form in an x-ray binary system or an active galaxy, where matter accretes onto a compact object. This mechanism also predicts a power law energy spectrum, which has a universal index very close to the real observed cosmic ray spectrum[27]! So the Fermi mechanism is generally accepted for cosmic ray lower than 100TeV

2.4.2 UHE Acceleration Mechanism

The cosmic ray can have energy up to 10^{20}eV, and has an almost power law energy spectrum (see Figures 2.2, 2.3). How they are accelerated beyond 100TeV?

Reviews on this topics are given in [5, 28], general speaking the source can be in galactic disk-like neutron star, new supernova remnants, binary stars, black holes etc. These are point sources, and anisotropy is expected.

The source can be galactic but not concentrated in the galactic disk. This class of theories include diffuse or discrete sources throughout a large halo of galaxy. Like galactic wind model[29], the same idea of Fermi mechanism is applied, and heavy

	Energy Cutoff	Composition	Anisotropy
point galactic sources	No	Unknown	Yes
galactic wind	No	Heavy	Weak
quasi-local extra-galactic	Yes	Unknown	Yes
universal source	Yes/No	Light	No/Yes

Table 2.1: *The models of acceleration mechanism for UHE cosmic rays and the corresponding properties of cosmic rays in energy, composition, and anisotropy.*

nuclei is expected, since the energy attained in Fermi mechanism is proportional to the nuclei charge.

There are also quasi-local extra-galactic source model, in which the cosmic rays are not homogeneous and isotropic. As mentioned in section 2.3, for proton energy higher than 1EeV, the gyro-radius is around 500 parsec. which is comparable to the thickness of the galactic disk. Since heavy elements have small gyro-radius at same energy, this simply picture prefer heavy elements and enhancement in the supergalactic plane at high energies.

There are also theories in which the UHE cosmic ray intensity is homogeneous and isotropic in the universe. This is so called universal sources. Both extra-galactic source models predicted the exist of GZK cut-off at an energy depends on the path-length from source to Earth[30]. Most recently Bahcall[6] showed that the inhomogeneous universe model can enhance the GZK cutoff events.

A summary of these acceleration mechanisms and their expected energy, composition and anisotropy are given in Table 2.1

From here we can see, in order to understand the acceleration and origin of UHE

cosmic ray, experimental measurement of energy spectrum, composition and isotropy or point source search are crucial.

2.4.3 GZK Mechanism

Shortly after the discovery of 2.7^o microwave background radiation. Greisen discovered that if the cosmic ray is nuclei and far enough away with energy extended beyond 100 EeV, it will interact with microwave radiation photon through

$$p + \gamma_{2.7^o} \longrightarrow \Delta^{*+}(1232MeV) \longrightarrow p + \pi^0 or n + \pi^+ \tag{2.4}$$

This interaction was also independently discovered by Zatsepin and Kuzmin[1]. The attenuation length for protons, due to this process is about 50 Mpc. So if cosmic rays are extra-galactic, the flux above 60 EeV will be cutoff, this is known as GZK cutoff. Hill and Schramm[30] considered the red shift of microwave background radiation and cosmic ray, and found the cutoff energy will be scaled by $1/(1+z)^2$ where z is the red shift. But before we have clear evidence about the z-dependence of the sources and the spectrum of the original particle, what is clear is that the cosmic ray reaching earth will be highly suppressed above 60 EeV.

In addition to the modification of cosmic ray spectrum. GZK mechanism also predicts the existence of an associated ultra-high energy neutrino flux through decay of charge pion:

$$\pi^+ \rightarrow \nu_\mu + \mu^+ \rightarrow \nu_\mu + \nu_\mu + \nu_e + e^+ \tag{2.5}$$

Observation of a neutrino flux above 1EeV would confirm that a charged particle

cutoff is indeed due to GZK mechanism. when the energy neutrino is less than 1EeV, neutrino flux also depends on red shift z. So the magnitude of neutrino flux for $E < 1EeV$ would yield important information about red shift and early galactic evolution.

The search for this cut-off is the driving motivation for all UHE cosmic ray experiments. In the past, a few cosmic rays above 100 EeV have been reported by different experiments[3, 4]. If these high energy cosmic rays really exist, the acceleration of cosmic ray to such high energy is really a challenge to theorists. Hillas[31] summarized possible sources of cosmic rays in Figure 2.6. Sources which are above the lines are capable of accelerating proton(iron) above 100 EeV. From this figure, very few candidates exist. And in the mean time, the source should not be farther than 50 Mpc as mentioned above.

Theorists also invented some models to explain these giant events. Before we go beyond that far, a very well measured energy spectrum is very important. Energy resolution is a very important systematic issue to answer this question. A small non-Gaussian energy resolution tail can easily produce structure in a E^{-3} power law spectrum that mimics a the continuation of the spectrum beyond GZK cutoff[32]. One of the most important issues I will study in this report is the energy resolution for HiRes monocular measurement, and also the systematics.

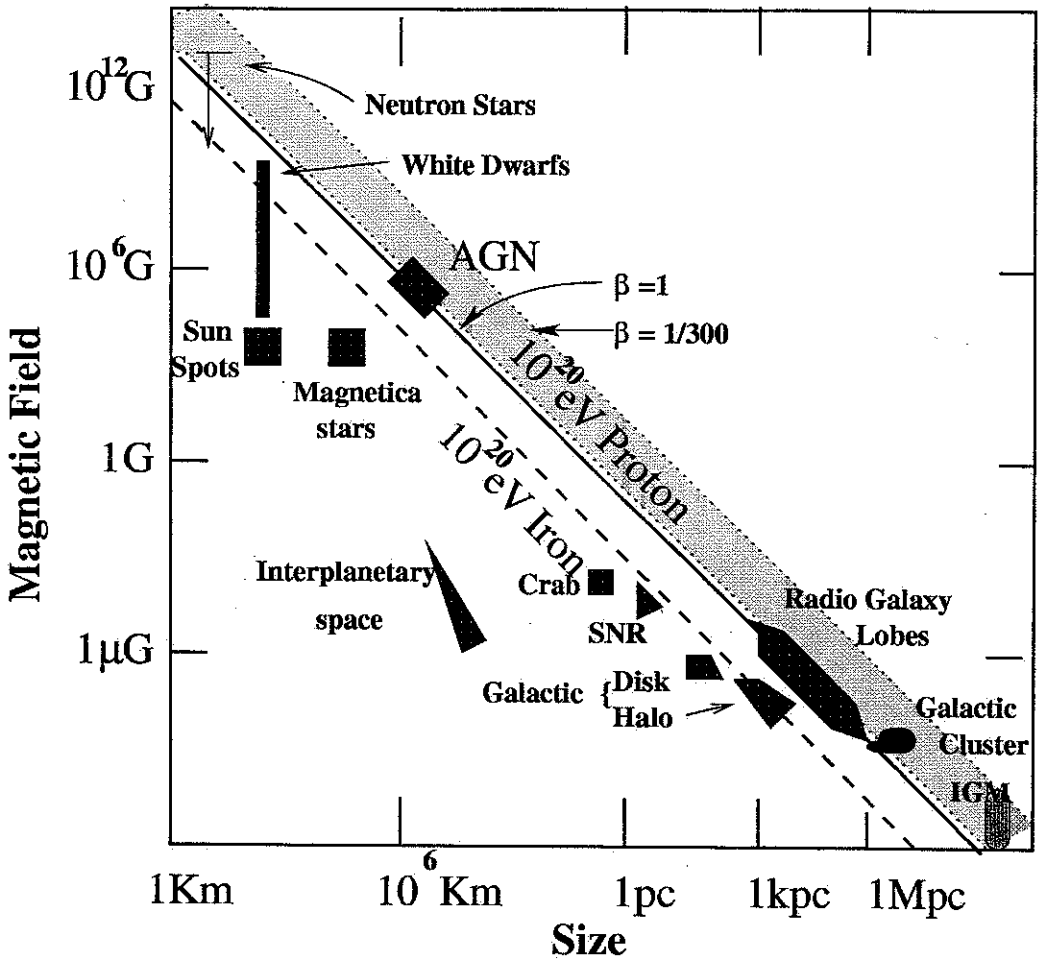

Figure 2.6: *Hillas diagram of possible source for* 10^{20} *eV cosmic rays. Objects below the solid line can not accelerate protons to* 10^{20} *eV, the dashed line corresponding to Iron. The edge of the shaded region represents a value of* $\beta = 1/300$ *which is typical for protons being accelerated by diffuse shock. Note very few candidate sites available.*

Chapter 3

Extensive Air Shower Physics

When a cosmic ray particle such as a proton enter the atmosphere, it will knock out a few nucleon from a target, and produce secondary particles such as nuclei and pions. In this process, the primary particle will also lose some of its energy. The primary particle and secondary particles will interact with air as they traverse the air. This results in a cascade of particles, which is called Extensive Air Shower(EAS). When the cosmic ray flux is very low, the detecting of EAS becomes the only way to detect cosmic ray. We can reconstruct the information of the primary particle such as the energy, composition, direction by studying EAS.

In this chapter, a review on the basic physics related to the EAS development is given. I'll also give the most recent experiment results on the properties of EAS. The COSIKA Mont Carlo simulation result is also presented.

3.1 Mechanism for EAS

The mechanism involved in the development of EAS includes electromaganetic interaction, weak interaction and strong interaction. These physics are well known when the energy is within terrestrial accelerator range. The cosmic ray energy is decades higher than what we can get on earth, in this case, we can only extrapolate the physics from terrestrial low energy to such high energy, and the result becomes model dependent. Sophisticated models of EAS are implemented in Mont Carlo packages such as CORSIKA[16]. A detailed study of this issue is beyond the scope of this report. Here I will only mention the physics which may impact the interpretation of the results for our experiment.

3.1.1 A Toy Model for EAS

A simply toy model to understand the development of EAS was made by Heitler[33, 27]. Suppose the primary energy of cosmic ray is E_0, each cascade generates M particles and passes $\lambda(gm/cm^2)$ of matter. Then the first interaction occurs at $\lambda(gm/cm^2)$ produces M secondary particles, each having energy E_0/M. The process continues to *nth* interaction, which takes place at $n\lambda(gm/cm^2)$ having M^n particles with mean energy E_0/M^n. When the average energy reaches critical energy E_c, the multiplying process stops. the total number of particles reaches maximum size $N_{max} = M^n$, the depth of shower maximum is $X_{max} = n\lambda$. After that, because the ionizing of the particles by atmosphere, the total number of particles will become less and less. We can get the following relationship about the shower maximum point:

$$N_{max} = N(X_{max}) = \frac{E_0}{E_c} \propto E_0 \tag{3.1}$$

$$X_{max} = n\lambda = \frac{ln(E_0/E_c)}{ln(M)}\lambda \propto ln(E_0) \tag{3.2}$$

Two important features of EAS can be illustrated from this simply model. First, the number of particles at shower maximum is proportional to primary particle energy. Second, the atmosphere depth of shower maximum is proportional to the logarithm of the primary particle energy. Of cause the real word is not this simply, the cascade process depends on the interactions cross sections of particles, which also depend on the energy of incident particles.

3.1.2 High Energy Interactions

When the cosmic ray interact with atmosphere nucleus, The first interaction can be simplified as:

$$\begin{aligned} &\textit{hadronic shower}: && \textit{Hadron} + N \textit{ or } O && \rightarrow && \textit{Hadron} + \pi^{\pm,0} \textit{ or } K^{\pm} \\ &\textit{gamma shower}: && \gamma + N \textit{ or } O && \rightarrow && \textit{Hadron} + \pi^{\pm,0} \textit{ or } K^{\pm} \\ & && \textit{or} && \rightarrow && e^+ + e^- \end{aligned}$$

After that there are three channels of interaction in terms of the type of secondary particles.

Hadronic channel:

$$\textit{inelastic scattering:} \quad \textit{Hadron} + N \textit{ or } O \rightarrow \textit{Hadron} + \pi^{\pm,0} \textit{ or } K^{\pm}$$

Electromagnetic channel:

$$\begin{aligned} &\textit{pion decay:} && \pi^0 && \rightarrow && 2\,\gamma \\ &\textit{pair production:} && \gamma && \rightarrow && e^+ + e^- \\ &\textit{compton scattering:} && e^{\pm} + \gamma && \rightarrow && e^{\pm} + \gamma \\ &\textit{bremsstrahlung:} && e^{\pm} && \rightarrow && e^{\pm} + \gamma \end{aligned}$$

Muonic channel:

$$
\begin{aligned}
\textit{charge pions decay:} \quad \pi^{\pm} &\rightarrow \mu^{\pm} + \nu_{\mu}(\overline{\nu_{\mu}}) \\
\textit{charge kion decay:} \quad K^{\pm} &\rightarrow \mu^{\pm} + \nu_{\mu}(\overline{\nu_{\mu}}) \\
\textit{or} \quad &\rightarrow \pi^{\pm} + \pi^{0} \\
\textit{nutral kion decay:} \quad K_S^0 &\rightarrow \pi^{+} + \pi^{-} \\
\textit{or} \quad &\rightarrow 2\pi^{0} \\
K_L^0 &\rightarrow \pi^{\pm} + e^{\mp} + \overline{\nu_e}(\nu_e) \\
\textit{or} \quad &\rightarrow \pi^{\pm} + \mu^{\mp} + \overline{\nu_{\mu}}(\nu_{\mu}) \\
\textit{or} \quad &\rightarrow 3\pi^{0} \\
\textit{or} \quad &\rightarrow \pi^{+} + \pi^{-} + \pi^{0}
\end{aligned}
$$

The hadronic interaction keeps a hadronic core along the direction of the primary cosmic ray. And feed the electromagnetic component and muon component of EAS through EM channel and muonic channel.

These interactions are well known at low energy, but are not known in high energy case. If we assume QED and QCD still work at highest energy. The difficulty for applying QCD to hadronic interaction is that perturbation method no longer works in extreme cases, and have to use some phenomenology model.

3.1.3 Hadronic Core

Understanding the physics involved in the hadronic core is the key to understand how EAS develops relating to primary particle. The exact interaction is unknown, it must be extrapolated from low energy physics, and rely on models to provide inclusive cross-sections for particle production. Comparison between the observed EAS development and the MC EAS development allows one to reassess the validity of the assumptions used in the interaction model.

The general picture for the hadron interaction is that, the interaction is inelastic, the particle production is normally considered in two regions - the fragmentation region and the central region. The fragmentation region contains the remnant of the primary particle and other leading particles, which includes most part of the energy. Central region corresponds to particles with small central momentum. most new particles are produced in this region. These two regions compose the hadronic core, and keep feeding the electromagnetic and muonic components of the shower. So the inelasticity is an important parameter in the development of EAS. Different mode extrapolates different inelasticity at high energy and gives different shower development. For example SYBALL model gives different X_{max} from QGSJET model in COSIKA[16].

Since we are interested in the composition of UHE cosmic ray, the property of proton initialized EAS will be different from that of iron. The simplest model to understand this is the superposition model. It assumes that a nucleus with energy of E_o and A nucleons is equivalent to N independent nucleons with E_0/A energy each. Then the cosmic nucleus can be looked as a beam of nucleons. From Equation 3.2 if substitute E_0/A for E_o and get:

$$X_{max} = \frac{ln(E_0/AE_c)}{ln(M)}\lambda \propto ln(E_0/A) \tag{3.3}$$

Thus the iron initialized shower will develop more rapidly than a proton shower with same primary energy. With same argument, The iron shower has more statistics in the hadron interaction, so the intrinsic fluctuation is less than proton shower.

Current hadronic interaction models using at highest energies (up to 10^{20}eV) include VENUS[34], DPMJET[35], HDPM, SIBYLL[36], and QGSJET[37]. And the

comparison was given in COSIKA package. The interpretation of the measurement will become model dependent. The most recent composition study in HiRes group prefers QGSJET model[20], which gives consistent result to the measurement in both elongation rate and muon rate.

3.1.4 Electromagnetic Component

The majority part of EAS is the electromagnetic component, which comes from the decay of pion through the electromagnetic channel in Section 3.1.2. About 90% of primary energy will eventually go into electromagnetic component [27, 57]. The development of electromagnetic cascade is well understood and very similar to the toy model discussed in Section 3.1.1. Review reference can be found in [27].

For a shower initialized by a photon with energy E_0, by energy lossing of the particle energy through Bremsstrahlung, pair production, and ionization, the energy loss can be characterized by $dE/dX = E_c/x_0$, in which E_c is the critical energy around 81 MeV and x_0 is radiation length is about 37.1 gm/cm^2. the longitudinal profile of the EAS can be described with Greisen function [38]:

$$N_e(E_0, X) = \frac{0.31}{\sqrt{X_{max}}} exp[X(1 - 1.5logs)] \tag{3.4}$$

where $N_e(X)$ is the number of electrons at depth X. $X_{max} = log(E_0/E_c)$ is the depth of shower maximum. $s = 3X/(X + 2X_{max})$ is the shower age parameter.

For a hadron initialized shower, the interaction is not simply electromagnetism. The electromagnetic component is feed by the hadronic core, and can be looked as superposition of many mini EM showers. The most resent HiRes experiment measured

the longitudinal profile of an EAS, it can be fitted with Greisen function with X_0 about 56 gm/cm^2[39].

People also used Gaisser-Hillas function to describe the longitudinal profile for hadron initialized shower:

$$N_e(X) = N_{max}(\frac{X - X_0}{X_{max} - X_0})^{\frac{X_{max}-X_0}{\lambda}} exp[\frac{X_{max} - X}{\lambda}] \tag{3.5}$$

where $N_e(X)$ is the number of electrons at depth X, X_{max} is the depth of shower maximum(where $N = N_{max}$), λ is a model dependent constant. From the equation X_0 is the point where N=0. But remember we always have at least 1 particle, so X_0 will be less than 0. This function catches both the buildup of EAS before maximum and the decreasing of particles after by ionization. The most resent HiRes measurement get $X_0 < 0$ and λ is about 65 gm/cm^2 for averaged shower profile around 5×10^{17} eV. Figure 3.1 shows the HiRes measurement on the shower profile development and fitted on different functions. This result is consistent with the CORSIKA simulation.

Coulomb scattering of electrons will result in lateral spreading of charged particles in EAS, Since EM component is about 90% of the particles in a shower, the lateral distribution function derived from pure EM shower will describe the lateral distribution of EAS. By approximately solving the cascade equations for electrons, Kamata and Nishimura and Greisen derived the NKG function[40] to describe the lateral distribution:

$$f_{NKG}(\frac{R}{R_m}) = \frac{\Gamma(4.5 - s)}{2\pi\Gamma(s)\Gamma(4.5 - 2s)}(\frac{R}{R_m})^{s-2}(1 + \frac{R}{R_m})^{s-4.5} \tag{3.6}$$

where R_m is Moliere unit, characterizing the scattering length. s is the shower age. The local density of charged particles at distance R from core is given by:

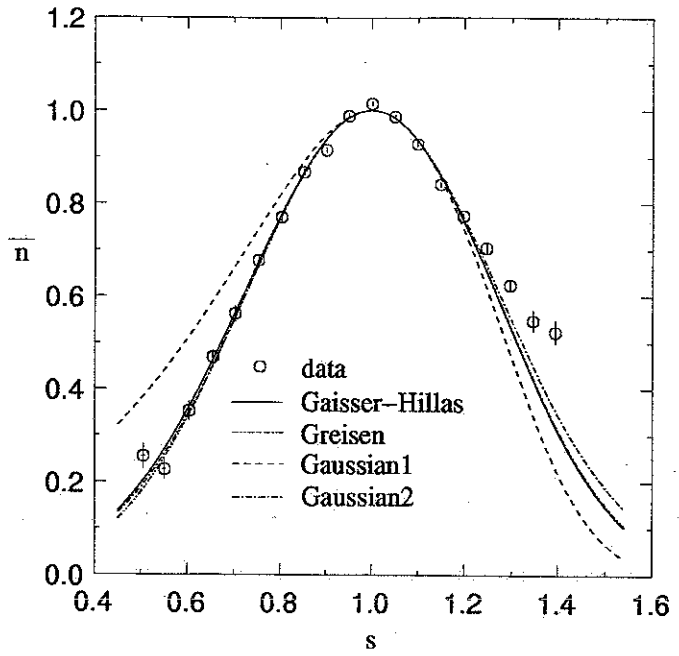

Figure 3.1: *The averaged longitudinal EAS profile for primary energy around* $5X10^{17}eV$. *The circle is the real data, the solid line is the fitted Gaisser-Hillas function, Greisen function fitting is also shown in the plot. Two Gaussian functions are also tried to fit the data, one Gaussian function is symmetry to the slant depth, the other one is symmetry to the shower age as shown as "Gaussian2".*

$$\rho(N_e, R) = \frac{N_e}{R_m^2} f_{NKG}(\frac{R}{R_m}) \tag{3.7}$$

where N_e is the total number of electrons.

3.1.5 Muon Component

Muon component is small in EAS but important for high energy physics. The muon is feed by the hadron core through muon channel in Section 3.1.2. Muon production

depends on the primary energy and composition. Generally speak, the number of muon goes as a power of energy for fixed composition with an exponent around 0.8[17, 20]. For different composition case, if we simply use superposition model, consider heavier nuclei is a superposition of A nucleons with energy 1/A of primary energy, then total number of muon proportional to $A(E/A)^{0.8}$, which is bigger than $E^{0.8}$. The detail calculation of the muon production strongly depend on hadron interaction model. The most resent HiRes-Mia result shows current hadronic model is deficient in muon production[20].

Muons will spread laterally in a disk, mainly due to the transverse momenta of the parent particles from the hadronic core. Muons are generated early in the shower, which results in large lateral spreading on the ground. As muons are weakly interacting particles, the muon lateral distribution function(LDF) detected on the ground is much flatter than that of electrons, and can be detected even kilometers away from the core[41].

Gamma ray induced shower has much less muons comparing with hadronic shower. This make ground array gamma ray physics possible[13].

3.2 Light Production in EAS

The electrons in EAS will emit Cherenkov light if their energy exceeds a threshold. These lights are very forward and can be detected by Cherenkov detector. The EM component in a shower eventually will be dissipate away by ionizing the atmosphere [42, 43], the presence of ionizing particles gives fluorescence light and can be detected by fluorescence detector. HiRes detector is a fluorescence detector. In this section, I will discuss the light production in EAS. The detail models on how to handle these

lights can be found in Chapter 5

3.2.1 Cherenkov Light

When a charged particle passed through a dielectric medium with a speed greater than the speed of light in that medium, it will give rise to Cherenkov radiation. The thorough discussion of Cherenkov light production can be found in the literature [44, 45]. The threshold energy for Cherenkov emission is 21 MeV at sea level and increase with the square root of atmosphere density at higher level.

The Cherenkov light cone is a few degree from the particle direction, so the lights will lateral spread out when they reach the ground. The lateral distribution of Cherenkov light has a Cherenkov ring around the shower core, which comes from early interaction at high altitude. This angular dependence and pulse profile information is correlated with the longitudinal development and shower maximum, can be used to measure the X_{max} of shower[46].

The energy loss of electrons due to Cherenkov is proportional to $1 - (E_0/E)^2$, which is much smaller than EM interaction process [42, 12].

Cherenkov light telescope is the most powerful gamma ray detector. The Cherenkov light comes from gamma ray shower is cleaner than that from hadronic shower, which means it is less lateral spread out. This is the criteria for gamma ray.

The HiRes detector can detect directly Cherenkov light when the shower is close to the detector. Even when the shower is far away from the detector, the Cherenkov light can still reach the detector through atmosphere scattering. So Cherenkov light can contaminate the scintillation light. How to correct this effect in HiRes detector is discussed in Chapter 5.

3.2.2 Scintillation Light

Ionized particles can excite nitrogen molecules, which then emit fluorescence photons. It has been found that the fluorescence spectrum consists almost entirely of N_2 2nd positive(2P) system and the N_2^+ first negative(1N) system [47].

The 1N upper lever of N_2^+ can be excited by ionization of N_2 when a high energy electron pass through:

$$N_2 + e \rightarrow N_2^{+*} + e + e \tag{3.8}$$

The 2P upper lever of N_2 can not be directly excited from ground state by a high energy electron because spin conservation forbid it [48]. This excitation is done by low energy electron collisions involving a spin change, or by cascading of N_2^+:

$$N_2 + e(\uparrow) \rightarrow N_2^* + e(\downarrow) \tag{3.9}$$

$$N_2^+ + e \rightarrow N_2^* \tag{3.10}$$

The energy levels of the above nitrogen molecule states is shown in Figure 3.2. N_2^{+*} or N_2^* will emit fluorescence light in Ultraviolet region within about 10 ns[43]. The wavelength of this fluorescence light is about 3100 A to 4400 A. The spectrum is shown in Figure 3.3. After the emission of a photon, N_2 or N_2^+ is not on the ground level. So the emitted fluorescence light will not be absorbed by N_2 when it pass through the atmosphere. Instead, the dissipation will be ozone absorption or by Rayleigh or Mie scattering. The attenuation length of atmosphere for these light is about 15 Km.

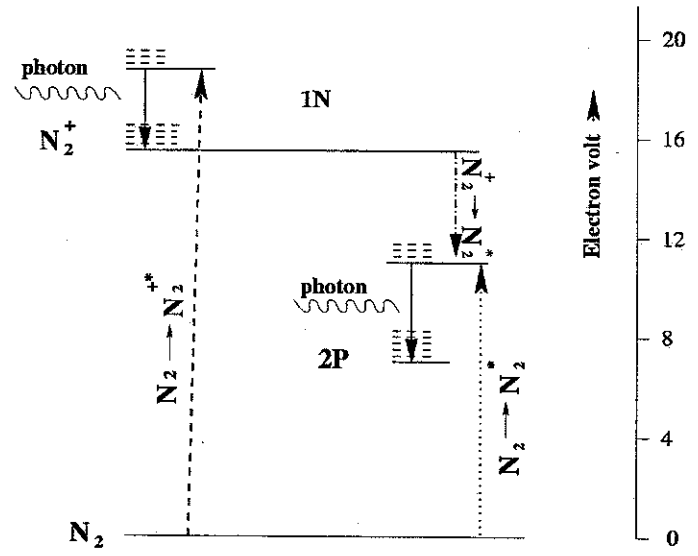

Figure 3.2: *A schematic energy level diagram of the N_2 molecule and N_2^+ ion. The dot arrows show the mechanism from N_2 states to N_2^+ or N_2 excitation states. The solid arrows show the scintillation photon emission.*

3.3 Detection Methods

Up to now we have a basic picture about the EAS. In summary, the EAS shower has a hadronic core along the direction of primary particle, the secondary particles produced through cascade give rise to EM and muon components, these components will laterally spread out, forming a disk of high energy particles passing through atmosphere. The number of particles will reach maximum size at some depth, after that it will decline. The charged particles will loss energy due to ionization, and give rise to isotropic fluorescence light. Along the moving direction, relativistic particles will also produce Cherenkov light, which will also spread out when reach ground.

In order to detect the basic properties of the primary particles such as direction, energy and composition. We can detect the electron component, muon component

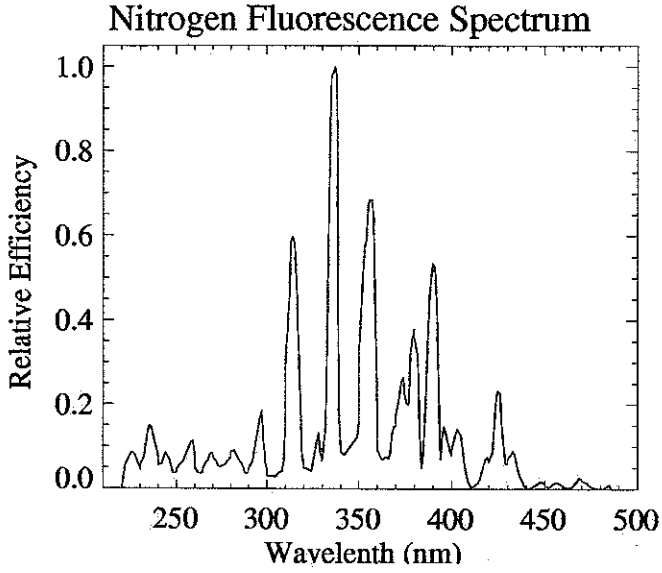

Figure 3.3: *Atmospheric fluorescence spectrum which arises mostly from the 2P band of N_2 and 1N band of N_2^+ as shown in figure 3.2 measured by Bunner [43].*

directly, detect Cherenkov light and fluorescence light, the hadronic core can also be detected by special instrument. In this Section. I will discuss these techniques. A summarize of the detecting methods is giving in Figure 3.4.

3.3.1 Ground Array Detectors

Ground array detector was pioneered by Rossi in 1940's. Linsley[49] extended this technique by creating big area array and first saw cosmic ray higher than 10EeV. Most ground array detectors are designed for PeV cosmic ray, especially for gamma ray. This technique uses a array of separated detectors, which sample the shower front density when it reaches ground. Depending on the components the detectors try to measure, there are three kind of detectors: electron detector- detecting the electron component using scintillation technique [Yakutsk, AGASA]; muon detector-detecting

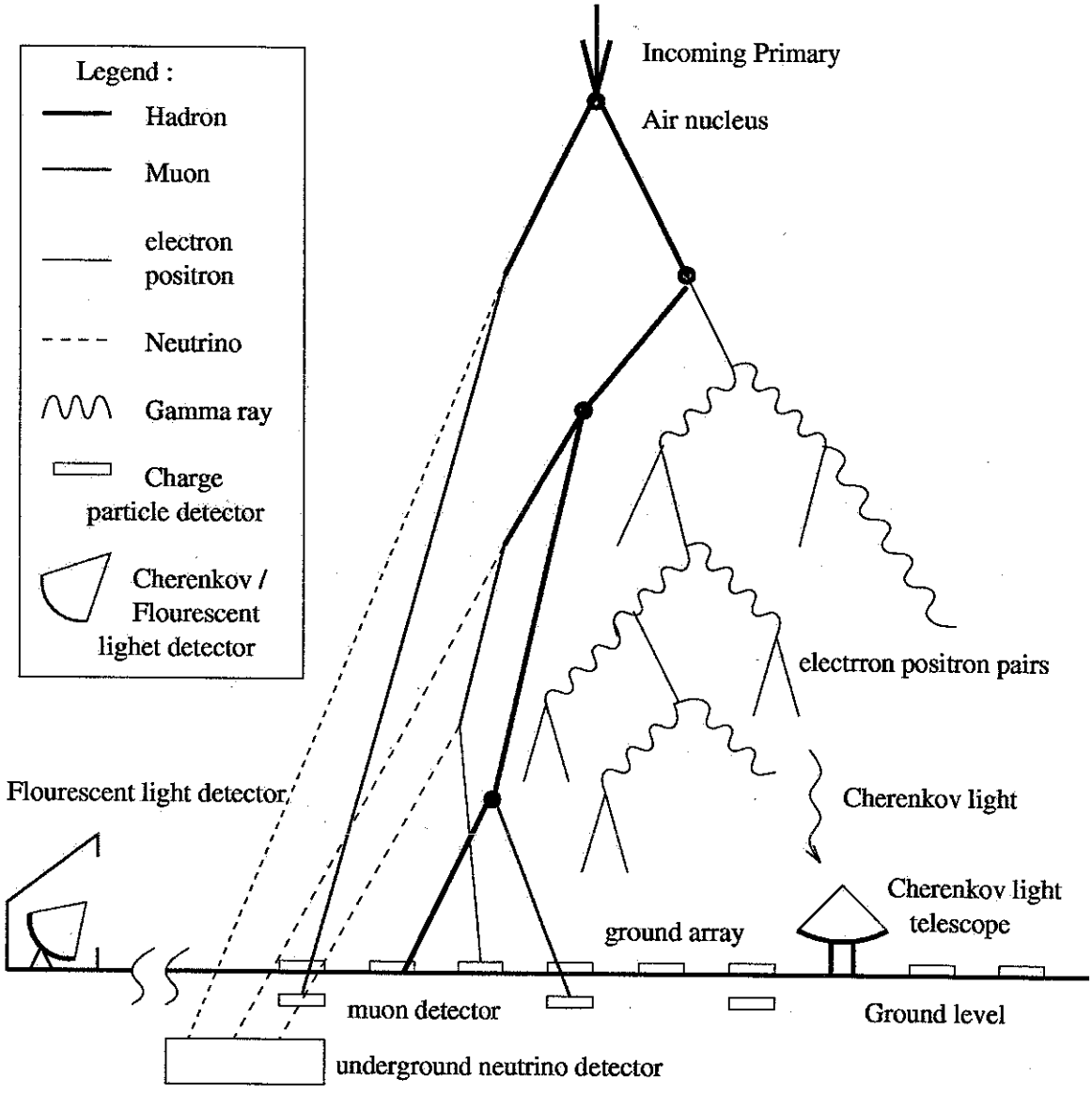

Figure 3.4: *Schematic of an EAS and the three channels of interactions and several types of detectors [22].*

the muon component using water Cherenkov or muon counter[SUGAR, Yakutsk, Akeno,MIA]; and Cherekov detector-detecting the air Cherenkov light[Yakutsk,DIS, BLANK].

The arrival direction of the primary particle can be determined by the arrival time measurements of the shower front at different sampling detectors. The core position can be directly measured from the lateral density distribution, when the core is within the array. Otherwise, it has to be inferred from the lateral density distribution. Generally speaking, ground array detector can measure the geometry very well when the shower core is within the array and shower is close to vertical.

One of the challenges for ground array experiment is the primary energy measurement, because it only measures the density of shower component at fixed depth. Hillas examined this problem through Mont Carlo shower simulation and developed a so called $\rho(600)$ method for energy estimation [50]. He found the density of electron component at 600 meters away from core is fairly insensitive to composition and fluctuation. Usually, experiments use Mont Carlo shower simulation to study the relationship between the primary energy to $\rho(600)$. Yakutsk [51] and AGASA [52] studied vertical showers and obtained a relationship like $E = C\rho_v(600)^\alpha$, in which C is a constant α is very close to 1.0.

The ground array technique can also measure the composition of the primary particle by muon counters, which measure the muon density distribution. The total number of muons is correlated with the primary component as discussed in section 3.1.5. Similar to energy measurement, by studying the relationship between muon density at 600 meters to the composition through Mont Carlo, using the measured density, people can get the primary composition[20].

For ground array Cherenkov detector, the people found the Cherenkov ring is

correlated with the X_{max} through Mont Carlo study[46]. By measuring the Cherenkov density distribution near core, people can get X_{max}, which is related to primary component.

From above discussion, we can see the advantage and disadvantage of ground array technique. The advantage is that, this technique can measure the core position very well. By using muon detector or Cherenkov detector the composition can be fairly done. If a hadron detector is put in the center of the array, some hadronic physics can also be studied. The disadvantage is that, this technique is confined by the area of the array, the aperture is not so big, to do UHE cosmic ray physics, a huge array has to be build. To get the information of the primary particle, the interpretation of measurement strongly depends on the Mont Carlo, especially on the hadronic models.

3.3.2 Fluorescence Detector

The air fluorescence technique was proposed in early 1960s by Greisen[38, 53], Suga[54], and Chudakov[55]. The first unsuccessful try was did by Greisen[56] in 1965. Fly's Eye experiment is the first successful fluorescence detector made by Utah in 1980s.

As pointed out in Section 3.2.2, charged particles will ionize nitrogen molecules, which will emit fluorescence light. Even though the fluorescence efficiency is not very big (about 4 photons per meter per electron), there are a large number of particles in high energy EAS, this makes the detection possible during no moon dark sky conditions.

The basic idea for this technique is treating the atmosphere as a calorimeter. This technique collects the weak fluorescence light emitted in the EAS longitudinally

by using big mirrors and PMTs, each PMT has a fixed direction in the sky. When a high energy EAS pass through the atmosphere, a set of PMTs will be fired by fluorescence light. The fluorescence light is proportional to the number of charged particles, which in turn is proportional to the primary energy. The geometry of the shower can be reconstructed by stereo fit or by using the trig time of every PMT.

The advantage for this technique is that, this is the only technique can see the longitudinal profile of an EAS directly, so it can measure X_{max}, and primary energy almost model independently and unaffected by shower fluctuations. If two detectors are operated at same time, stereo measurement can give a very good geometry. So the properties of a cosmic ray we are interested in such as energy, direction and composition can be measured very well. Another advantage is that fluorescence light is emitted isotropically, this allows for detection of showers at large distance. So this detector has a very big aperture. The higher the primary cosmic ray energy is, the farther it can be detected from, the bigger aperture the detector has.

The disadvantage of this technique is that it can only be used on clear moon-less nights, the operating duty cycle is only about 10%. When the shower is far away, how the light processes to the detector becomes very important, the scattering of light by molecules and aerosols in the atmosphere will make the light processing strongly depend on the weather condition. The energy resolution will depend on the absolute atmosphere calibration and fluorescence efficiency measurement. HiRes detector is the successor of Fly's Eye detector, the detail of this detector and the important issues mentioned above will be discussed in the following chapters.

3.4 COSIKA Simulation

COSIKA[57] is a versatile package for simulating air shower over a wide range of primary energies. Choices are available for the hadronic interaction model at the highest energy, electromagnetic sub-showers are simulated with the EGS4 code, in which the cross sections and branch ratios are extended to 10^{20}eV by assuming QED is still valid. The following results was calculated by HiRes group based only on QGSJET model [57], which is in good agreement with HiRes measurements. Here I will include only the results which are important for HiRes experiment.

3.4.1 Shower Development and Fluctuation

HiRes detectors measure the longitudinal profile of EAS. The EAS development has been simulated by using COSIKA package for both proton shower and iron shower from 10^{17}eV to 10^{20} eV, the longitudinal profile has been fitted to Gaisser-Hillas function (Eq. 3.5). The lateral distribution fits very well by using NKG function (Eqs. 3.6, 3.7). Figure 3.5 shows an example CORSIKA generated shower fitted by Gaisser-Hillas function. Figure 3.6 shows the lateral distribution of a shower at shower maximum stage (s=1), the solid line is the corresponding NKG distribution.

In order to study the average behavior and the fluctuation of EAS, hundreds of EAS have been generated by CORSIKA and fitted to Gaisser-Hillas function.

The distribution of the parameters in the Gaisser-Hillas function in equation 3.5: X_0, X_{max}, λ and N_{max} depending on the primary energy is given in Figure 3.7 and 3.8 for Proton showers and Iron showers.

It has been found that only N_{max} and λ are correlated. Figure 3.9 shows this

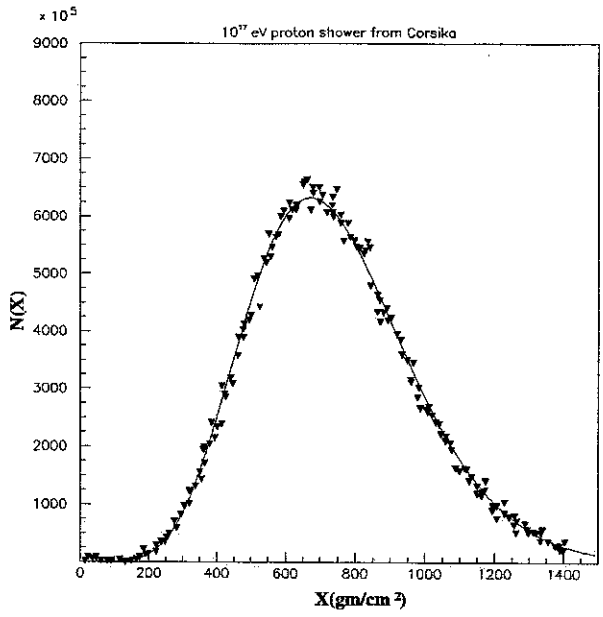

Figure 3.5: *An example longitudinal profile of an EAS generated from CORSIKA, the solid line is the best fitted Gaisser-Hillas function.*

correlation for 10^{18} eV proton showers.

The above distribution and correlation will be used as shower generator driver for Detector MC in Chapter 5.

3.4.2 Primary Energy Reconstruction

In the past, the energy of the pure electromagnetic shower has been determined by[57].

$$E_{em} = \frac{E_c}{X_0} \int_0^\infty N_e(X) dX \tag{3.11}$$

where X_0 is the electron radiation length in air, E_c is the critical energy of an electron in air, and N_e is the electrons in the shower at stage x→x+dx. This

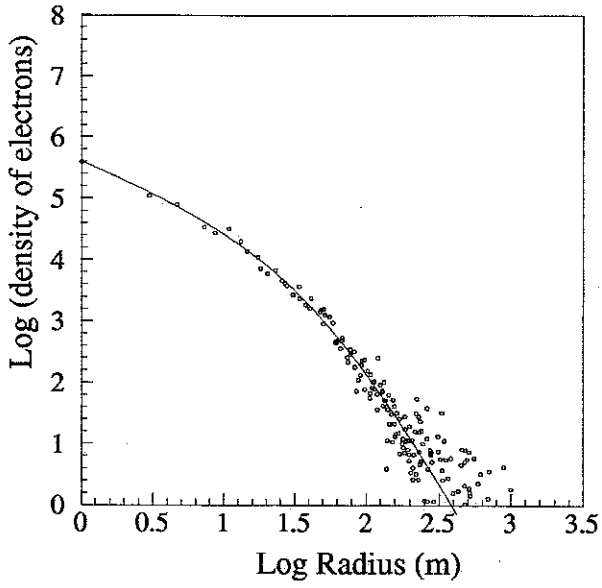

Figure 3.6: *The lateral distribution of an EAS generated by CORSIKA at $s = 1$ stage. The solid line is the corresponding NKG function at $s = 1$.*

equation implies the EM energy of a shower is multiply of total track length of all charged particles with energy loss rate dE/dx given by $E_c/X_0 \approx 2.18 Mev/(gm/cm^2)$ [59].

HiRes detector looks the atmosphere as a calorimeter, and detects the fluorescence light emitted when electron component of EAS pass through atmosphere. It has been found that the fluorescence light efficiency is proportional to dE/dx of the charged particles[58]. Song[57] calculated the mean ionization loss rate (dE/dx) for the electrons in the shower with energy > 100 KeV at age s as given in Figure 3.10. s is defined as age of shower.

By using the averaged energy loss rate $< dE/dX >_s$ at different age s, the air deposited energy of a shower can be calculated by

$$E_{em} = < \frac{dE}{dX} >_s \int_0^\infty N_e(X) dX \tag{3.12}$$

There are other components in an EAS besides the EM component. The energies carried by high energy muons neutrinos and hadronic core ultimately deposit most of their energy in the ground instead of in the air. HiRes detector only measured the energy deposited in the air. So this "missing" energy part has to be corrected from simulation in order to get the primary energy of the cosmic ray.

The relationship between calorimetric energy and primary energy has been previously done by Linsley. Song use the COSIKA simulation studied this effect again, and parameterized the relation with:

$$E_{cal}/E_0 = (0.959 \pm 0.003) - (0.082 \pm 0.003) E_{cal}^{-(0.150 \pm 0.006)} \tag{3.13}$$

in which the energy is in unit of EeV. E_{cal} is calculated based on Equation 3.12 with average $< dE/dX >= 2.19$ [57]. This is an average behavior for proton and iron shower. Since in the real experiment, we can not know the primary particle mass on shower by shower basis, so this average correction must be used. Compare with the pure proton, or iron shower parameterization in Figure 3.11. It can be seen this lack of composition knowledge translates to the energy estimated uncertainty in about 5%.

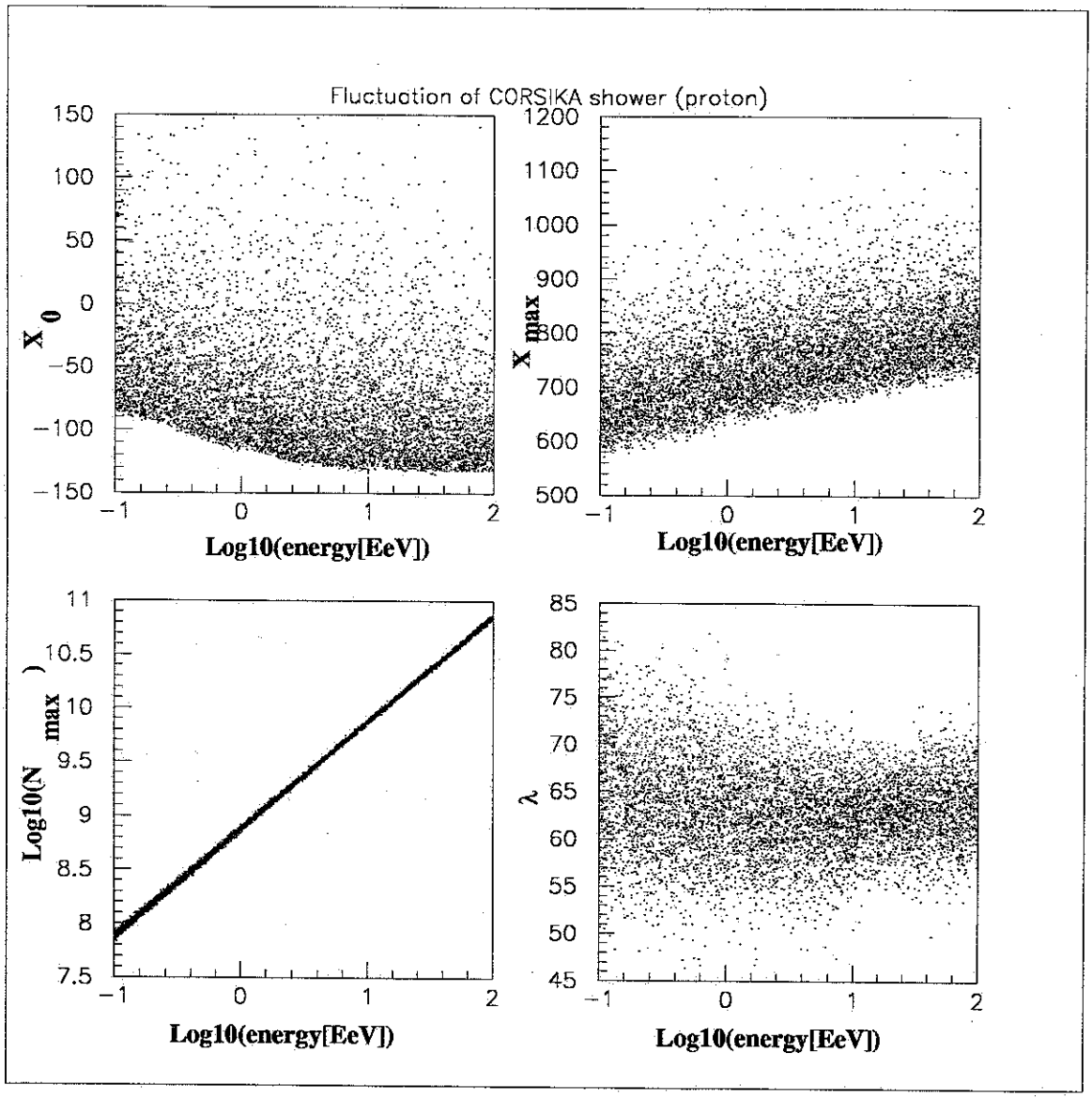

Figure 3.7: *The distribution of Proton initialized EAS generated from CORSIKA, the primary energy is from* 10^{17} *eV to* 10^{20} *eV.* X_0, X_{max}, N_{max} *and* λ *are the best fitting parameters of the shower profile to Gaisser-Hillas function.*

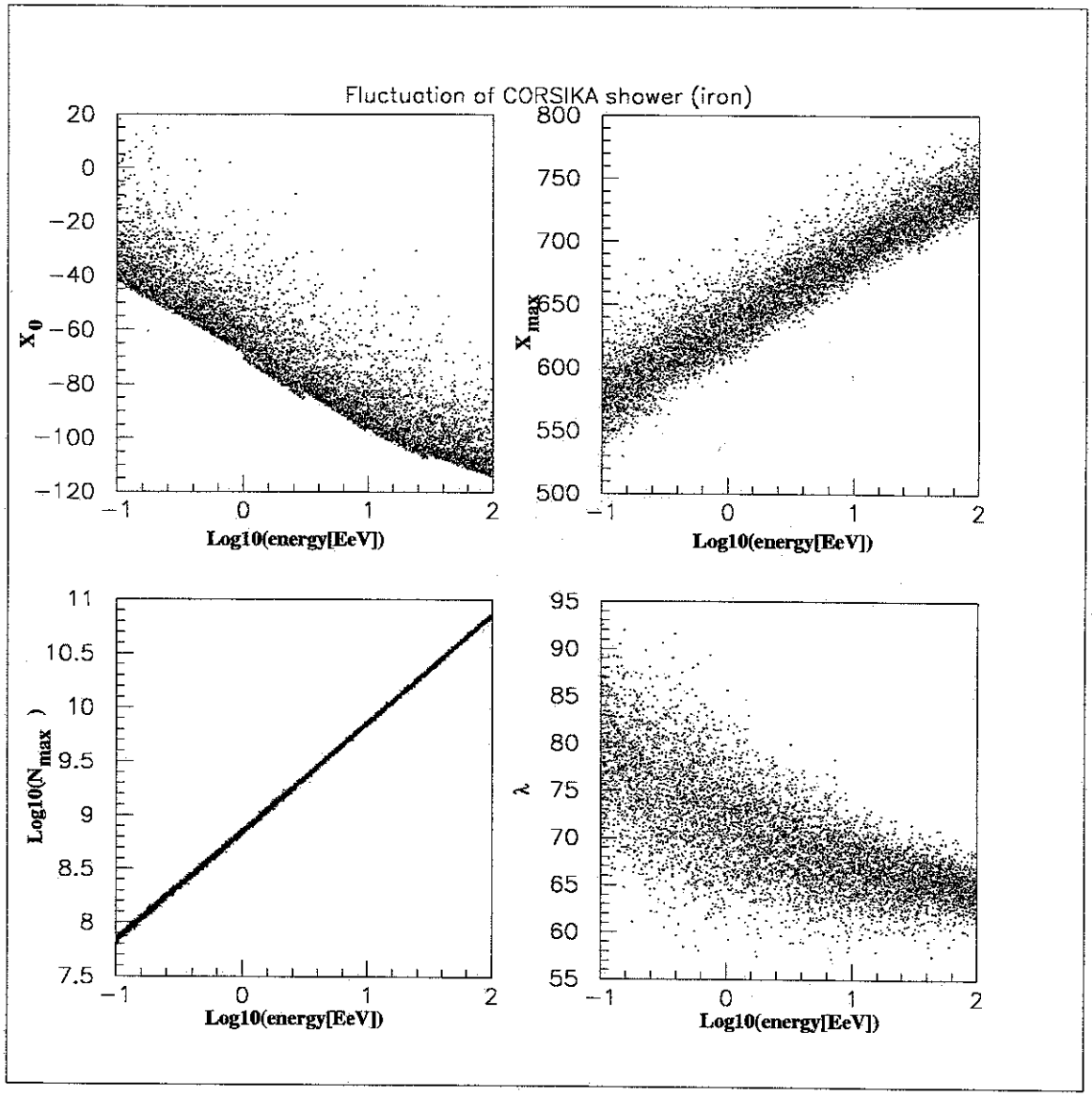

Figure 3.8: *The distribution of Iron initialized EAS generated from CORSIKA, the primary energy is from* 10^{17} *eV to* 10^{20} *eV.* X_0, X_{max}, N_{max} *and* λ *are the best fitting parameters of the shower profile to Gaisser-Hillas function.*

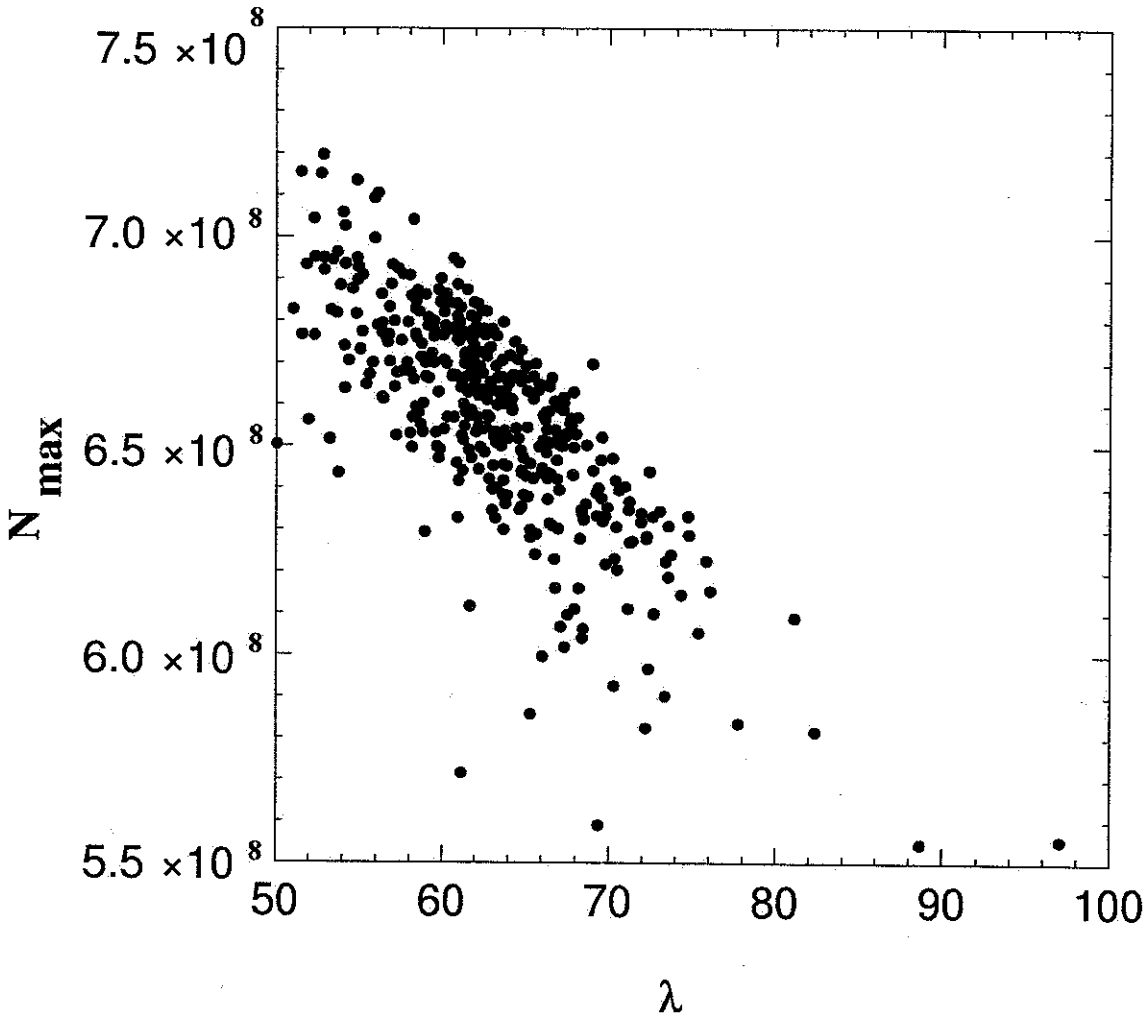

Figure 3.9: *The correlation between N_{max} and λ for the CORSIKA generated proton EAS at energy 10^{18} eV.*

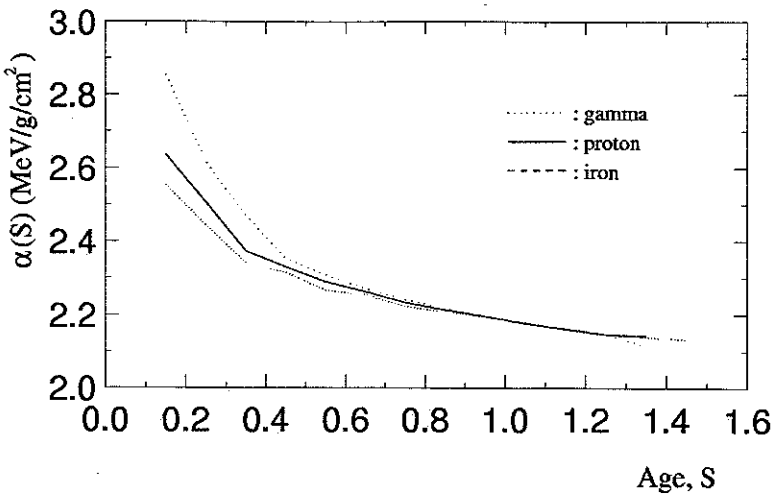

Figure 3.10: *The mean ionization loss rate dE/dX as function of age for gamma-ray, proton, and iron induced shower at 10^{17} eV*

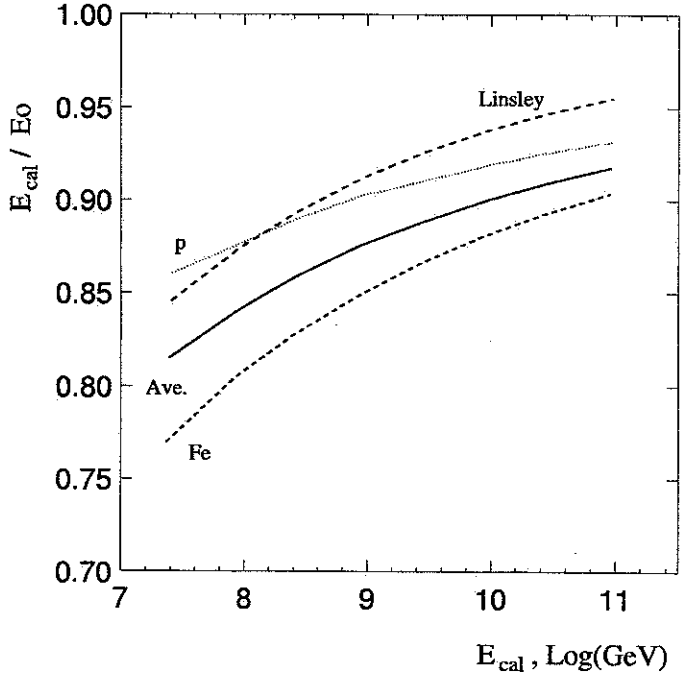

Figure 3.11: *The functions for correcting the calorimetric energy to the primary energy, as a function of calorimetric energy. Shown are the corrections for proton showers(dotted line), and iron showers (short dashed line) and an average of the two (solid line). For comparison, Linsley's function is also shown.*

Chapter 4

HiRes Detector

The High Resolution Fly's Eye(HiRes) detector is an atmospheric fluorescence detector for cosmic rays. As point out in Chapter 3, because of the advantages of fluorescence technique, HiRes is designed to study the energy spectrum, composition and anisotropic of UHE cosmic ray in very high resolution way. The detector is optimized for cosmic ray energy of 1 EeV and above. HiRes is located at Dugway Proving Ground in western Utah and includes two sites separated by 12.6 Km distance. One is the 22 mirror HiRes-I detector at the Five Mile Hill site, The GPS determined coordinates are $112^o50'08.8764''$W longitude, $40^o11'42.6156''$N latitude, and 1597m above sea level. The other is the 42 mirror HiRes-II detector at the Camel's Back Ridge site, the GPS determined coordinates are a longitude of $112^o57'32.292''W$, latitude of $40^o07'55.452''W$, and an 1553m above sea level. HiRes-I site started taking data from May 1997. The construction phase of HiRes-II detector was completed in the end of 1999. These two sites are operated independently, the data can be treated in stereo model or in monocular model for each site. When a cosmic ray shower triggers both sites, we call it a stereo shower. When a cosmic ray shower triggers only HiRes-I or

Trigger Model	Trigger Aperture
HiRes-I Monocular	$1.6 \times 10^4 Km^2 str$
HiRes-II Monocular	$1.8 \times 10^4 Km^2 str$
HiRes-I&II stereo	$1.2 \times 10^4 Km^2 str$
Combine HiRes-I&II monocular	$2.2 \times 10^4 Km^2 str$

Table 4.1: *The trigger apertures of HiRes detectors for cosmic rays with energy of* 10^{20} *eV. The combined monocular trigger aperture is almost double the stereo trigger aperture.*

HiRes-II, we call it a monocular shower. Thus there are four totally different apertures. For cosmic ray events with energy 10^{20}eV, the trigger apertures are shown in Table 4.1

The trigger aperture is bigger in order of magnitude than any other cosmic ray experiment in history, and will have a very good statistics on UHE cosmic ray study. Unfortunately the stereo model was in full time running only since the end of 1999. This report will only focus on the monocular observation from HiRes-I detector, even though the author is involved in construction of HiRes-II detector.

4.1 Detector Overview

HiRes detector is the successor of Fly's Eye detector, which was the first successful fluorescence detector[45]. HiRes detector increases the signal to noise through decreasing the field view of each PMT from 5.5^o to 1^o and increasing the mirror size from 1.5m to 2.0m. This improvement increases the trigger aperture of the detector.

The small pixel design will also help in studying the EAS longitudinal and lateral profile. A prototype HiRes detector started to employ in 1991. The prototype HiRes detector with 14 mirror at HiRes-I site and 4 mirror at HiRes-II site was in full operating from 1994-1996. The detectors at the two sites have different electronic systems. The stereo running model of prototype detector helps the reconstruction study on future stereo detector. The combined running of prototype detector with CASA-MIA detector was the first hybrid detector in UHE cosmic ray, this helps the composition and longitudinal profile study for cosmic ray[20, 39].

The prototype detector was shutdown and reorganized for HiRes-I final configuration in the winter of 1996/97. The HiRes-I detector began operating with 14 mirrors/PMT clusters re-deployed from HiRes-I prototype during May/June 1997 running period. For the June/July run, three of the mirrors from HiRes-II prototype at Camel's Back Ridge were moved to HiRes-I site and bring up to 17 mirrors. This was the configuration until May 1998, when construction finally started to deliver new PMT clusters and electronics and bring HiRes-I up to 21 mirrors. The 22th mirror is not installed. HiRes-I detector has totally 22 mirrors, it has optimized aperture for 10^{20} eV cosmic rays. The 22 mirrors were arranged to cover the full azimuth range and between 3 degree and 17 degree of elevation. Figure 4.1 shows the HiRes-I detector angular coverage on the sky. The outer edge represents 3^o above the horizon.

The layout of the mirrors is shown in Figure 4.2. The experiment is run from the central facility, which houses the central computing facilities, central timing electronics, Yag laser and operator quarters. Ethernet line is used for communication between the control software and the mirrors. Optical fibers are also connected from Yag laser to every mirrors for calibration purposes (see section 4.6.6). The control software is also connected with the xenon flashers installed between HiRes-I and II field and

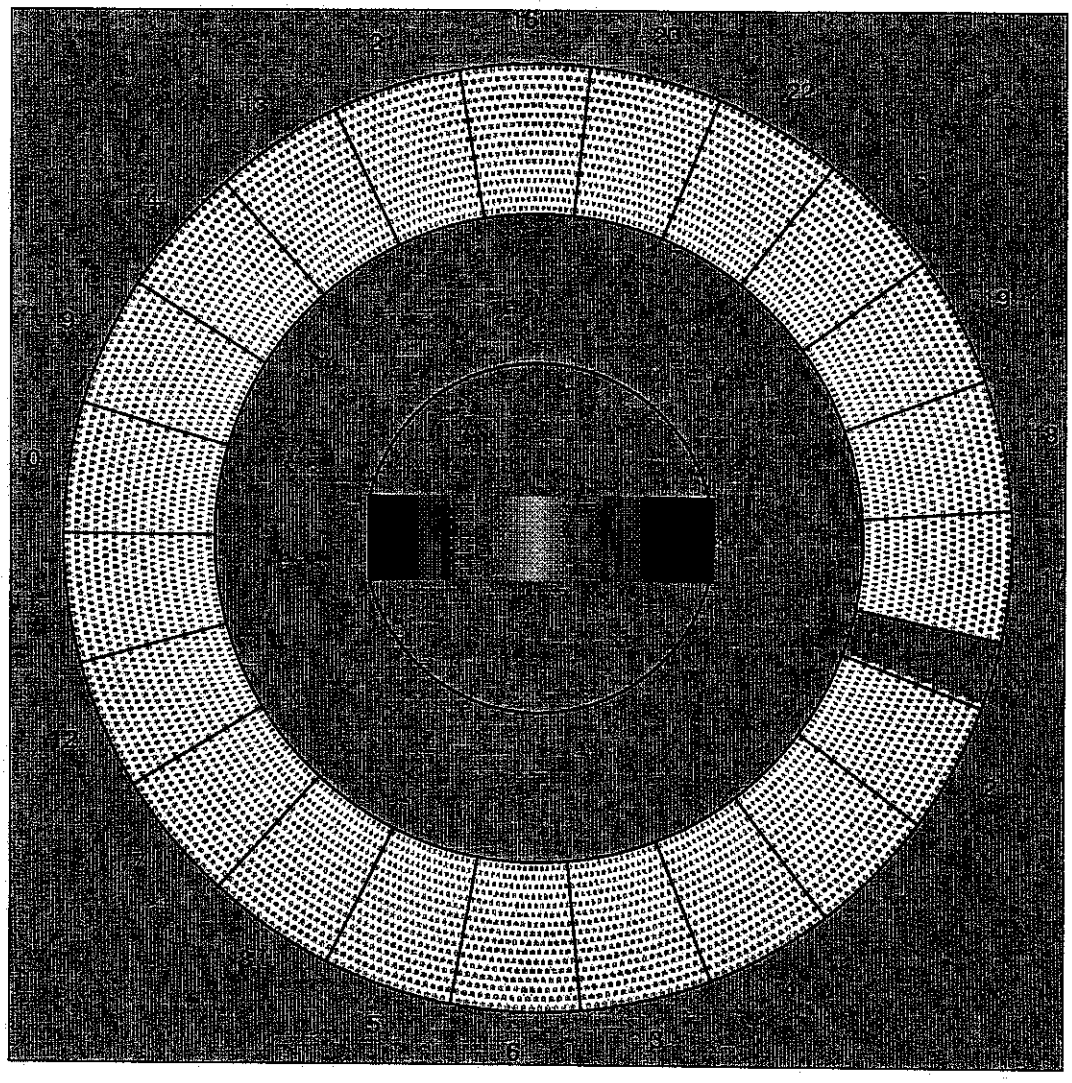

Figure 4.1: *The field view of HiRes-I detector mirrors. The outer edge is 3° above horizon.*

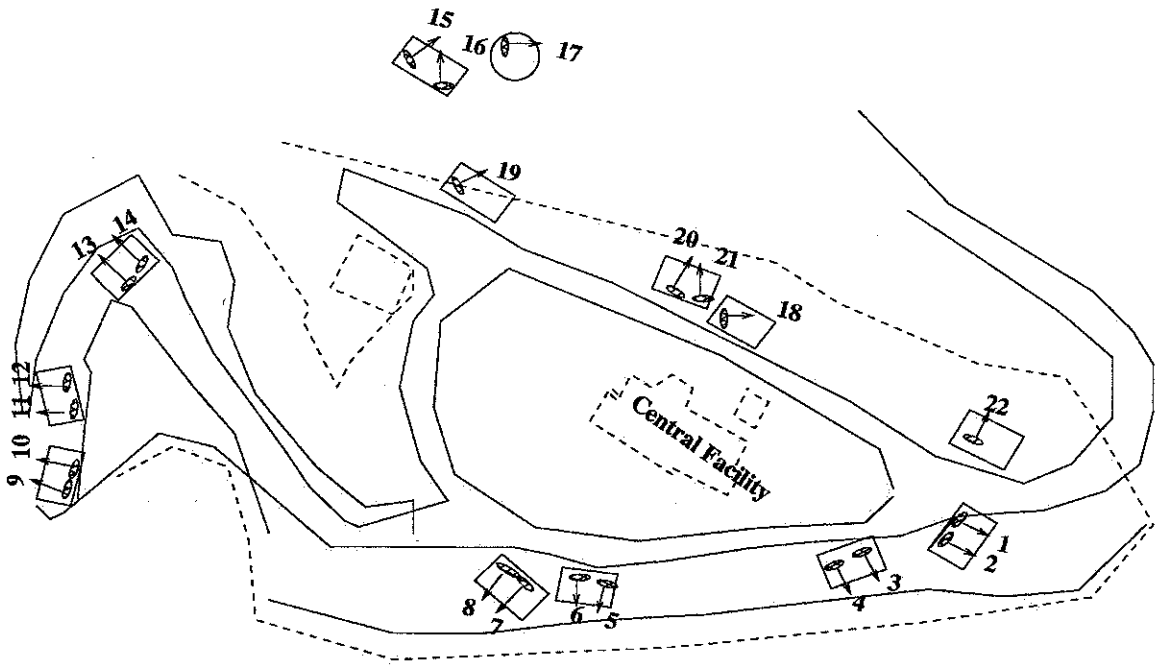

Figure 4.2: *Physical layout of the HiRes-I detector mirrors.*

a steerable Yag laser installed at HiRes-II site, these systems are for atmosphere calibration.

4.2 Mirror Components

HiRes-I detector is mainly re-deployed from HiRes prototype detectors, the additional 4 mirrors are also designed same as HiRes-II prototype mirrors. The hardware of prototype detectors has been described in very detail by Kidd[41] and Wilkinson[60]. AbuZayyad[61] has described the modification from prototype to HiRes-I. Here I will simply review the mirror components, and complement those given in above references.

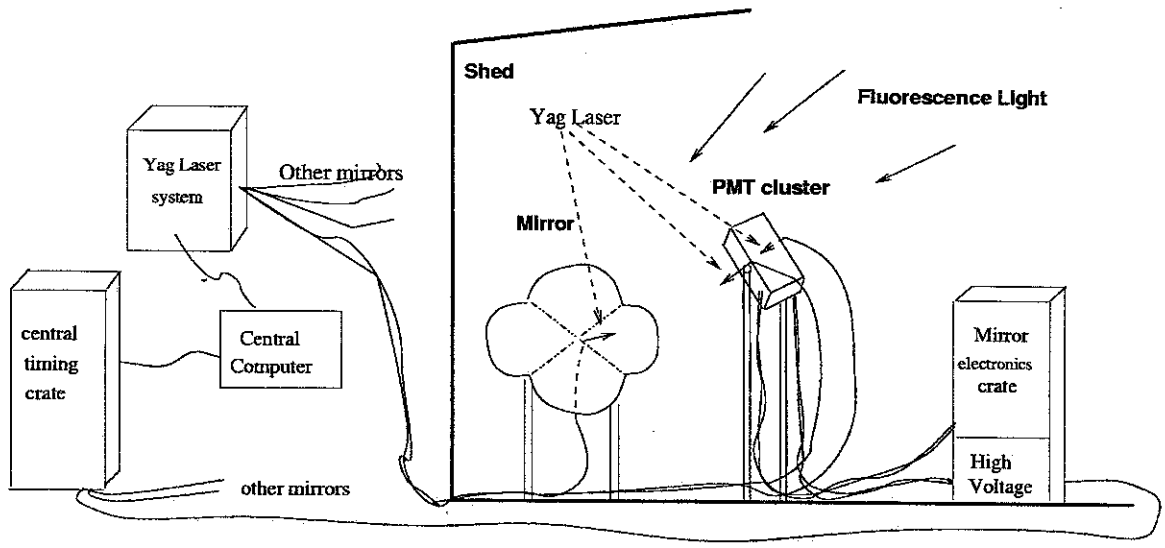

Figure 4.3: *The basic HiRes detector system. In the figure one building with one mirror data acquisition system is shown. Every building is connected to the central computer, central timing crate and central Yag laser system.*

The basic system for one mirror is shown in Figure 4.3. Each mirror unit has an optical system, PMT cluster, and HV supply with electronics crate. The unit is housed in a building. The mirror unit is connected with central building through Ethernet and optical fibers. Fluorescence light is collected by mirror, focused onto the PMT cluster, trigger PMT and digitized by electronics, the information is stored on disk by central computer via Ethernet.

4.2.1 Mirror

Each mirror unit has a 2 meter diameter spherical mirror in clover shape with the effective area of 3.75 m^2, which focuses light onto a PMT cluster. The mirror has a radius of 474 cm. The mirror reflectivity is wavelength dependent as shown in Figure

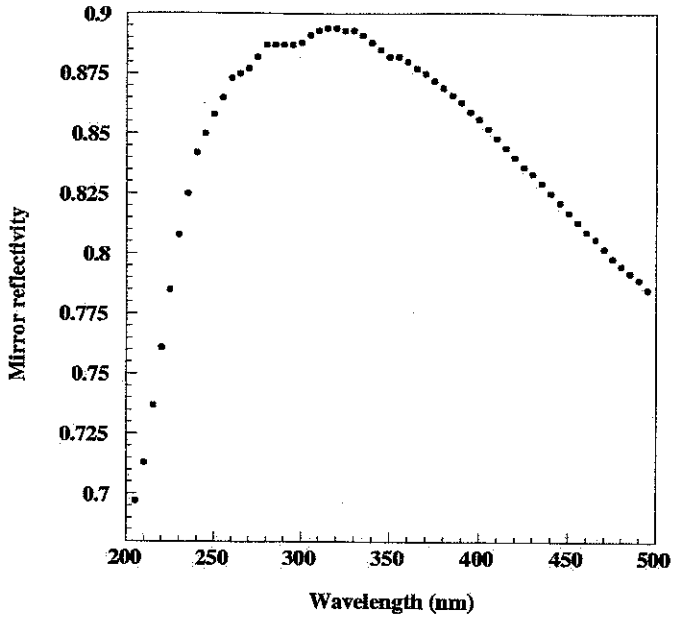

Figure 4.4: *The measured wavelength dependence of the mirror reflectivity*

4.4, In this figure the measurement is taken from a washed "clean" mirror. It has been found that this reflectivity will decrease as the time going and dust accumulating on the surface. But the average reflectivity in the field over the wavelength band of 300 - 400 nm is about 0.82 when it is stable. The mirror to cluster distance is optimized to minimize the spot size across the face of the cluster, The optimal mirror-cluster separation is 0.485 times the mirror radius. The pointing direction and the position of the mirror and cluster were carefully surveyed into position during installation by using a theodolite. In 1999 every mirror and cluster were re-surveyed by using stars position.

4.2.2 PMT Cluster

The PMT cluster consists of 256 close packed 40 mm diameter hexagonal PMT in a honeycomb geometry of 16 rows and 16 columns. Each PMT has 1 degree field of view.

The absolute gain and quantum efficiency of PMT across the face were measured, only PMTs with no greater than 10% non-uniformity of quantum efficiency across the face were used. Each PMT is soldered to a high voltage bleeder chain used to supply HV to PMT and a preamp circuit. The preamp adds a gain of 100 onto PMT pulse and generate differential signal which remove the DC night sky background, test PPG pulses can also be injected to preamp circuit to calibrate electronics. The PMT cluster is wrapped in magnetic shielding metal. A cooling fan located at the top of cluster, heat conducting paste on the sides of cluster box and aluminum sheet runs through the center of the cluster are used to cool the cluster. A temperature sensor is located in the center of the cluster. An absorption UV filter is mounted in the front of the cluster, which enhances the signal to noise by a factor of 1.7.

4.2.3 Electronics And Data Acquisition

The mirror electronics, high voltage supply and distribution system and low voltage supply are set in a VME crate per mirror. The voltage supply provides power for every PMT in the cluster. Both high voltage and low voltage are read back by the crate for every PMT.

The mirror electronics is shown in Figure 4.5. including (a) A 68030-based Vxworks Force controller board (mirror CPU); (b) 16 data acquisition boards (Ommatidial boards) (C) a programmable pulser generator(PPG) board; (d) a trigger board; (e) a sensor/delay board (Garbage board). The PPG produces square pulses of varying width and amplitude and is used for diagnostic and calibration purposes. The garbage board handles the high voltage readout system, controls preamp power to individual PMT sub-cluster through the cluster relay board, opens and shuts shed

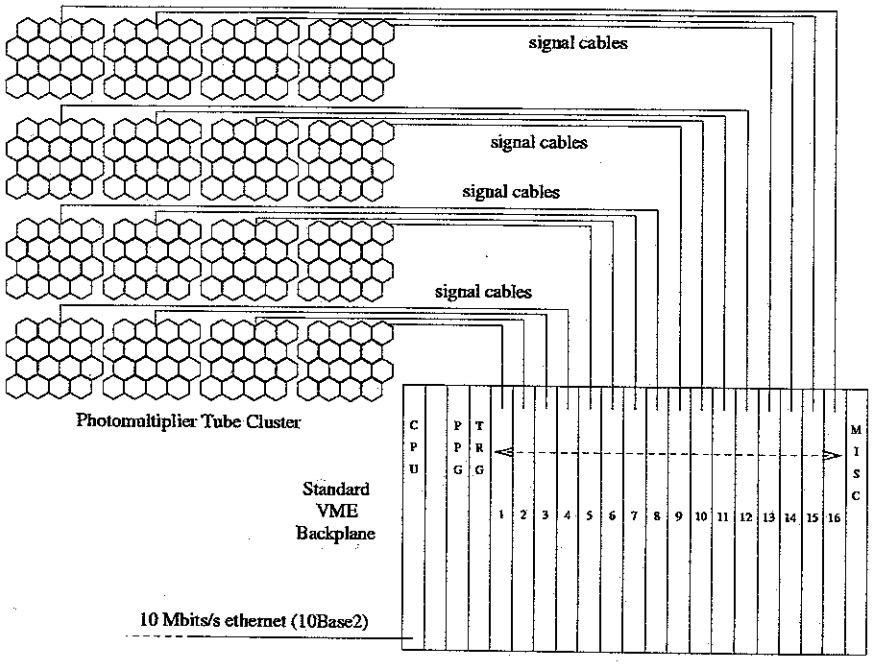

Figure 4.5: *Block diagram of mirror electronic crate components.*

doors, and monitors crate temperature.

The mirror CPU board is the interface between the central computer and the mirror crate. The mirror CPU receives commands from central computer for calibration or data collection, and then send to the relevant boards. It collects the TDC and QDC information for PMTs in a mirror event, places them in an event packet, sends back to central computer. It also collects information on trigger rates, thresholds, network performance and dead time.

The Ommatidial boards store the integrated waveform charges and waveform leading edge arrival times above threshold, integrate and digitize the PMT signal, save the trigger time of PMT, monitor the trigger rate, and send these information to mirror CPU. There are two version of basic S/H systems used for BigH mirrors.

Rev. 3 mirrors were employed by the HiRes-I prototype mirrors, Rev. 4 mirrors are the four HiRes-II mirrors and the additional mirrors. The basic structure is same for both version. The block diagrams is shown in Figure 4.6.

In order to maximize the sensitivity to cosmic ray EAS signals whilst minimizing the effects of night sky background noise, thus two channels are designed for each PMT: channel A optimized for fast, close pulse and channel B for wider more distant pulses. In both reversion, the tube signal is split into two and driven through two readout channels A and B. For each channel the signal is further split into two lines, one passing through a filter and into a comparator to check trigger status of that tube; the other passing through a delay line and into integration circuitry. The main difference of these two reversions is that, for Rev. 3 only one of Channel A or Channel B is allowed to trigger, but in Rev. 4 either channel can be triggered independently. As HiRes-I(BigH) detector is dedicated for highest energy cosmic ray study, which correspond to wide farther pulse, so only Channel B is opening.

The triggering rate of each PMT is measured using a 16 bit scaler and is monitored by an 80188 micro-controller chip, which maintains a constant triggering rate preset to 200 Hz. The PMT triggering time is measured using TDC.

The Trigger Board handles the event trigger pattern. The Ommatidial board store the time and charge integrals for each PMT in each sub-cluster. When a PMT signal rises above threshold, the PMT trigger flag is set for 25 us. A sub-cluster trigger is formed when a pattern of PMT triggers within a sub-cluster matches a trigger pattern. Normal operation defines a sub-cluster trigger as three triggering PMTs with at least two hexagonally adjacent. The output of the sub-cluster trigger lookup is reshaped into a 25 us pulse and used to check mirror trigger pattern. Normal operations require at least two sub-clusters to trigger in the 25 us window. A mirror trigger

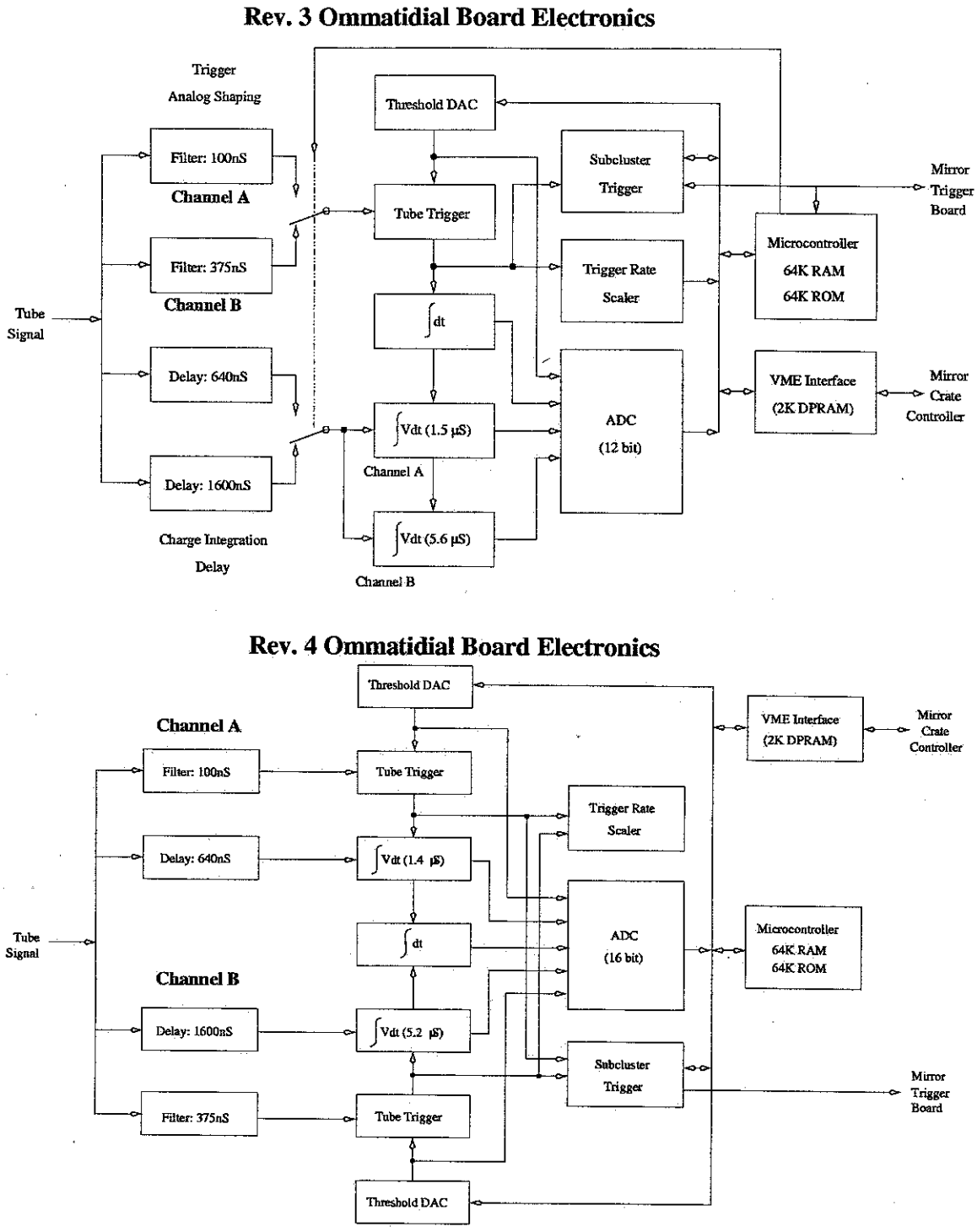

Figure 4.6: *Block diagram for HiRes data acquisition 'Ommatidal' board for Rev.3 (top) and Rev. 4 (bottom) for both channel A and channel B. For HiRes detector only channel B is in use.*

is also sent to adjacent mirrors, allows the adjacent mirrors triggering requirements down to a single sub-cluster. A mirror trigger generates a mirror save condition in the detector electronics and prevent the PMT charge integrals from being cleared. At the end of this period, a mirror trigger signal is sent to central timing crate so that the absolute mirror time is recored.

4.3 Central Timing

The central timing crate (CT) provides the master clock which is used to record mirror triggering times, and to provide timing pulse to the mirrors. The basis of the timing system is a 24 bit, 4MHz scaler (25ns resolution) which is synchronized to absolute UTC to within 340ns by a global position system(GPS) clock. The detail of this timing system is described by Wilkinson [60].

The GPS clocks produce a synchronization pulse at the start of the UTC second. This is used to latch the 40MHz scaler. The 40MHz scaler is used to provide inter-second times with the resolution of 25ns. When a mirror trigger hold-off is raised, a signal is sent down a dedicated line to latch the value of the 40MHz scaler. The tens and ones of the absolute millisecond time are also recorded from the GPS. The mirror that triggered, the scaler value and lower digits of the millisecond time are packaged together and placed in a timing packet. This timing packet is then sent to the central computer and added to the data stream, the event and timing packets are matched later in software.

4.4 YAG Laser

The Yag laser system is used for nightly calibration of the PMTs response[62]. The Yag laser system is set in a facility. Optical fibers drive the laser output to every mirror building as shown in Figure 4.3. One fiber sets at the center of the mirror cloves and illuminate the cluster face directly, this is used to calibrate the PMTs gain. Another two fibers set on both sides of the cluster box and illuminate the mirror which reflect the light back onto cluster, this is used to calibrate the mirror reflection efficiency. The Yag laser system is connected to the central computer, the operate drives the system when calibration is needed. The detail of the calibration by using Yag laser is discussed in Section 4.6.6.

4.5 HiRes2 Steerable Laser System(HR2SLS)

A steerable laser system is installed at HiRes-II site[63]. This system is used for atmospheric calibration.

The system provides a pulsed beam of 355nm light that can be steered in any direction above horizon. The direction, energy, and time of each pulse is measured and recored locally. Different energies and polarizations can be selected. The system is remote operated.

Figure 4.7 shows the components of HR2SLS. HR2SLS uses a pulsed YAG laser which produces a linearly polarized beam at 355nm. with a duration of 5.5 ns and a beam divergence less than 0.05°. The energy of each laser shot is monitored by sampling 10% of the beam by a microscope slide (after Jan. 2000 this sampling changed down to 1%). This fraction of beam is then measured by a calibrated phot-

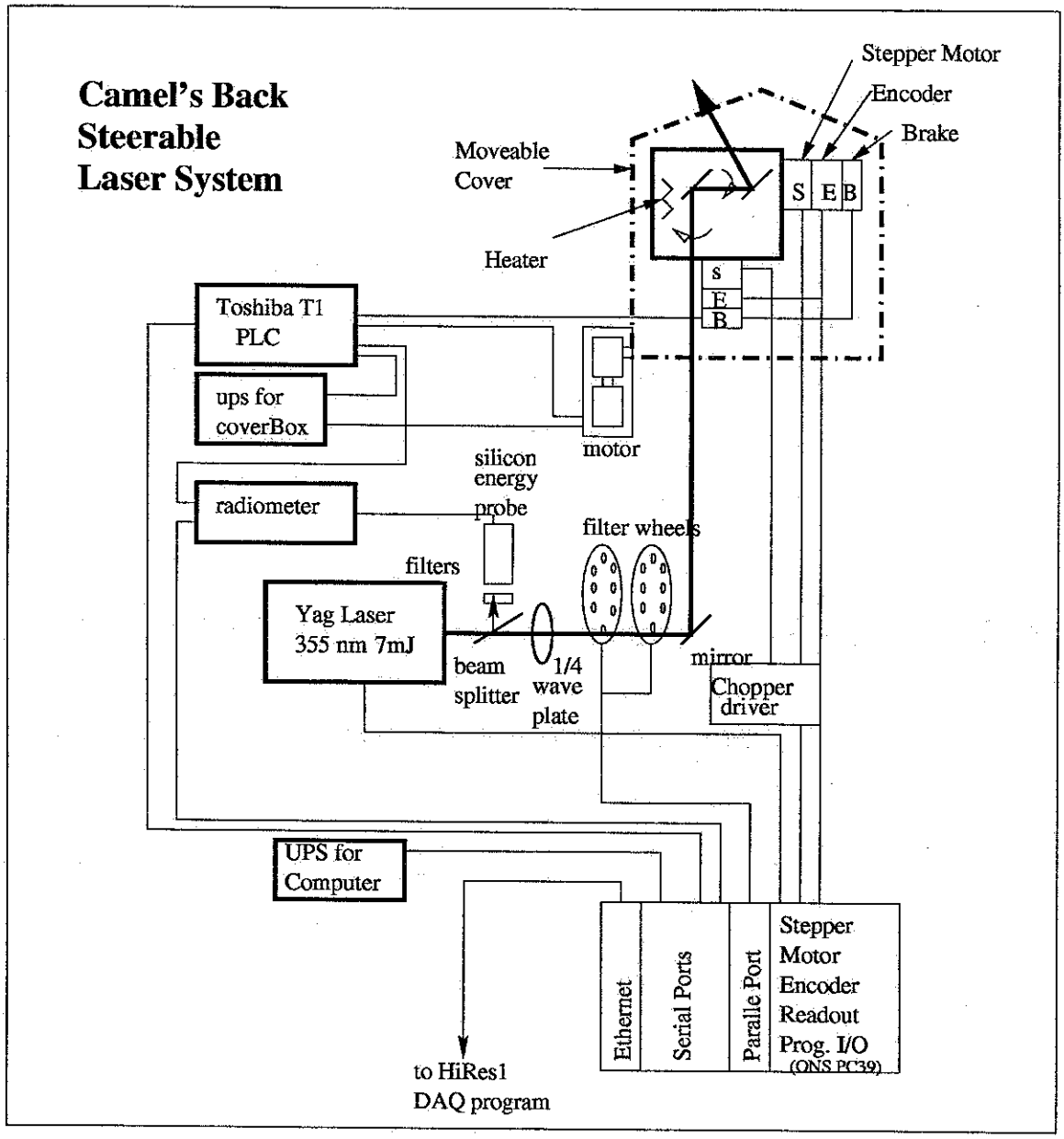

Figure 4.7: *Schematic diagram of HR2SLS components.*

diode probe and radiometer. The energy measurement accuracy is 2% relatively and 10% absolutely. Following the slide, the beam passes through a 1/4 wave plate and becomes a circularly polarized beam. Then the beam passes through two computer controlled filter wheels. These two wheels combined give the operator the ability to change the intensity(from 48% to 0.08% of the maximum intensity which is 6 mJ) and the polarization of the beam (Circular , Vertical Linear or Horizon linear) remotely. Then the beam enters a large vertical pipe, and can be directed to any direction above horizon by rotating two 45^o dielectric mirrors through a mechanism system. The laser direction is read out by rotary encoders that measure the azimuthal and zenith angles of rotation. The accuracy of this encodes is about 0.1^o. The over view of the HR2SLS pointing direction and the detector is shown in Figure 4.8, the circle has 25 km radius. HR2SLS is trying to cover the range the real shower can be detected by HiRes-I.

The HR2SLS is controlled by a 166 MHz PC which is networked to HiRes-I and II site. Two special boards are installed to control the laser system. One is a four-port serial board communicates with the radiometer, the laser, an Uninterrupted Power Supply(UPS) and a Programmable Logic Controller (PLC). Another motion control board is used to articulate the laser steering head.

The Laser energy and direction can be measured very well locally by HR2SLS, in the mean time the light scattered out of the beam is also measured by HiRes-I detector 12.6 km away. The intensity of the scattered light measured at HiRes-I depends on the atmosphere condition especially the aerosol attenuation and the phase function. So by using this laser system, the atmosphere condition can be calibrated. Since we can not really generate a beam of cosmic ray showers to calibrate HiRes detector. The well known energy and direction of laser shots work as a calibration

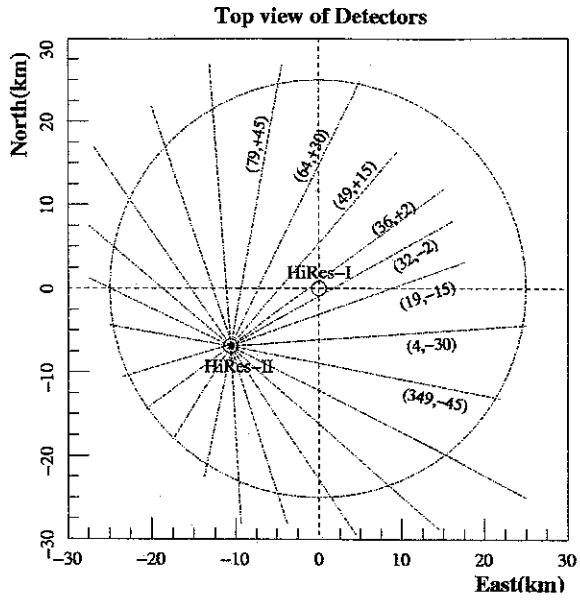

Figure 4.8: *The over view of the HR2SLS laser pointing directions and the HiRes-I detector. The angles shown are the azimuth angle and the opening angle from laser direction to HiRes-I detector.*

system for HiRes detector. As one of the most important work done by the author, how this calibration is done will be given in Chapter 7

Inter-site flashers are also installed in the field between HiRes-I and II sites[64]. In this report these flasher information is not used in the atmosphere calibration, so I will not describe it. For reader who are interested in it be refer to [64].

4.6 Detector Calibration

The HiRes detector has significant difficulty in calibration. Unlike a typical particle physics experiment where the detector response to a well understood test beam can be measured, there is no test beam for HiRes. So detector calibration has too be absolute rather than just relative. HiRes calibration can be broken into five components:

mirror behavior, PMT response,filter response, electronic response, and atmosphere. Calibration parameters are obtained for the different components and are combined to enable us to calibrate data from normal detector operation. In the following I will discuss how these components are calibrated. Atmosphere Calibration will be discussed in Chapter 7.

4.6.1 Mirror Behavior

Mirror Reflectivity. The are two sets of Yag lasers shining to the PMT when the calibration data is taking: one laser is mounted at the mirror center shining directly to the PMT cluster, the other is mounted on the side of cluster such that the light shining to the mirror can be reflected to the PMT cluster. The relative night to night variation in the absolute mirror reflectivity can be measured by comparing the average PMT response for this two situations. The absolute mirror reflectivity is about 0.82. this value will be used in the data analysis.

Mirror Spot Size. The angular coverage of the whole cluster is 16×14 degree. Because the mirrors are not parabolic, they can not focus light onto flat faced clusters uniformly through out the whole angular range. So a ray tracing program was used to calculate the spot shape across the cluster (described in section 5.4.2). The result is shown in Figure 4.9. It can be seen that when the image moves to the edge of the cluster, the spots coma grows worse and the central spot size grows larger. Randomly trace millions of rays from any given source direction to the PMT cluster, the number of rays collected by every tube can be counted, a complete ray tracing table is built up in this way. This table will be used in both the detector Mont Carlo and reconstruction.

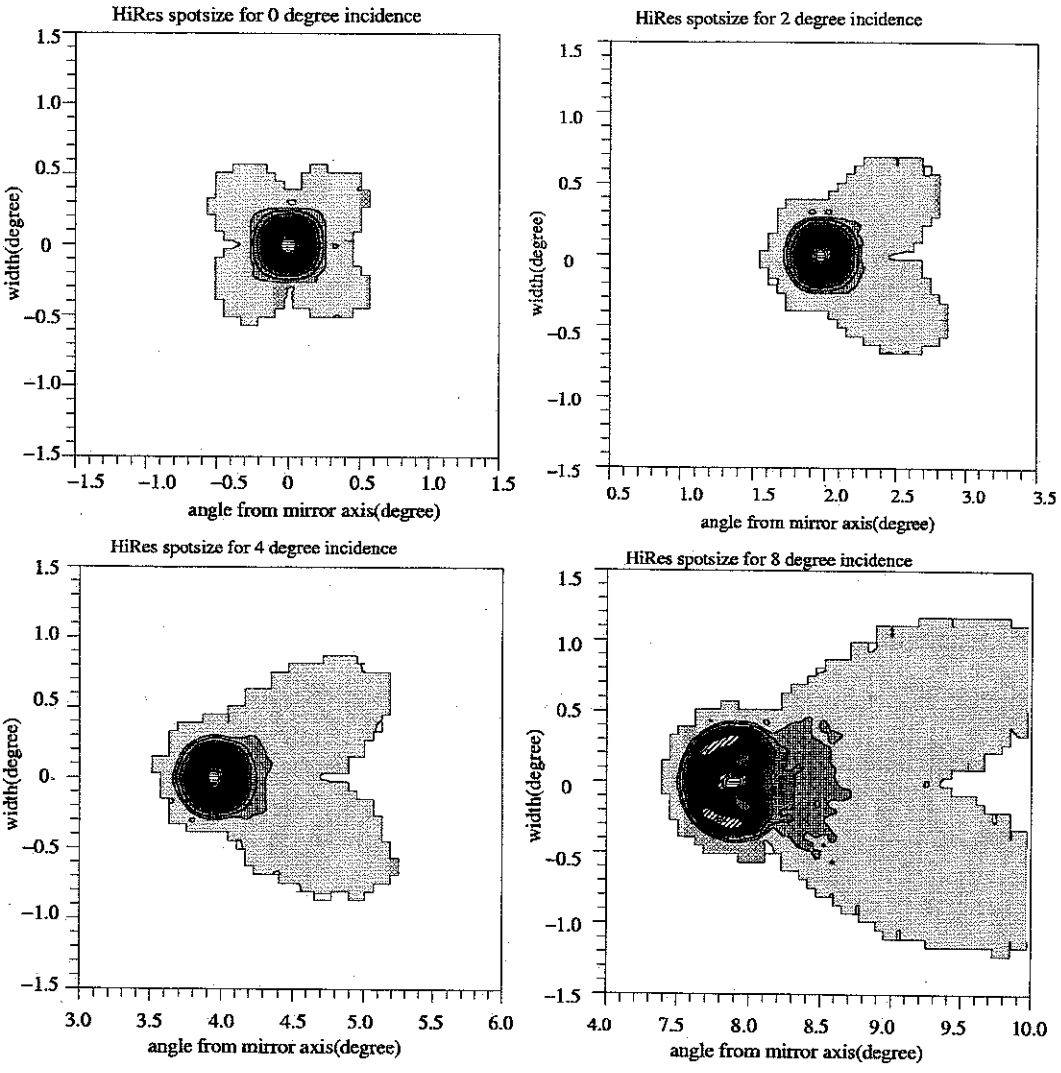

Figure 4.9: *The mirror spot patterns on the PMT cluster for different light source direction: source point laying 0, 2, 4, and 8 degree away from the mirror axis.*

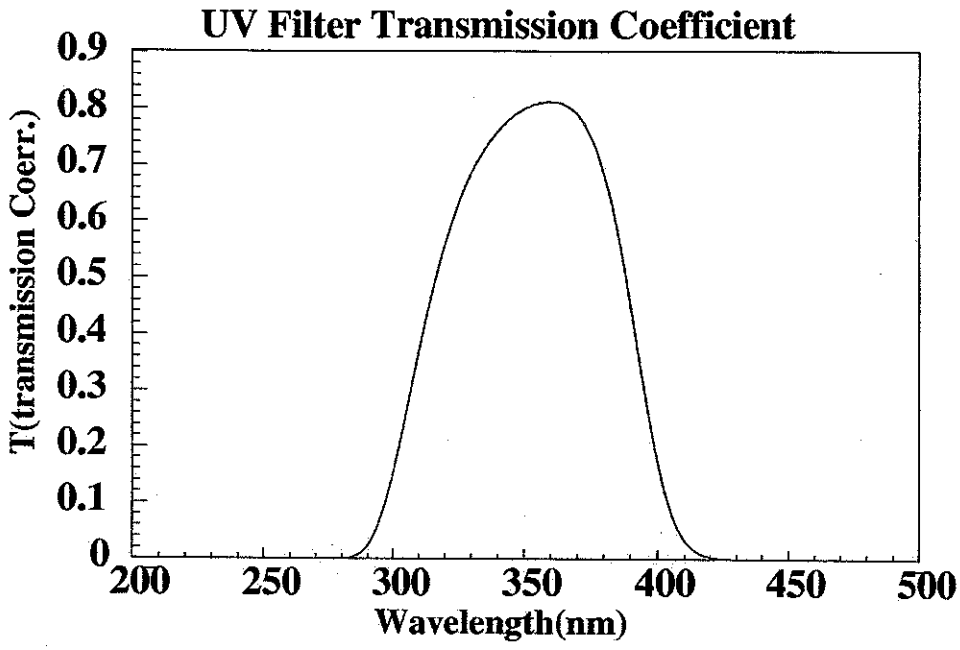

Figure 4.10: *Transmission curve for HiRes UV filter.*

4.6.2 UV filter Response

In front of the PMT cluster, there is a UV filter with 0.2 inches thick coving the entire cluster. They were custom manufactured for HiRes in a single batch. The transmission of each filter was measured. The standard transmission curve of this UV filter is shown in Figure 4.10. The uniformity within each filter is about 3%.

4.6.3 PMT Response

PMT response includes the quantum efficiency as a function of wavelength, absolute gain as a function of applied voltage, temperature dependence, the two-dimensional response function mapped across the face of the PMT. In order to understand PMT response, a testing station was built at the University of Utah as diagrammed in

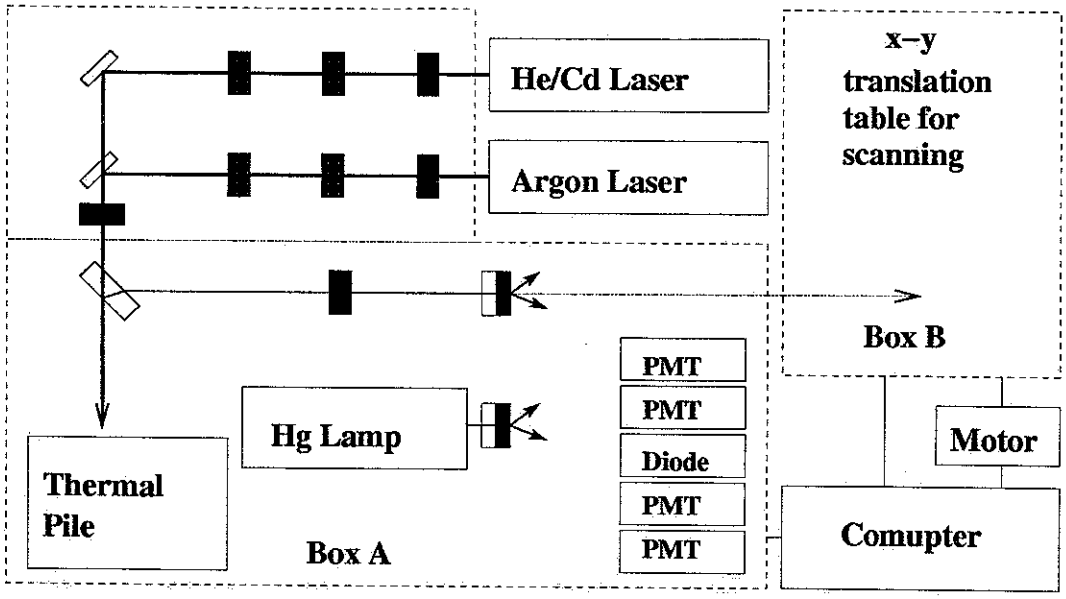

Figure 4.11: *PMT response testing facility*

Figure 4.11. This setup is described in [65]. Here I only briefly describe how the calibration is done.

Most of the system is located in a light tight box, except the laser. Box A is used to measure the anode sensitivity and cathode quantum efficiency, Box B is used to measure the spatial uniformity of gain and quantum efficiency. The light source is either the 351 nm or 364 nm line of Argon laser or the 325 nm line of a He-Cd laser. The light beam is split and attenuated, the intensity is monitored by a thermopile. Stray light along the light process is absorbed and minimized. For measurements in Box A, the laser beam passed through a Teflon diffuser to uniformly illuminate 4 PMTs and a NIST calibrated diode which provides an absolute calibration for the system. The typical light intensity is arriving at PMT is 8×10^6 photons/cm^2/s. The Teflon diffuser is moved when scan the PMT face, computer controlled stepper motors allows X-Y scanning, up to 16 PMTs can be scanned in a single cycle. The

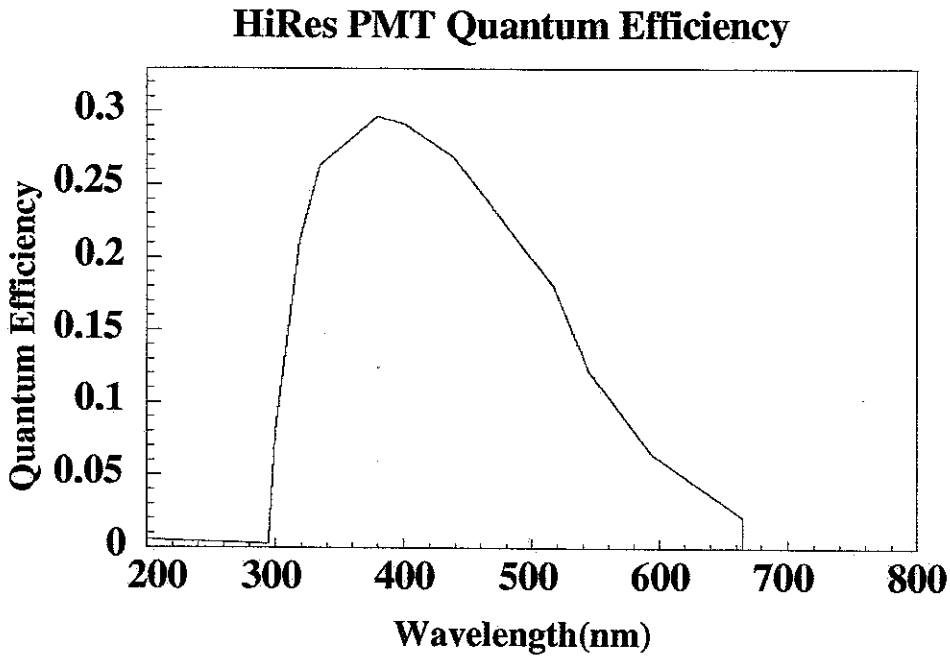

Figure 4.12: *Standard quantum efficiency as a function of wavelength for the PMT's used in HiRes detector.*

results are saved in the computer.

PMT Quantum Efficiency Quantum efficiency was measured for every PMT used in HiRes detector. The quantum efficiency changes little from PMT to PMT. The standard quantum efficiency is given in Figure 4.12. The UV filter in front of the PMT cluster will also affect the sensitivity of the detector to the atmospheric nitrogen fluorescence spectrum. The standard UV filter efficiency is given in Figure 4.10. The combination of quantum efficiency and UV filter efficiency gives the resultant sensitivity of the detector to fluorescence spectrum which is given in Figure 4.13

PMT Gain The PMT gain depends on the HV applied between the tube anode and cathode. It can be well described by the function:

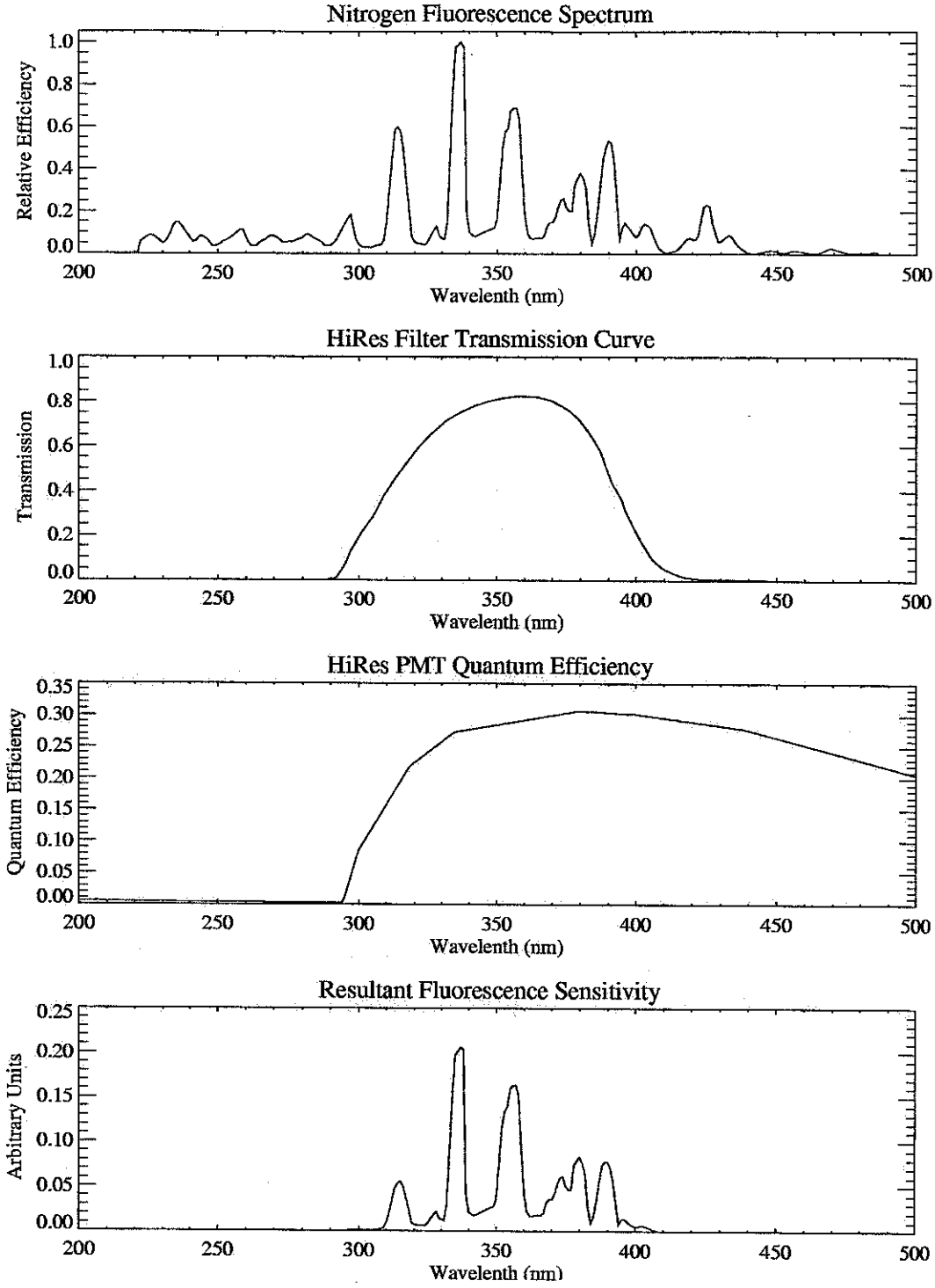

Figure 4.13: *Resultant fluorescence spectrum after taking into account UV filter and PMT quantum efficiency.*

$$gain = exp(\alpha) \times V^{\beta} \tag{4.1}$$

where α, β are measured for every PMT. The distribution of α and β were roughly $\alpha = -31.70 \pm 0.77$ and $\beta = 5.89 \pm 0.14$. The PMTs are operated at a gain about 10^5 for HiRes detector.

PMT gain also depends on temperature in about $0.5\%/^oC$ which is significant because the detector is operated over temperature range $-15^oC - 40^oC$. The heat cooling system attempt to maintain a uniform cluster temperature. The variation of the temperature is measure by an temperature sensor and recorded by the Garbage board.

PMT Response Profile are measured by the scan facility given above. The standard profile is given in Figure 4.14.

The testing scan facility is also used to keep or reject PMTs. When a PMT has too small active area or have a 20% or more non-uniformity across the PMT face (except for the area with 3mm of the edge) will be rejected. Tubes must also have a minimum gain at a set voltage. Tubes with similar response are grouped in same cluster and make it easier to set same gains within cluster. But remember the tube scan only gives the initial information about the tube response, the real on time detector calibration will be done in other way given following.

4.6.4 Electronics Response

The electronic system for each channel includes a preamp in the photo-tube and one Ommatidial board for every 16 tubes. The PPG board in each crate injects a square

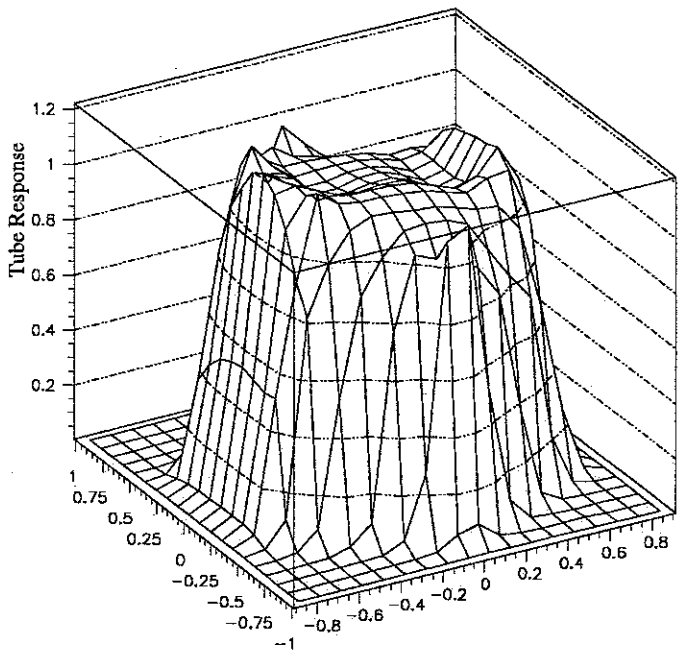

Figure 4.14: *The standard tube profile function measured from local testing facility. It will be used in the ray tracing and data analysis.*

pulse of varying width and amplitude into the input of the preamp of each PMT. The entire tube response can be mapped out. This is done both at the start and end of every run.

It has been found the PPG and OMB linearity is very good by checking with a high quality digitized oscilloscope. Unfortunately the preamp is nonlinear at both the high and low end of QDC range. This nonlinearity has been calibrated with the PPG pulse and modeled by the three parameter functional form:

$$gain = (asymptotic - gain) \times [1 - exp(\frac{\alpha + amp}{\beta})] \tag{4.2}$$

where α, β, and *asymptotic gain* are constants for each channel, the amplitude

of the signal in volts, depends on the width of the signal.

The PMT pedestals, electronic noise, and sky noise are calibrated by "snapshots" when all tubes are forced to repeatedly trigger for a period of time. The mean value of the QDCs give the PMT pedestal, the RMS variation provides the electronics noise and sky noise. Snapshot data taken with shed doors closed is used to indicate the electronic noise. When the door is open the snapshot data indicates the combination (in quadrature) electronic noise and sky noise. The combine of electronic noise and sky noise for channel B for Hires-I detector is found to be 200 photoelectrons.

4.6.5 TDC Calibration

The TDC calibration is performed by using snapshots to start the TDCs and the hold-off counter (which issues a signal to stop TDC integration when the counter reaches a specified value). The hold-off times used range from 1μs to 50μs in 1μs step. 20 TDC integrations performed at each step so that the mean and standard deviation of the TDC counts can be determined. A quadratic function is then fitted to relate TDC values with physics times. It has been found the uncertainty of TDC calibration is about 20ns[60]. This is much smaller than other time error like time slewing which will easily increase the triggering time uncertainty to the order of 100ns.

4.6.6 PMT Sensitivity Calibration.

The initial tubes sensitivities were set to 15000 A/W for all BigH tubes. But the real sensitivity of every tube must be calibrated. HiRes detector has been calibrated by using Roving Xenon Flasher (RXF). RXF is an extremely stable light source over

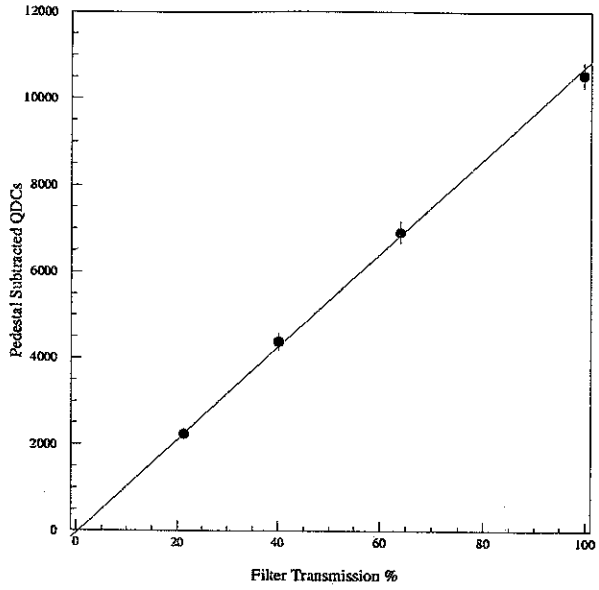

Figure 4.15: *The Pedestal subtracted QDC counts depending on the neutral filter transmissions with same RXF light source. The PMT gain is determined by the slope of the fitting line.*

long periods of time. It can be mounted at the center of mirrors, by using teflon diffusers, a uniform light pulse over the PMT cluster is provided.

The RXF has been used ever since 1996 during the operation of HiRes prototype detector. Based on very well calibrated PMT tube's measurement. It was assumed that 12000 photons/tube light is provided by RXF when it is mounted at the center of the mirror. Neutral density filters were also used to get different light density. For HiRes-I detector, four sets of 200 RXF shots were taken for each mirror with four attenuation factor: 100%, 64%, 41%, and 21%. For each sets, the average and standard deviation of each tube's QDC were recorded. Figure 4.15 shows an example of the averaged QDC versus the expected photons (100 % correspond to 12000 photons) measured from a PMT. The data points were then fitted with a straight line, the PMT gain is obtained as the slope of the fitted line.

The current analysis in this thesis is based on this calibration which was taken in May of 1998. There are a few problems for this calibration method: The output of the RXF assumed to be 12000 photons/tube is correct within 10%-20% based on other independent measurement; this calibration is only done once in 1998, it is possible the detector can be changed during these time period, and also the mirrors installed after were still not calibrated; it is known that there is non-linearities at the low and high end of the QDC range, fortunately the data we using is not in those ranges.

Another independent PMT calibration method is also in progress. The advantage of the new method overcome the disadvantages of the above method: instead of assume how many photons coming out from RXF, the Poisson statistics of QDC account is used to determine the photo-electron number; the non-linearities are treated by using PPD data with different pulse widths and heights; the calibration data is taking monthly to monitor the stability of the detector.

Because of the photoelectrons statistics and the response of a multiplicative dynode system amplification to a single photoelectrons, a PMT's QDC mean signal Q_{QDC} and standard deviation σ_{QDC} are related to the photoelectron number Q_{pe} in the following equation[66]:

$$Q_{pe} = (1 + \alpha) \times Q_{QDC}^2 / \sigma_{QDC}^2 \tag{4.3}$$

in which the $\alpha > 0$ depends on what kind of tube and also the high voltage setting. This factor is measured within laboratory from single photoelectron spectrum. The result is 0.4-0.5 for HiRes tubes[67].

The RXF shots data and Yag laser shots data were analysised by using this method. Again four sets of RXF data were taken as described above. The Yag laser

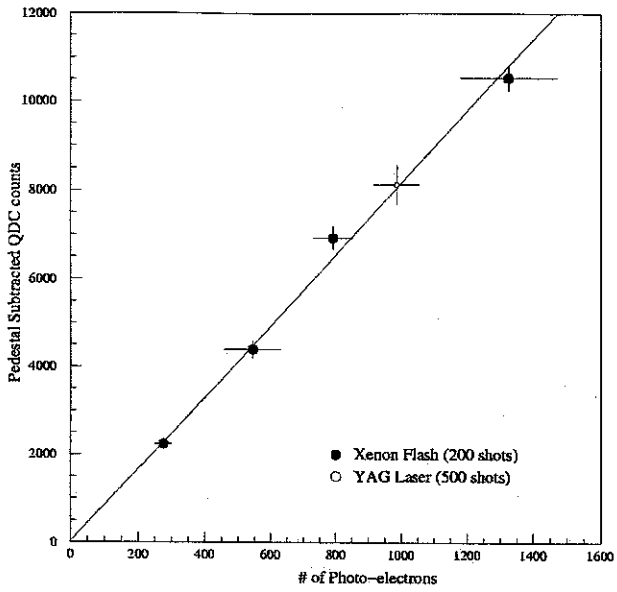

Figure 4.16: *The Pedestal subtracted QDC counts versus the photoelectron number. Two different light source were used, one is Xenon flasher with different filter, the other is Yag laser. The PMT gain is determined by the slope of the fitting line.*

is mounted in the center of mirrors and taking data nightly as described in section 4.4. The mean and standard deviation of the PMT's QDC are calculated, and the number of photoelectron can be calculated from equation 4.3. The result is shown in figure 4.16. The points were fitted to a linear line, and the tube gain is the slope of the line. From the figure the Yag laser calibration result is consistent with the RXF calibration, even though these two are different light sources with different wavelength.

In above two different PMT calibration methods are described. The preliminary results shows these two methods are different within 10%. The new method looks more reasonable, unfortunately solid final calibration of this new method is still in progress.

Chapter 5

Detector Mont Carlo

The HiRes detector is carefully modeled through Mont-Carlo (MC) simulation. The detector MC serves three important functions: one is the detector aperture calculation, the second is the resolution study for the reconstruction method, the third is the real data and MC comparison.

For all of the above purposes, the detector simulation has to mimic the real detector as close as possible. The simulated event has to be representative of real event. In this chapter, I will describe in detail how the HiRes detector detects the cosmic ray shower. All the physics involved in the MC will also be used in the data analysis. So the physics in MC must be modeled accurately.

The HiRes detector MC is based on the work through out the last 20 years of Fly' Eye experiment and HiRes prototype experiment, the author modified the code for HiRes-I detector. In the following I will describe in the order of physics processing of a cosmic ray event and the detection by HiRes. The MC procedure is shown in Figure 5.1. In the following I will describe it in step by step.

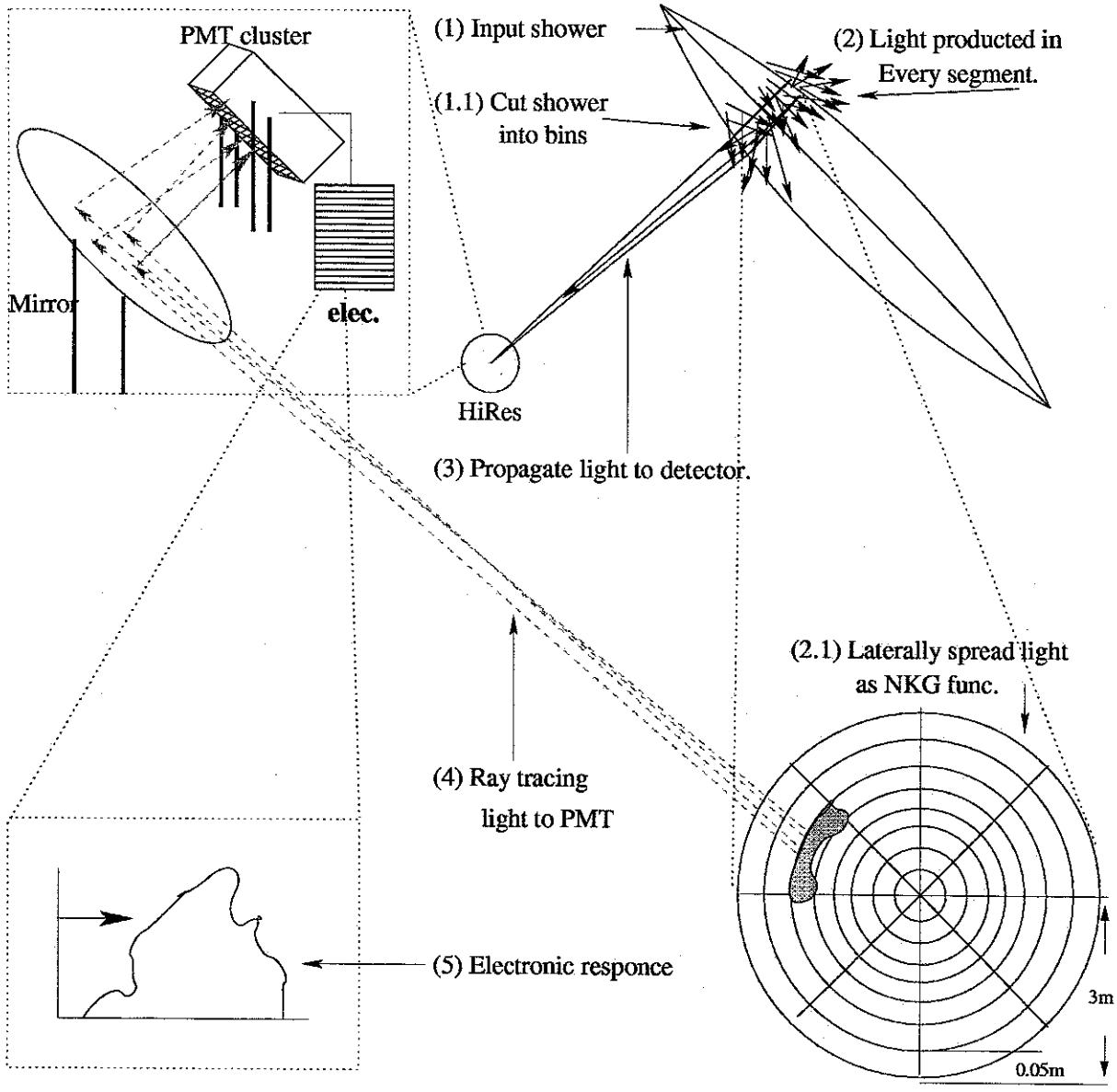

Figure 5.1: *Schematic of the procedure for the detector MC (Note the picture is not in scale).*

5.1 EAS Input

5.1.1 EAS Generator

The first part of detector MC is to input EAS corresponding to cosmic ray energy of E. How the shower is developed from a cosmic ray has been discussed in Chapter 3. HiRes detector measures the profile of EAS, we use the Gaisser-Hillas function to parameterize the shower longitudinal profile, which is given in Equation 3.5, and the NKG function to parameterize the lateral distribution of EAS, which is given in Equations 3.6, 3.7. From CORSIKA simulation result given in Section 3.4 both functions fit the shower very well.

The fluctuation of EAS development has also been put in the shower generator. Because of the fluctuation in the shower development, the shower X_0, X_{max}, N_{max}, and λ in Gaisser-Hillas function can be fluctuated. Based on CORSIKA results these fluctuations are put in as Figures 3.7, 3.8.

5.1.2 Geometry generator

The simulated showers are generated with an isotropic random flux. The arrival direction is generated from uniform distribution of $cos(\theta)$ and ϕ, in which theta is the zenith angle, and ϕ is the azimuth angle. The shower core position hitting on the ground is uniform randomly chosen between 0 to hundreds Km away on both X and Y coordinate.

The shower track is then divided into up to 4000 segments, each segment has 0.04 degree as seen from the detector. At each middle point of track segment, the air density, temperature and slant depth X from the top of atmosphere are calculated

based on US standard atmosphere model. After that the shower size $N_e(X)$, age and Moliere multiple scattering radius are calculated. The shower size is calculated from Gaisser-Hillas function

$$N_e(X) = N_{max}(\frac{X - X_0}{X_{max} - X_0})^{\frac{X_{max}-X_0}{\lambda}} exp[\frac{X_{max} - X}{\lambda}] \tag{5.1}$$

The shower age is defined as:

$$s(X) = \frac{3X}{X + 2X_{max}} \tag{5.2}$$

The Moliere radius, r_m characterize the shower lateral spread out in Equations 3.6, 3.7, which is given by

$$r_m = X_0 \times \frac{E_s}{E_c} \approx 9.3 g/cm^2 \tag{5.3}$$

where $X_0 = 37.1(g/cm^2)$ is the radiation length for electronics in air,

$E_s = m_e c^2 (4\pi\alpha)^{1/2} \approx 21$ MeV and the critical energy $E_c = 97$ MeV. The air density at the point is used to convert the Moliere unit into meters.

Because the lateral spread out of the electrons within every segment along the track, the segment looks like a pancake, then I divide the pancake into small sells laterally.

5.2 Light Production

The charged particles in EAS will produce Cherenkov light when they travel faster than the speed of light in air and scintillation light by ionizing nitrogen molecules.

The physics of the light production is given in Section 3.2 Here I will describe how we model these lights.

5.2.1 Cherenkov Light Production

The charged particles will generate Cherenkov light when their energy exceed a minimum threshold E_{min}[68]. This threshold is 21 MeV at sea level. It depends on the speed of light in air in equation:

$$E_{min} = \frac{0.511(MeV)}{\sqrt{2\delta}} \tag{5.4}$$

with $\delta = n - 1$, n is the index of refraction at a given atmosphere height H.

$$\delta \propto exp(-H/H_s) \tag{5.5}$$

H_s is the atmosphere scale height, which is 7.5 kilometer.

The number of Cherenkov photons per meter generated by a particle of energy E is given by

$$\frac{dn_p(E)}{dl} = 4\pi\alpha[1 - (\frac{E_{min}}{E})^2]\int \frac{\delta}{\lambda^2}d\lambda \tag{5.6}$$

The total number of Cherenkov light per meter produced by an EAS segment at stage X is:

$$\frac{dN_{cv}(X)}{dl} = \int_{E_{min}}^{\infty} N_e(X)f(E,X)\frac{dn_p(E)}{dl}dE \tag{5.7}$$

where the electron energy distribution $f(E,X)$ is defined by the integral relation

$$F(E,X) = \int_E^{\infty} f(E',X)dE' = (\frac{0.89E_0 - 1.2}{E_0 + E})^s (1 + 10^{-4}sE)^{-2} \tag{5.8}$$

$F(E,X)$ is the fraction of electrons in the shower with energy greater than E at stage X. It has been calculated using shower MC technique[32]. $E_0 = 44 - 17(s - 1.46)^2$, s is shower age defined in Equation 5.2, which depend on the shower stage X. E is kinetic energy in MeV. $N_e(X)$ is the total number of electrons at stage X given in Equation 5.1.

The angular distribution of Cherenkov light from EAS observed on the ground is mainly due to the angular spread of the electrons by multiple scattering, and to the Cherenkov emission angle. This angular distribution is approximated by[32]:

$$\frac{d^2N_{cv}(X)}{dld\Omega} = \frac{dN_{cv}(X)}{dl}\frac{e^{-\theta/\theta_0}}{sin\theta} \tag{5.9}$$

with $\theta = 0.83E_{min}^{-0.67}$.

Since the Cherenkov light is mainly along the track direction, at the later stage X of the shower, all the Cherenkov light produced at earlier stage will be added up after the atmosphere attenuation between the stages. At stage X the total number of Cherenkov light produced along track direction is:

$$N^{cv0}(X) = \int_0^X \frac{dN_{cv}(X')}{dl} T(X',X)dl(X') \tag{5.10}$$

where $T(X',X)$ is the transmission factor after atmosphere attenuation, which will be described in Section 5.3.

5.2.2 Scintillation Light Production

The amount of scintillation light emitted at every segment in the shower development is proportional to the number of electrons in that segment. The fluorescence light emission efficiency depends on the energy of electrons, the atmosphere density and the temperature[43]. The formula for fluorescent yield used in detector MC is based on most recent experiment result[58]. In that experiment, the fluorescent yield is measured for different electron energy beams at various air temperatures and pressures, it has been found that the fluorescent yield is proportional to the dE/dX, the result has been fitted to the function:

$$Y = \frac{(\frac{dE}{dX})}{(\frac{dE}{dX})_{1.4MeV}} \rho \{ \frac{A_1}{1 + B_1 \rho \sqrt{T}} + \frac{A_2}{1 + B_2 \rho \sqrt{T}} \} \tag{5.11}$$

where Y is the fluorescent yield in photons/electron/meter, dE/dX is the electron energy loss, ρ is the air density in kg/m^3, T is the temperature in K. $A_1 = 89.0 m^2 kg^{-1}$, $A_2 = 55.0 m^2 kg^{-1}$, $B_1 = 1.85 m^3 kg^{-1} K^{-1/2}$, $B_2 = 6.50 m^3 kg^{-1} K^{-1/2}$ these are the empirical fitting results.

Since the fluorescent yield is proportional to the electron dE/dX, and there is energy distribution for electrons at a shower stage. We used CORSIKA to calculate the average dE/dX for every shower age[57], the result is given in Figure 3.10. This averaged dE/dX is used for the scintillation light calculation.

Scintillation light is emitted isotropically, the number of photos produced per unit length per unit solid angle at stage X is given by:

$$\frac{d^2 N_{sc}(X)}{dl d\Omega} = \frac{Y N_e(X)}{4\pi} \tag{5.12}$$

where Y is given in Equation 5.11, $N_e(X)$ is the number of electrons in the segment at stage X, which is given in Equation 5.1.

5.3 Light propagation

The light produced along EAS development can be detected by HiRes detector. From EAS to detector the light will be attenuated by scattering and absorption. For scintillation light, we only need to consider the attenuation between EAS to detector in the first order approximation. In the case of Cherenkov light, which is mainly along the EAS track direction, the light can be scattered out from the track direction into the detector, or there is some direct Cherenkov light can be seen by the detector. Scintillation light will be contaminated in both cases.

Basically there are two kinds of scattering sources, one is air molecule, the other is aerosol. Air molecule scattering is well known and following Rayleigh scattering theory[68]. Aerosol scattering is much more complicated and can be described by Mie scattering theory. Comparing to the scattering, the absorption by the air molecules and aerosols is less important for the wavelength range between 300nm to 400nm[69]. The Ozone absorption is also important for these wavelength.

For the scintillation light and direct Cherenkov light, the atmosphere including air molecule, aerosol and ozone attenuates the light from EAS to detector. If we assume the transmission factor of light passing through the atmosphere due to Rayleigh scattering, aerosol scattering and Ozone absorption is T_R, T_M, and T_{O_3}, then the total transmission is:

$$T = T_R T_M T_{O_3} \tag{5.13}$$

The equation is correct when the multiple scattering of light is not important.

For the scattering Cherenkov light calculation, since the track segment is very small, the density of scatterer like air molecule and aerosol can be looked as constant, then scattering efficient $d^2N_\gamma/dld\Omega$, which means the number of photons scattered out of the beam per unit length into a given solid angle, can be used to calculate the number of Cherenkov light scattering out of the shower track direction into the direction of the detector by the scatterer in the track segments. After multiply the transmission factor given in Equation 5.13, we get the number of scattering Cherenkov light hitting the detector, In the section, I will describe how to model these scattering and absorption.

5.3.1 Rayleigh Scattering

The scattering of air molecules can be described by Rayleigh scattering theory, in which the number of scattered photons per unit length is:

$$\frac{dN_R^\gamma}{dl} = -\frac{\rho}{X_R}(\frac{400nm}{\lambda})^4 N_R^\gamma \tag{5.14}$$

where ρ is the atmospheric density, The mean free path for scattering X_R at $\lambda = 400nm$ is 2970 gm/cm^2.

The probability of scattering into a given solid angle is given by:

$$\frac{d^2N_R^\gamma}{dld\Omega} = \frac{3}{16\pi}\left|\frac{dN_R^\gamma}{dl}\right|(1+cos^2\theta) \tag{5.15}$$

Then the transmission factor due to Rayleigh scattering for a light passing slant depth of dX can be written as:

$$T_R = exp[-\frac{dX}{X_R}(\frac{400}{\lambda})^4] \tag{5.16}$$

5.3.2 Aerosol Scattering

Aerosol scattering is quite complex, it strongly depends on the aerosol size, aerosol shape, dielectric constant and chemical components etc. This complexity makes no reliable prediction for the aerosol scattering. A simplified model for the aerosol scattering is given by Eterman. He modeled the concentration of aerosol in an approximately exponential fashion with a scale height of 1.2 km. Figure 5.2 shows the averaged extinction coefficient as a function of altitude near Tuson, Arizona[70]. The exponential approximation fits very well.

The average aerosol size distribution is given by: $A(a) = a^{-\nu}$. Fly's Eye group used Mie scattering theory to calculate the phase function for $\nu = 4$ case. The phase function is given in Figure 5.3. There is a very strong peak in the forward region. It has been found this phase function is very close for the aerosol at HiRes site, this will be given in Chapter 7.

Based on the above models, the number of photos by aerosol scattering is:

$$\frac{d^2N_A^\gamma}{dld\Omega} = -\frac{N_A^\gamma}{L_A(\lambda)}\rho_a(h) \times P(\theta) \tag{5.17}$$

where $L_A(\lambda)$ is the wavelength dependent horizontal extinction length. $P(\theta)$ is the phase function given in figure. $\rho_a(h)$ is the reduced aerosol density at height h above ground in the form of:

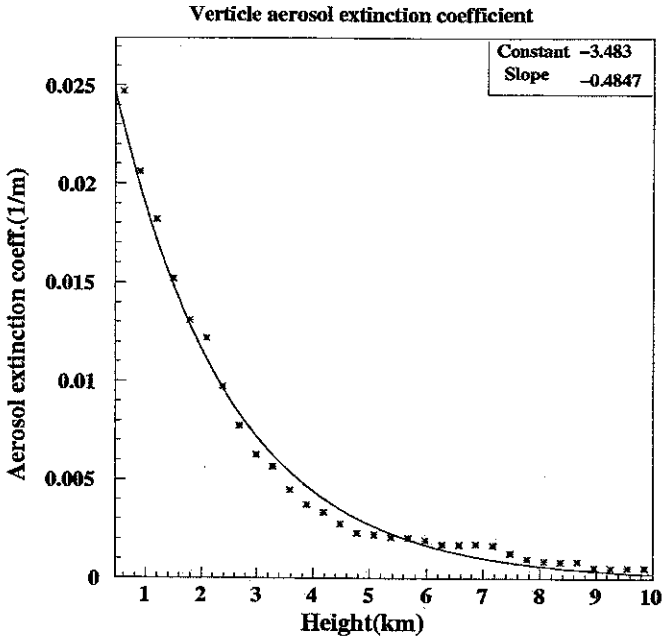

Figure 5.2: *The average vertical aerosol extinction coefficient measured from a Lidar system. The star is the real data [70], the solid line is the best fitted exponential function with a scale height 2.0 km.*

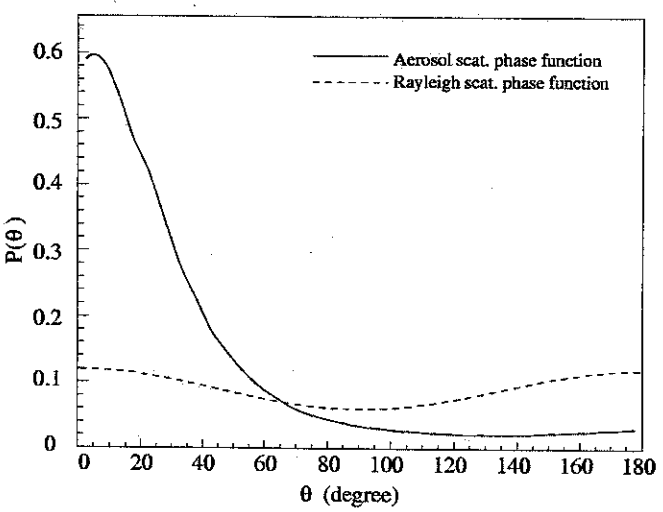

Figure 5.3: *The normalized aerosol phase function calculated from Mie theory. θ is the scattering angle. For comparison, Rayleigh scattering phase function has also been shown. These phase functions are used in the data analysis and detector MC.*

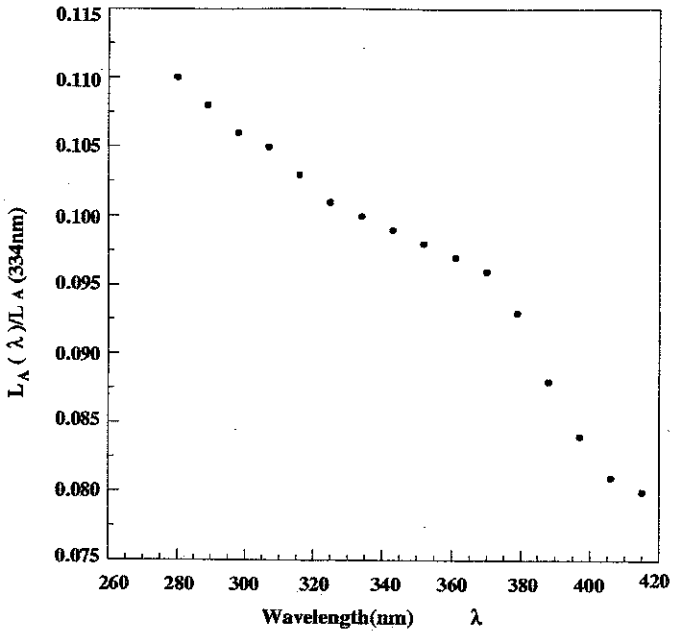

Figure 5.4: *The Etterman model of relative aerosols extinction length as a function of wavelength. The extinction length has been normalized to 1 at* $\lambda = 334nm$.

$$\rho_a(h) = \begin{cases} 1 & h \leq h_m \\ e^{-(h-h_m)/H_s} & h \geq h_m \end{cases} \tag{5.18}$$

where H_s is the scale height, we chose 1.2 km as the standard desert model (after we get the real scale height of the aerosol condition at HiRes site in Chapter 7, we plug that value into MC.), h_m is the mixing layer measured from ground, since HiRes detector is set on top of hills, we simply chose it as 0 km. These parameters are equivalent to the U.S. Standard Desert Atmosphere model.

The horizontal extinction length is not quite sensitive to the wavelength, here we used the wavelength dependent of extinction length based on the work of Etterman, it is shown in Figure 5.4. This plot shows the ratio of extinction length to that at 334nm.

Then the transmission factor due to aerosol scattering for a light passing from a point at height h_1 to a point at height h_2 with $h_1 < h_2$ and total distance of dl is:

$$T_M = exp[\frac{H_s dl}{(h_2 - h_1)L_M}(e^{-\frac{h_1}{H_s}} - e^{-\frac{h_2}{H_s}})] \tag{5.19}$$

5.3.3 Ozone Absorption

Ozone absorption is also important for the UV light. The light attenuation due to Ozone absorption can be expressed as:

$$\frac{dN^\gamma}{dl} = -N^\gamma A_{O_3}(\lambda)\rho_{O_3}(h) \tag{5.20}$$

where $A_{O_3}(\lambda)$ is the Ozone absorption coefficient, which is strongly wavelength dependent. Here we used the data from USAF Handbook of Geophysics and Space Environment, the wavelength dependent is shown in Figure 5.5. $\rho_{O_3}(h)$ is the ozone density distribution which is shown in Figure 5.6.

The transmission factor for a light pass through Ozone with ozone slant depth of dX_{O_3} is:

$$T_{O_3} = exp[-dX_{O_3}A_{O_3}] \tag{5.21}$$

5.4 Detector Optical Response

After we calculated the light production in EAS in Section 5.2 and light transmission in Section 5.3, easily we can calculate the number of photons hitting the detector

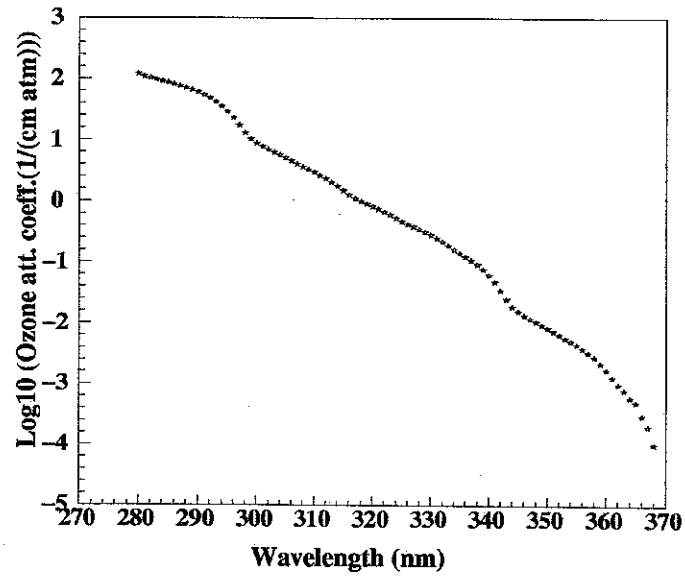

Figure 5.5: *The Ozone attenuation coefficient as a function of wavelength*

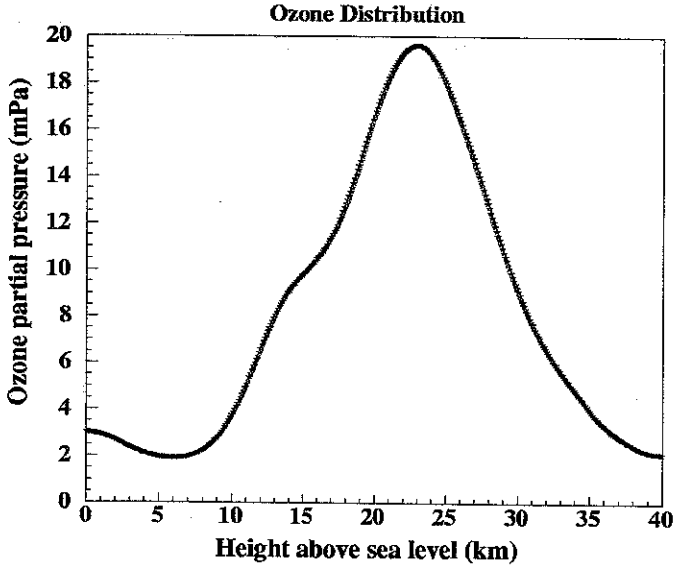

Figure 5.6: *The Ozone concentration as function of height.*

mirrors. Since the EAS is longitudinal and laterally spread out, and the detector mirror is not uniformly focused on the PMT cluster as discussed in Section 4.6.1, the ray tracing technique is used to calculate the number of photons hitting individual tubes on the PMT cluster. Sky noise and Poisson fluctuation of the signal will also be put in to simulate the real HiRes detector.

5.4.1 Photoelectron calculation

The number of photoelectrons produced at the track segment at stage X and collected by the HiRes mirror is

$$\begin{aligned} N_{pe}(X) = & \sum_{\lambda=280}^{420} \left(\frac{d^2N_{sc}(X)}{dld\Omega}(\lambda,\theta)\mid_{scin} + \frac{d^2N_{cv}(X)}{dld\Omega}(\lambda,\theta)\mid_{ckv}\right. \\ & \left. + \frac{d^2N_R^{cv0}(X)}{dld\Omega}(\lambda,\theta)\mid_{rscat} + \frac{d^2N_A^{cv0}(X)}{dld\Omega}(\lambda,\theta)\mid_{ascat}\right) \\ & \times T_R(\lambda)T_A(\lambda)T_{O_3}(\lambda)T_{UV}(\lambda)R_m(\lambda)Qe(\lambda)\delta l(X)\delta\Omega(X) \end{aligned} \quad (5.22)$$

Where the sum is over the wavelength λ in 9 nm step, θ is the emission angle from the shower track direction to the detector direction at segment X, *scin*, *ckv* means the direct scintillation light and Cherenkov light given in Equations 5.12, 5.9, *rscat*, *ascat* means the Rayleigh scattering and aerosol scattering of Cherenkov light out of the track direction given in equations 5.15 5.17. $N^{cv0}(X)$ is the total Cherenkov light at stage X given in Equation 5.10. T_R, T_A, $T_{O_3}$are the Rayleigh, aerosol and Ozone transmission factor given in Equations 5.16, 5.19, 5.21 respectively, T_{UV} is the UV filter transmission factor given in Figure 4.10, R_m is the mirror reflectivity given in Figure 4.4, here we only use the averaged mirror reflectivity as 0.82, which is the value when the mirror stayed for a longer time and is stable. Qe is the averaged

PMT quantum efficiency shown in Figure 4.12. δl is the physical length of the track segment. $\delta\Omega$ is the solid angle of the mirror surface relative to the track segment center, and is given by:

$$\delta\Omega = \frac{A_{eff}}{d^2} \tag{5.23}$$

A_{eff} is the projected area of the mirror along the direction from the mirror position to track segment, this will be calculated by the ray tracing way discussed in the following. d is the distance from mirror position to track segment. In the above calculation the real HiRes mirror physical position and direction has been put in.

Up to now, I only calculated the first order light hitting the detector. When the shower is far from the detector, because of the multiply scattering by the atmosphere, more light can be collected by the detector, how this effect is considered will be discussed in detail in Chapter 6. Because multiply scattering takes a lot of CPU time, in most of the detector MC simulation, I did not include it in.

5.4.2 Ray Tracing

We calculate the total number of photoelectrons from one segment of EAS collected by one mirror of the detector by assuming all the light coming only from the central point of the segment. But we know the shower has laterally spread out within the longitudinal segment, and also because the mirror is not focused uniformly on the PMT cluster surface. We use a ray tracing way to calculate the number of photoelectrons collected by individual tubes. When we do the ray tracing, we first generate a ray tracing table.

Ray tracing table To build the ray tracing table, I used the MC technique. In this MC, I trace millions of light from a fixed direction relative to the local mirror coordinate randomly onto the clover shaped mirror, reflected by the mirror onto the PMT cluster and hit individual tubes. Figure 5.7 shows the spot shape of the lights coming from same direction onto the cluster. The relative photon numbers hitting every tube can be seen. The ratio R_t is the number of rays hitting individual tube to the total number of rays hitting the mirror has been saved.

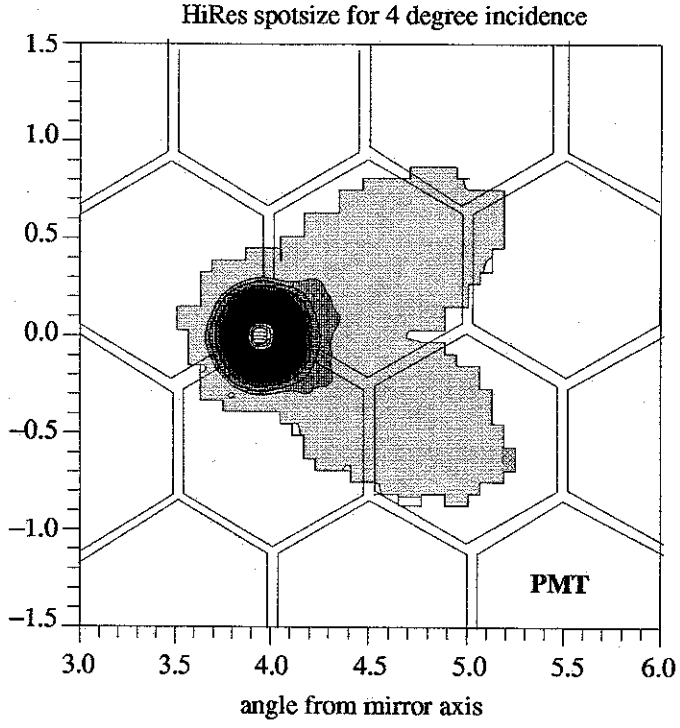

Figure 5.7: *The spot-size on the PMT cluster for the light source 4 degree off from mirror axis, and the relative number of photons hitting individual PMT.*

To simulate the real mirror spot shape, the light is fluctuated by a Gaussian of $\sigma = 0.254cm$ on the landing position of the mirror. The real cluster shape, which will block part of the incoming light, has also been put in to calculate the effective mirror area A_m correspond to the source direction. The real tube surface is not uniform

as shown in Figure 4.14, so the effective number of photons hitting the tube is also weighted by the tube response profile function.

The ray tracing table has 4 parameters, x and y correspond to the light source direction on longitude and latitude relative to the mirror center direction. t is the tube id hit by the light, S_t is the effective mirror area seen by the tube, which equal to the total mirror effective area A_m multiply R_t, which is the rate of the number of rays hitting the tube to the total number of rays hitting the mirror. In order to cover all the direction the PMT cluster can be hit and keep the table size reasonable, I simulate the direction from $-8.4^o \rightarrow 8.4^o$ for x and $-7.2^o \rightarrow 7.2^o$ for y in step size as 0.05^o, which is the resolution for the mirror direction surveyed in HiRes detector. After we build up this ray tracing table, if we know the light source direction, we can directly get the number of photons hitting individual tubes by calling this table.

Tracing Light from EAS Segment to Mirror The total number of photoelectrons has been calculated in Equation 5.22 from one segment of EAS, these photoelectrons are spread out within this segment laterally. The lateral spread out of electrons in EAS can be described by NKG function as in Section 3.4. If we assume the photons in the segment is also spread out same as the electrons, then we can describe it by NKG function (This is not always true, the scintillation light is distributed same as the electrons, but the Cherenkov light lateral distribution is different[32]. Considering the HiRes detector dedicated on measuring showers more than 5 km's away, Cherenkov contamination for HiRes detector is small, this difference is ignorable) The NKG function describes the electron density as a function of the shower age and the radial distance from the shower axis in the unit of Moliere unit r_M, which has peaks in the center and spreads out from the center as shown in Figure 3.6. In order to save CPU time in the MC, and to include all the electrons,

I normalized the NKG function from $r = 0$ to $r = 3r_M$ and cut it into rings with $0.05r_M$ radial step (This correspond to 0.05^o angular step when the track is 3 km away. HiRes detector only collects shower more than 5km away, this dividing will not bring ray tracing bias later). Each ring is also cut into 2n-1 cells azimuth (n is the ring number) if the total number of photoelectrons is more than 2n-1, otherwise the photoelectrons will be randomly distributed in the ring.

The electrons distributed laterally in the EAS segment are then traced to the mirror by calling the ray tracing table. The effective number of photoelectrons hitting every tube can be calculated. After we add up all the segments along the EAS track, we can get the total number of photoelectrons collected by every tube in every mirror.

The real HiRes detector collects the photons by the tube over a time window of 5.6 μs around the tube's trigger time. Sky noise will also be collected during this time window. And also because the Poisson fluctuation in the PMT, the real number of photoelectrons collected by the tube will be fluctuating. To simulate this, we also include same amount of sky noise (40pe/μs) and Poisson fluctuation in the detector MC.

5.5 Detector Electronics Response

The detector electronic response has also been simulated in the detector MC. The goal for this is to check the S/H electronic system and the mirror trigger condition, and also to calculate the triggering time for every hit tube. So the real electrons has been put in detector MC, and the same process has been gone through as real detector. The real electronics has described in Section 4.2.3. Here I will simply describe the process for the electronics.

We first set a total time window as $T_{tot} = T_d + T_t + T_h$, in which T_t is the transit time of the shower crossing the mirror based on the shower geometry, $T_d = 25\mu s$ is the dead time pre-pended to T_t to simulate a noise tube trigger prior to the transit of the shower, which will prevent the tube trigger by the shower signal. $T_h = 50\mu s$ added to the end of transit time to simulate the mirror hold-off time, which permits additional tube triggers be includes in the same event. The time window T_{tot} is then divided into 5ns time bins, in each bin sky noise has been added in from a Poisson distribution with a mean of 40pe/μs.

The tube photoelectrons calculated above is then distributed in the time bins within the time range of T_t according to their real hitting time (Poisson fluctuation has also been added in as describe above). Then this tube time series signal passes through PMT pre-amplifier and electronic gains. Then it pass through the Ommatidial board with channel B given in Figure 4.6 to check the trigger. If the tube is triggered, the real trigger time is recorded, and then the tube signal is integrated in the 5.6 μs time window. After all tubes in the mirror has been tested for trigger. all triggered tube signal and trigger time are save in ascending triggering time order. Then the sub-cluster trigger, mirror trigger and mirror cross trigger are tested same as the function of trigger board described in Section 4.2.3. If more than one mirror is triggered, then all information of this event will be save in dst banks. The input shower parameters such as the Gaisser-Hillas parameters and shower geometry parameters will be saved in an constant bank for reconstruction resolution checking. The tube triggering time and total signal is saved same as the real data for later analysis.

5.6 Laser Shot Simulation

The detector MC simulates the Laser shots parallel to the cosmic ray shower. The laser shots simulation is much easier compare to the cosmic ray shower. I will describe how to simulate the laser shots, since I will use these laser shots in the atmosphere calibration in Chapter 7. The real laser system has been described in Section 4.5. Figure 5.8 shows a schematic for the laser shot and HiRes detector. In the following I will describe the MC procedure.

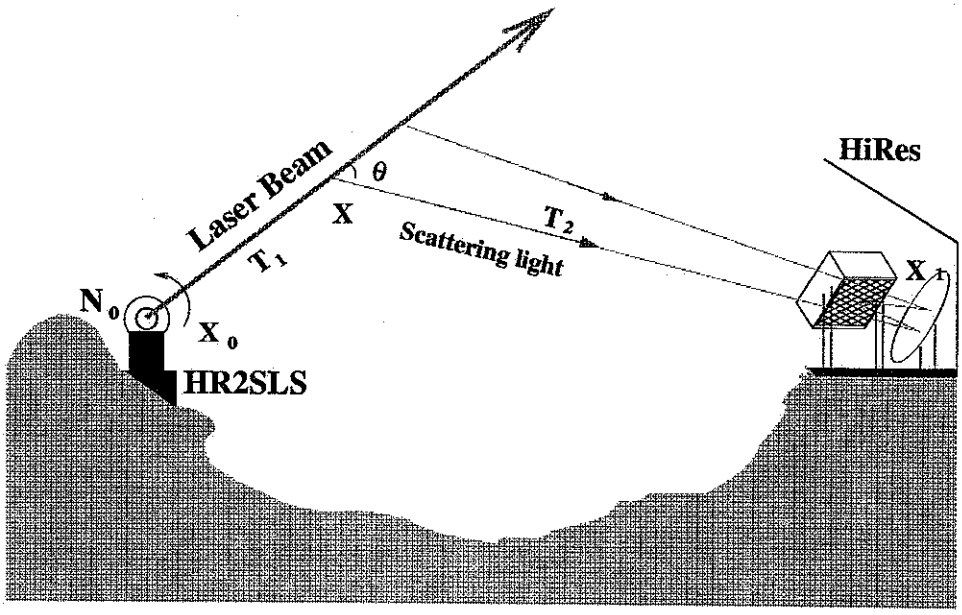

Figure 5.8: *The schematic of laser shot from HR2SLS and HiRes detector.*

5.6.1 Laser Shot Input

The laser is fixed at real position X_0 relative to HiRes-I detector with energy of 5 mJ and wavelength of 355nm. The line beam is upward, and can be chosen either

randomly or same as the real laser shooting direction, which is read from an direction loop table. Along the laser track direction, The track is then divided into 0.04^o segment relative to HiRes-I detector with maximum of 180^o from the direction of laser core to HiRes-I detector. The segment is so small, the atmosphere can be looked as constant within the segment.

5.6.2 Light processing

The photons coming out of the HR2SLS system will be attenuated by atmosphere and can be scattered into the detector. Let N_0 be the total number of photons coming out of the laser system, which can be calculated from the laser energy and the wavelength. At point X in the sky, after the atmosphere attenuation, the number of photons is:

$$N(X) = N_0 T_R(\lambda, X_0, X) T_A(\lambda, X_0, X) T_{O_3}(\lambda, X_0, X) \tag{5.24}$$

where $T_R(X_0, X)$, $T_A(X_0, X)$, $T_{O_3}(X_0, X)$ are the transmission factor from point X_0 to X due to Rayleigh scattering, aerosol scattering and Ozone absorption respectively given in Equations 5.16, 5.19, 5.21. $\lambda = 355nm$ is the laser wavelength.

The photons within the segment at point X can be scattered out from the laser direction into HiRes-I detector by Rayleigh scattering or aerosol scattering. So the number of photos scattered into the direction of HiRes-I can be given as:

$$N'(X) = [\frac{d^2 N_R(X)}{dld\Omega}(\lambda, \theta)\mid_{rscat} + \frac{d^2 N_A(X)}{dld\Omega}(\lambda, \theta)\mid_{ascat}]\delta l \delta\Omega \tag{5.25}$$

where $rscat$ and $ascat$ are Rayleigh scattering and aerosol scattering respectively given in Equations 5.15, 5.17. θ is the light emission angle out from the track direction.

δl is the length of the segment. $\delta\Omega$ is the solid angle of the mirror surface relative to the track segment center, and is given in Equation 5.23.

The total number of photoelectrons hitting the mirror at position X_1 from this segment X will be:

$$N_{pe}(X, X_1) = N'(X) \times T_R(\lambda, X, X_1)T_A(\lambda, X, X_1)T_{O_3}(\lambda, X, X_1)T_{UV}(\lambda)R_m(\lambda)Qe(\lambda) \tag{5.26}$$

where T_R, T_A, T_{O_3} are the transmissions factor due to Rayleigh scattering aerosol scattering and Ozone absorption from X to X_1, T_{UV}, R_m and Qe is same as in Equation 5.22.

Then the ray tracing table is called to get the number of photoelectrons hitting every individual tube as describe in Section 5.4.2. the only difference is that, we do not need to consider the lateral spread for the laser beam in the first order approximation.

5.6.3 Electronic Process

The tube signal passes through same electronic system as in Section 5.5 to check the triggering status. If the mirror is triggered, then the input information of the laser shot and the trigger tube information are saved in dst banks for later analysis.

Chapter 6

Multiply Scattering Effect

The basic mechanism contribute to the generation of the light signal seen by HiRes detector is nitrogen fluorescence light which relates directly to the number of charged particles in an EAS. The fluorescence light is emitted isotropically from the shower, allowing for detection of showers at large distances. By HiRes detector, UHE shower can bee seen as far as 40 km's away. This makes a very big aperture, and has high statistics for the cosmic ray energy spectrum. The disadvantage is that, the multiply scattering effect will become important when the shower is far away. In this chapter, I will study this effect on the energy estimation of this technique.

The multiply scattering of light by molecules and aerosols in the atmosphere gives rise to a radiance field about a point-like source. This contribution, or called aureole, depends on many parameters, such as the single scattering albedo, the optical thickness, the scattering phase function, the off angle of the detector from the source direction, the field view solid angle of the detector, and also the integration time window of the detector. This effect has been studied for the last 25 years by the people who are interested in solar blind ultraviolet communication and warning systems or

atmospheric study. However most studies were devoted mainly to the total aureole effect [71] [72] [73]. There were few studies on the time-dependent aureole effect. But they were either for the case of very large optical thickness (fog, cloud, etc) [74] or only for very low order of scattering which is for the case of small optical thickness [75, 76].

Since the shower detected by HiRes can be in the range from a few km to more than 40 km, on good weather (less aerosol) or bad weather (dense aerosol). The detector is integrating the signal within about 5 micro second time window. We will present calculations of the time-dependent aureole radiance field about an impulsive isotropic source in a scattering and absorbing medium. The approach used is generally applicable to any case, and does not involve any approximation. The calculation of the temporal characteristics of the scattering radiation are based on the work of Trakhovsky *et al.* [76].

In Section 6.1, I will present the recursive approach to calculate the scattering radiation effect initially developed by Zachor [71], and generalized by Trakhovsky *et al* [76] to time-dependent case. In Section 6.2, I will present a Mont Carlo way to calculate the temporal scattering radiation. The results are given in Section 6.3 for both cases in different atmosphere conditions and detector setup.

In Section 6.4, we apply the results of multiply scattering of point source to any cosmic ray shower detected by HiRes detector, and calculate the effect on the energy estimate.

6.1 Recursive Approach

As shown in Figure 6.1 The first-order scattering term can be decomposed into three steps: direct transmission from the source to the volume element dV, scattering inside dV in the detector direction, and direct transmission from dV to the detector. Assume an isotropic point source which emits at an instant t = 0 an pulse of total photo Q. The irradiance (power/unit area) incident on element $dV = r_2^2 dr_2 d\Omega$ is:

$$\mathcal{E} = \frac{Q}{4\pi r_1^2} exp[-\alpha + \beta) r_1]. \tag{6.1}$$

in which β is the volume scattering coefficient, α is the absorption coefficient. According to the definition of scattering coefficient β and single-scattering phase function $P\,(cos\theta)$, the scattered intensity of radiation by dV toward detector is:

$$d\mathcal{I}_s = \mathcal{E}\beta P(cos\theta) dV. \tag{6.2}$$

The irradiance incident on the detector is:

$$d\mathcal{E}_s = \frac{d\mathcal{I}_s}{r_2^2} exp[-(\alpha + \beta) r_2]. \tag{6.3}$$

Then the radiance (photo/unit area/unit solid angle) received at O is:

$$d\mathcal{N}_s = \frac{d\mathcal{E}_s}{d\Omega} = \frac{Q\beta P\,(cos\theta)}{4\pi {r_1}^2} exp\left[-\left(\alpha + \beta\right)\left(r_1 + r_2\right)\right] dr_2 \tag{6.4}$$

Since we are interested in a time-resolved measurement. Following Reilly and Warde [75]. we chose a prolate spheroidal coordinate system with a source positioned

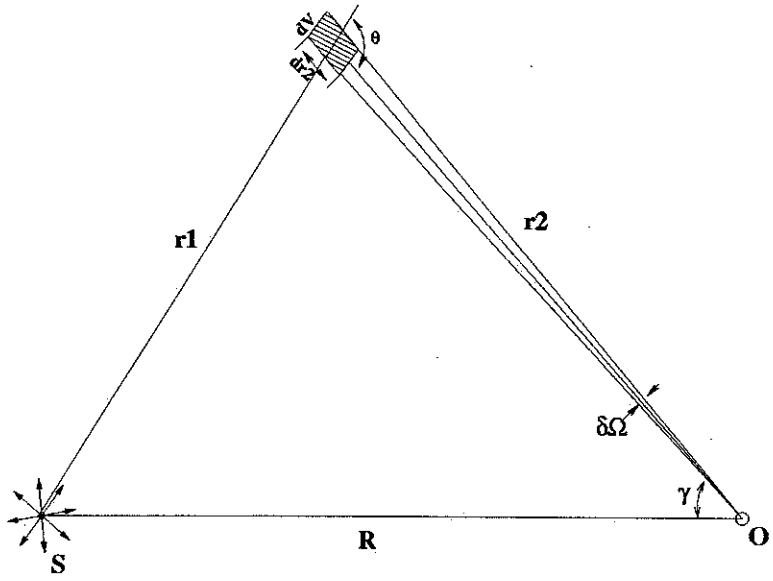

Figure 6.1: *Geometric parameters involved in the calculations of first order scattering. S is the source point; O is the detector point. γ is the off angle; θ is the scattering angle; $\delta\Omega$ is the detector field view solid angle*

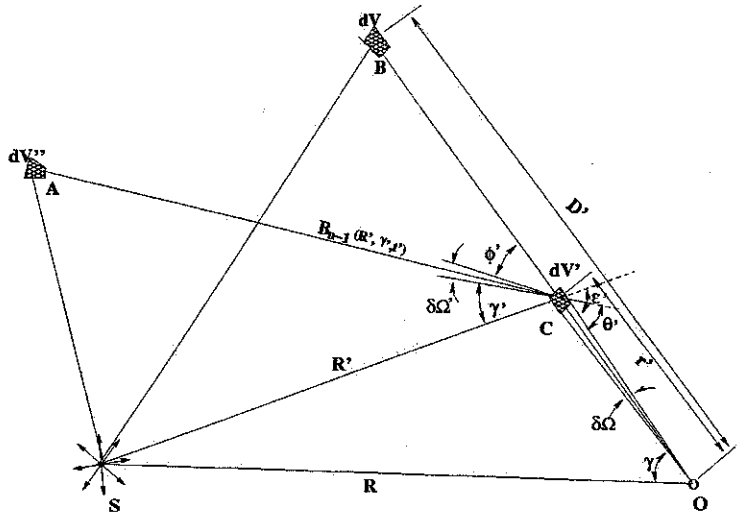

Figure 6.2: *Geometric parameters involved in the calculation of nth-order scattering based on (n-1)th order scattering (SOC and SOB are in the same plane; ϕ' is the the angle from the plane SAC to the plane SBC; θ' is the angle from AC to CO; ϵ' is the angle from SC to CO).*

at one local point and a detector at the other. It may be shown [75] that the parameters of Figure 6.4 $(r_1, r_2, \theta, \gamma)$ are transformed into prolate spheroidal coordinates using the following relationships:

$$r_1 = \frac{R}{2}(\xi + \eta), \tag{6.5}$$

$$r_2 = \frac{R}{2}(\xi - \eta), \tag{6.6}$$

$$cos\theta = \frac{2 - \xi^2 - \eta^2}{\xi^2 - \eta^2}, \tag{6.7}$$

$$\gamma = cos^{-1}\left(\frac{1 - \xi\eta}{\xi - \eta}\right). \tag{6.8}$$

let $ct = r_1 + r_2$. t is the scattered photon time of flight. Using Equations 6.5 and 6.6 we obtain:

$$\xi = \frac{r_1 + r_2}{R} = \frac{ct}{R}, \tag{6.9}$$

Transforming Equation 6.8 we have

$$\eta = \frac{1 - \xi cos\gamma}{\xi - cos\gamma}, \tag{6.10}$$

Using above Equations. then Equation 6.4 can be mathematically transferred to

$$d\mathcal{N}_s(R, \gamma, t) = \frac{cQ\beta P\{cos[\theta(R, \gamma, t)]\}}{2\pi R^2} \bullet \frac{exp[-(\alpha + \beta)ct]}{\xi^2 - 2\xi cos\gamma + 1} dt. \tag{6.11}$$

Where θ is calculated by Equations 6.7, 6.9 and 6.10. Let

$$N_1(R,\gamma,t) = \frac{d\mathcal{N}_s(R,\gamma,t)}{dt}. \tag{6.12}$$

is defined as the temporal radiance. In order to remove the singularity in Equation 6.11, and also for convenience of calculating high order scattering, we define the apparent temporal radiance as:

$$B_n(R,\gamma,t) = \frac{4\pi R^2 sin\gamma}{Q}\sigma^{-n}N_n(R,\gamma,t) \tag{6.13}$$

Then Equation 6.11 can be transferred to:

$$B_1(R,\gamma,t) = ck_{ext.}\frac{2P\{cos[\theta(R,\gamma,t)]\}sin\gamma}{(\xi^2 - 2\xi cos\gamma + 1)}exp(-k_{ext.}ct). \tag{6.14}$$

where $k_{ext.} = \alpha + \beta$ is the total extinction coefficiency, $\sigma = \frac{\beta}{\alpha+\beta} = \frac{\beta}{k_{ext.}}$ is the single-scattering albedo.

Following the same way as [76], assume the apparent temporal radiance of *(n-1)* th order incidented at instant t' at an angle γ' on a volume element dV' located at distance R' from the source through a field view solid angle $d\Omega'(\gamma',\phi')$ (see Figure 6.5) is $B_{n-1}(R',\gamma',t')$.

Geometrically it is easy to get the following relationship:

$$R' = (R^2 + r'^2 - 2Rr'cos\gamma)^{1/2}. \tag{6.15}$$

$$\epsilon' = cot^{-1}\left(\frac{cos\gamma - \frac{r'}{R}}{sin\gamma}\right), \tag{6.16}$$

The scattering angle θ' is defined [71] by

$$cos\theta' = cos\gamma' cos\epsilon' + sin\gamma' sin\epsilon' cos\phi'. \tag{6.17}$$

then the nth order apparent temporal radiance is

$$B_n(R,\gamma,t) = sin\gamma \int_0^{D'} dr' \int_0^{\pi} d\gamma' \left(\frac{R}{R'}\right)^2 B_{n-1}(R',\gamma',t')\overline{P(cos\theta')}. \tag{6.18}$$

where $\overline{P(cos\theta')}$ is an azimuthally integrated scattering phase function [71]:

$$\overline{P(cos\theta')} = \int_0^{2\pi} d\phi' P(cos\theta'). \tag{6.19}$$

where

$$D' = \frac{R}{2}(\xi - \eta). \tag{6.20}$$

$$SB + BC = ct' = ct - r'. \tag{6.21}$$

ξ, η is defined in Equations 6.9 and 6.10.

With the above equations, theoretically we can calculate any order of scattering radiance for any given geometry setup (R,γ,t) and any atmosphere (σ, $P(cos\theta)$, $k_{ext.}$). But in the real calculation, it will take tremendous of CPU time to calculate the radiance high than 3rd order of scattering, because of the 3-dimension integration in Equation 6.18.

The total apparent temporal scattering radiance is:

$$B(R,\gamma,t) = \sum_{n=1}^{n=\infty} \sigma^n B_n(R,\gamma,t) \tag{6.22}$$

For simplification purpose, we define

$$c = k_{ext.} = 1. \tag{6.23}$$

Then in the following, both the distance and time are in the unit of extinction length.

We then define regular grids for both the geometry setup and the atmosphere: R is from 0.0 to 6.0 with interval of 0.1; γ is from 0.01^o to 179.99^o with interval 0.2^o when $\gamma \leq 2^o$, with interval 2^o when $\gamma > 2^o$; $t - R$ is from 0 to 2 with interval 0.1; σ is from 0.0 to 1.0 with interval 0.2; The atmospheric phase function is a weighted average of single-scattering phase functions $P_R(cos\theta)$ and $P_A(cos\theta)$, which represent, respectively, the Rayleigh and aerosol components. The weights are the corresponding scattering coefficients:

$$\begin{aligned} P(cos(\theta)) &= \frac{\beta_R P_R(cos(\theta)) + \beta_A P_A(cos(\theta))}{\beta_R + \beta_A} \\ &= \rho P_R(cos(\theta)) + (1-\rho) P_A(cos(\theta)). \end{aligned} \tag{6.24}$$

$$\rho = \frac{\beta_R}{\beta_R + \beta_A}. \tag{6.25}$$

ρ is from 0.0 to 1.0 with interval of 0.2.

The grids chosen above to calculate the scattering radiance are simply trying to cover all the different situations the HiRes experiment will meet, and also considering

the CPU time and calculation errors. To calculate the nth order, we only need to interpolate the result of the *(n-1)*th order, and then calculate the integration in Equation 6.18 by using Gauss-Legendre procedure. The error of this calculation is about a few percent.

6.2 Mont Carlo Calculation

We made Mont Carlo calculations for the scattering radiance also. There are many references on this method [73]. Here we follow the way as [73]. The basic idea of MC method is to decompose light into a set of pencils of light that are called photons for the sake of brevity. The program follows the path of each photon inside the medium. Since the source is an isotropic point source, so it is very simple to setup the MC process (it can be generated to more completed case):

The geometry for the MC is shown in Figure 6.3 Source S is assumed to be placed at the center of a sphere of radius R_{max}. The photon trajectory is then simulated by successive straight lines between collisions with scattering and absorbing centers inside the sphere of radius R_{max}. Each interaction between a photon and a scattering center obeys the law of single scattering. The scattering coefficient is used in computing the probability of the photon's being scattered between distance l to $(l+dl)$ as $\beta exp(-\beta l)dl$. To take into account of absorption along the path, we weight a photon by factor W_i that is initially set at 1 and then multiplied by $exp(-\alpha l)$ at each collision. After the scattering, the new direction of the photon is determined by the scattering phase function $P(cos\theta)$. To take the advantage of the spherical symmetry, we look the whole spherical surface with radius R as a detector with normal direction.

When a photon crosses the detector's surface, we record two quantities: the

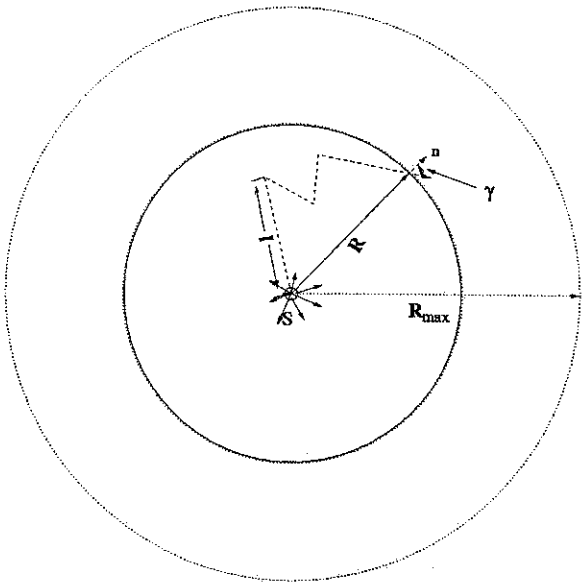

Figure 6.3: *Geometric parameters involved in the MC simulation of multiply scattering from point source. S is the source point. The sphere with radius R the detector. n is the local norm direction of the detector.*

real path length ct, the angle γ between the photon's direction and the local normal direction of the detector. Then the weight of the photon W_i is:

$$W_i = exp(-\alpha ct). \tag{6.26}$$

If a photon does not hit the detector at time $t \longrightarrow t + dt$, within direction $\gamma \longrightarrow \gamma + d\gamma$, then

$$W_i = 0. \tag{6.27}$$

The total number of photons hit the detector at time $t \longrightarrow t+dt$, within direction $\gamma \longrightarrow \gamma + d\gamma$, with the detector area dS is:

$$\mathcal{B}_{mc}(R,\gamma,t)dtd\Omega dS = \sum_{i=1}^{i=Q_T} W_i(R,\gamma,t) \tag{6.28}$$

where Q_T is the total number of input photons. (in the real calculation we simulate up to 10^8 photons). From the spherical symmetry of the detector, it is easy to get the detector area:

$$dS = 4\pi R^2 cos(\gamma). \tag{6.29}$$

and the field view solid angle $d\Omega$:

$$d\Omega = 2\pi \int_{\gamma}^{\gamma+d\gamma} sin(\gamma')d\gamma'. \tag{6.30}$$

Same as the definition in Equations 6.13 and 6.22 From Equations 6.26, 6.27, 6.28, 6.29 and 6.30 we get the apparent temporal radiance:

$$\begin{aligned} B_{mc}(R,\gamma,t) &= \frac{4\pi R^2 sin\gamma}{Q_T} \frac{\mathcal{B}_{mc}(R,\gamma,t)dtd\Omega dS}{dtd\Omega dS} \\ &= \frac{\sum_{i=1}^{i=Q_T} W_i(R,\gamma,t)}{Q_T} \frac{sin\gamma}{cos\gamma} \frac{1}{2\pi \int_{\gamma}^{\gamma+d\gamma} sin(\gamma')d\gamma'}. \end{aligned} \tag{6.31}$$

In order to get good statistics, we simulate as many photons as possible within reasonable CPU time.

As described in Section 6.1. the atmosphere is completely defined by extinction coefficient k_{ext}, single-scattering albedo σ, and total phase function $P(cos\theta)$ which is described in Equations 6.24, 6.25. In the following we will describe how we model the phase functions.

The Rayleigh scattering phase function is modeled as the simplified form:

$$P_R(cos\theta) = \frac{3}{16\pi}(1 + cos^2\theta) \tag{6.32}$$

Usually the aerosol phase function is described by a modified Henyey-Greenstein function, with an additional parameter f that gives rise to a backward peak:

$$P_A(cos\theta) = \frac{1-g^2}{4\pi}[\frac{1}{(1+g^2-2gcos\theta)^{3/2}} + \frac{f(3cos^2\theta - 1)}{2(1+g^2)^{3/2}}]. \tag{6.33}$$

where g is asymmetry parameter.

Since we are interested in the HiRes experiment, which is set in the desert of western USA. Here we will use a desert aerosol phase function calculated from Mie scattering theory with a aerosol particle size distribution function a^{-4}, where a is aerosol particle size. The phase functions are shown in Figure 5.3. This phase function is very close to the real aerosol phase function at HiRes site [Chapter 7].

6.3 Results for Point Source

The recursive calculation was performed for up to 15 order for 6 optical depth.

In Figure 6.4, we show the first a few order of scattering for $\sigma = 0.8$, $\rho = 0.8$ $R = 1$, and *time* is defined as $t - R$, which is the traveling time of scattering light t different from the direct light traveling time R. In Figure 6.4(a) $\gamma = 2^o$, in Figure 6.4(b) $\gamma = 20^o$. The signal is defined from Equations 6.18, 6.22 and the unit has been scaled by $1/4\pi$.

In Figure. 6.5, we show the first a few order of scattering for the same condition as Figure 6.4 except $R = 4$. From these Figs. we can see when the view angle γ

become bigger, or source detector distance R becomes longer, the high order scattering becomes important.

In Figure 6.6, we show the dependency of the total scattering radiance on the single scattering albedo σ. σ is from 0.2 to 1.0 from bottom to up (when σ is 0.0 there is not scattering, so we did not plot it out). The other conditions are $\rho = 0.8$, $R = 1$, in figure 6.6(a) $\gamma = 2^o$, in figure 6.6(b) $\gamma = 20^o$. It is very clear when the single scattering albedo is bigger the scattering is stronger.

In Figure 6.7 we show the dependency of the total scattering radiance on the rate of aerosol scattering coefficiency ρ. ρ is from 0.0 to 1.0 from top to bottom. $R = 1$, $\sigma = 0.8$, 6.7(a) $\gamma = 2^o$, 6.7(b) $\gamma = 20^o$. Remember the aerosol phase function is more forward distributed(see Figure 5.3). This can explain why the scattering is stranger when ρ is high at small time range.

In Figure 6.8, we show the comparisons of the result from Mont Carlo to the iterative method. for $\sigma = 0.8$, $\rho = 0.8$ $R = 1$, In 9(a) $\gamma = 3^o$, in 9(b) $\gamma = 19^o$.

In Figure. 6.9 we show the same thing as Figure 6.8 except $R = 4$. The difference between the two methods are a few percent. except at large optical depth, where it reaches 10%. The difference mainly come from the iterative calculation, as pointed out in Section 6.1, by the interpolating and Gauss-Legendre integration. The statistical fluctuations of MC results is poor even we used 48 hours of CPU on an 500-MHZ machine. From application point view, the iterative calculation is a more useful way. The error from iterative calculation can be lowered by more notes of interpolation and integration. As will be pointed out later in Section 6.4 the current result is good enough for the application on HiRes experiment.

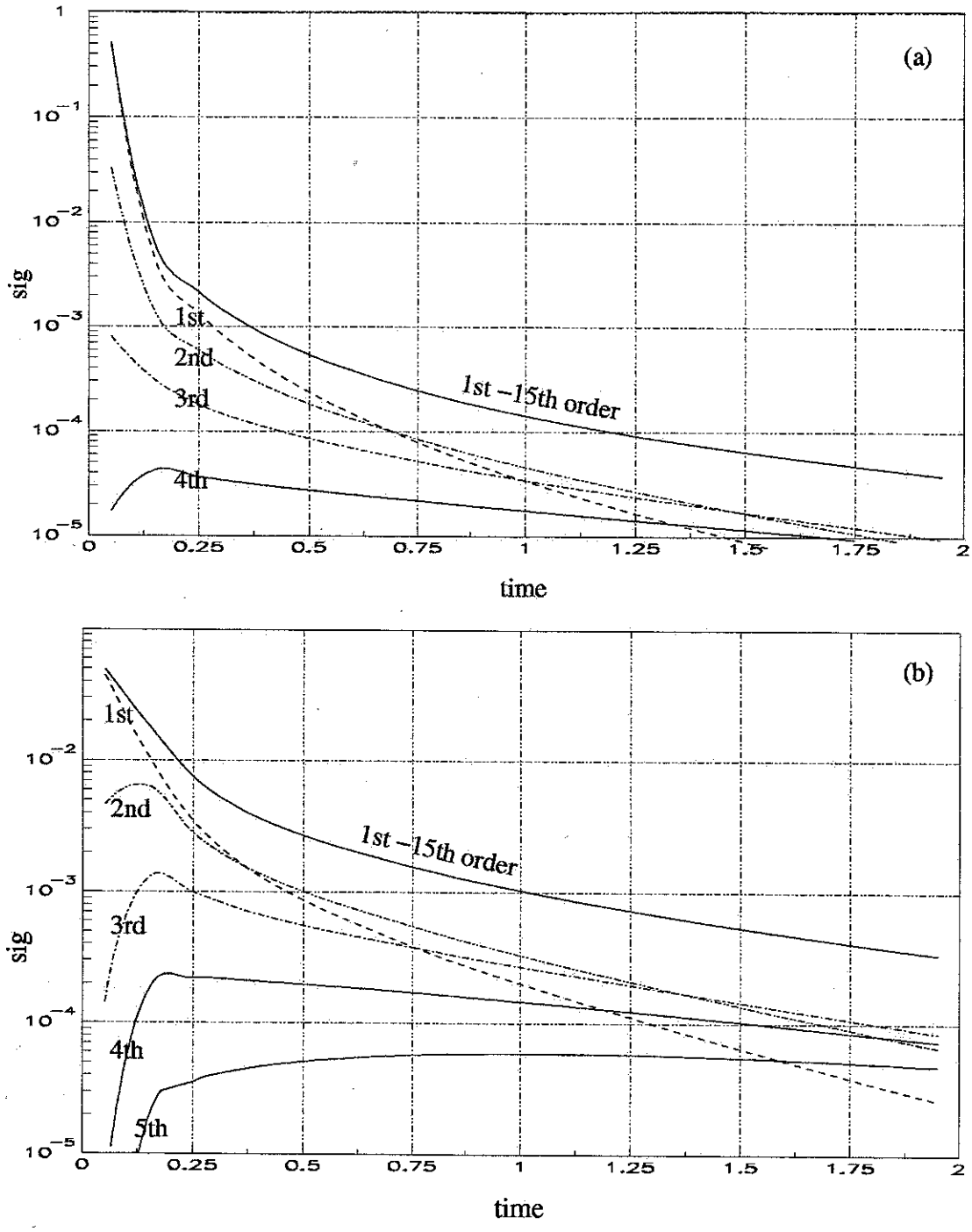

Figure 6.4: *The first a few order of temporal scattering radiance and the sum of first 15th order of radiance. For* $\rho = 0.8, \sigma = 0.8, R = 1$, $\gamma = 2^o$ *for(a), and* $\gamma = 20^o$ *for (b). The X axis is the scattering light traveling time different from the direct light traveling time. The Y axis is the scattering signal*

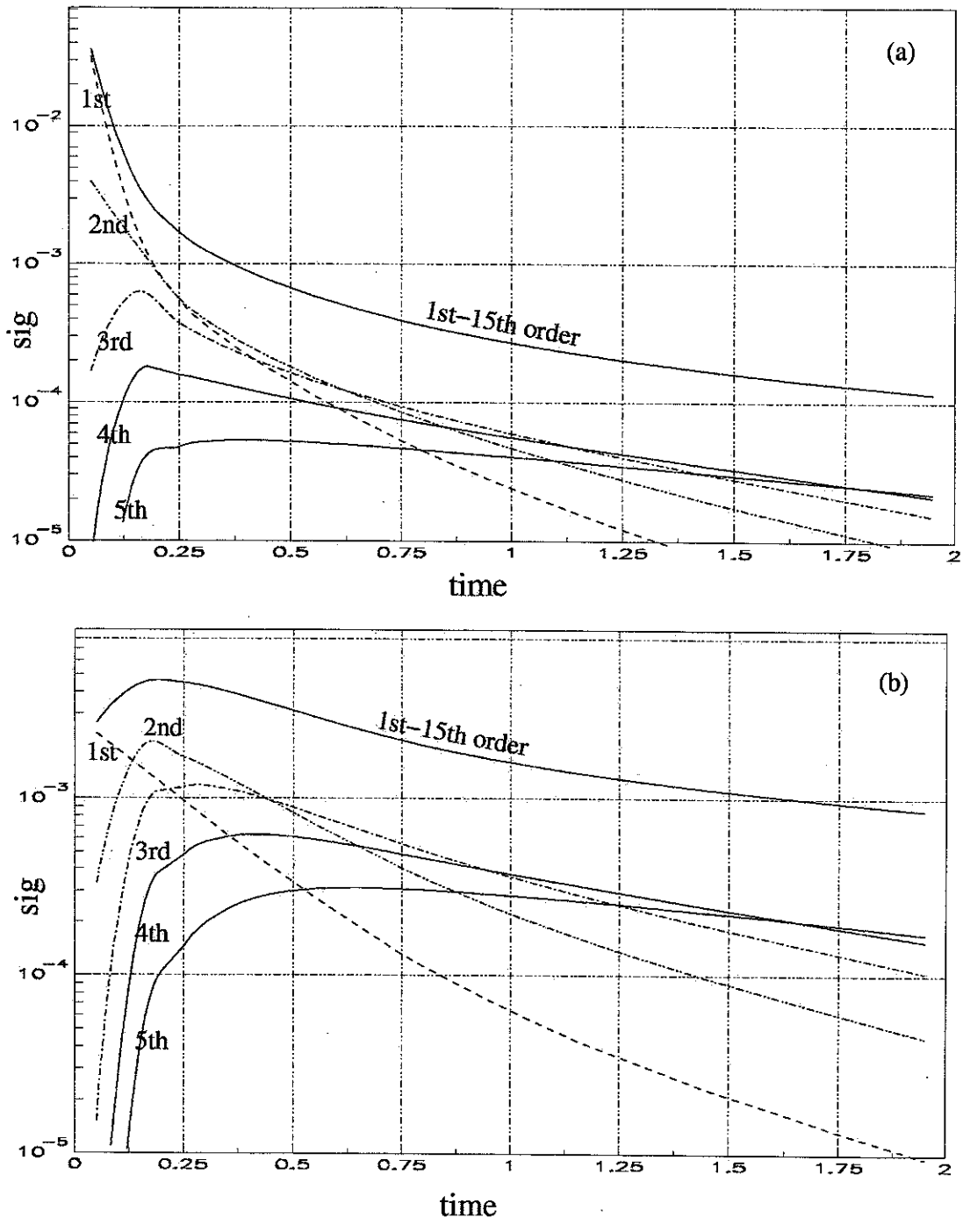

Figure 6.5: *The first a few order of temporal scattering radiance and the sum of first 15 order of radiance. For* $\rho = 0.8, \sigma = 0.8, R = 4$, $\gamma = 2^o$ *for(a), and* $\gamma = 20^o$ *for (b).*

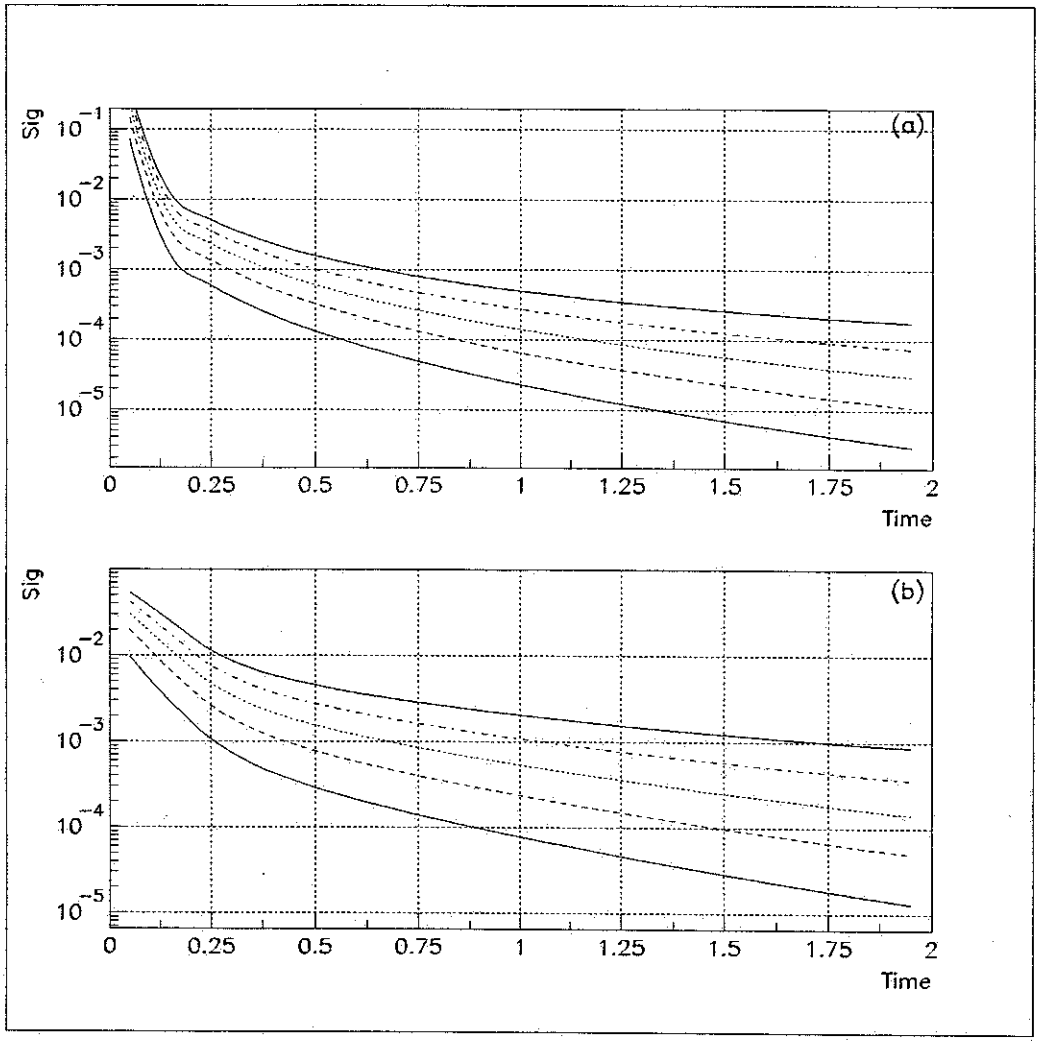

Figure 6.6: *The dependency of the total scattering radiance on the single scattering albedo σ. σ is from 0.2 to 1.0 from bottom to top.* $R = 1$, $\rho = 0.8$, $\gamma = 2^o$ *for(a), and* $\gamma = 20^o$ *for (b).*

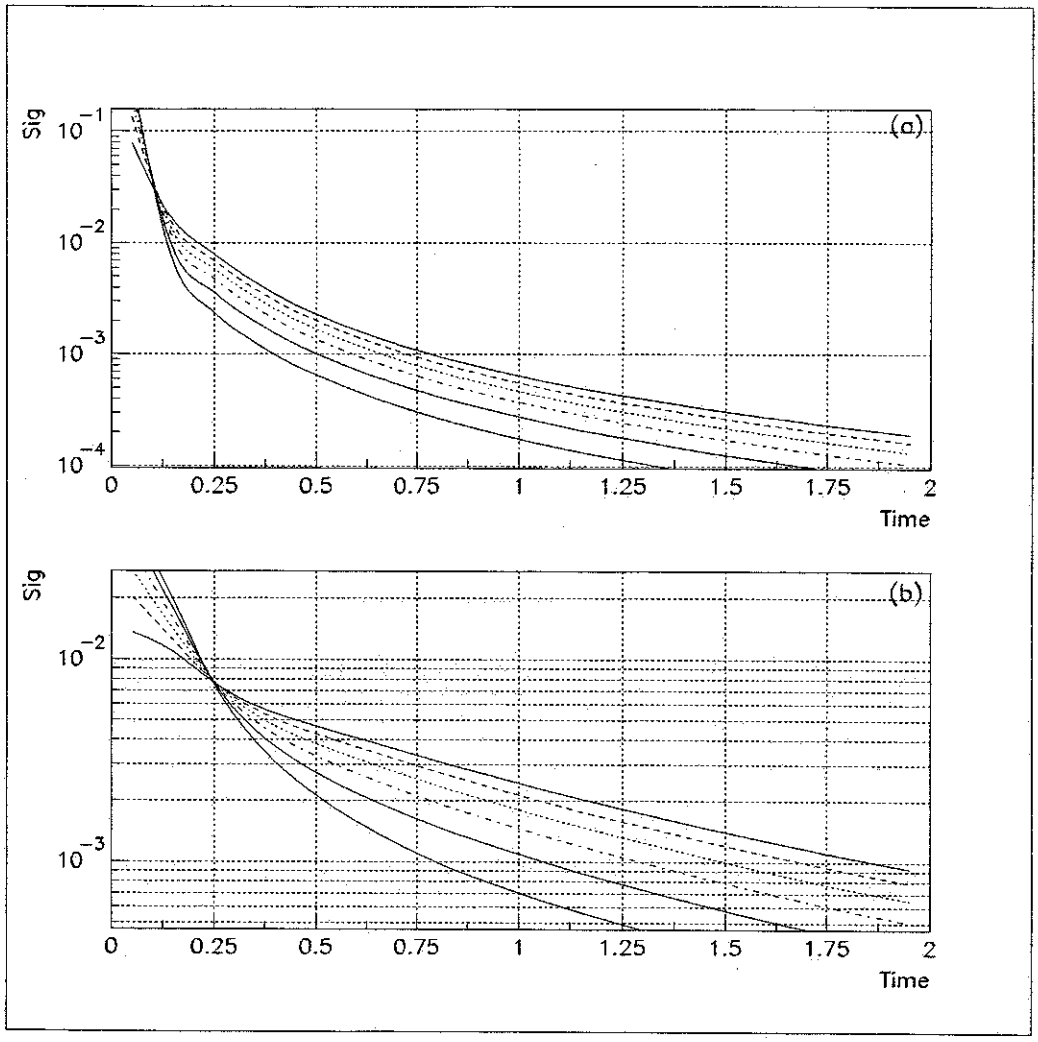

Figure 6.7: *The dependency of the total scattering radiance on the rate of aerosol scattering coefficient ρ. ρ is from 0.0 to 1.0 from top to bottom.* $R = 1$, $\sigma = 0.8$, $\gamma = 2^o$ *for(a), and* $\gamma = 20^o$ *for (b).*

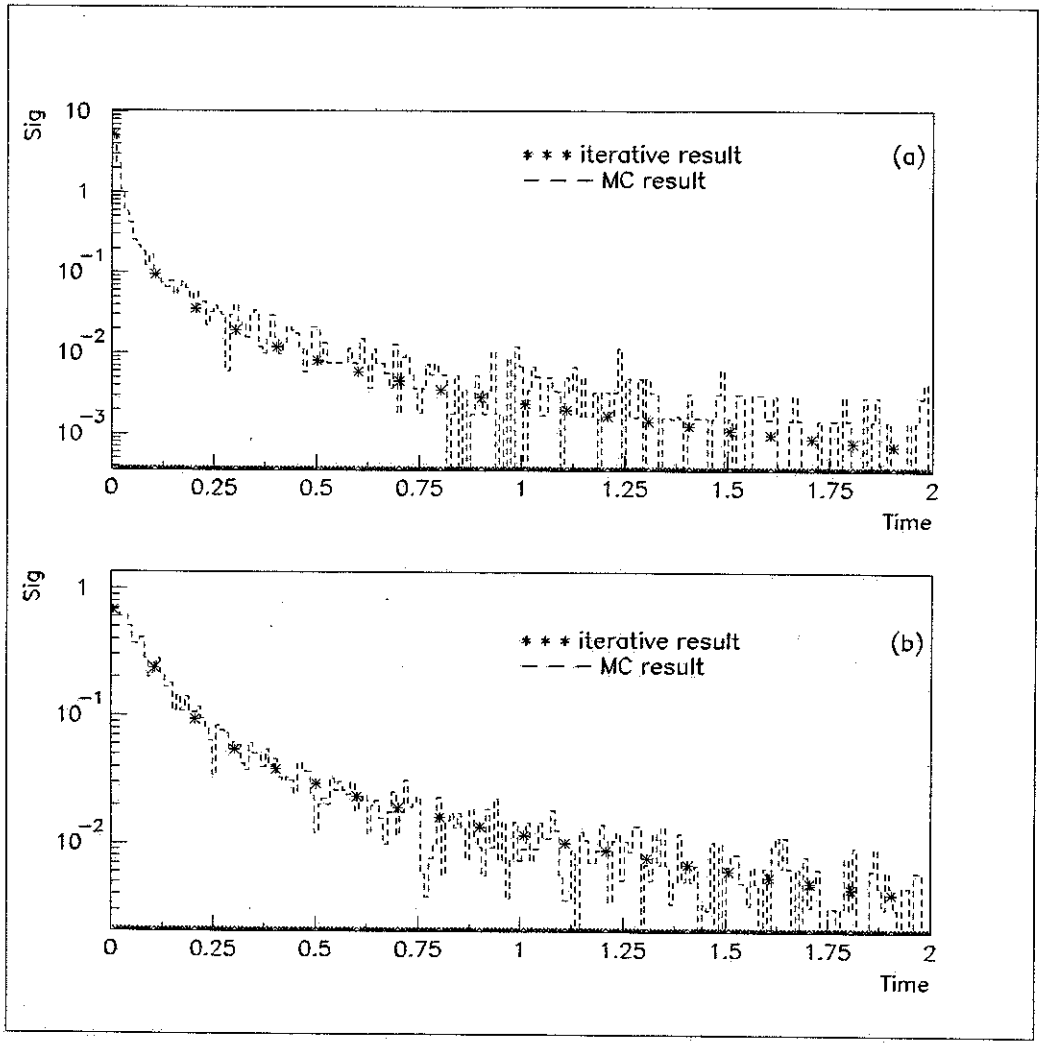

Figure 6.8: *The comparisons of result from Mont Carlo calculations and the iterative method.* $\rho = 0.8$, $\sigma = 0.8$, $R = 1$, $\gamma = 3^o$ *for(a), and* $\gamma = 19^o$ *for (b).*

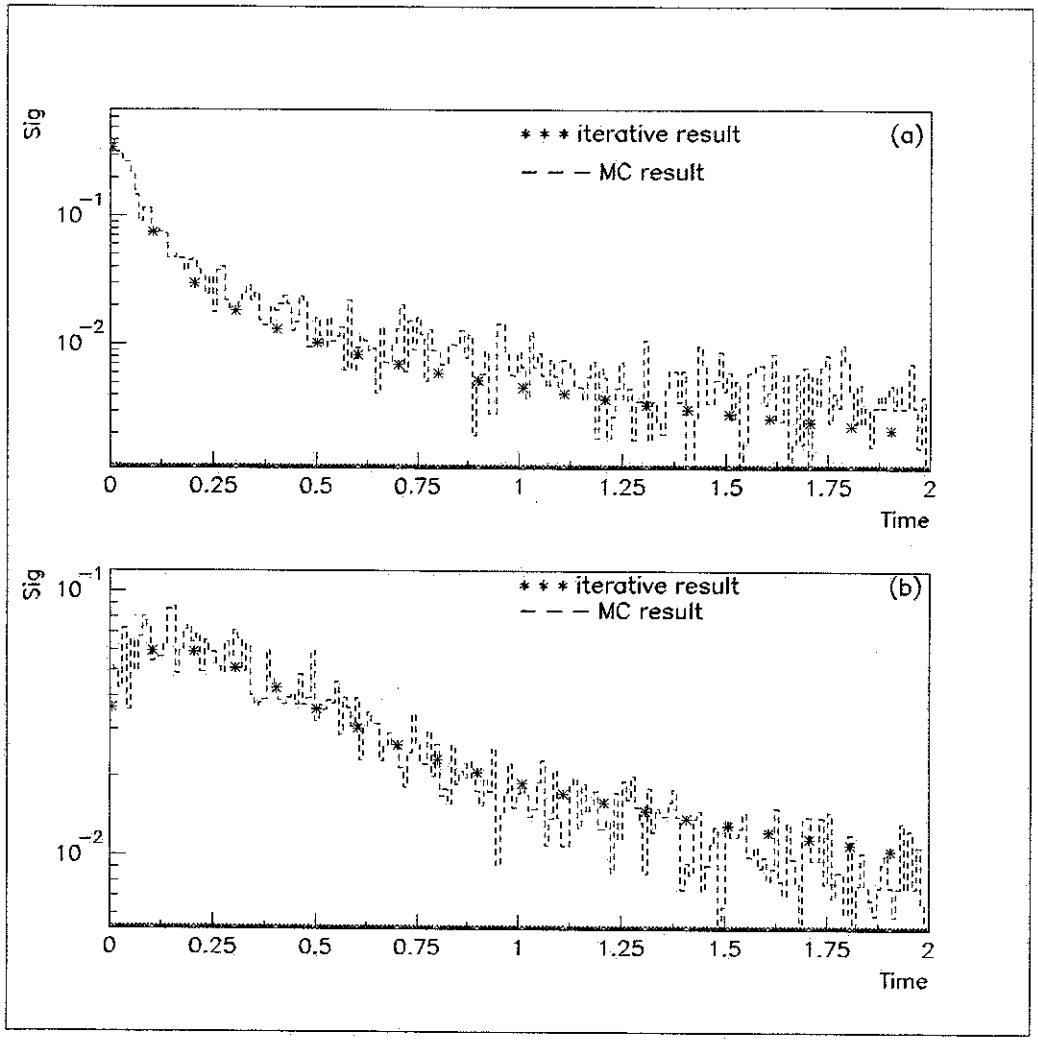

Figure 6.9: The comparisons of result from Mont Carlo calculations and the iterative method. $\rho = 0.8$, $\sigma = 0.8$, $R = 4$, $\gamma = 3^o$ for(a), and $\gamma = 19^o$ for (b).

6.4 Application to EAS Measurement

In this section, we will use the above iterative calculation results to study the multiply scattering effect in the energy estimate of cosmic ray by fluorescence technique, such as HiRes experiment. In the past 10 years, HiRes group has developed a detailed MC code to simulate the detector response for any given EAS. The detail of detector MC can be found in Chapter 5.

The EAS was generated from CORSIKA package [16, 57]. The basic idea for the HiRes detector MC is that, start from the input shower, calculate the light produced at every stage, which includes fluorescence light and Cherenkov light. The fluorescence light then transmit to the detector. The Cherenkov light is mainly in the direction of the input shower, which can be scattered into the detector by Rayleigh scattering or aerosol scattering. The fluorescence light is directly related to number of charged particle at given stage, but the Cherenkov light is more complicated, and related to the history of the shower development. Fortunately, the Cherenkov light is much weak than the fluorescence light when the shower does not directly shoot to the detector. When the shower are within the direction of the detector, we simply drop it for better understanding of the data. All the good events we chose is only fluorescence light dominated. Then the above calculation can be directly used here.

Let $\mathcal{Q}(x)dx$ is the total fluorescence light generated at stage $x \longrightarrow x + dx$, $F(x)$ is the detector coefficient relate to the source at point x. $r(x)$ is the distance from the source to the detector.

Then the direct light from stage $x \longrightarrow x + dx$ to the detector is:

$$S_{dir.}(x) = F(x)\frac{\mathcal{Q}(x)dx}{4\pi r^2(x)} exp(-k_{ext.}r(x)). \tag{6.34}$$

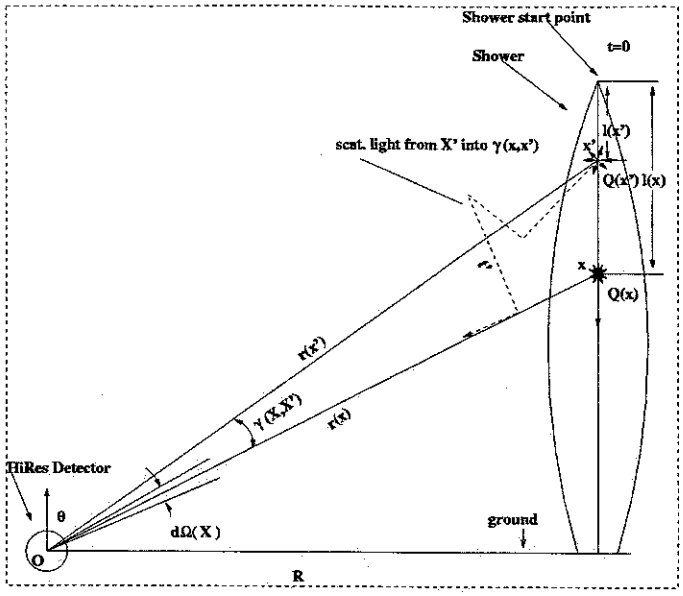

Figure 6.10: *The Geometric parameters involved in the calculation of multiply scattering effect for an EAS. X' is the source point, with total number of photons $Q(x')dx'$. The time clock is set to 0 at the start point of shower, t' is the real time the photon from X' point hit the detector with $\gamma(x', x)$ angle off from source X'.*

If we define the shower start at time $t = 0$, the time the direct light flight to the detector is (see Figure 6.10:

$$t(x) = \frac{r(x) + l(x)}{c} \tag{6.35}$$

let

$$c = k_{ext.} = 1 \tag{6.36}$$

Since the electronics of the detector will integrate all the signal come to the detector from point x within field view solid angle $\Omega(x)$, within a fixed time window W, the scattering light from point x' will also be integrated if it is in the time window

and in the right direction. The geometric parameters for calculation of this effect is in Figure 6.10. This effect can be represented as:

$$S_{sct.}(x) = F(x)\int_{t(x')\leq t(x)+W/2} dx' \int_{t(x)-W/2}^{t(x)+W/2} dt' \int_0^{\Omega(x)} d\Omega \frac{\mathcal{Q}(x')}{4\pi r^2(x') sin(\gamma(x',x))} B[r(x'),\gamma(x',x),t']. \quad (6.37)$$

in which $B(r(x'),\gamma(x',x),t)$ is calculated from Equations 6.14, 6.18 and 6.22.

In the real calculation, we first build up a table about $B(r(x'),\gamma(x',x),t)$ as described in Section 6.1 For Equation 6.37, we simple interpolate the result from the table for any given geometry $r(x'),\gamma(x',x),t$ at any atmosphere ($k_{ext.},\sigma$) condition. We chose W as 5.6 micro second, which is the real time integration window for HiRes detector. The detector opening field view solid angle $\Omega(x)$ is a lit complicated, which is related to the stage of the shower and also the detector pixel.

The Calculation also depends on the atmosphere model, the following results based on the standard US atmosphere model. The aerosol part based on an exponentially decay model with an scale height of 1.2 Km, the extinction length on the ground is 10 Km.

The results are show in Figures 6.11, 6.12, 6.13,6.14. for vertical EAS showers with primary energy 10^{20} eV at 10 km, 20 km, 30 km and 40 km away from the detector respectively. In Figures 6.11(a), 6.12(a), 6.13(a), 6.14(a) we show the longitudinal shower profile at every stage from top of atmosphere to the ground. The solid lines are the total signal, the dashed lines are the direct light, the dot lines show the multiply scattering light. The X axis is the zenith angle for given stage, the Y axis is the signal measured at the detector site. Because of the detector trigger threshold

condition, only the parts of shower around $\pm 10^o$ from the maximum signal point will be seen by the detector and gotten triggered.

In Figures 6.11(b), 6.12(b), 6.13(b), 6.14(b) we show the rate of the multiply scattering light contribution to the directly light, define as $S_{sct.}(x)$ / $S_{dir.}(x)$ from Equations 6.34, 6.37, We can see the effect is around 10% within the range the detector can see, and becomes stronger when the shower is farther. At the stage close to the ground, because both the atmosphere and aerosol density is higher, the extinction length is shorter, so the optical depth is longer the multiply scattering effect becomes stronger. For 6.11 (b), the multiply scattering effect at early stage is stronger, this is simply because the geometrical distance is longer for early stage than later stage with a factor $1/sin\theta$ (Figure 6.10), which makes the optical depth longer even when the density of atmosphere become lower when it go up. The thickness of atmosphere is fixed, when the shower is farther like 6.12(b), 6.13(b) and 6.14(b). this geometrical effect becomes less important.

In order to see directly how the multiply scattering effect contribute to the energy estimate of this experiment. We draw the longitudinal profile versus the shower depth X in unit of gm/cm^2, as Figure 6.15. The shower to detector distance is 30 Km away. The areas under the lines are directly proportional to the primary energy of the Cosmic ray [57] (see also Section 3.4) as:

$$E_{primary} \propto \int dX\, sig(X). \tag{6.38}$$

We can easily get the contribution to the primary energy estimation. The result shown in Figure 6.16 is the rate of the area from scattering light to the area from the total light in percentage. Here we also studied how much this effect is, based on

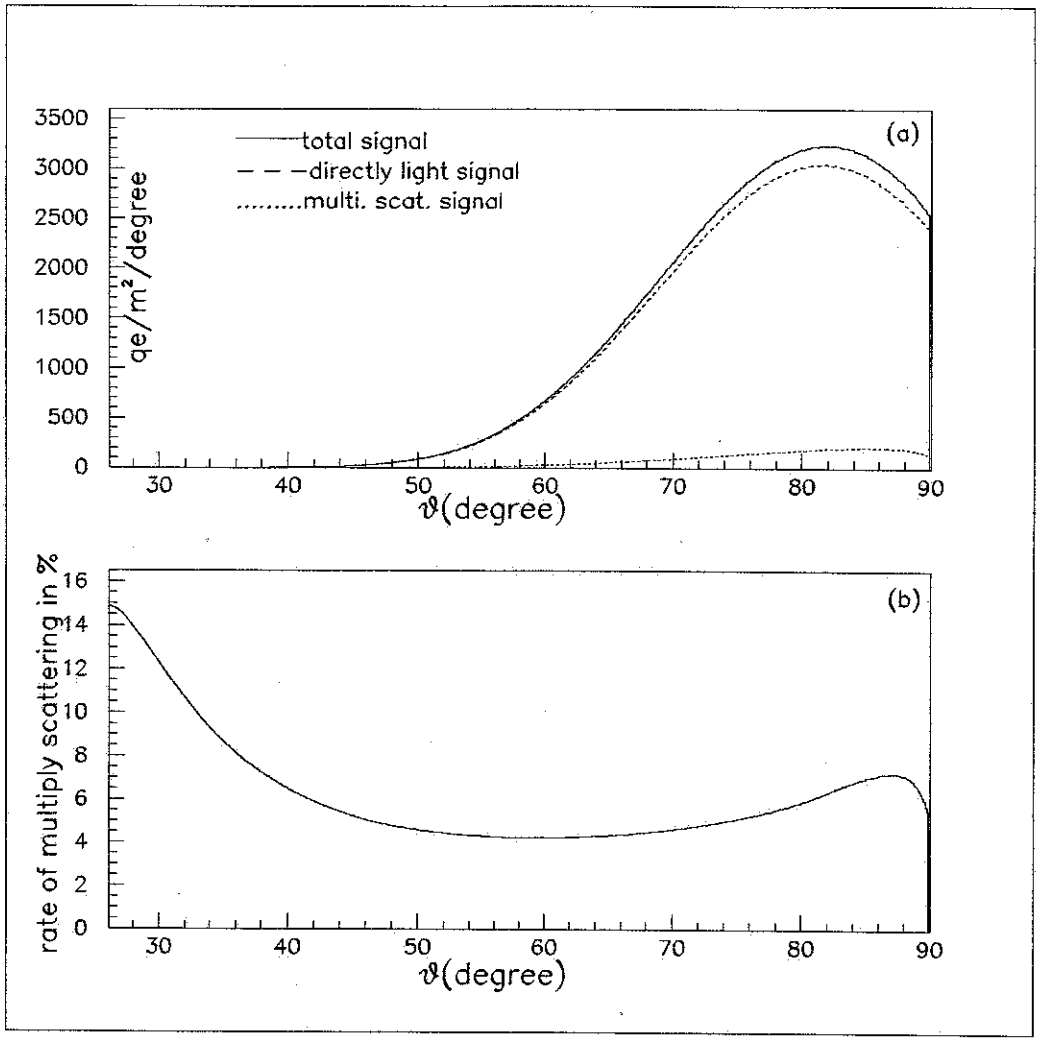

Figure 6.11: *The effect of multiply scattering on vertical the EAS shower 10 Km away from the detector. (a) The EAS shower longitudinal profile seen from HiRes detector. X axis is the zenith angle in degree; Y axis is the signal detected from HiRes site. Because of the threshold of the detector, only the bins $\pm 10^o$ from the maximum point will trig the detector. (b) The rate of multiply scattering signal to the directly light signal.*

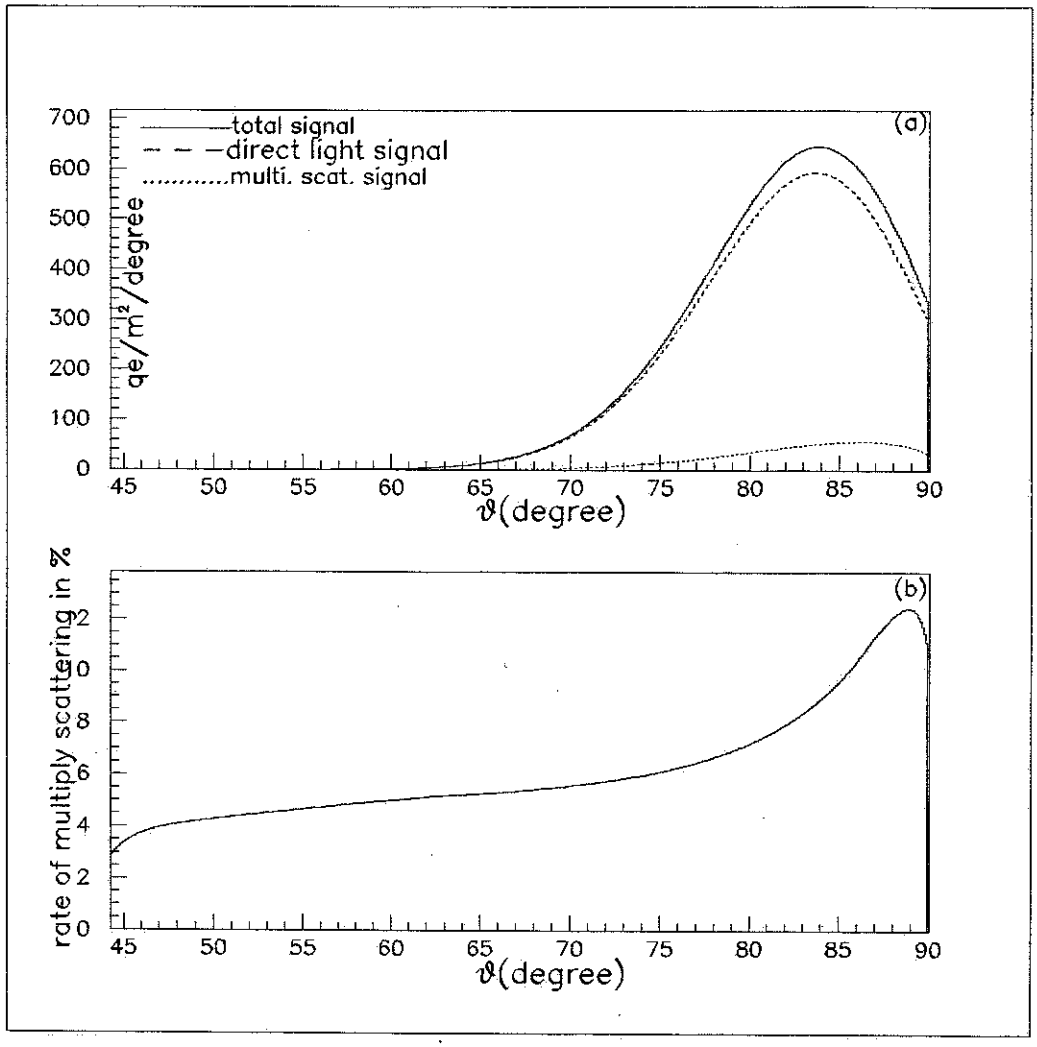

Figure 6.12: *Same as Figure 6.11. except the shower to detector distance is 20 Km*

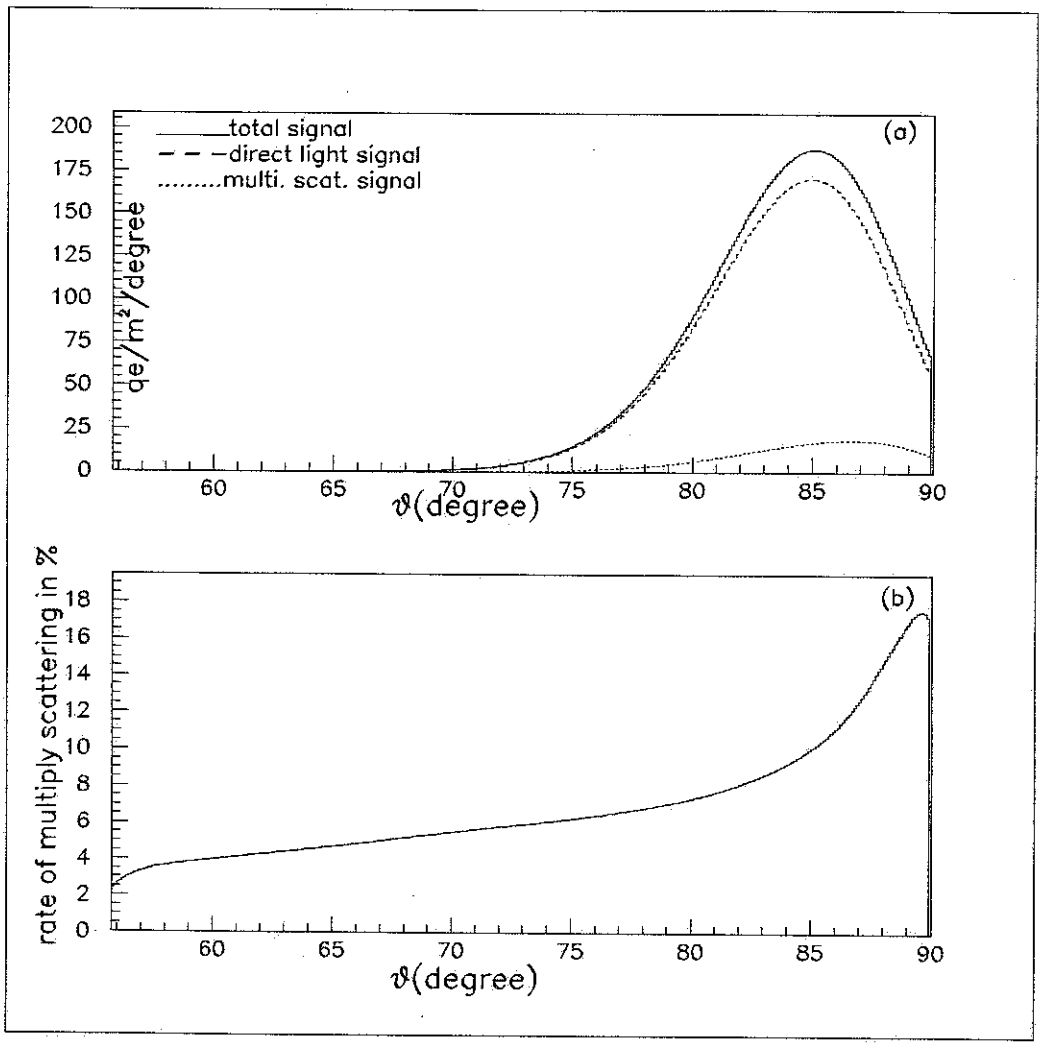

Figure 6.13: *Same as Figure 6.11 except the shower to detector distance is 30 Km*

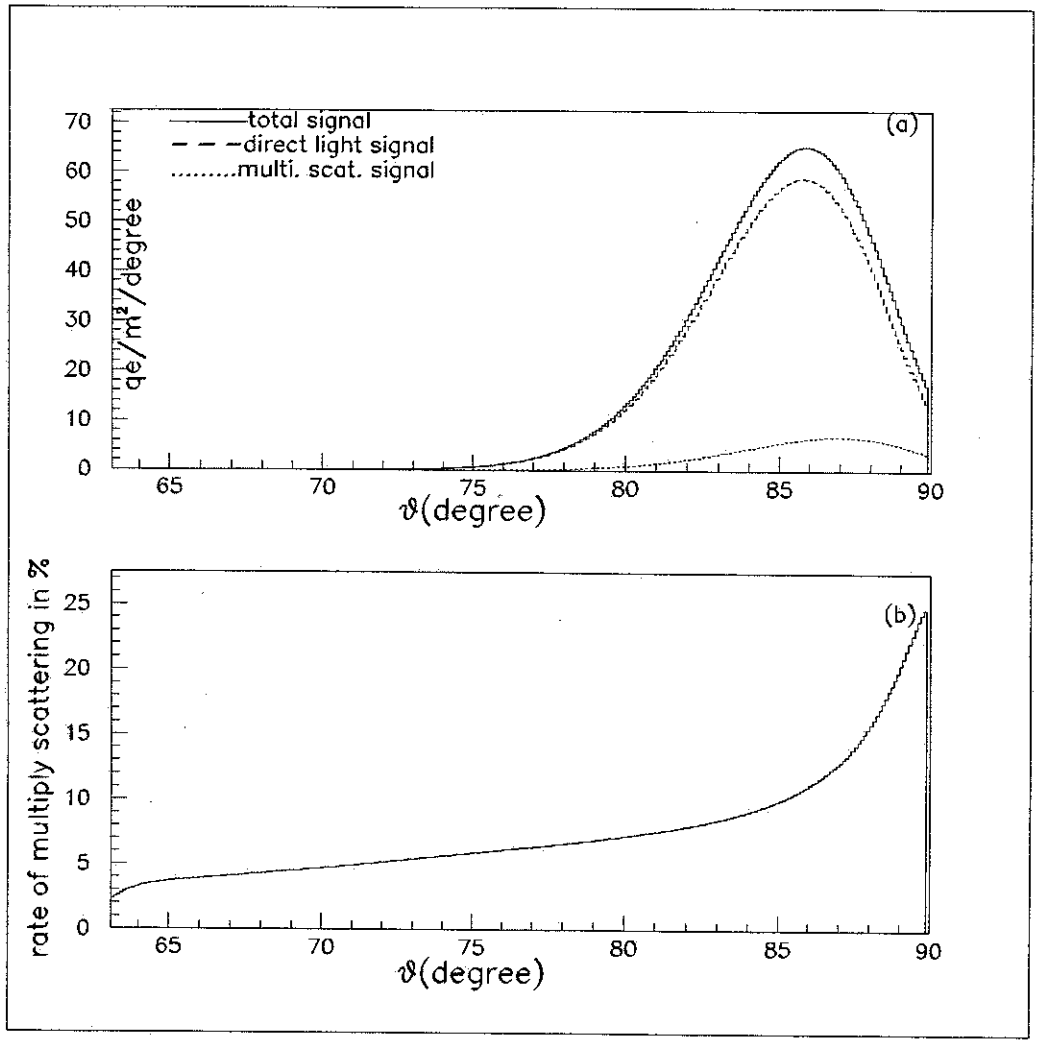

Figure 6.14: *Same as Figure 6.11. except the shower to detector distance is 40 Km*

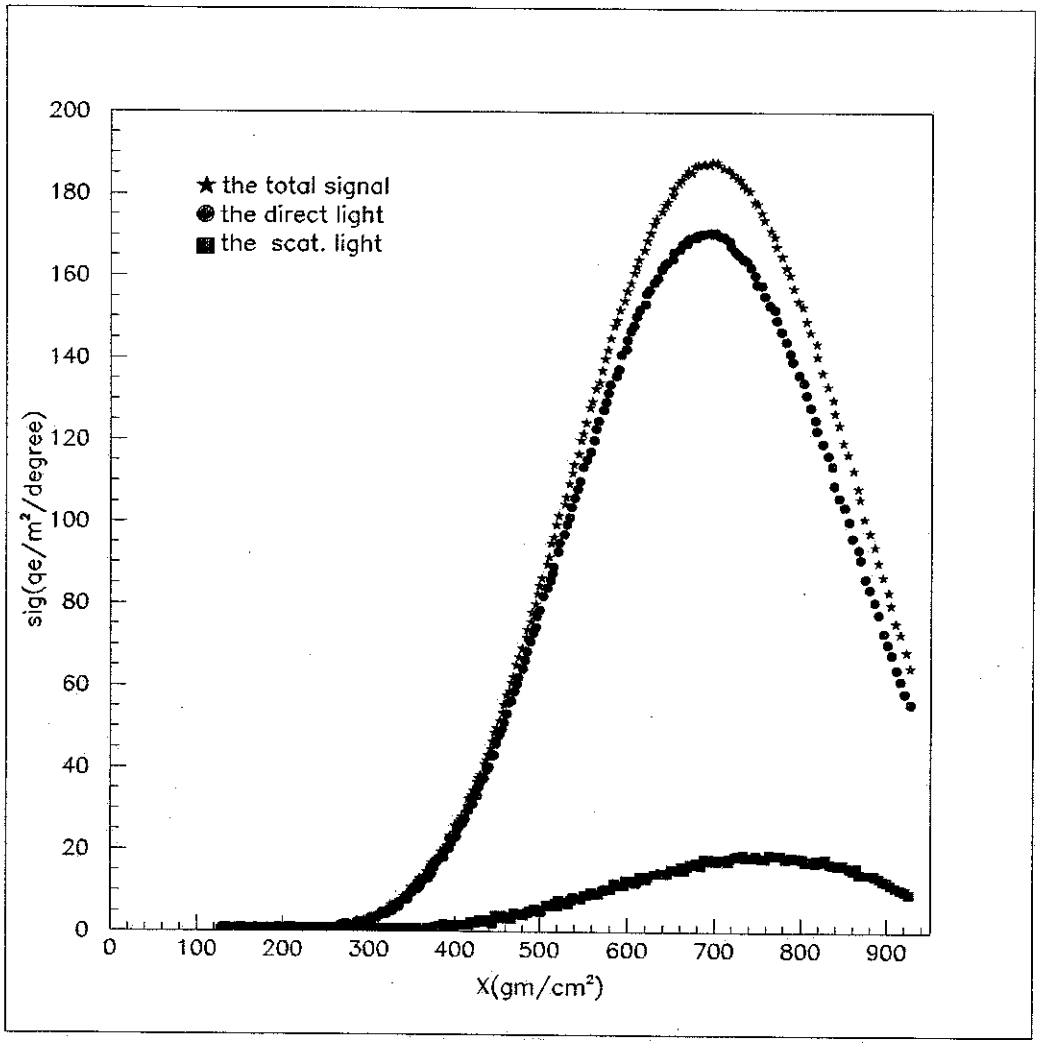

Figure 6.15: *The same shower longitudinal profile as in Figure 6.13. The X axis is the slant depth of the shower at every stage. The total area under the line proportional to the primary energy of the Cosmic ray.*

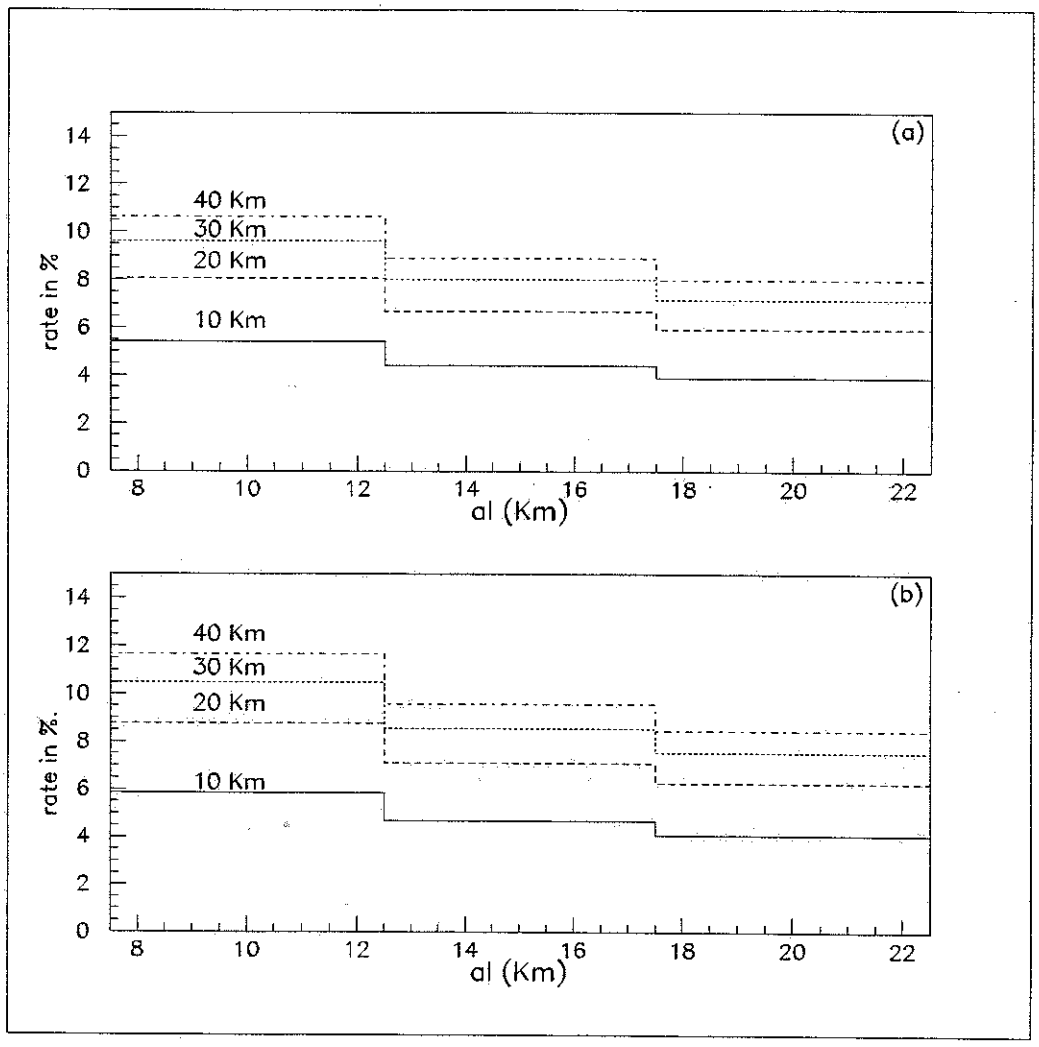

Figure 6.16: *The contribution of the multiply scattering light to the primary energy estimation in percentage depends on different atmosphere model for different shower detector distance. X axis is the aerosol horizontal extinction length. (a) the aerosol scale height is 1.2 Km. (b)the aerosol scale height is 1.5 Km.*

different aerosol models. We changed the horizontal aerosol extinction length from 10 Km to 20 Km, with the scale height change from 1.2 Km to 1.5 Km. We can see the scattering light contributes to the energy estimation in about 10%.

It is interesting to see that when the shower to detector distance is moved from 10 Km to 40 Km, the scattering effect does not increase dramatically. This is because we only integrate the signal within a fixed time window.

More generally, the EAS can not be vertical, we also simulated showers with arbitrary zenith angle, and the multiply scattering effect on the shower longitudinal profile will change shower by shower depend on the shower geometry. But the effect on the primary energy estimate is still about 10%. In the real HiRes data analysis, we will calculate this effect for every shower.

As point in Section 6.3, there is about 10% error in the scattering radiance calculation. But since the multiply scattering light itself is only about 10% for the total light, so the error transferred from the scattering radiance calculation is only about 1%, which is much small than the systematics of this experiment

6.5 Conclusion

The properties of an aureole about a point source that are due to atmospheric scattering were calculated by two approaches: the Mont Carlo method and iterative technique. For the iterative technique we have an applicable approach to calculate as high order of scattering as you want within reasonable calculation time for any kind of atmosphere and any detector setup. The results match very well with the MC results within error of about 10%. The iterative method is more useful than MC

method if we are interested in the temporal aureole problem. We studied the properties of the temporal aureole depend mainly on single-scattering albedo, scattering phase function, optical depth between source and detector, detector view angle.

Then we apply the multiply scattering property of a point source to the EHE cosmic ray shower detected by the atmosphere fluorescence technique. And found the contribution of the scattering light is about 10% , which depends on how far the shower is from the detector in the unit of optical depth. This means the energy estimate will be corrected by 10% because this effect.

Chapter 7

Atmosphere Calibration

The importance of understanding atmospheric conditions for the HiRes experiment are two folds. The first, it is the correction for the light transmission from the EAS to the detector. Second, the observed signal by HiRes includes both air fluorescence and some scattered Cherenkov light from air shower. The Cherenkov light must be subtracted from the signal when the data is reconstructed. How much of Cherenkov light can be scattered to the detector depends on the atmospheric condition.

As described in Section 5.3, various properties of the atmosphere must be known to understand the observed fluorescence light plus scattered Cherenkov light back to the source point at the EAS. This includes:

(a) the vertical profile of the atmosphere: density $\rho(z)$ and temperature $T(z)$ as a function of height z. As of first order this is well represented by U. S. Standard Atmosphere model.

(b) the Rayleigh scattering differential cross section as a function of wavelength.

(c) the vertical profile of aerosols as a function of height above HiRes detector

site.

(d) the aerosol scattering differential cross section (in another word, the extinction length and the phase function) as a function a wavelength

(e) the Ozone absorption efficiency.

In these items the light attenuation due to Rayleigh scattering is well known and described in section 5.3, depending on atmospheric vertical profile. The variation from the mean is only about 3% [77]. The Ozone density can change, but the ozone density just above ground is very low (see Figure 5.6), the impact of this variation on the HiRes signal is very small and can be ignored. The aerosol part is a challenge for HiRes experiment. Variations in size, shape, dielectric constant and vertical distribution, all these contribute in making aerosol scattering difficult to understand. The amount of aerosols changes dramatically with time and location, this gives the major source of systematic for the energy determination for far away showers.

In order to understand the aerosol part of the atmosphere, HiRes experiment uses steerable Laser systems to calibrate the atmosphere. In this chapter I will use the steerable laser system installed at Camel's Back HiRes-II site(HR2SLS), which is described in Section 4.5, to retrieval the aerosol condition including the vertical profile distribution, the horizontal extinction length and phase function, by assuming we understand the molecule part and Ozone part. The method described here is also used as an absolute energy calibration for nearby lasershots in clear weather condition.

7.1 Laser Equation and Aerosol Model

The Geometry setup for a laser shot is shown in Figure 5.8. Let N_0 be the total number of photons coming out from the laser system to sky. X_0 is the original position of the Laser system. X_1 is the original position of HiRes detector, $\lambda = 355nm$ is the laser wavelength, within δl length at point X, the photons are scattered away from laser direction with angle θ into HiRes detector. The light propagation for the photons has been described in detail in Section 5.3. Here I summarize the results and express it as a Laser equation, which gives the relationship between the number of photoelectrons measured at HiRes detector to the total number of photons coming out from laser system and the atmosphere conditions:

$$\begin{aligned} N_{pe}(X_0, X, X_1, \theta, \lambda) &= \{(\frac{d^2}{dld\Omega}(\lambda,\theta)\mid_{rsct} + \frac{d^2}{dld\Omega}(\lambda,\theta)\mid_{asct}\} N_0 T(X_0, X, \lambda)\delta l \delta\Omega \\ & \quad T(X, X_1) T_{UV}(\lambda) R_m(\lambda) Qe(\lambda) \end{aligned} \tag{7.1}$$

where $T(X_1, X_2) = T_R(X_1, X_2)T_A(X_1, X_2)T_{O_3}(X_1, X_2)$ is the transmission factor from X_1 point to X_2 point, which depends on the Rayleigh scattering, aerosol scattering, and Ozone absorption. *rsct* and *asct* are Rayleigh scattering and aerosol scattering respectively, $\delta\Omega$ is the solid angle of the mirror surface relative to point X. T_{UV} is the UV filter transmission factor, R_m is the mirror reflection factor, and Qe is the quantum efficiency of the PMT. all these variable has been described in Section 5.4.1, except the aerosol scattering factor which is unknown. In this equation, the Rayleigh scattering part and Ozone absorption are well understood, If we can calibrate the laser energy which related to N_0, laser direction, and HiRes detector which related to N_{pe} to reasonable accuracy, therefore it is possible to obtain the aerosol scattering properties by subtracting the Rayleigh scattering and ozone absorption.

In order to understand the aerosol scattering, we first modeled the aerosol distribution. If we assume the aerosol is uniform horizontally, and exponential decay vertically with a scale height of H_s, as explained in Section 5.3. Thus the aerosol scattering is given by:

$$\frac{d^2}{dld\Omega}|_{asct} = \frac{\rho_a(h)}{L_A(\lambda)} \times P(\theta) \tag{7.2}$$

where L_A is the horizontal extinction length, $P(\theta)$ is the normalized phase function with

$$\int_{4\pi} P(\theta)d\Omega = 1 \tag{7.3}$$

ρ_a is the aerosol density function depends on height and in the form:

$$\rho_a(h) = exp(-h/H_s) \tag{7.4}$$

In this model, if we understand the horizontal extinction length L_A, the aerosol scale height H_s, and the normalized phase function $P(\theta)$, then we understand everything about the aerosol scattering. Of course the real aerosol distribution can be different from this model, such as it is not uniform horizontally or it is not exponentially distributed vertically[70]. The model given here gives at least the first order approximation about the aerosol properties, and it fits the average real aerosol distribution as shown in Figure 5.2. In the following only this model will be discussed.

7.2 Procedure of Retrieval Algorithm

The basic idea for the aerosol retrieval method is by comparing the difference between the calculated laser signal from Equation 7.1 to the measured signal, adjusting the aerosol model, trying to get the difference as small as possible. The phase function is involved together with the aerosol distribution in Equation 7.2. To retrieval these parameters individually, I use two separated steps.

The basic procedure in the algorithm is as following:

(1) measure the signal by HiRes-I detector for a laser shot with energy and direction calibrated.

(2) correct the measured signal by ray tracing technique described in section 5.4.2. The main effects include the spots sizes of the mirror on the focal plane, the non-uniform response at the surface of PMT and gap between the pixels, and the lateral spread out of the laser shot from pointing direction. Then re-organize the pixel signal into a series of bin signal with a 1^o step in scattering angle θ.

(3) calculate the laser equation 7.1 to get a series of simulated bin signal in the same direction θ as in the real measurement given in (2) by using an arbitrary normalized phase function. Compare the simulated signal to the real measured signal, by adjusting the aerosol horizontal extinction length L_A, and scale height H_s, find the best L_A and H_S which correspond the smallest difference between the simulated laser track to the real laser track.

(4) repeatedly apply step (3) for all the laser shots shooting at different time with different energy and direction by assuming same input aerosol phase function, calculate the average aerosol horizontal extinction length L_A, and scale height H_s.

(5) using the average aerosol horizontal extinction length L_A, and scale height H_s calculated in step (4), solve the laser equation to get the simulated Rayleigh scattering light, subtract the calculated Rayleigh scattering light from the measured signal to get the aerosol scattering light, calculate the aerosol phase function by using equation 7.2.

(6) apply step (5) for all laser shots, calculate the average aerosol phase function. extrapolate and interpolate the points where the detector did not see directly, then normalize the phase function with equation 7.3.

(7) use the average normalized aerosol phase function as input, apply steps (3), (4), (5), and(6) repeatedly until the difference of the average aerosol horizontal extinction length L_A, and scale height H_s between consecutive steps is small enough or the total iteration exceed a maximum number.

In the above algorithm, steps (3) and (4) are to calculate L_A and H_s by using all kinds of laser shots with input phase function, steps (5) and (6) are to calculate phase function by using input L_A and H_s. Suppose the implicate relationship between L_A, H_s to $P(\theta)$ is:

$$\begin{cases} L_A, H_S = f(P(\theta)) & (a) \\ P(\theta) = g(L_A, H_S) & (b) \end{cases} \tag{7.5}$$

our goal is to solve L_A, H_S and $P(\theta)$ separately. Mathematically there are sophisticated way to solve the above equation, such as Newton-Raphson algorithm.

In Equations 7.1 and 7.2, the aerosol extinction L_A and H_S will contribute to the measured signal N_{pe} in two ways: for a hazy night (L_A is small), the aerosol transmission factor T_A will become small, in the mean time the aerosol scattering in

Equation 7.2 will become strong. These two factors are concealing each other. Which factor dominates the other depends on the source to detector traveling distance. by simulating vertical shots, it has been found that[64] when the source to detector is farther than 3 km, the attenuation factor dominates. In our case, we are going to deal with the laser shot sitting at HiRes-II site, which is 12.6 km away from HiRes-I detector, so the attenuation factor will dominate.

With this argument, in step (5), if the input L_A is smaller than the real one, then the calculated average phase function $P(\theta)$ will be bigger than the real phase function, which means the integral of $P(\theta)$ with solid angle will be bigger than 1. But in step (6) we force $P(\theta)$ be normalized (by assuming the aerosol absorption efficiency is ignored at UV wavelength range [69]), and then plug the normalized $P(\theta)$ into steps (3) and (4) to get new L_A. It has been found this algorithm converges very well.

In practice, if L_A and H_S is oscillating, we simply use a self-adjusting constant C, or so called relaxation parameter, to ensure the convergence of the calculated L_A and H_S:

$$[L_A]_{new} = [L_A]_{old} + C\Delta[L_A] \tag{7.6}$$

$$[H_s]_{new} = [H_s]_{old} + C\Delta[H_s] \tag{7.7}$$

in which $\Delta[L_A]$ and $\Delta[H_s]$ is the difference between consecutive steps. The initial value of C is set to 1. In each iteration, the algorithm keeps track of the previous value of $\Delta[L_A]$ and $\Delta[H_s]$, if it increases, which suggests that the L_A and H_s is over corrected, then C is decreased by half. When there are relatively large errors, C may become too small. In this case, C is reset to 1.

The criteria we used in the retrieval algorithm are (a) the absolute percentage difference between consecutive calculated value $\Delta[L_A]/[L_A]$ and $\Delta[H_s]/[H_s]$ is smaller than 0.1%, or (b) the number of iterations exceeds a certain value (100).

One step left in this algorithm is to calculate the averaged phase function in step (6). Because the detector does not cover all scattering angle from $[0^o, 180^o]$. When the scattering angle is less than 20^o or bigger than 160^o, the detector either can not see it or the signal is very poor. In this case we have to extrapolate the phase function to the whole range of $[0^o, 180^o]$ from the detectable range, and then normalize it. To do this, I use the modified Henyey-Greenstein function given in Equation 6.33, which is usually used to describe the aerosol phase function, to fit the measurable part of the phase function and then extrapolate it.

7.3 Simulation Results

To evaluate the performance of the retrieval algorithm, I use MC laser shots. The detail of the laser shots simulation is given in Section 5.6, and tried to simulate the laser shots as close to the real laser shot as possible. A variety of aerosol conditions (aerosol horizontal extinction length L_A, scale height H_S, and phase function $P(\theta)$) and different laser shots have been used to generate pseudo data for HiRes detector. The performance of the retrieval algorithm is evaluated by comparing the retrieved aerosol condition with the aerosol condition used in creating the pseudo data, referred to as the true aerosol condition.

7.3.1 Retrieval Results of Random Laser Shot

I first use the simulated laser shots pointing in randomly directions, and use the above algorithm to retrieval the aerosol condition. Figure 7.1 shows the retrieval results of the aerosol horizontal extinction length L_A, scale height H_s, and phase function $P(\theta)$. The input parameters are $L_A = 10km$, $H_s = 1.5km$. Total two thousand shots have been simulated. The input aerosol phase function is same phase function as shown in Figure 5.3, which is calculated from Mie scattering. The figure shows the histogram of the retrieval parameters from all the shots. The retrieval phase function is the average result from all shot. Figure 7.2 shows the retrieval results of the aerosol parameters with input values as $L_A = 20km$, $H_s = 1.5km$. Compare this two figures, we can see the more aerosol there is (corresponds to small L_A) the better this method works.

Consider there is measurement uncertainty in the real experiment, this can be either from the laser energy measurement or detector calibration. If I assume 5% total calibration error, the retrieval result is shown in Figure 7.3 and Figure 7.4 for $L_A = 10km$ and $L_A = 20km$ respectively and $H_s = 1.5km$ for both cases. Comparing these results with Figure 7.1 and 7.2, we can see the result becomes worse, but still the mean value of the retrieval aerosol parameters are within 5% error from the real value, and RMS is about 20%.

7.3.2 Retrieval Results of Geometry Fixed Laser Shots

For real experiment, the multiply scattering becomes important, and it has been found out (Section 7.4.1) that when the laser track is farther from the detector, the stronger the multiply scattering effect is. In the following section 7.4, when we analysis the real laser data, we calculate up to second order scattering only (it is difficult to calculate

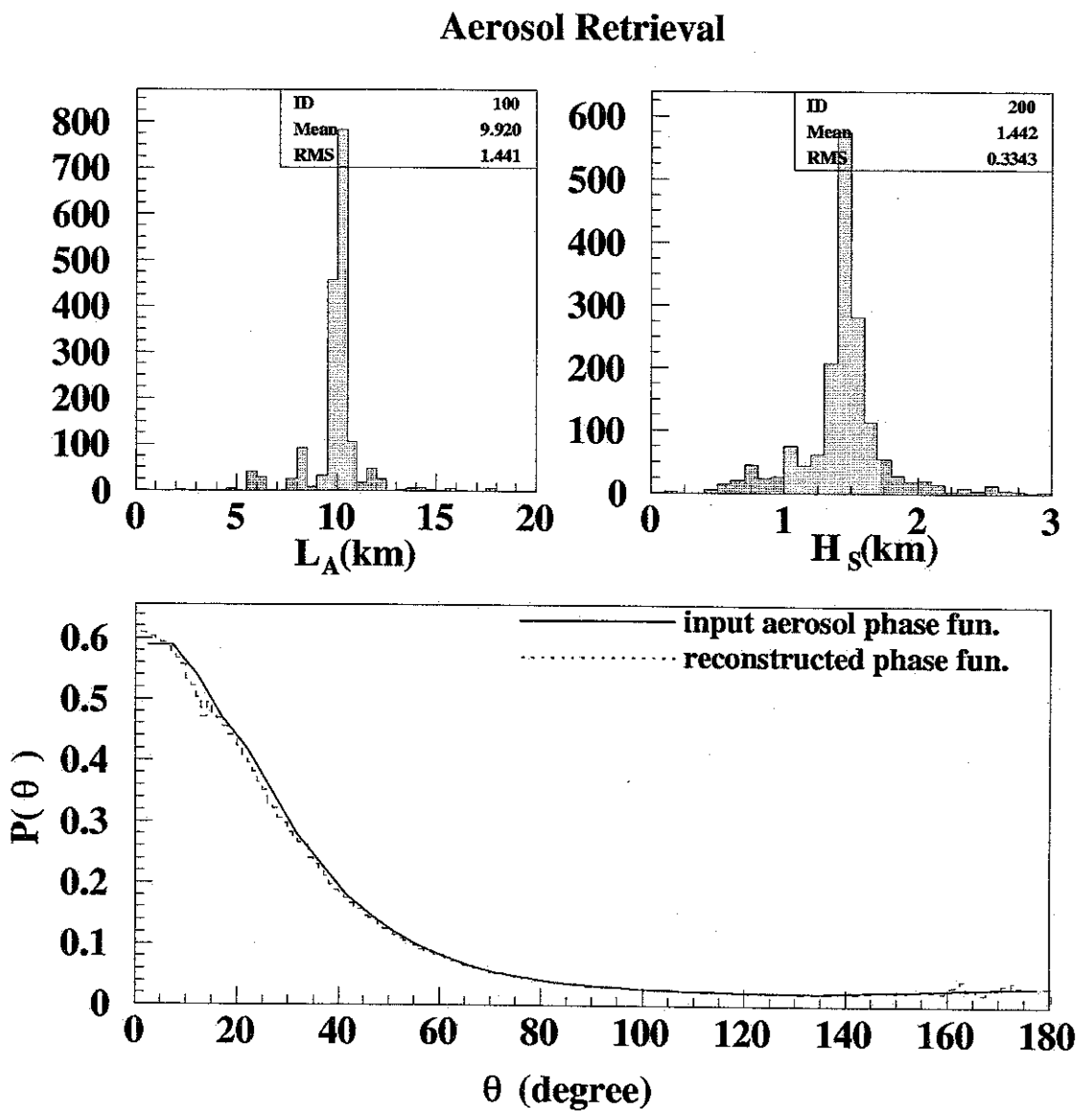

Figure 7.1: *The retrieval results of the aerosol parameters from MC random directed laser shots. The input value of the aerosol parameters in the MC laser simulation is* $L_A = 10km$, $H_s = 1.5km$.

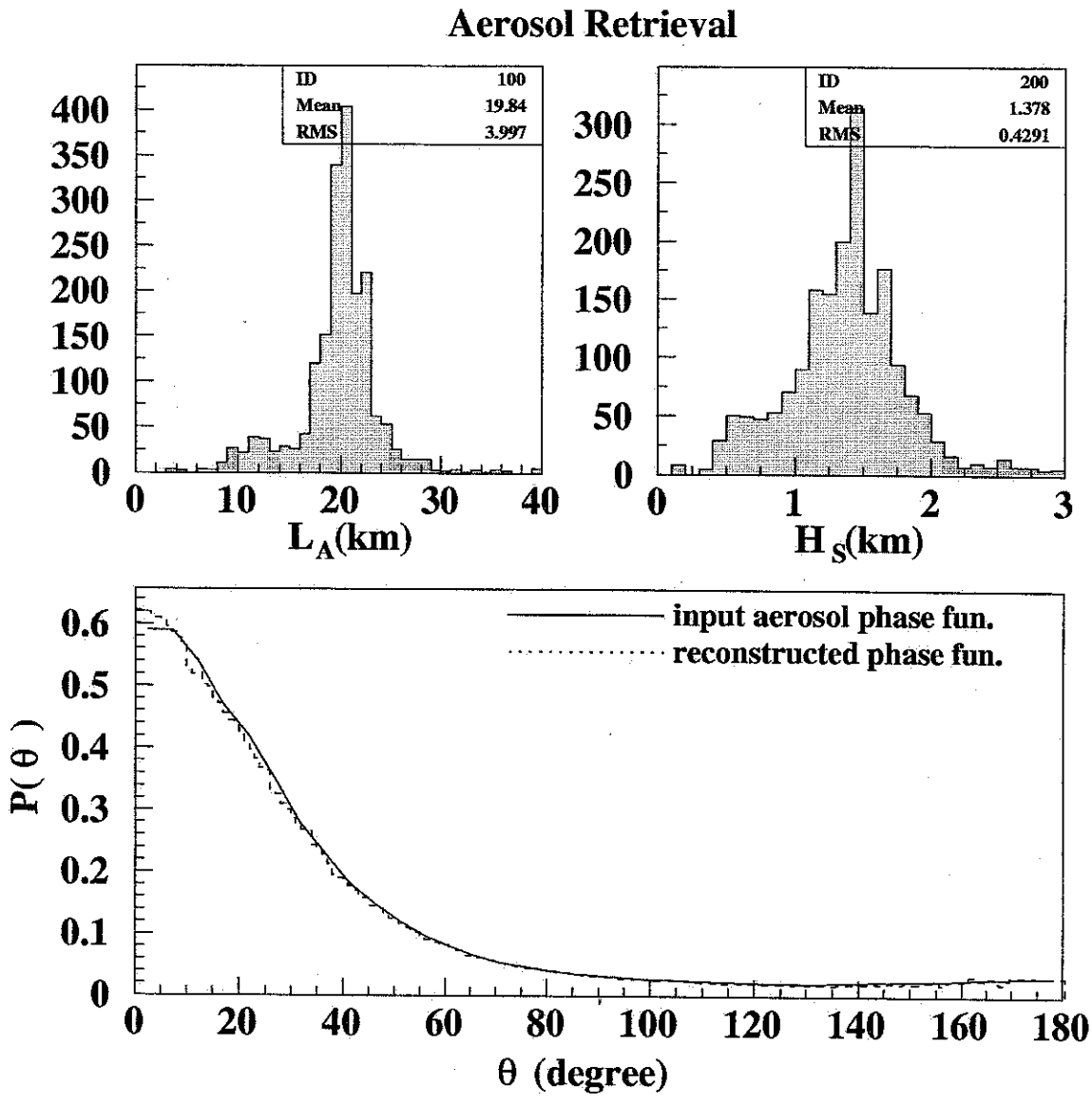

Figure 7.2: *The retrieval results of the aerosol parameters from MC random directed laser shots. The input value of the aerosol parameters in the MC laser simulation is* $L_A = 20km$, $H_s = 1.5km$.

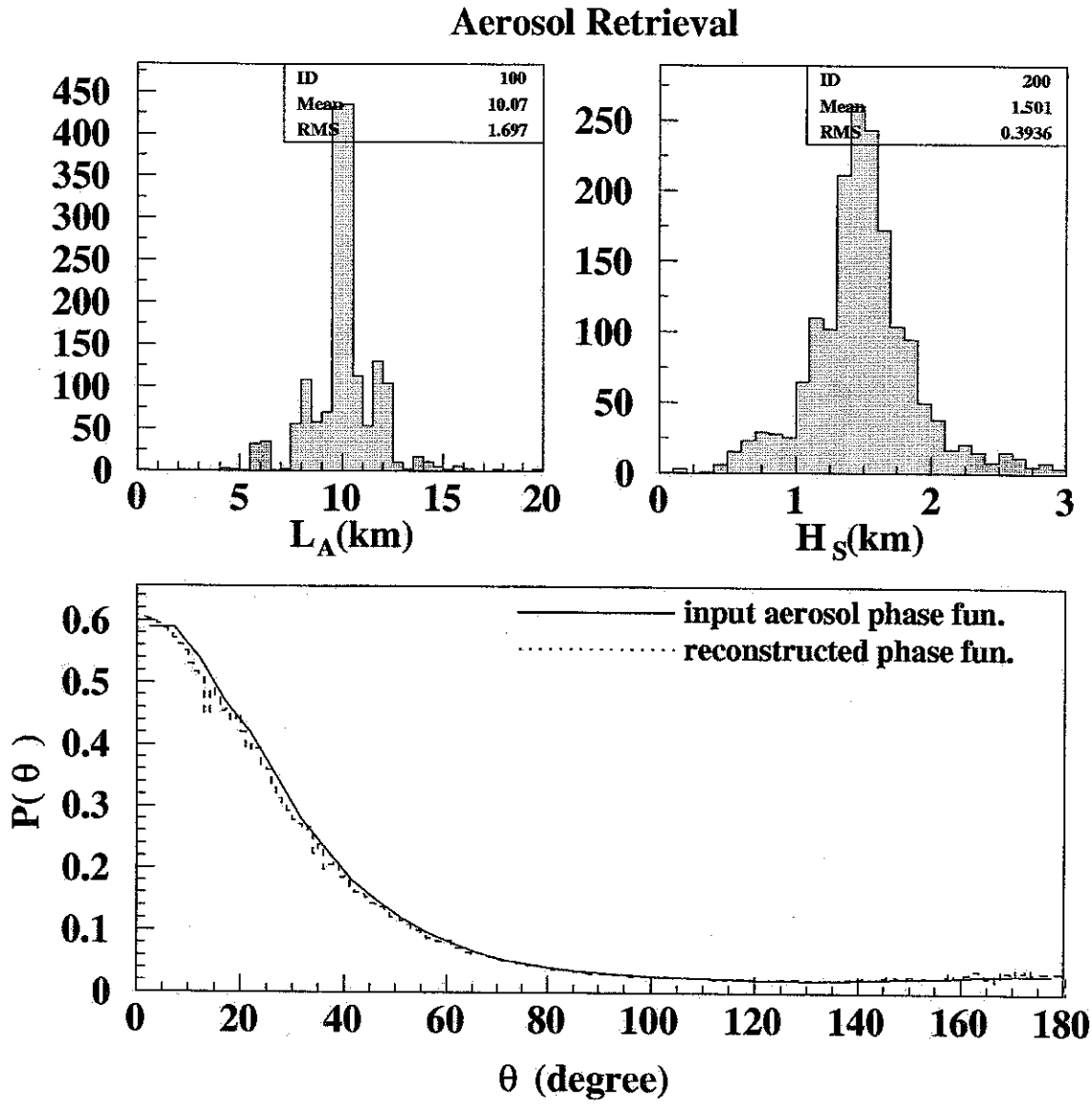

Figure 7.3: *The retrieval results of the aerosol parameters from MC random directed laser shots. The input value of the aerosol parameters in the MC laser simulation is* $L_A = 10km$, $H_s = 1.5km$. *Here we assume 5% calibration error.*

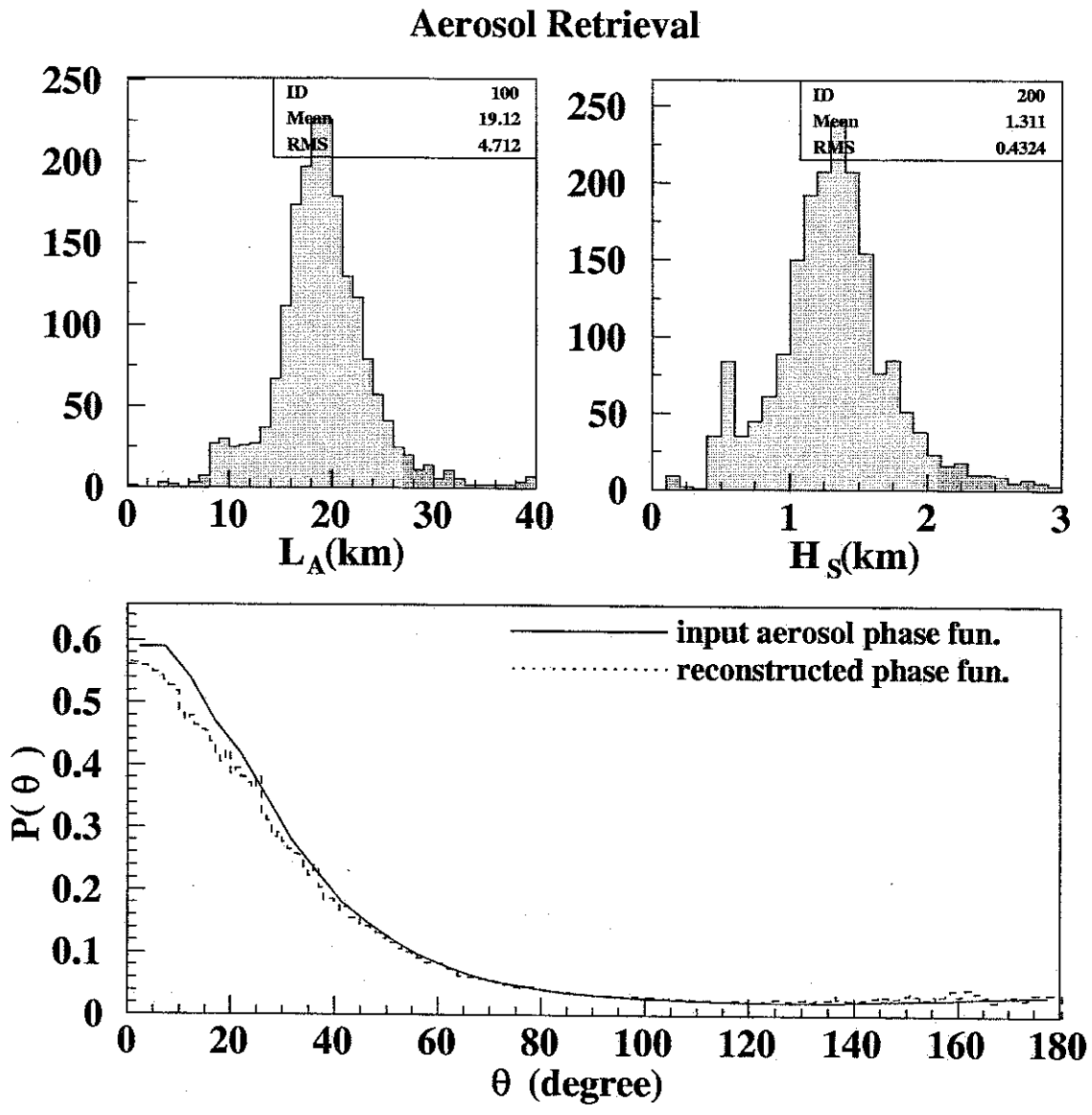

Figure 7.4: *The retrieval results of the aerosol parameters from MC random directed laser shots. The input value of the aerosol parameters in the MC laser simulation is* $L_A = 20km$, $H_s = 1.5km$. *Here we assume 5% calibration error.*

all order of scattering effect by current method). In order to minimize the effect of higher order multiply scattering, we will use only the laser shots closest to the HiRes detector, which correspond to 2 degree and 15 degree off from HiRes detector with the elevation angle is 0.6 degree and 4 degree respectively (referring to figure 4.8 for the direction). In this section, I simulate only these two sets of laser shots and retrieval the aerosol condition.

In Figure 7.5, a laser shot with azimuth 15 degree away from HiRes-I direction and 4 degree elevation is shown. Figure 7.5(a) shows the track on the HiRes-I detector event display; (c) shows the bin signal measured from the triggered tube signal at HiRes-I detector and also the signal calculated from the best fitted aerosol model; (b) shows the components of the two kinds of scattering light: the Rayleigh scattering light and the aerosol scattering light.

Figure 7.6 shows the retrieval results of the aerosol horizontal extinction length L_A, scale height H_s, and phase function $P(\theta)$. The input parameters are $L_A = 10km$, $H_s = 1.5km$. Figure 7.7 shows the retrieval results of the aerosol parameters with input values as $L_A = 20km$, $H_s = 1.5km$. Here we assume there are 5% calibration uncertainty same as in figures 7.3 and 7.4. By comparing these figures, we can see the retrieval result of scale height is worse than before. The reason is because with these fixed laser shots, the detectable laser part only covers from 0 km to 1.3 km height, but in the case of random shot, the height of the detectable part can be as high as 5 km depending on the geometry. Mathematically, the longer the rang is, the better it can be fitted to a exponential function.

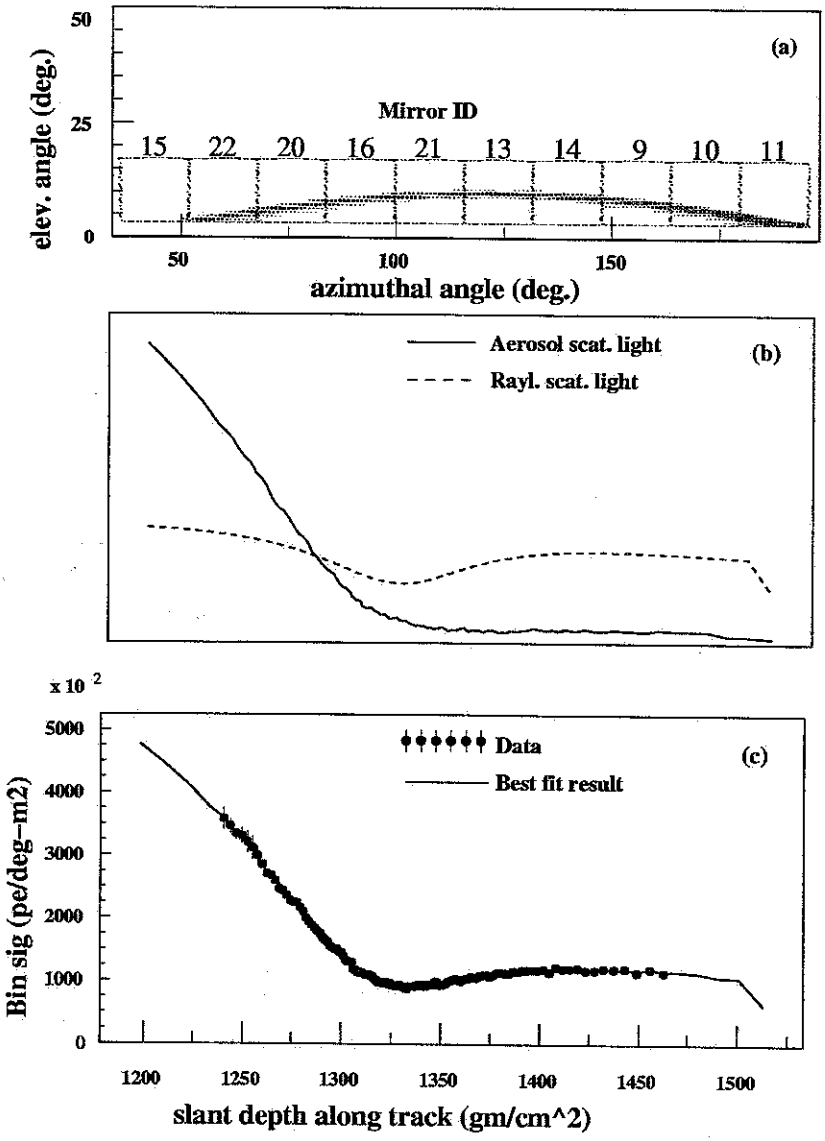

Figure 7.5: *An example Laser track and the fitted result.*

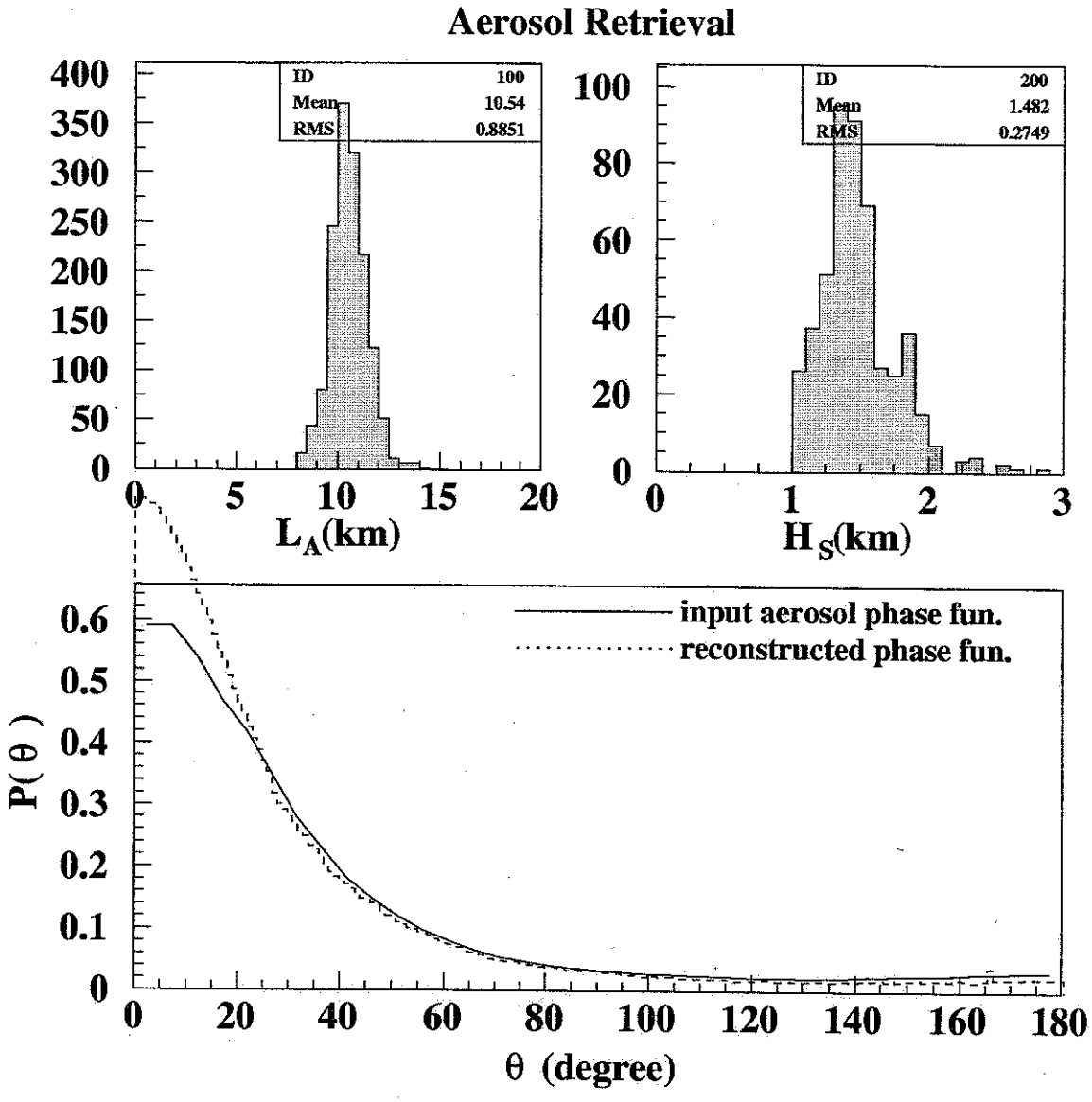

Figure 7.6: *The retrieval results of the aerosol parameters from MC laser shots with fixed geometry. The input value of the aerosol parameters in the MC laser simulation is* $L_A = 10km$, $H_s = 1.5km$. *Here we assume 5% calibration error.*

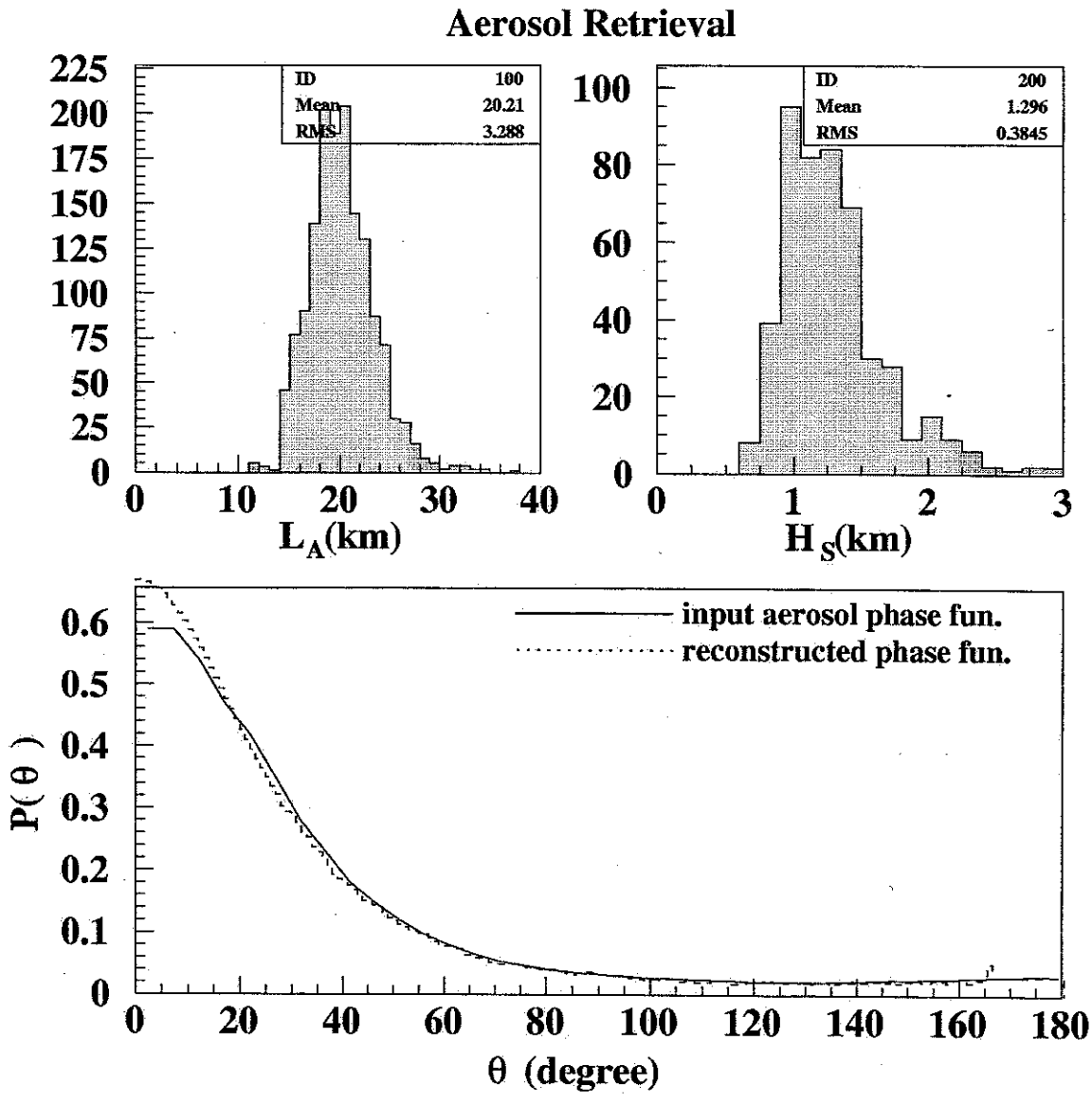

Figure 7.7: *The retrieval results of the aerosol parameters from MC laser shots with fixed geometry. The input value of the aerosol parameters in the MC laser simulation is $L_A = 20km$, $H_s = 1.5km$. Here we assume 5% calibration error.*

7.4 Real Atmosphere Calibration Results

HR2SLS is running and data taking every since September 1999 during the detector running time. Up to Apr. 2000, there are about 6 full months laser shots data. In this section, I will analysis these laser shots by using the method described before to calibrate the atmosphere condition. Ideally the atmosphere condition should be monitored on time, but since we do not have laser shots covering the whole time when HiRes I detector was running, so I will get the averaged atmosphere condition during this period, this result will be used later in the data analysis for real cosmic ray analysis. The fluctuation of the atmosphere condition from average will also be considered as systematics in the data analysis.

7.4.1 Multiply Scattering Effect

The MC simulation of the laser shots given in this chapter only deals with first order scattering. But as discussed in chapter 6, because the forward scattering peak of aerosol phase function, when the source is far way, the multiply scattering effect will become important. For the real laser shots analysis, the second order scattering effect has also been included. Figure 7.8 shows this result. Figure 7.8 (a) shows the event display of the laser on HiRes detector with 15 degree off from HiRes detector horizontally. The second order scattering effect is calculated based on the aerosol condition, the results is shown in figure 7.8 (b). From top to bottom, the aerosol horizontal extinction is assumed to be 9km, 15km, 24km, 36km and 100km, the scale height is fixed to 1.5km. The x axis is the bin number in degree depending on the scattering angle and let the first good tube as bin 0. The y axis is the rate between the second scattering light to first order scattering light from laser track to the detector.

It can be see that the dense the aerosol is, more second order scattering light will contribute to the detected signal.

It has also be found out that the second order scattering effect depends on the opening angle of the laser direction to the direction from HR2SLS to HiRes-I detector direction: the bigger this opening angle is, the more important the second order scattering effect is. So in order to avoid this multiply scattering effect, we only used the closest two sets of laser shots: The first set laser shot is azimuth 2 degree off from HiRes-I detector, which have directions in azimuth and zenith as (32,0.6) and (36,0.6); the second set is azimuth 15 degree away from HiRes detector: (19,4.0) and (49,4.0), the geometry is shown in figure 4.8. This geometry is same as in MC simulation.

7.4.2 Laser Energy Calibration

Now what left for the atmosphere retrieval method is the laser energy calibration. As described in section 4.5. HR2SLS has its own laser energy monitoring system. In order to eliminate the effect of the calibration error either from HiRes detector or from HR2SLS energy measurement in the atmosphere retrieval, a different way will be used to get the laser energy.

The laser equation related in the laser energy calibration is same as equation 7.1. If we assume the best weather condition we can get is aerosol free or very little aerosol (which means the aerosol scattering term is very small compare to the Rayleigh scattering term), then from equation 7.1, we can reconstruct the laser energy from the PMT signals.

In order to check how well this method works, I simulate laser shots, and then

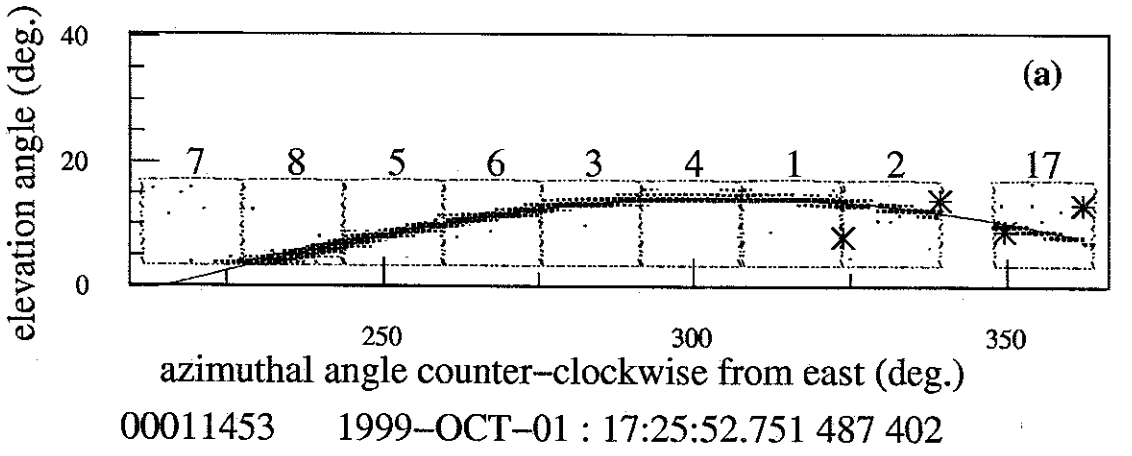

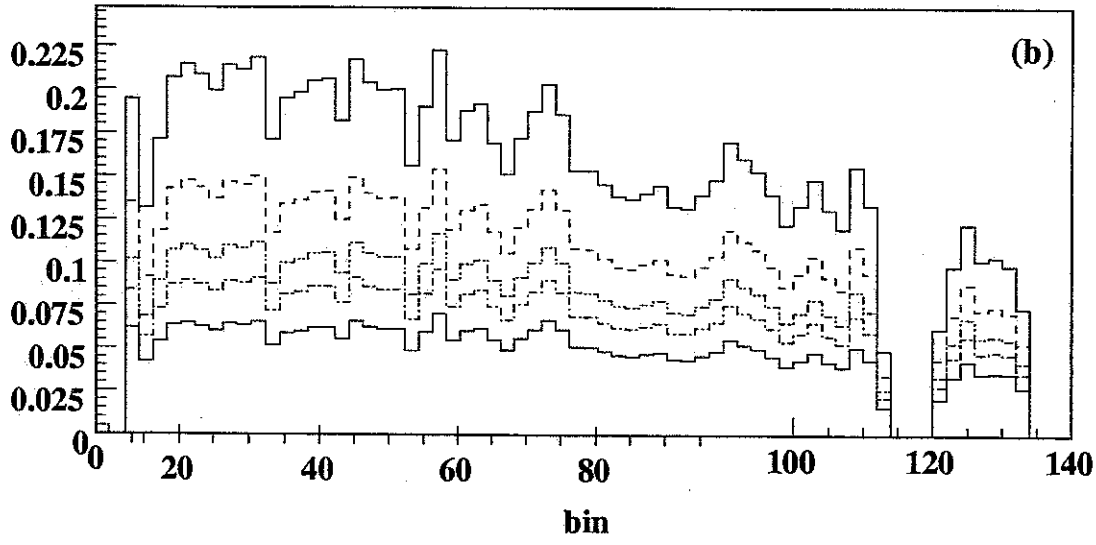

Figure 7.8: *Second order scattering effect for laser track. The track is 15 degree off from the detector. (a) shows the event display on HiRes detector; (b) shows the rate of the second oder scattering light to the first order scattering light from laser track to HiRes detector along the laser track. The different line correspond to different aerosol horizontal extinction length as described in text. X axis in figure (b) is in bin number in degree depending on the scattering angle, the bin number defined as 0 for the first good tube.*

reconstruct the laser original energy. By comparing with the input laser energy, we can get the resolution of this calibration method. The results are shown in figure 7.9. Figure 7.9 (a) gives the energy resolution of randomly pointing laser shots; 7.9 (b) gives the energy resolution of geometry fixed laser shots as described in section 7.3.2. For both cases, this method works with a resolution of a few percent.

In the real experiment, either the laser original energy measurement or the HiRes detector calibration can have systematic errors. In order to see how well both calibration are, I used the best weather conditioned laser shots we can get, by comparing the reconstructed laser energy from the PMT signal detected by HiRes to the original laser energy measurement at HR2SLS, the result is shown in figure 7.10. In the figures, E1, E0 is the reconstructed laser energy from HiRes and directly measured laser energy from HR2SLS respectively. Here we assume the horizontal extinction length of aerosol is 60Km with scale height of 1.5 km. The data covers 6 months period time. During these time range we can see both HiRes detector and HR2SLS are very stable with combined RMS about 10%, but the energy shift by 25% combined from this two method, of course we can not eliminate the case that both HiRes and HR2SLS have systematics in the same direction.

Why there is such kind of shift with these two different methods of measuring laser energy is still not clear. It is possible either the HiRes-I detector is not calibrated correctly or HR2SLS system which is a commersure laser system is not correctly calibrated, it is also possible that the method discribed here is limited in application. New calibration methods are on the way for both the HiRes detector and HR2SLS system. When more solid calibration results for these systems are aviable, this question will be answered. In order to eliminate this energy shift effect in the atmosphere calibration for general weather condition, in the following, the HR2SLS

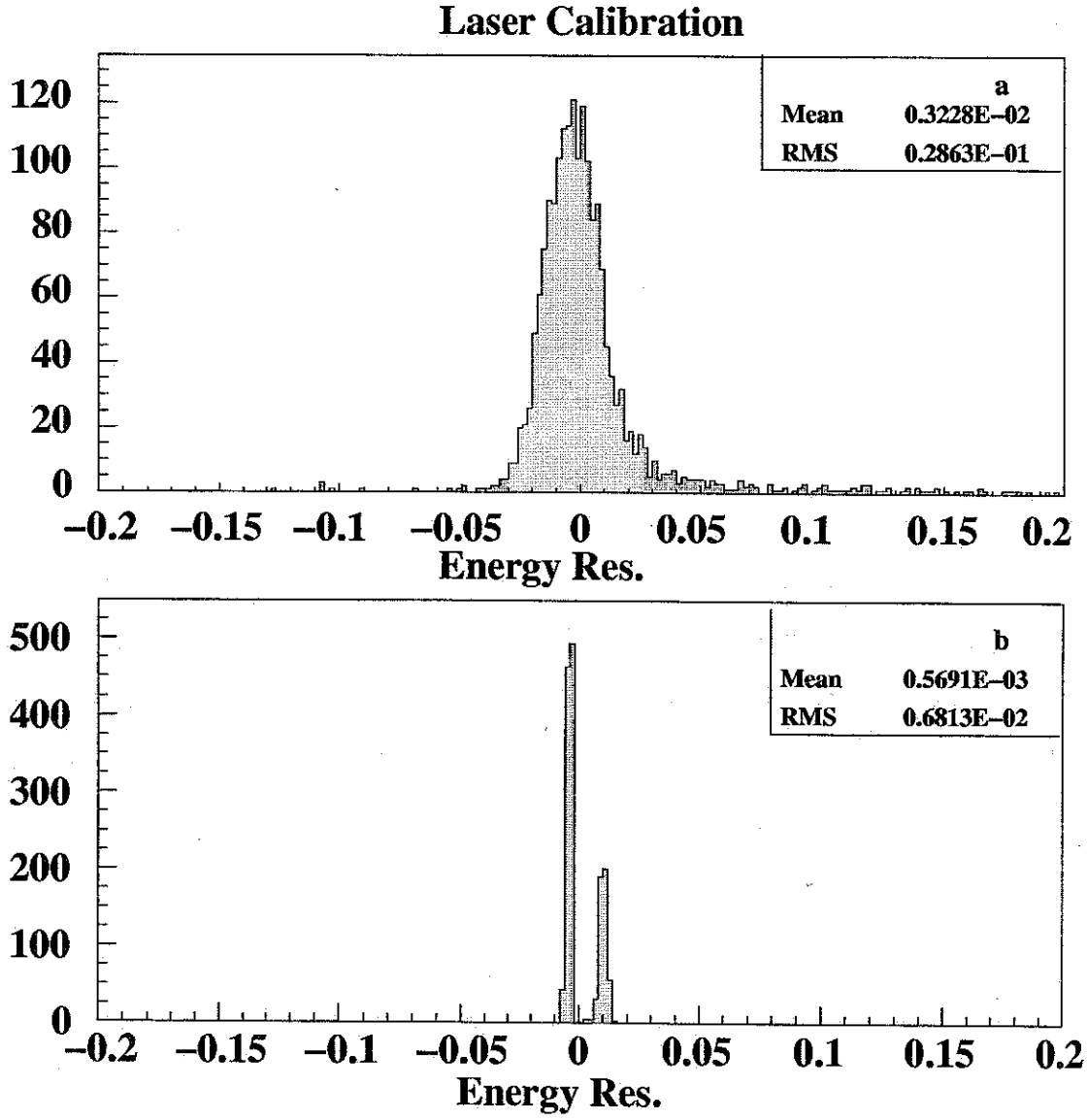

Figure 7.9: *MC Resolution of laser shots energy reconstruction. figure (a) is for randomly pointing laser shots, figure (b) is for geometry fixed laser shots.*

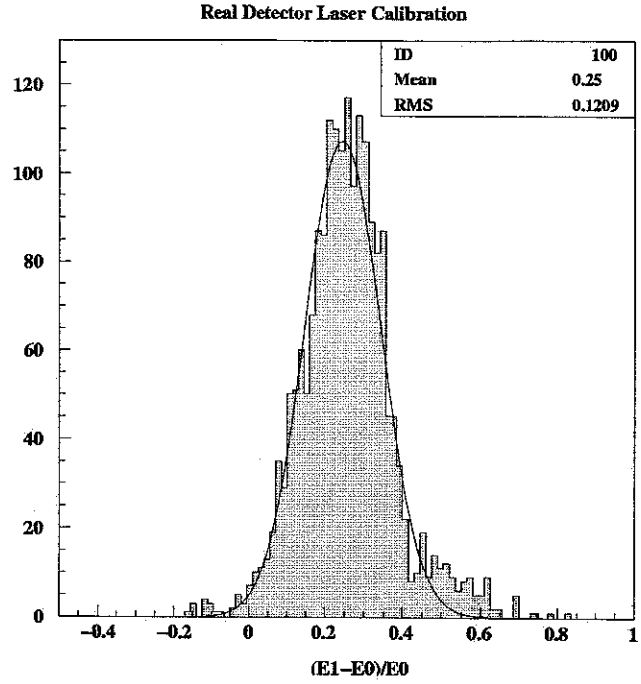

Figure 7.10: *The laser energy calibration by using best weather fixed geometry laser shots. E1 is the reconstructed laser energy from HiRes laser track PMT signals, E0 is the laser energy measured on time at HR2SLS. An aerosol model with horizontal extinction length of 60km and 1.5km scale height is assumed in the calculation.*

measured laser energy will be simply increased by 25%. This assumption is equal to assume that the HiRes detector calibration is correct and the clearest weather for HiRes detector has extinction length of 60 Km as given above. The general weather has more aerosol than that.

7.4.3 Experiment Results of Aerosol Condition for Single Day

The atmosphere at HiRes site can change from very clear to very hazy. I used the retrieve method described in this chapter before to analysis all available laser data.

Figure 7.11 shows an example of a laser track under an averaged weather condition on Oct. 3rd 1999. Figure 7.11(a) shows the event display. figure 7.11(b) shows the components of the scattering light along laser track detected by HiRes with the best fitted aerosol model, the sum of these two components is shown in figure 7.11(c) with solid line. The signal detected by HiRes is shown as dot.

The retrieval parameters of the aerosol model are shown in figure 7.12 for Oct. 3rd 1999. In figure 7.12(a), (b) the best fitted aerosol horizontal extinction length L_A and scale height H_S for every laser shot are shown respectively; figure 7.12(c) shows the fitted average scattering phase function $P(\theta)$. For comparison purpose, I also put together the standard aerosol phase function we used through out the Mont Carlo code, which is described in section 5.3 and figure 5.3.

An example of laser track under hazy weather condition on Oct. 5th 1999 is shown in figure 7.13. Comparing to figure 7.11 (b) we can see component of the aerosol scattering light is more under hazy weather condition, this result is reasonable. To see how hazy that night is, the retrieval aerosol parameters are shown in figure 7.14. The aerosol horizontal extinction is only about 8km compare to 18km in figure 7.14. In figure 7.14(c), we can see the aerosol phase function is very close to the standard aerosol phase function. But this two phase function are derived from two totally different methods.

7.4.4 Average aerosol condition

The available laser data covers from September 1999 to April 2000, in the mean time the HiRes is data taking from April 1997. we do not have daily laser data for the atmosphere monitoring. So what I am going to use is the average atmosphere

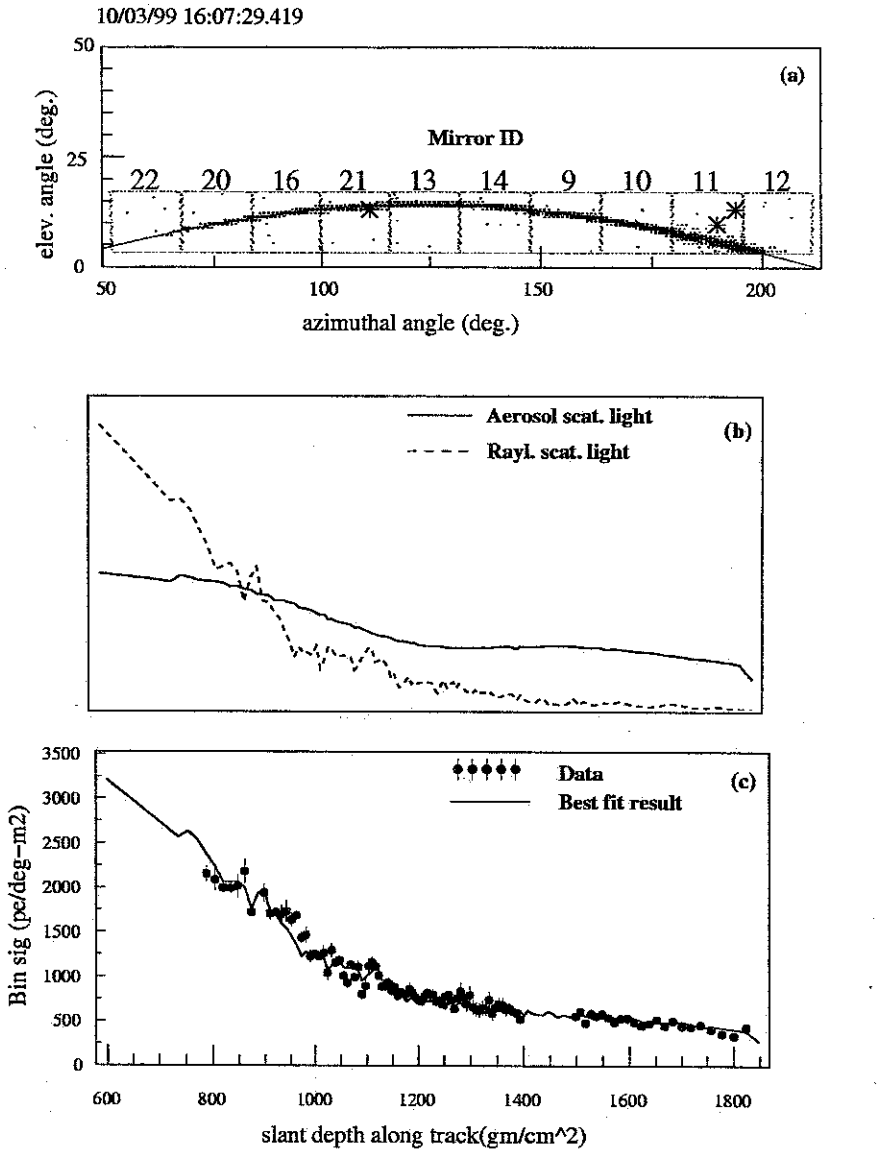

Figure 7.11: *Laser track and the best fitted result for an average aerosol condition. (a) shows the event display of laser track on HiRes detector; (b) shows the components of the two kinds of scattering light aerosol scattering and Rayleigh scattering; (c) shows signal detected by HiRes and also the fitted result with the best fitting aerosol condition by using known laser energy.*

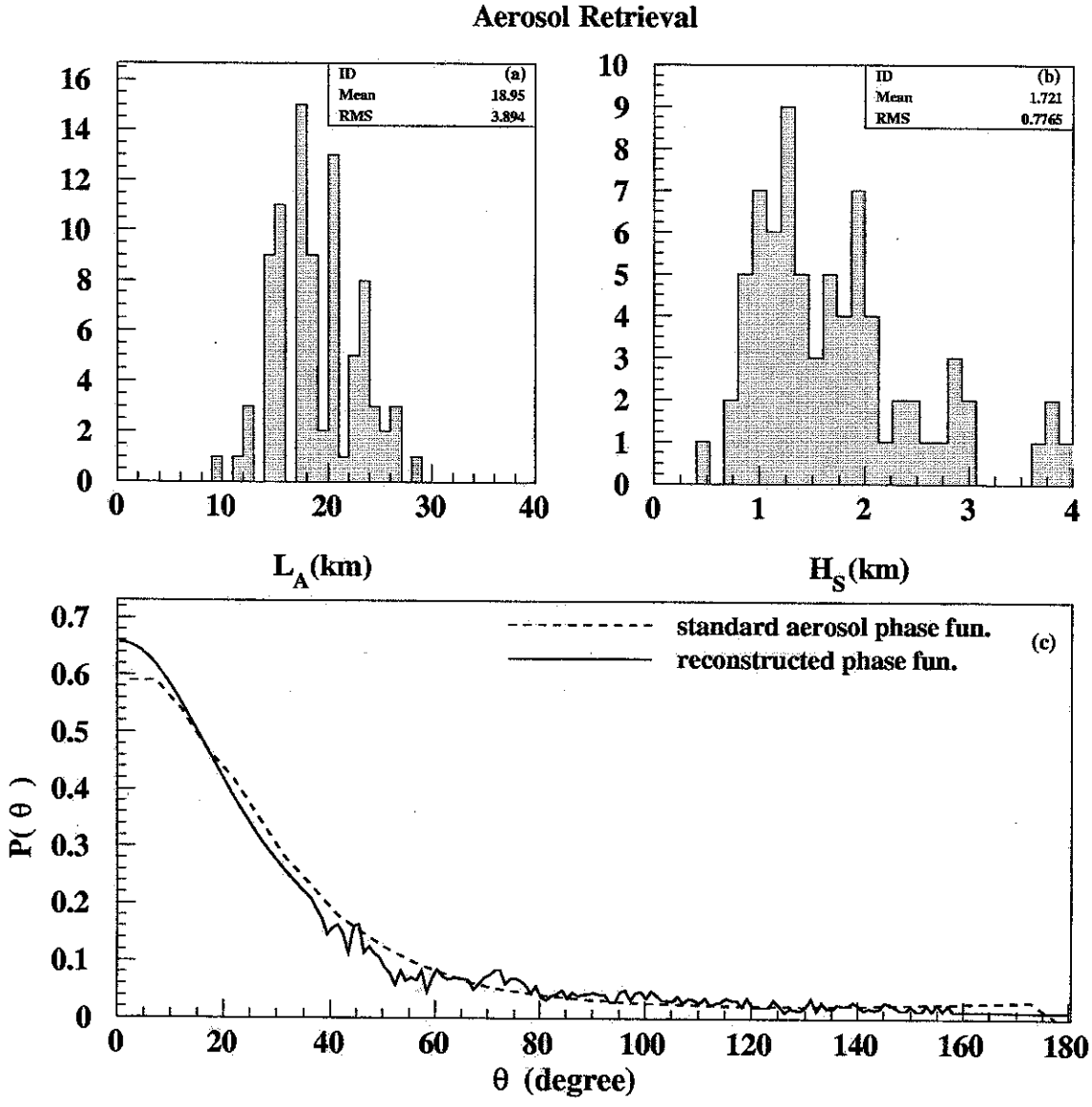

Figure 7.12: *The averaged aerosol condition for the night of Oct. 3rd 1999. (a) shows the fitted aerosol horizontal extinction length L_A; (b) shows the aerosol scale height H_S; (c) shows the averaged aerosol phase function $P(\theta)$, the standard aerosol phase function described in section 5.3 is also shown.*

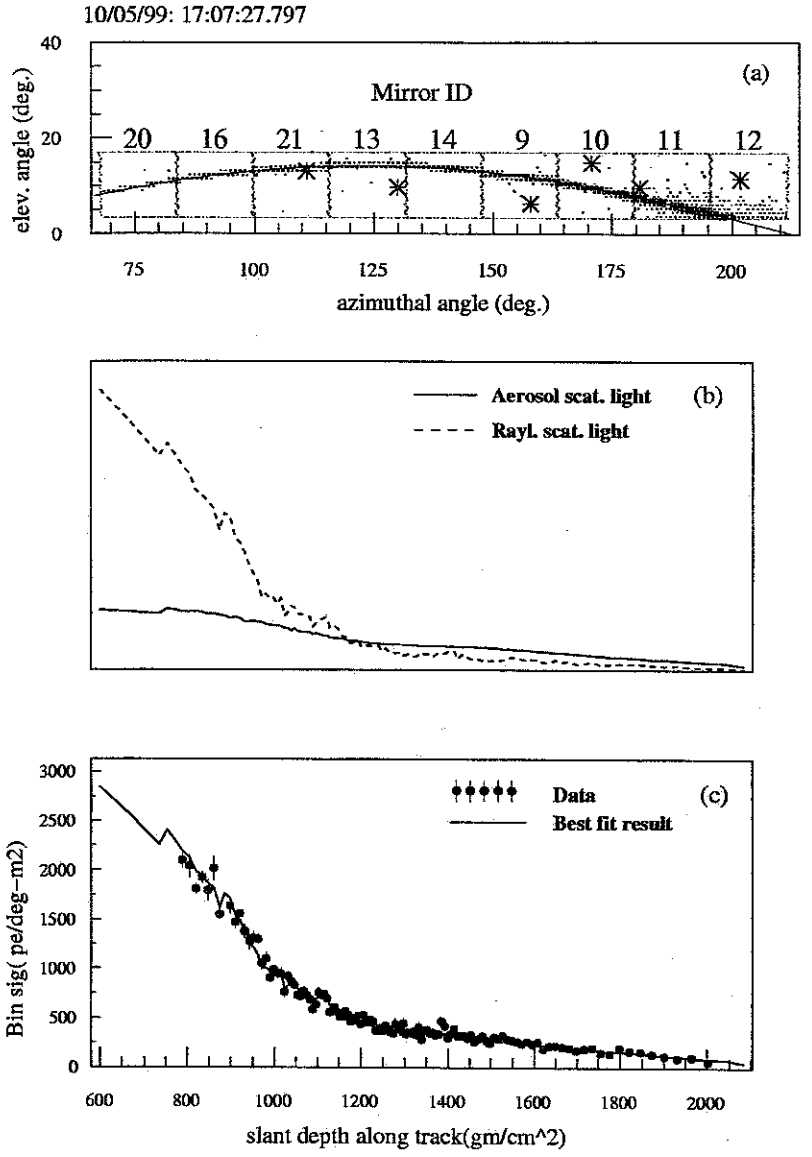

Figure 7.13: *Laser track and the best fitted result under bad aerosol condition. (a) shows the event display of laser track on HiRes detector; (b) shows the components of the two kinds of scattering light aerosol scattering and Rayleigh scattering; (c) shows signal detected by HiRes and also the fitted result with the best fitting aerosol condition by using known laser energy.*

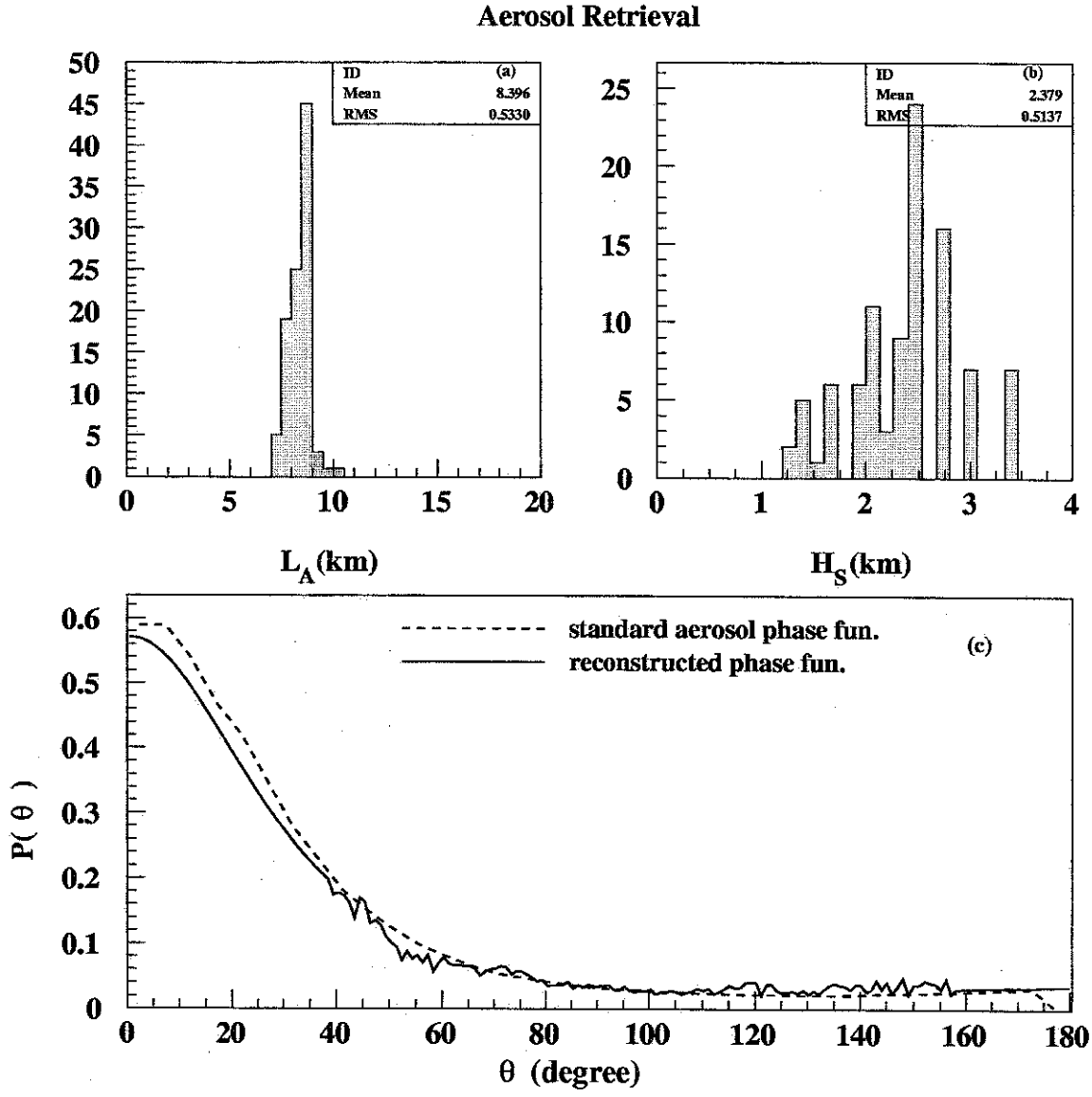

Figure 7.14: *The averaged aerosol condition for the night of Oct. 5th 1999. (a) shows the fitted aerosol horizontal extinction length L_A; (b) shows the aerosol scale height H_S; (c) shows the averaged aerosol phase function $P(\theta)$, the standard aerosol phase function described in section 5.3 is also shown.*

condition.

Figure 7.15 shows the histogram of the parameters for the aerosol model from September 1999 to April 2000. Figure 7.15(a) shows the aerosol horizontal extinction length L_A, figure (b) shows the scale height H_S, figure (c) shows the correlation between L_A and H_S. From figure (a) and (b) we get the medium value of L_A as 18 km and H_S as 1.0km, the width is 6km and 0.5km for L_A and H_S respectively. These parameters will be used for the cosmic ray analysis. From figure (c) we can see L_A and H_S has some correlation, this means the retrieval method does not complete separate this two parameters. HiRes group is still trying some other method to measure this two parameters separately. This will not be included in this thesis.

7.5 Discussion

In this chapter, I described a method to retrieval the aerosol condition from energy and direction known laser shots. And I also gave the average results of the aerosol condition for HiRes site from September 1999 to April 2000. From Mont Carlo study this method works well.

In the real experiment case, in order to avoid more than second order multiply scattering effect, this method is only limited to the closest to HiRes-I detector laser shots. This effect limits the success of decoupling aerosol horizontal extinction length to scale height, limits the application of this method only for the area close the detector. In order to fully apply this method, the complete multiply scattering effect should be studied for laser shots as in Chapter 6 for EAS.

In this method, an one dimension exponential aerosol distribution model is assumed. But the real case can be more complicated than that, especially for hazy

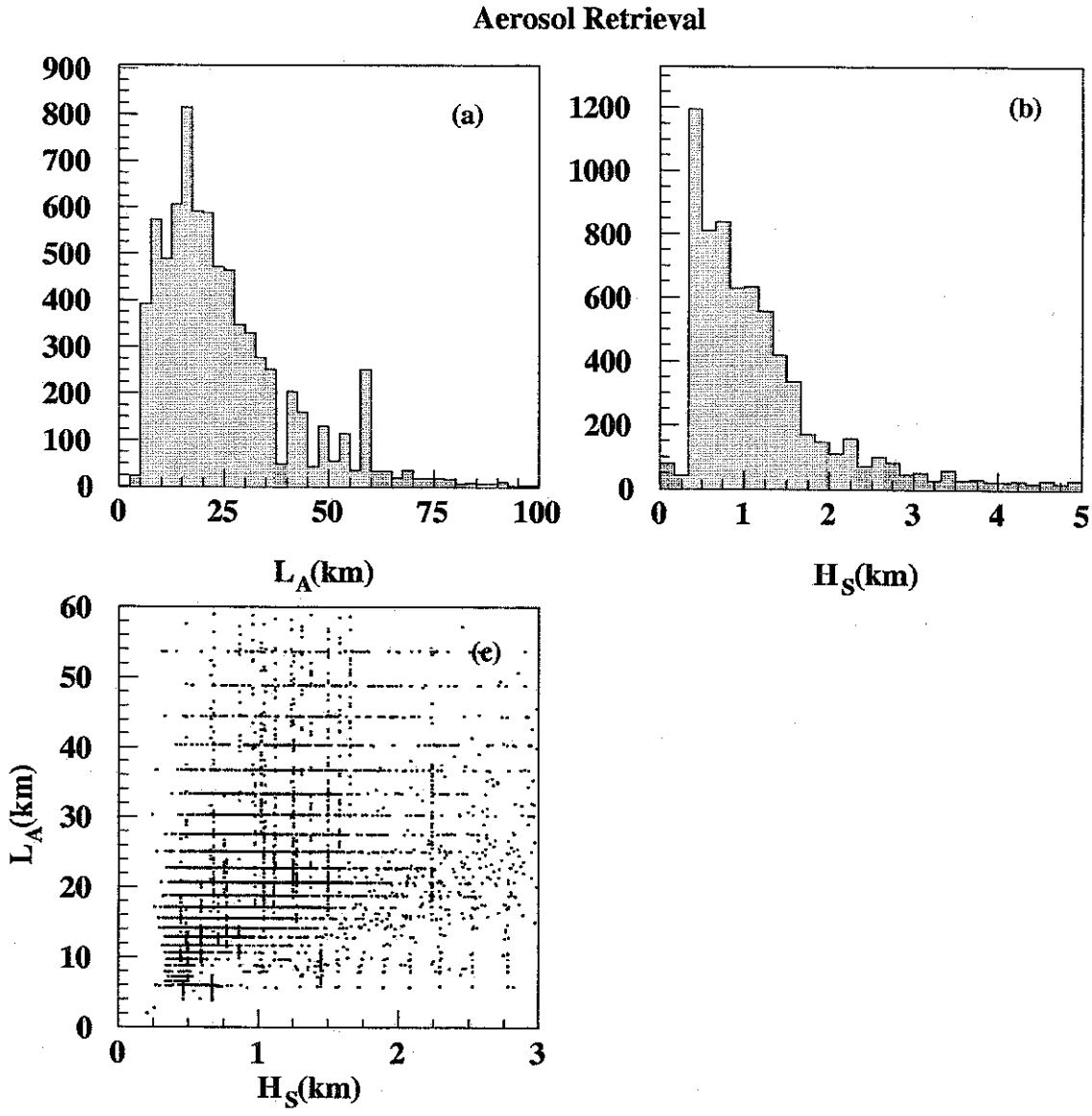

Figure 7.15: *The histogram of aerosol horizontal extinction length L_A and scale height H_S from September 1999 to April 2000. figure (c) shows the correlation of these two parameters.*

weather condition, the aerosol can be very different locally. For single day weather, the aerosol can be chaotic vertically. To avoid this problem, HiRes only uses good weather data and drop those chaotic weather data. The vertical profile of aerosol distribution can also be retrieved out by modifying current method.

HiRes is also trying Ladar to directly measure aerosol vertical profile, and try to use CCD camera to measure horizontal extinction length and phase function directly. But before the success of these new methods, the result given in this chapter is the only quantitative result about the aerosol condition for HiRes site. Even the new methods are making work later, the result from current method can still be cross checked or be used as hybrid measurement.

Chapter 8

EAS Monocular Reconstruction

8.1 Introduction

A step by step approach to reconstruct EAS (Extensive Air Shower) is described in this chapter.

a. From cosmic ray to EAS

The primary energy of the cosmic ray can be reconstructed from EAS longitudinal profile which has been parameterized by Gaisser-Hillas function. The composition can be studied by looking at the distribution of X_{max}[20].

b. From EAS to detector signal.

The charges in the EAS will produce scintillation light and Cherenkov light when they pass through air. These lights are collected by the HiRes detector. The light collected at HiRes not only depends on the properties of EAS itself, but also the geometry of the shower relative to the detector, and the scattering efficiency of the atmosphere from the shower to the detector.

Even if the scintillation production by charges is well known (in experiments[58]), the light propagation between EAS to detector(Chapter 7), iii) and the multiply scattering effect which enhances the signal (Chapter 6) are also well know, there still is challenge to reconstruct the geometry of shower track and the EAS longitudinal profile successfully.

Currently, a shower is defined by total of eight parameters. The geometry of the shower uses four parameters. Two parameters: $\hat{n}_1$ and $\hat{n}_2$, are comprised of a vector defining shower detector plane(SDP). Within the shower detector plane, two additional parameters are needed to determine the shower track: the incline angle of the shower track from horizontal ψ, and the normal distance between the detector to the shower track R_p which is also called impact parameter. These parameters are shown in Figure 8.1.

The shower profile distribution $N(X)$ describes the total number of charged particles along the path of the shower X, which has been parameterized by Gaisser-Hillas function:

$$N(X) = N_{max}(\frac{X - X_0}{X_{max} - X_0})^{\frac{X_{max}-X_0}{\lambda}} exp(\frac{X_{max} - X}{\lambda}) \tag{8.1}$$

which uses the remaining four parameters (X_0, is the pseudo first interaction depth about $-80 gm/cm^2$, X_{max} the depth along the path of shower maximum, and N_{max} the number of particles in the shower at shower maximum. λ is the interaction length around 65 gm/cm^2). It has been found[20] that X_0 and λ are correlated in a shower, so either X_0 or λ can be fixed.

Traditionally, the reconstruction procedure was carried out in 4 consecutive steps:

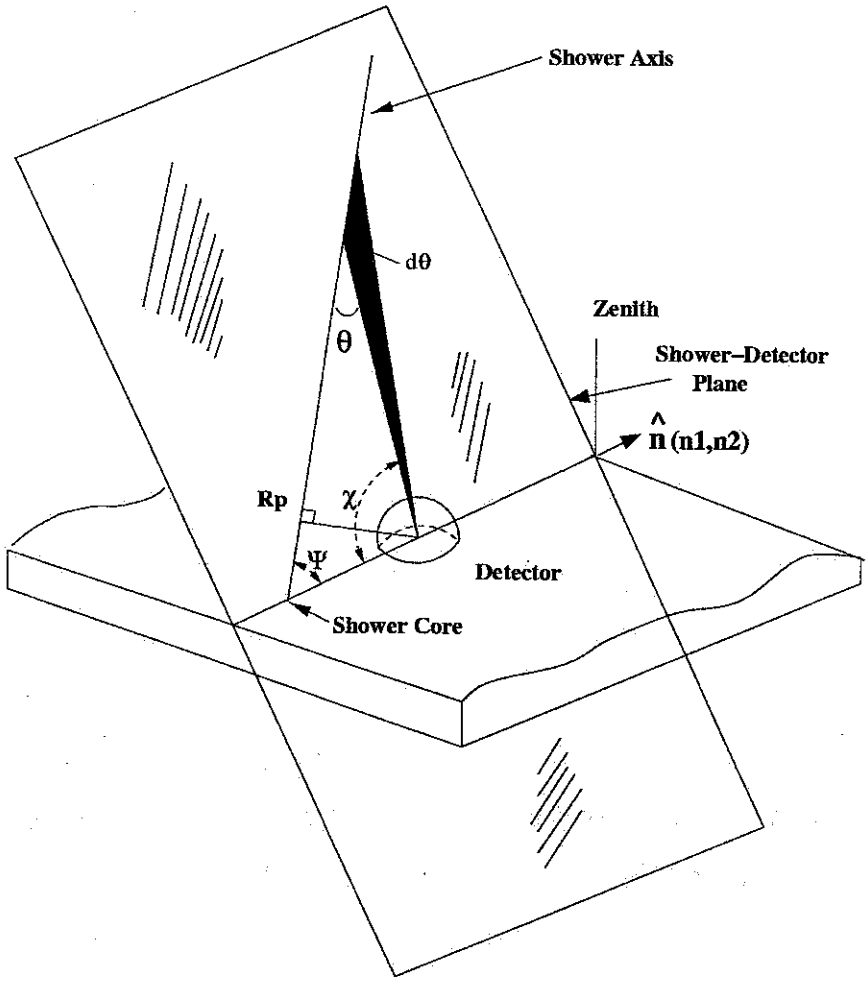

Figure 8.1: *Geometry of an EAS illustrating the SDP relative to detector.*

(1). Determining the SDP from the triggered PMTs pointing directions by amplitude weight fitting (get $\hat{n}_1$and $\hat{n}_2$).

(2). Monocular time fitting or stereo fitting to get the shower track within SDP (get R_p and ψ).

(3). Binning the tube signal into 1^o bin by correction of the spots size on focal plane, PMT gap, shower lateral spread out etc.

(4). Fit the bin signal by Gaisser-Hillas function after considering the light

production and propagation(get N_{max} , X_{max}, X_0, and λ)

The resolution of time fitting given in step (2) strongly depends on the track length. Based on prototype HiRes detector experience, good time fits can be gotten only for shower with 30^o track length or more. HiRes-I monocular detector has only one ring setup, and is dedicated for far away showers. Most showers observed have only about 12^o track length, it is too short to get a good geometry resolution if we use the monocular time fitting only. Even after we get the geometry, 12^o shower track can only given you 12 bins after steps (3). This is too few data points for a good Gaisser-Hillas profile fitting in step (4), which has 4 or 3 parameters need to be fitted.

To solve this short track problem, I used a new way to do the monocular reconstruction. The basic idea is that, the tube signal and trigger time we get in the detector are correlated to both the shower geometry and longitudinal profile. The correlation between the shower geometry to trigger time and tube signal to shower profile is apparent, and this is the idea for the traditional fitting given in step (2) and step (4) above. But considering even at same geometry, different shower profile can give different tube trigger time information; from a same shower, the tube signal is strongly depend on where the shower track is. So instead of separating the shower geometry fitting from the shower profile fitting, I will fit both the shower geometry and the profile together and directly by the tube signal and trigger time. For HiRes-I detector, a 12^o track has about 24 tubes. In this way, we can also increase the data points for fitting.

In this chapter, I will describe this new global fitting method. The geometry ,energy resolution, and X_{max} resolution are studied by MC events. To see how well this method can dealing with the real HiRes events, I will also compare the monocular reconstructed geometry to the stereo reconstructed geometry for the available stereo

data set. If we assume the stereo reconstructed geometry is very close to the real geometry, then the difference of these two gives the geometry resolution for monocular reconstruction.

8.2 Plane Fitting

The first step in reconstruction is the SDP fitting. There is a spots size of the optical system, and the pixel response is not uniform across the PMT cluster surface due to the un-uniform tube profile and the gaps between tubes, so a small plane shift or twist will give different tube signals, especially when the track is crossing the gap between tubes. A a good plane fitting is very important for the success of final reconstruction.

Traditionally the plane fitting is done by *amplitude weighted fitting method.* This method fits the SD plane by using the triggered tube pointing direction and weighting every tube with its pulse. The triggered tube pulse signal is directly related to the plane direction, there is another way to do plane fit, I call it *ray tracing planing fitting* method: by tracing light from plane to the tube, adjusting the plane to get the best tube pulse signal compare to the measured signal. It has been found that this new way of plane fitting can improve the plane fitting a lot.

8.2.1 Amplitude Weighted Fitting

The pattern of the trigger tubes can be used to determine the SDP under 2 assumptions: (a) all mirrors are at same position, or detector is a "point" detector, the mirror physical spread out can be ignored. (b) the detector has uniform response for light source from any direction.

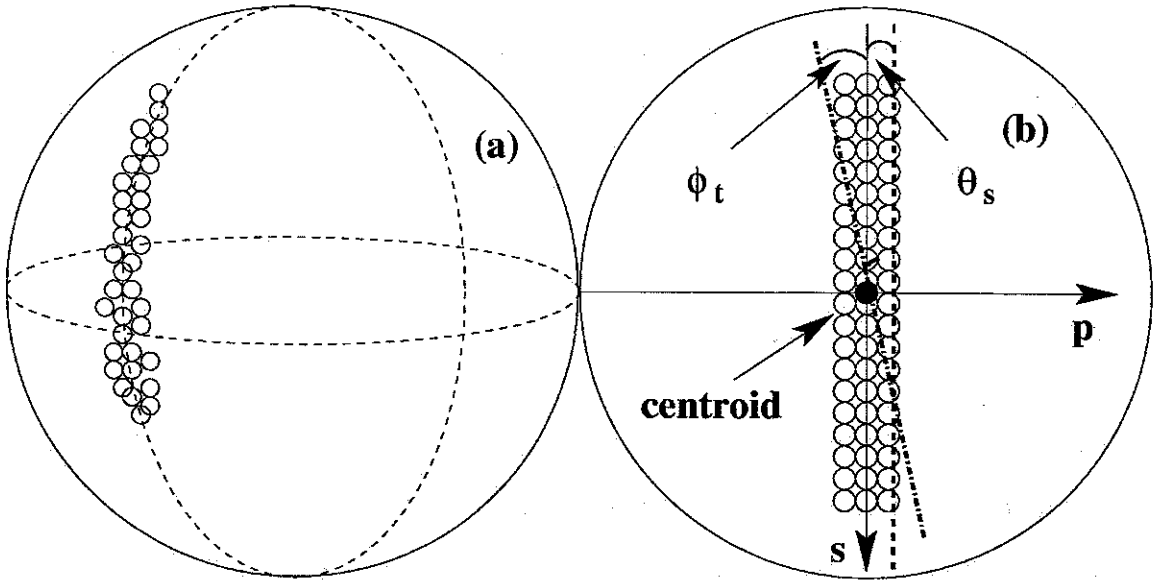

Figure 8.2: *(a) View of a track on unit sphere. (b) Illustration of The plane fitting error θ_s and ϕ_t.*

With assumption (a) we can define the directions seen by the tubes from HiRes as a point on a unit sphere. The shower detector plane passes through the center of the sphere and intersects this unit sphere gives a great circle (Figure 8.2(a)). With assumption (b), the light hitting the detector will distribute along the arc with left right symmetry(Figure 8.2(b)).

Then the plane fitting can be done by minimizing a χ^2 function defined as:

$$\chi^2_{amp} = \sum_i \frac{[(\hat{n} \cdot \hat{n}_i)]^2 \cdot w_i}{\sigma_i^2} \tag{8.2}$$

where the sum is over all good tubes. $\hat{n}$ is the plane unit vector, $\hat{n}_i$ is the tube unit viewing direction vector, w_i is the number of photo-electron number seen by tube, σ_i^2 is defined as $(w_i + S_{skyns})/w_i$ with $S_{skyns} = 200$ as sky noise. This method uses the tube signal as weight, and be called *amplitude weighted fitting.*

A real event usually contains noise-trigger tubes. These tubes are either separated from the pattern of the good tubes spatially, or temporally separated from the real track. The plane fitting procedure uses this idea to get rid of the noise tubes. To do this, we first group the triggered tubes into clusters if they are close to each other both spatially and temporally, get the special longest cluster and assume it corresponds to the real track; do the plane fit within this cluster; and then look for the good tubes, which are not neighboring to the cluster spatially but not far from the plane, and they must be close to the cluster temporally. This look-back step is trying to save some good tubes which can be separate from the cluster spatially by dead tube or dead mirror or by tubes not triggered.

The MC resolution of the plane fitting is shown in Figure 8.3. Here I define two parameters to qualify the plane fitting: one is the center shift angle θ_s, the other is the twist angle ϕ_t along the center direction as shown in figure 8.2. The plane fitting resolution improves for higher energy events. It is also apparent that when the track is longer the plane fitting is better as shown in Figure 8.3.

In above, theoretically the amplitude weighted plane fitting should work very well, but the real life is not that simply and will bring errors for the plane fitting. For assumption (a) in above, the mirrors are not at the same position, so different mirror actually has different planes. To correct this effect, I used the averaged triggered mirror position as detector position. For assumption (b), the HiRes tube has one degree field of view, the light distributed on both sides of the plane are sampled by the trigger tubes, due to noise, Poisson fluctuation, the spot size of the focal plane, the gap between tubes *etc.*, the light detected by the detector can not be exactly symmetry on both sides of the plane.

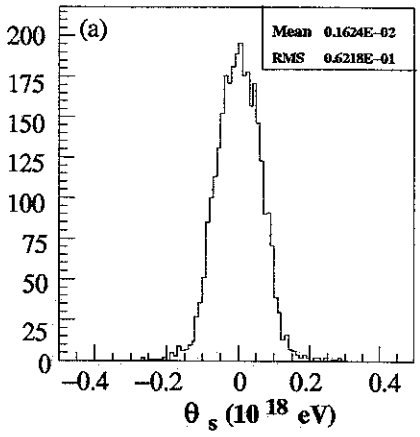
(a)
Mean 0.1624E-02
RMS 0.6218E-01
θ s (10 18 eV)

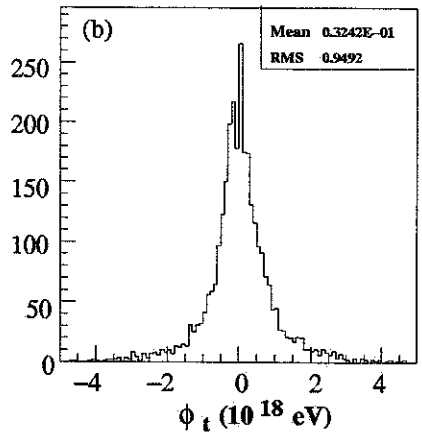
(b)
Mean 0.3242E-01
RMS 0.9492
ϕ t (10 18 eV)

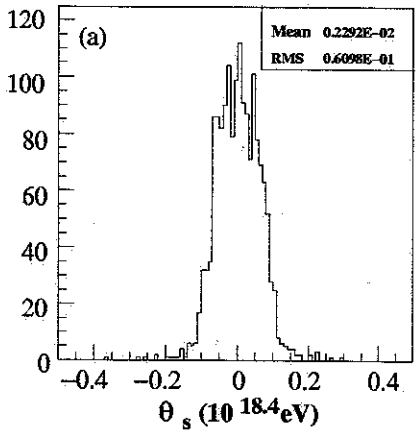
(a)
Mean 0.2292E-02
RMS 0.6098E-01
θ s (10 18.4eV)

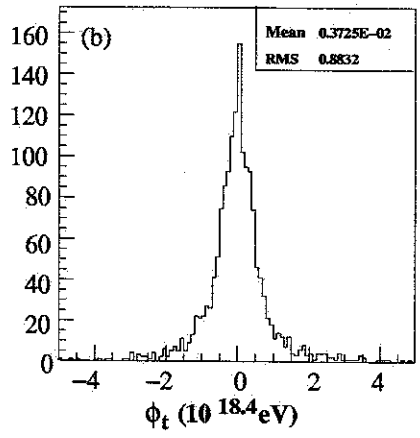
(b)
Mean 0.3725E-02
RMS 0.8832
ϕt (10 18.4eV)

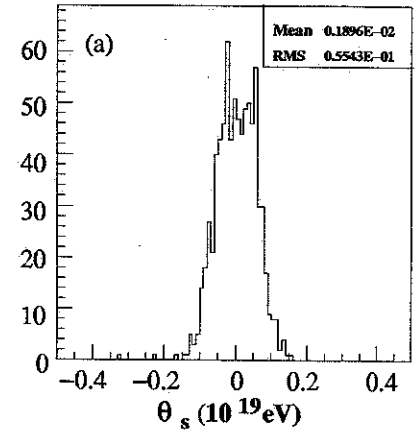
(a)
Mean 0.1896E-02
RMS 0.5543E-01
θ s (10 19eV)

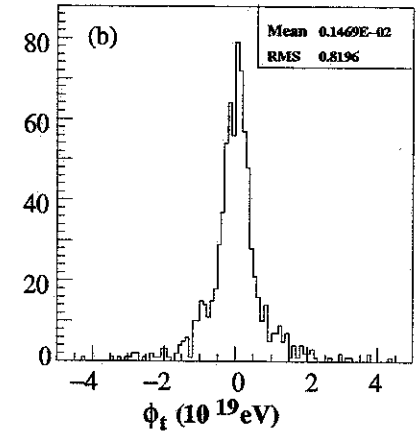
(b)
Mean 0.1469E-02
RMS 0.8196
ϕt (10 19eV)

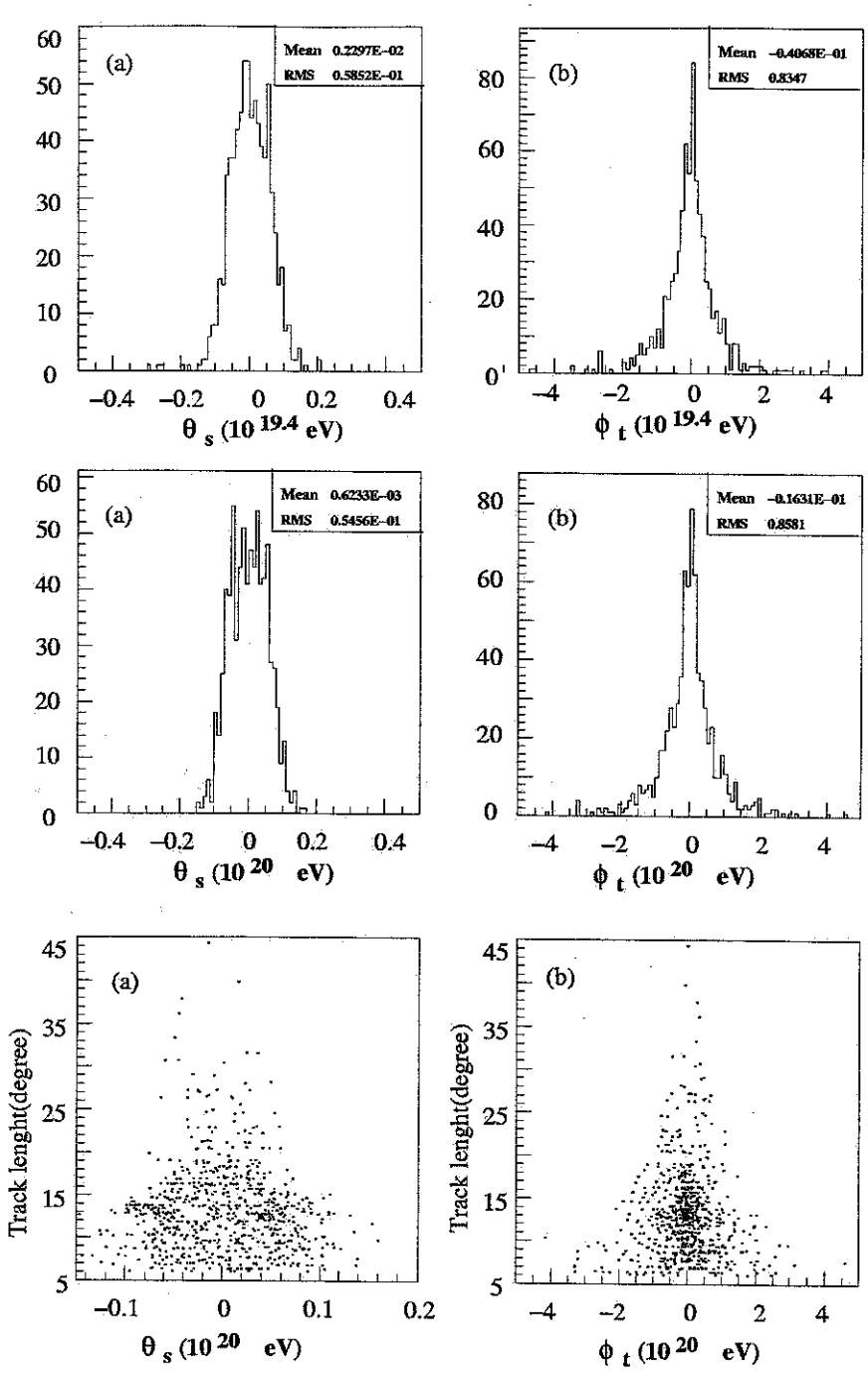

Figure 8.3: *The amplitude weighted plane fitting resolution from* 10^{18} *eV to* 10^{20} *eV. The plane fitting error* θ_s *and* ϕ_t *is defined in figure 8.2(b). The track length dependence of the plane fitting resolution is also shown for* 10^{20} *eV.*

8.2.2 Ray Tracing Plane Fitting

With the reasons given above for the amplitude weighted plane fitting uncertainty, we can try to improve the plane fitting if we understand our challenges. (a) The mirrors are not in the same position, so every mirror has actually different plane. This problem (called parallax) can only be solved if we know the real shower track geometry. But for most of the HiRes-I track, the event is far away and only one mirror is triggered, so if we use the real triggered mirror position as the detector position, this is no longer a problem. (b) The asymmetry of the tube signal on both sides of the SD plane. To correct this effect, I come up a new way to do plane fit.

As point out above, in the real situation there is Poisson fluctuation and sky noise in the measured tube signal, but nobody can clean this out. The real optical system is not as good as idea, the focal spot size changes on the focal plane surface, the tube does not has uniform response surface, and there is gaps between tubes. This problem can be corrected by ray tracing technique as given in Section 5.4.2. Thus the new method is called *ray tracing plane fitting.*

The plane fitting is done by minimizing χ^2 function defined as:

$$\chi^2_{ray} = \sum_i \frac{(Sig_i - Sigmc_i)^2}{Sig_i + S_{skyns}} \tag{8.3}$$

where the sum is over all good tubes, Sig_i is the measured tube signal in photo-electrons by tube i. $Sig_i + S_{skyns}$ is the σ_i^2 of Sig_i due to Poisson fluctuation and Sky noise. $Sigmc_i$ is the calculated tube signal correspond to the given SD plane.

The tube signal Sig_i corresponds to a real shower which has longitudinal profile and laterally spreading out, before we reconstruct out all the shower information,

we can not really calculate the tube signal $Sigmc_i$ correctly. But here we are only focusing on the SD plane, the shower longitudinal profile and lateral spreading out effects can be simplified by the following procedures:

(a) Let the shower track be within the SD plane, laterally assuming gauss function with Sigma depending on the track width. Then ray tracing a set of line sources with longitudinal uniform and laterally gauss spreading-out to the detector to get tubes signals $Sigmc_i'$.

(b) longitudinally fit the signal to a quadratic line within every mirror by minimizing:

$$\chi^2_{mirror} = \sum_i \frac{[Sig_i - (a + bx_i + cx_i^2)Sigmc_i']^2}{Sig_i + S_{skyns}} \tag{8.4}$$

where x_i is the tube view angle. Then the best fitted tube signals is:

$$Sigmc_i = (a + bx_i + cx_i^2)Sigmc_i' \tag{8.5}$$

which is corresponding to the input SD plane after the correction of shower shape.

(c) calculate χ^2_{ray}defined in equation 8.3, change the SD plane direction, go through (a) (b) step by step until getting the minimized χ^2_{ray} point.

In order to use the symmetry information of the shower track, the final plane is getting by minimizing the combined χ^2_{com} defined as:

$$\chi^2_{com} = \chi^2_{amp} + \chi^2_{ray} \tag{8.6}$$

and forcing $\chi^2_{amp}|_{min} = \chi^2_{ray}|_{min}$. with $|_{min}$ means the minimized point.

The resolution of this new plane fitting method is shown in Figures 8.4. By comparing with figures 8.3, we can see it has been improved a lot, especially for higher energy cosmic ray case.

8.3 Global EAS Fitting

HiRes-I monocular detector has only one ring, and dedicated to highest energy cosmic rays. The average track length is just around 12^o, which is to small to reconstruct the shower geometry accurately by monocular time fitting. A new reconstruction method called *global EAS fitting* was invented by the author to handle this situation, and optimized to reconstruct the shower as beast as we can. This method minimizing a combined timing and shower profile fitting χ^2 function.

8.3.1 Stand-along Time Fitting

Time Fitting. After we get the SD plane, the remaining geometric parameters R_p, ψ within SD plane can be found with EAS front arrival times for each tube. Figure 8.1 illustrates the shower track geometry within SD plane. Projecting the tube center direction vector onto the SDP, each tube has a unique viewing angle χ_i. By simply geometry calculation we can get the relation between the time the light hitting the detector $Tcnt_i$ to the tube viewing angle χ_i:

$$Tcnt_i = T_0 + \frac{R_p}{c} tan(\frac{\pi - \psi - \chi_i}{2}) \tag{8.7}$$

where T_0 is the time at which the shower passing the point closest to the detector. ψ is the the incline angle of the track, R_p is the impact parameter, c is the speed

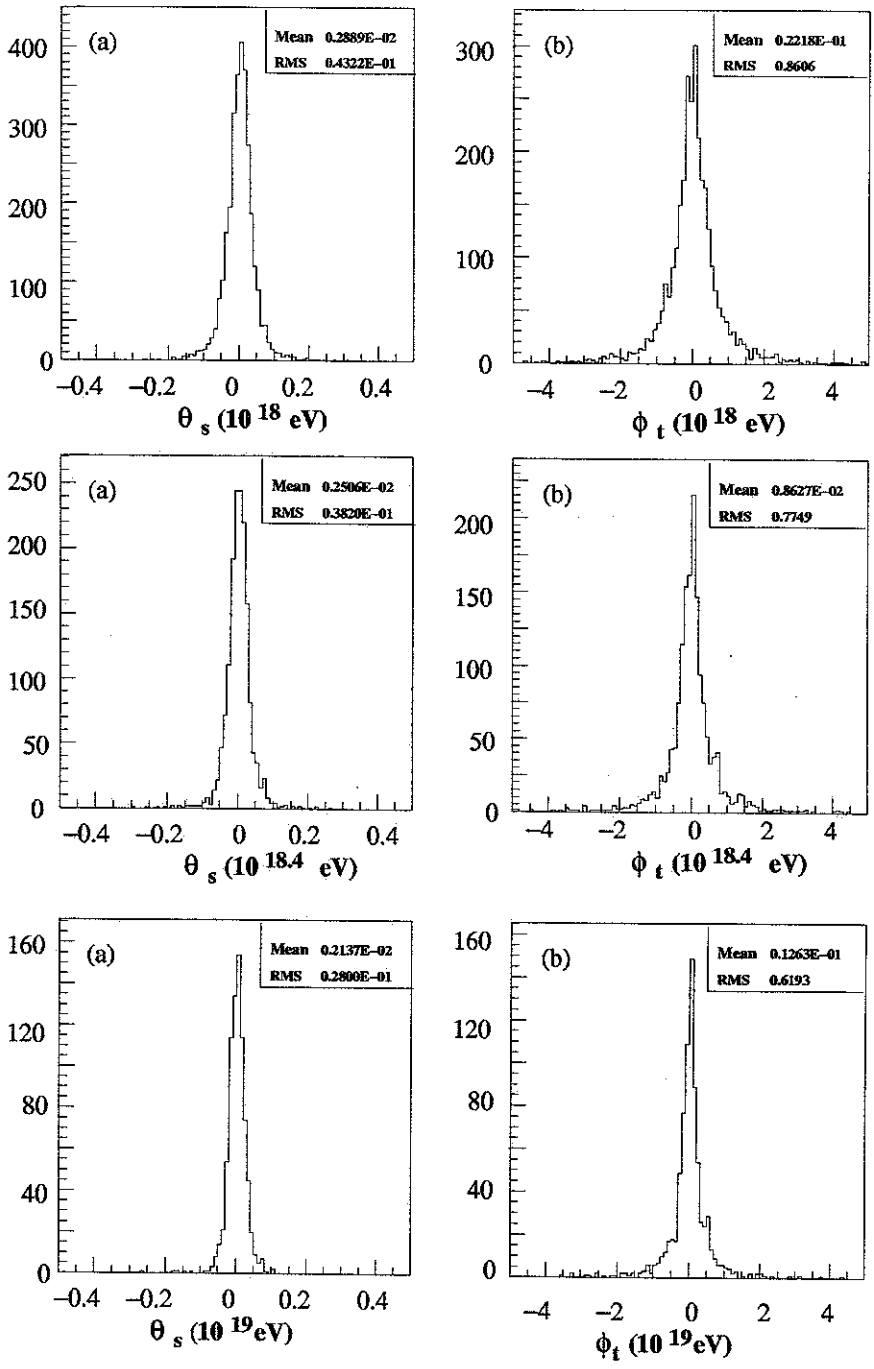
(a)
Mean 0.2889E-02
RMS 0.4322E-01
θ s (10 18 eV)
(b)
Mean 0.2218E-01
RMS 0.8606
ϕ t (10 18 eV)
(a)
Mean 0.2506E-02
RMS 0.3820E-01
θ s (10 18.4 eV)
(b)
Mean 0.8627E-02
RMS 0.7749
ϕ t (10 18.4 eV)
(a)
Mean 0.2137E-02
RMS 0.2800E-01
θ s (10 19eV)
(b)
Mean 0.1263E-01
RMS 0.6193
ϕt (10 19eV)

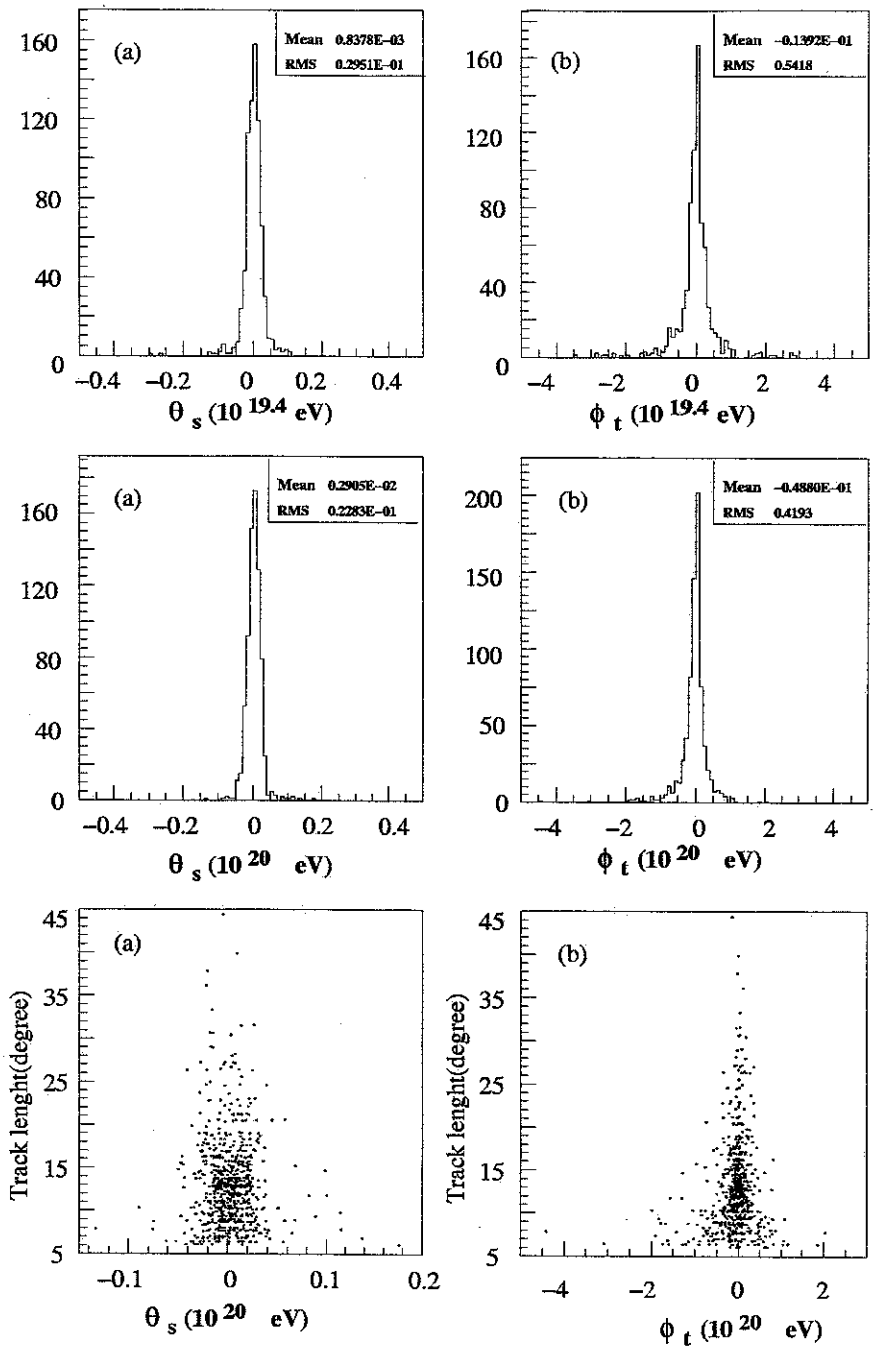

Figure 8.4: *The ray tracing plane fitting resolution from* 10^{18} *eV to* 10^{20} *eV. The plane fitting error* θ_s *and* ϕ_t *is defined in figure 8.2(b). The track length dependence of the plane fitting resolution is also shown for* 10^{20} *eV.*

of light. As shown in Figure 8.1, the tube viewing angle χ_i is related to the light emission angle θ_i by $\theta_i = \pi - \psi - \chi_i$.

If we assume the real tube trigger time T_i corresponds to the time the light hitting the detector in the tube center direction. Then the shower geometry can be obtained by minimizing the χ^2 function of the form:

$$\chi^2_{tim} = \sum_i \frac{(T_i - Tcnt_i)^2}{\sigma(tim)_i^2} = \sum_i \frac{1}{\sigma(tim)_i^2}[T_i - (T_0 + \frac{R_p}{c} tan(\frac{\pi - \psi - \chi_i}{2}))]^2 \qquad (8.8)$$

where $\sigma(tim)_i^2$ is the trigger time error. It is difficult to obtain an accurate estimation of the trigger time error. $\sigma(tim)_i = (500/\sqrt{S_i})ns$ is used with S_i being the tube signal in photoelectrons. This relationship reflects the fact that the trigger time error becomes smaller when the tube signal amplitude is larger. With this error estimation, it is impossible to obtain a normalized $\chi^2 \sim 1$ at minimized point. So we simply scale the errors such that the normalized χ^2 at minimized point as $\chi^2_{min} = 1$.

In equation 8.8, when the track is short, *tan()* function is nearly linear, this reduces equation 8.8 to a linear fit with three unknown parameters. R_p and ψ are highly correlated. Therefore the success of monocular time fitting relies on the curvature of the time fit data, which depends on the track length of the shower. The time-along geometry fitting is success only when shower track length $\geq 20^o$. But most HiRes-I events have track length less than that.

Time Slewing. In principle, the monocular time fitting should success if we know exactly the time the light hitting the detector along the tube center direction. But for a S/H system, the time the actual filtered signal crossing the triggering threshold is not the time the light hitting the detector along tube center direction. This difference is called time slewing.

The time slewing effect is very difficult to be calculated, which depends on how the tube responds to the given signal. Signal strength, signal shape, the light spot crossing the tube, tube response function, tube direction *etc*, all these are related to the real tube trigger time. Even all these are known, photoelectrons fluctuation, the plane fitting uncertainties will limit how well the expected time slewing could be determined.

The author invented a way to partially correct the time slewing effect. The basically idea is to calculate the tube trigger time instead of the time $Tcnt_i$ in equation 8.7, After this correction the calculated trigger time is:

$$Ttrig_i = T_0 + T_{slew}(i) + \frac{R_p}{c} tan(\frac{\pi - \psi - \chi_i}{2}) \tag{8.9}$$

where $T_{slew}(i)$ corresponds to the time slewing of tube i, which is the difference between the tube trigger time to the central crossing time.

And the χ^2 defined as:

$$\chi^2_{tim} = \sum_i \frac{(T_i - Ttrig_i)^2}{\sigma(tim)_i^2} \tag{8.10}$$

To calculate $T_{slew}(i)$, we will use the real tube trigger threshold and the pulse area, but we must also know the time profile of the tube signal. This is impossible for S/H electronic system. From ray tracing results given in Section 4.6.1, we known the tube field view is about 1^o with a spot size about 1^o, so the signal a tube detected can cross $\pm 1^o$ view space, as shown in Figure 8.5, the shape is very close to Gaussian. If we simply assume the real signal time profile is also Gaussian centered at the tube central-crossing-time, with Sigma of $1/3^o$. we can calculate the tube trigger time.

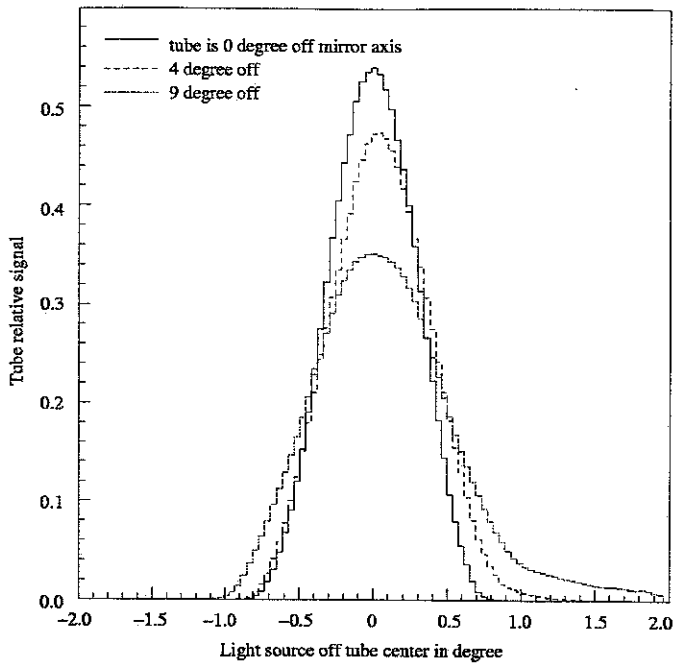

Figure 8.5: *The relative tube signal for different light source off tube central direction. The solid line corresponds to a tube along mirror axis. The dash line corresponds a tube 4° off from mirror axis. The dash dot line corresponds to a tube 9° off from mirror axis. In average a tube can see signal within 1° from tube central direction.*

To check how well this time slewing calculation is, we studied vertical laser shots from HR2SLS system (see section 4.5). We use the above monocular time fitting method to reconstruct the laser geometry, by constraining the core of the laser to the real laser core position. Figure 8.6(a) gives the reconstructed ψ without time slewing correction. Figure 8.6(b) gives the reconstructed ψ after the time slewing correction. Remember the real laser shots are vertical, which means $\psi = 90°$. It is very clear with the time slewing correction the geometry fitting is improved.

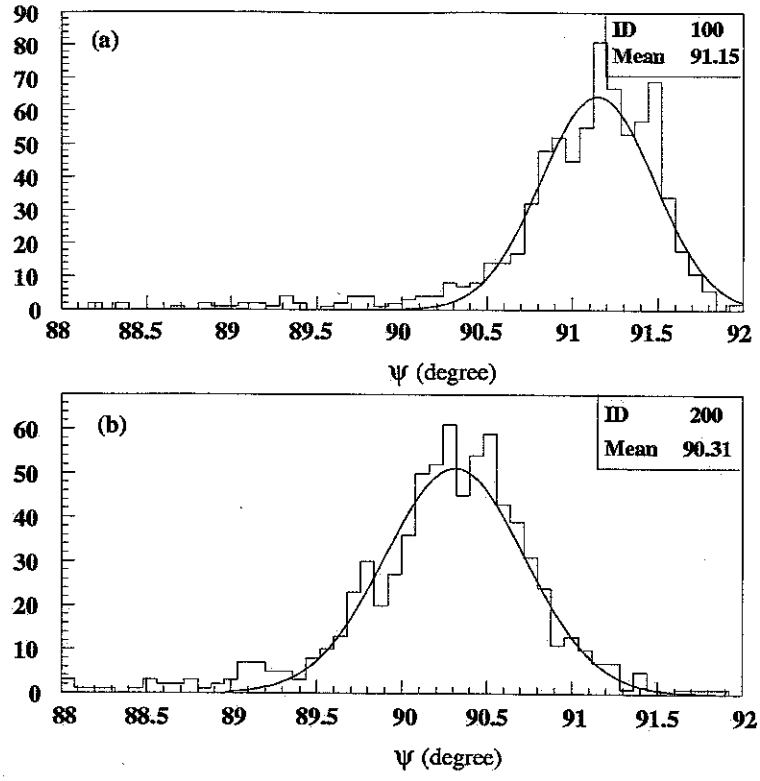

Figure 8.6: *The reconstructed ψ of vertical laser shot (real $\psi = 90^o$) from stand-alone time fitting by constraining the laser core position to real laser core position. (a) without time slewing correction. (b) with time slewing correction.*

8.3.2 Stand-along Shower Profile Fitting

After we get the shower geometry, the Gaisser-Hillas parameterized shower profile (equation 8.1) can be fitted by comparing the observed tube signal to the calculated tube signal based on the trial set of parameters in Gaisser-Hillas function and minimizing χ^2 function defined as:

$$\chi^2_{pfl} = \sum_i \frac{(Sig_i - Sigmc_i)^2}{\sigma(sig)_i^2} \tag{8.11}$$

where the sum is over the good tubes, Sig_i is the measured tube signal in photo-

electrons, $Sigmc_i$ is the calculated tube signal correspond the input shower geometry and profile, $\sigma(sig)_i$ is the error estimation, and defined as:

$$\sigma(sig)_i^2 = \sigma_{sta}^2 + \sigma_{skyns}^2 + \sigma_{mc}^2 \tag{8.12}$$

with $\sigma_{sta} = \sqrt{Sig_i}$ be the Poisson fluctuation, $\sigma_{skyns} = \sqrt{200}$ be the sky noise fluctuation correspond to the HiRes-I detector per tube. σ_{mc} is the tube signal calculation error transfer from the geometry error, including the shower geometry calculation error, the real mirror direction survey error, the real spot size effects etc.

To calculate the tube signal for a given shower geometry and profile, we go through the whole MC procedure as described in the Chapter 5, from light production (section 5.2) to light propagation (section 5.3) and detector optical response (section 5.4). The only difference from detector MC is that we do not put in noise here. For light propagation, the real atmosphere condition from the laser calibration (Chapter 7) is put in when the real data is analyzed.

To save CPU time, we modified from detector MC in two ways: first, the shower has been longitudinally cut into segments with 0.1 degree instead of 0.04 degree as in MC. Within a segment, the shower lateral distribution is still characterized by NKG function, but in the final ray tracing, we only ray trace the lateral distribution of the shower in one dimension perpendicular to the SD plane, the other dimension within the SDP has been integrated out.

8.3.3 Global EAS Fitting

The global EAS fitting method is going to fit both the shower geometry and shower profile together by minimizing the combined χ^2 defined as:

$$\chi^2_{comb} = \chi^2_{tim} + \chi^2_{pfl} \tag{8.13}$$

with χ^2_{tim} define in equation 8.10 and χ^2_{prfl} define in equation 8.11. As described in section 8.1, 8 parameters are needed to determine an EAS. It is almost impossible to search the whole space with 8 dimensions to get the best fitting result. The fitting space can be compressed by the following ideas:

(a) Within the SD plane, in equations 8.9, 8.10, χ^2_{tim} linearly depends on R_p. So by minimizing χ^2_{tim}, we can analytically get R_p for given ψ angle.

(b) In the shower profile fitting in equation 8.11, $Sigmc_i$ is proportional to shower maximum N_{max} in equation 8.1, and χ^2_{pfl} is again linear to N_{max}. So N_{max} is uniquely determined for any trial shower when all the other parameters have been specified by minimizing χ^2_{pfl}. But mathematically this method biases the N_{max} a little lower than the real number.

Another way to determine N_{max} is by constraining:

$$\sum_i Sig_i = \sum_i Sigmc_i$$

In this way, the N_{max} is going to be over estimated if the geometry of the shower is not correct, especially there is plane fitting error.

In the real fitting, the above two ways to determine N_{max} have been used, and the final N_{max} has been chosen as the average.

The left six parameter space is still too big, so the fitting is farther cut into two steps:

(1) **Starting point search.** In this step we first search over ψ restricted within the SD plane (calculated in section 8.2) in the range $(0^o, 180^o)$ as input, R_p is de-

termined from above idea (a). By fixing $X_0 = -80$ (gm/cm^2) and $\lambda = 65(gm/cm^2)$ (those are the average values for the EAS from CORSIKA simulation for shower from $10^{18}eV$ to $10^{20}eV$ as shown in section 3.4) searching X_{max} from 550 gm/cm^2 to 1100 gm/cm^2 to get the best fitting point. Considering this best fitting point is very sensitive to the input SD plane, and this plane has a plane fitting error as shown in figure 8.4, we also search the best fitting point correspond to $\pm\sigma$ of the best fitted plane in section 8.2. Within the three plane fitting points, we chose the one with smallest χ^2_{comb} as the starting point for the following search in step (2).

As point out in section 8.3.1, the trigger time error is very difficult to estimate, in order to put same weight in the combined χ^2_{comb} defined in equation 8.13, we scale the trigger time error $\sigma(tim)_i$ in equation 8.10 by forcing:

$$\chi^2_{pfl}\,|_{min} = \chi^2_{tim}\,|_{min} \tag{8.14}$$

at the starting point.

(2) **Best point search.** From the starting point, a refined search is performed by the *amoeba* minimization routine. The routine searches all the 6 dimensional space centered at the starting point to get the minimized χ^2 point. These six parameters include: ψ the incline angle, α, β two parameters to defined the SD plane, X_0, X_{max}, and λ to determine the shower profile.

After we get best fitted EAS shower, the shower primary energy can be determined by using equations 3.12, 3.13, which has been parameterized for CORSIKA generated showers as discussed in section 3.4.

In Chapter 6, we known the multiply scattering of light from shower to detector will enhance the measured tube signal. To correct this effect, in principle we should

calculate the multiply scattering light for every trial shower in above. But this will spend a lot of CPU time. The multiply scattering effect is important only for the shower energy estimation within about 10%, if we ignore the effects on the shower geometry fitting and shower profile fitting, then we will only calculate the multiply scattering effect for the best fitting shower got in step (2), and calculate the shower primary energy after this correction.

8.4 Global Fitting Resolution

To study how well the global fitting method works, we will study both Mont Carlo showers and real stereo HiRes showers.

8.4.1 Quality Cut

A set of quality cuts was identified through the examination of the reconstruction results for MC events. These cuts are applied to both the MC events and the real events. events are rejected if they satisfy any of the following conditions:

- 1. Track length is less than 8 degree.
- 2. Total Cherenkov light greater than 80%.
- 3. The best combined χ^2 is greater than 5 per degree of freedom.
- 4. The best residual for bin signal is greater than 5 per degree of freedom.
- 5. The measurable shower energy is less than 10% of the primary energy.
- 6. The error of lambda is bigger than 150 gm/cm^2.

- 7. The X_{max} is within [Dep0-150gm/cm^2, Dep1+150gm/cm^2], Dep0 is the slant depth of the first bin, Dep1 is the slant depth of the last bin.

8.4.2 MC Resolution

Extensive Mont Carlo showers were generated and reconstructed to study the resolution and systematics of Global Fitting Method. The showers were generated by using the Detector Mont Carlo method described in Chapter 5. The showers were pass through all stages of reconstruction procedures will be described in 9.1 start from PASS2. The reconstructed data passing the quality cut in section 8.4.1 were then used in the following resolution study. All these reconstruction procedures and quality cuts are the same as to the real data.

Two types of events were considered: one is mono-energy proton or iron showers, the other is energy continual proton/iron shower generated with spectrum of E^{-3}. The resolution for various of shower parameters are shown in figure 8.7 through figure 8.12.

It can be seen that resolution for R_p, ψ , and energy improves as the energy goes from 1EeV to 100 EeV, and is acceptable for showers above 1EeV. This improvement is mainly due to that higher energy events are observed at greater distances and so large fraction of the shower development is seen. As we are using the shower profile fitting, this is critical for the success of the fitting. Another advantage of the high energy shower is that the signal to noise ratio is higher, this also improves the resolution.

8.4.3 Geometry Resolution of Real Data

In order to see how well the Global Fitting Method can handle the real HiRes data, we also processed the HiRes prototype stereo data with the Global Fitting Method.

The HiRes prototype stereo data has been discussed in detail by Wilkinson in reference [60]. Comparing to Monocular data, the stereo data has much better geometry reconstruction resolution. If we assume the reconstructed EAS geometry by stereo method gives the correct shower geometry, then monocular reconstruction geometry resolution can be defined as the difference between monocular reconstruction geometry to stereo reconstructed geometry divided by stereo geometry.

In order to simulate the HiRes-I Monocular, which has only one ring mirrors, I only used one mirror information of Prototype HiRes-II of a prototype stereo event, and reconstructed the geometry of that shower by Monocular Global fitting Method. The stereo geometry of the shower is reconstructed by stereo-time fitting method[60]. After the reconstruction, the data set pass through the same quality cut given in section 8.4.1.

The geometry resolution of this real data set is shown in figure 8.13. Figure 8.13(a) shows the resolution of R_p, figure 8.13(b) shows the resolution of ψ. The reconstructed EAS primary energy of this data set has average of 1EeV. Compare to the geometry resolution shows in figures 8.7 and 8.8 for 1Eev showers, we can see the resolution of the real data is almost same as the Mont Carlo resolution. This also means the Monocular Global Fitting Method can handle the real HiRes data well.

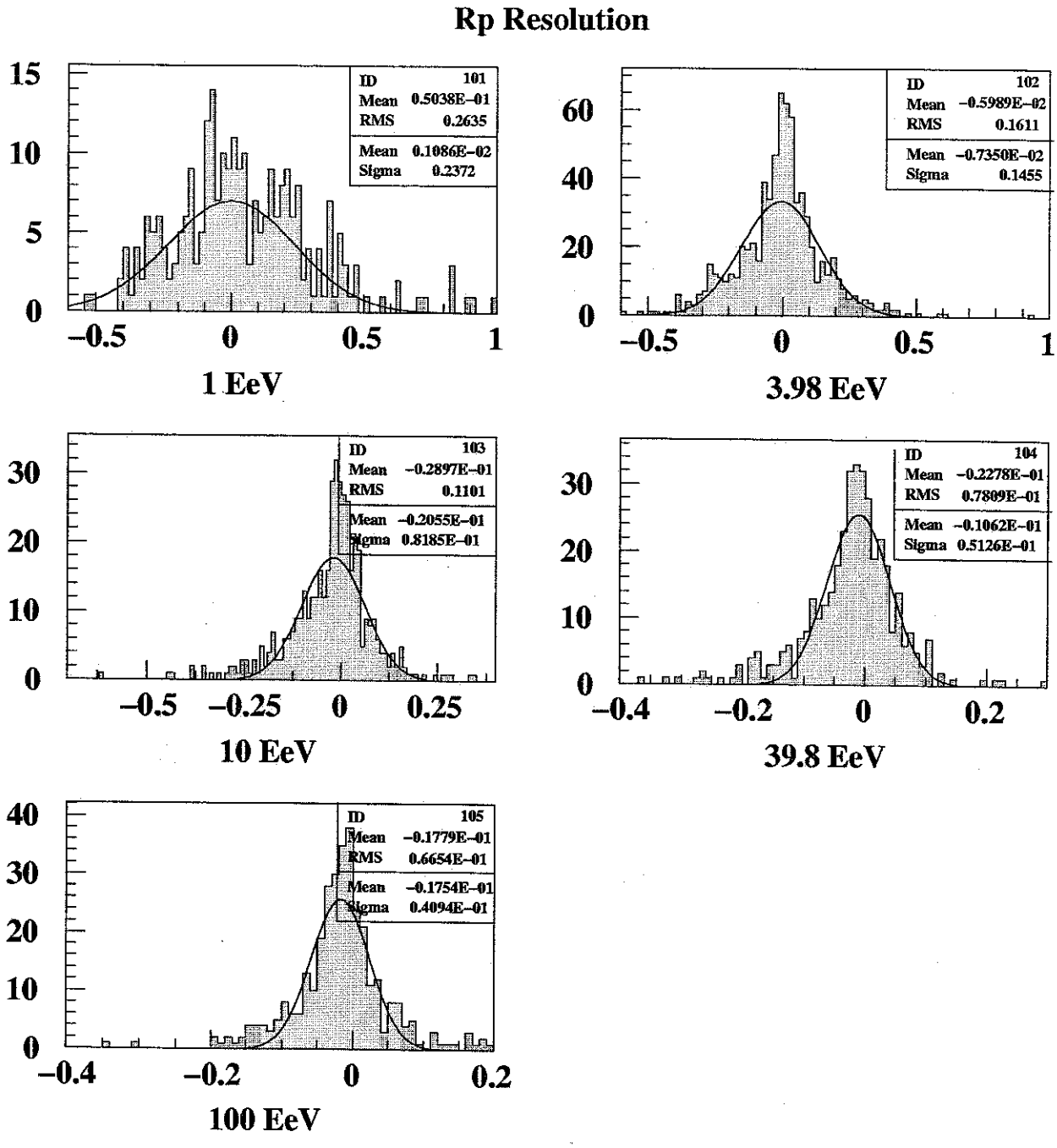

Figure 8.7: *R_p resolution of proton shower $(R_{p_{out}} - R_{p_{in}})/R_{p_{in}}$. $R_{p_{out}}$ is the reconstructed value, $R_{p_{in}}$ is the real value in MC generation. Different figures correspond to different proton energy.*

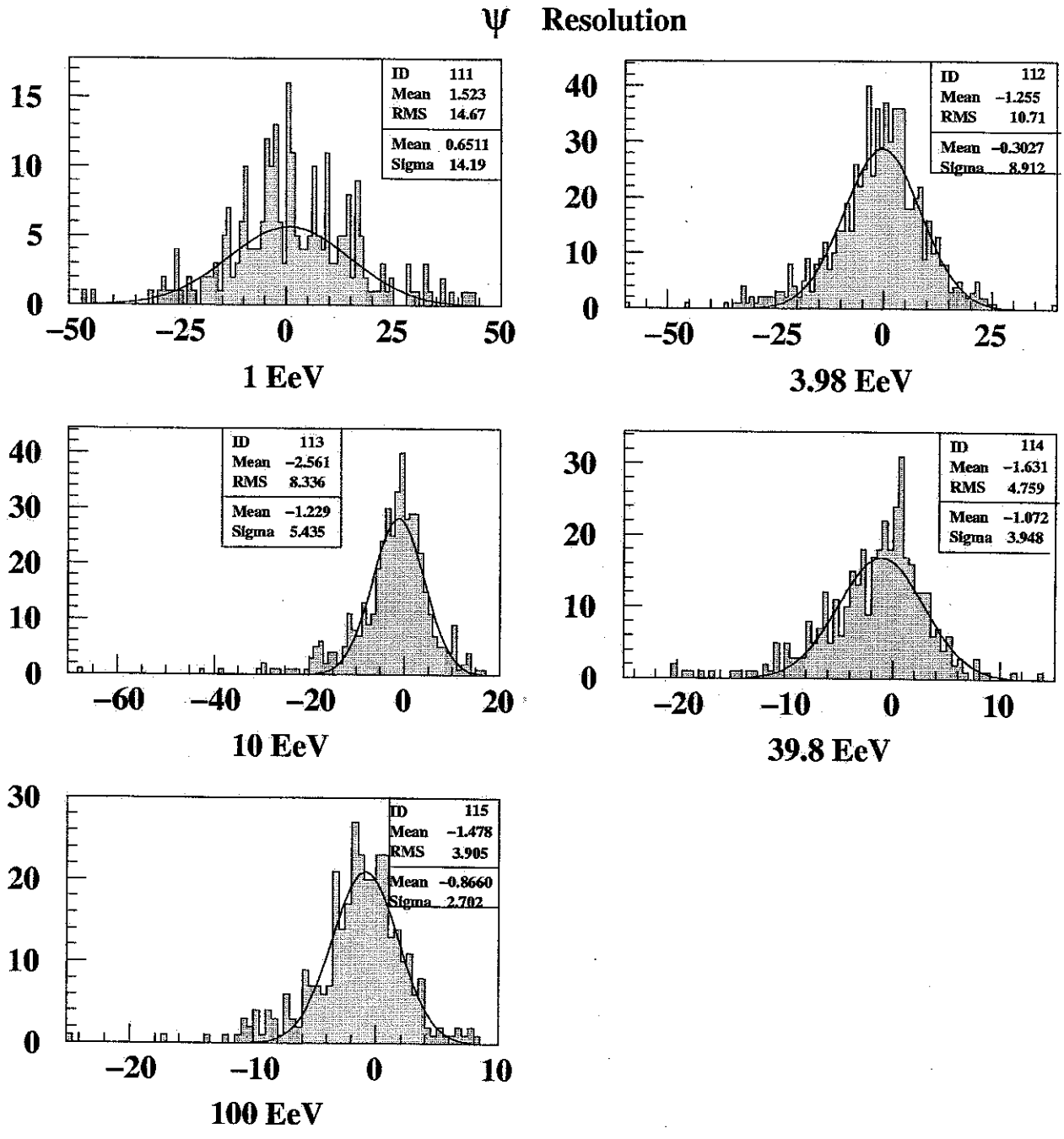

Figure 8.8: *ψ resolution of proton shower: $(\psi_{out} - \psi_{in})$ in degree. ψ_{out} is the reconstructed value, ψ_{in} is the real value in MC generation. Different figures correspond to different proton energy.*

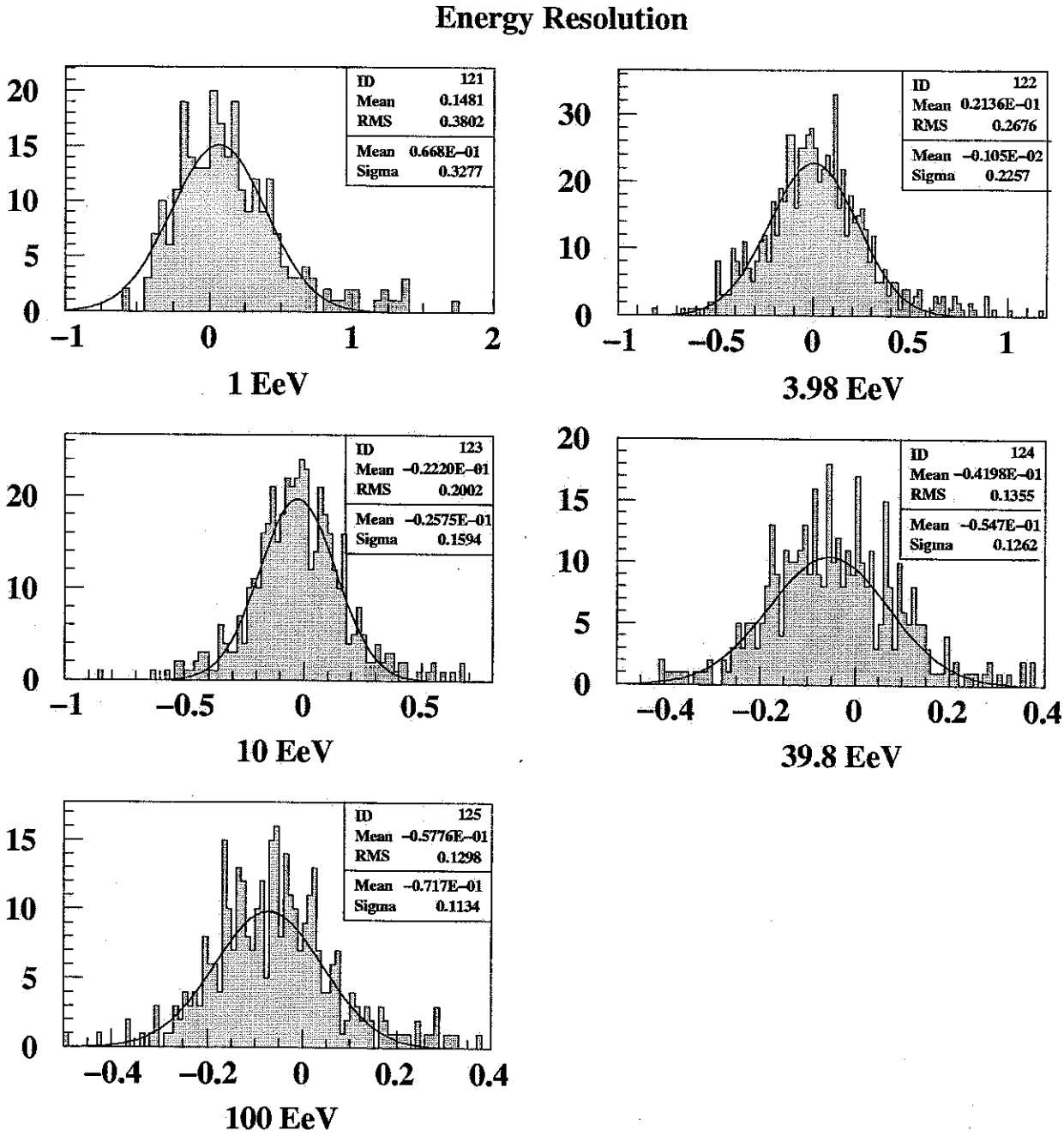

Figure 8.9: *Energy resolution of proton shower:* $(E_{out} - E_{in})/E_{in}$. E_{out} *is the reconstructed value,* E_{in} *is the real value in MC generation. Different figures correspond to different proton energy.*

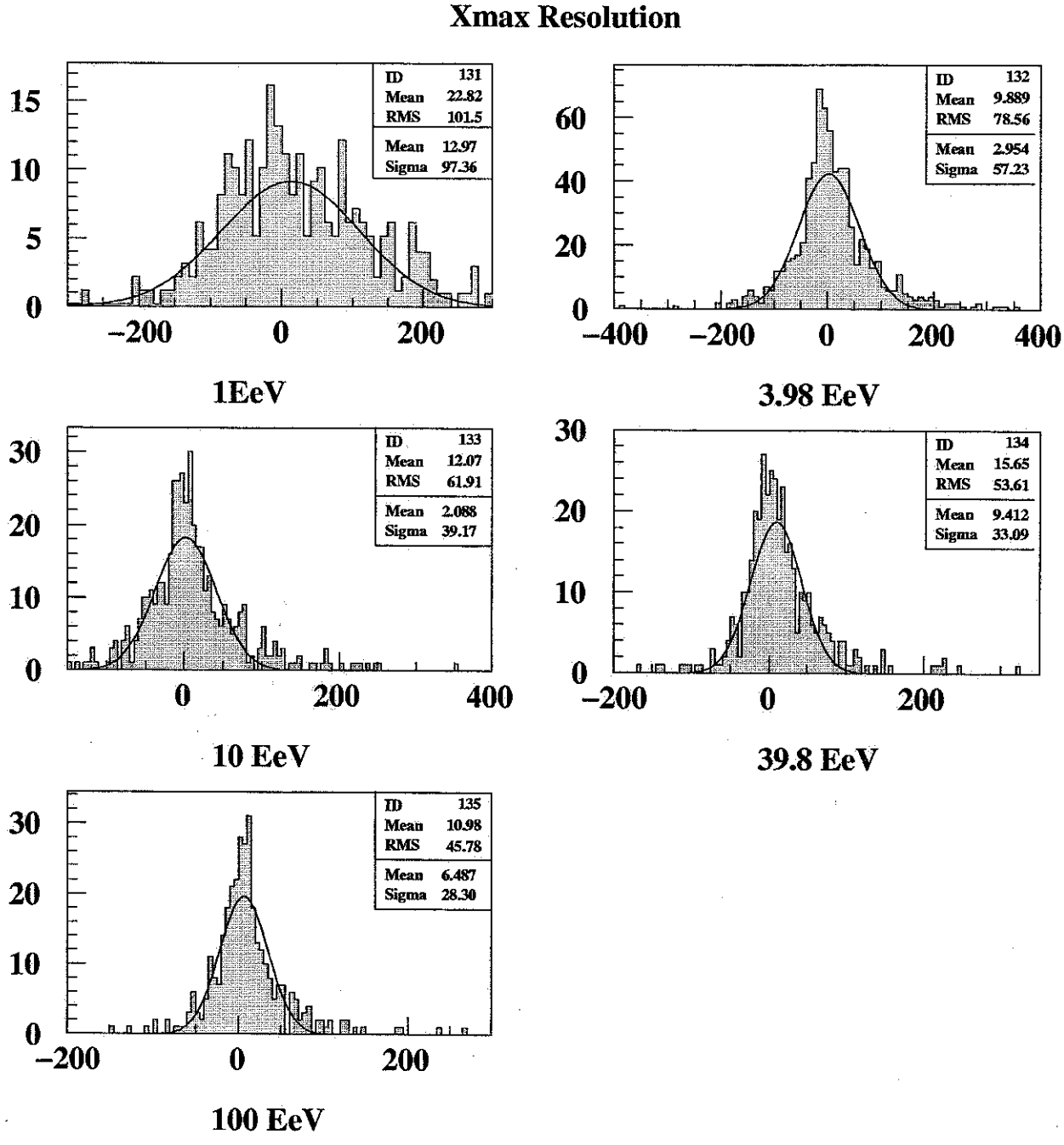

Figure 8.10: *X_{max} resolution of proton shower: $(X_{max_{out}} - E_{max_{in}})$. $X_{max_{out}}$ is the reconstructed value, $X_{max_{in}}$ is the real value in MC generation. Different figures correspond to different proton energy.*

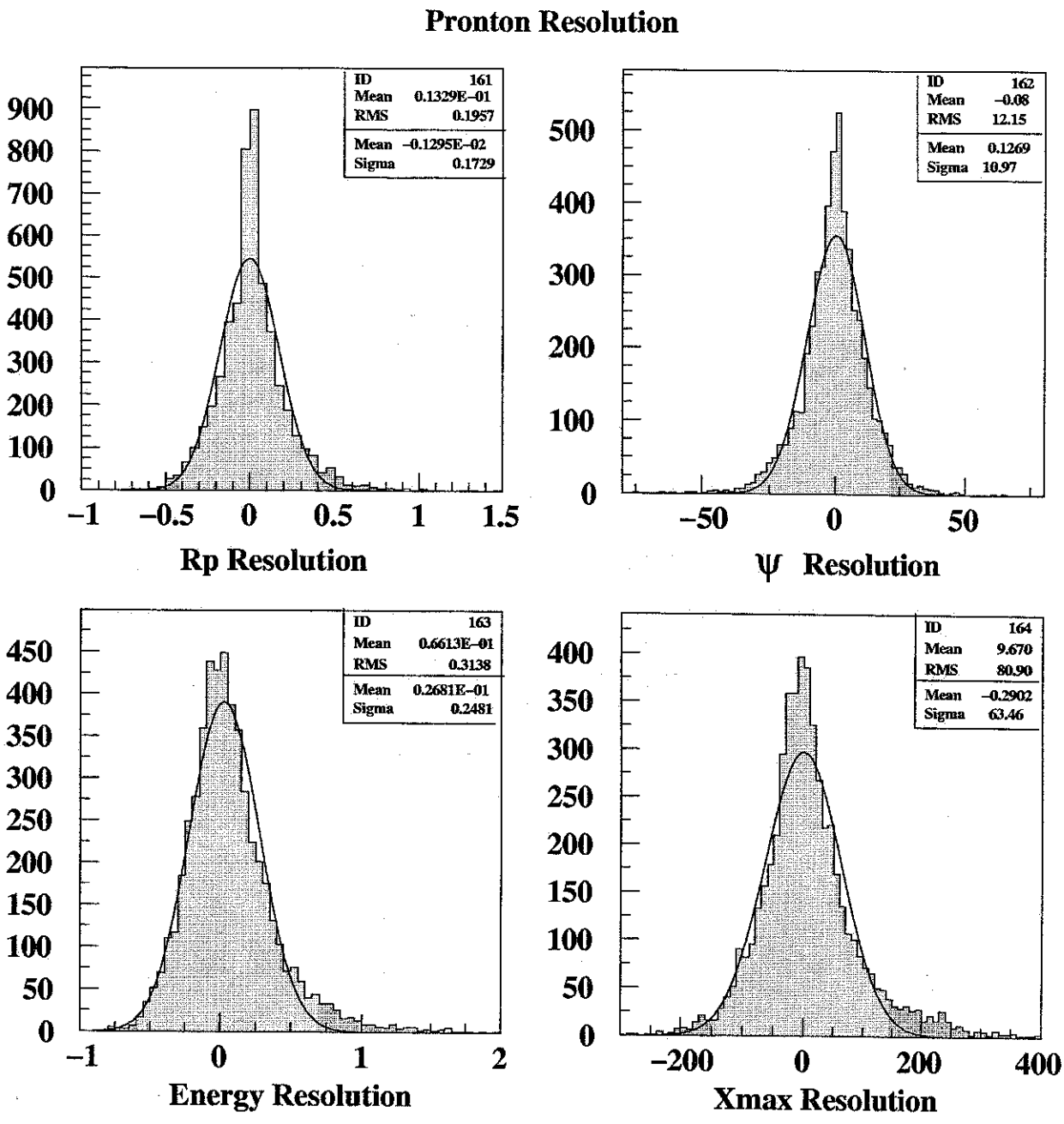

Figure 8.11: *Resolution of proton shower generated with E^{-3} spectrum. The resolution is defined same as in figure 8.7, 8.8, 8.9, 8.10.*

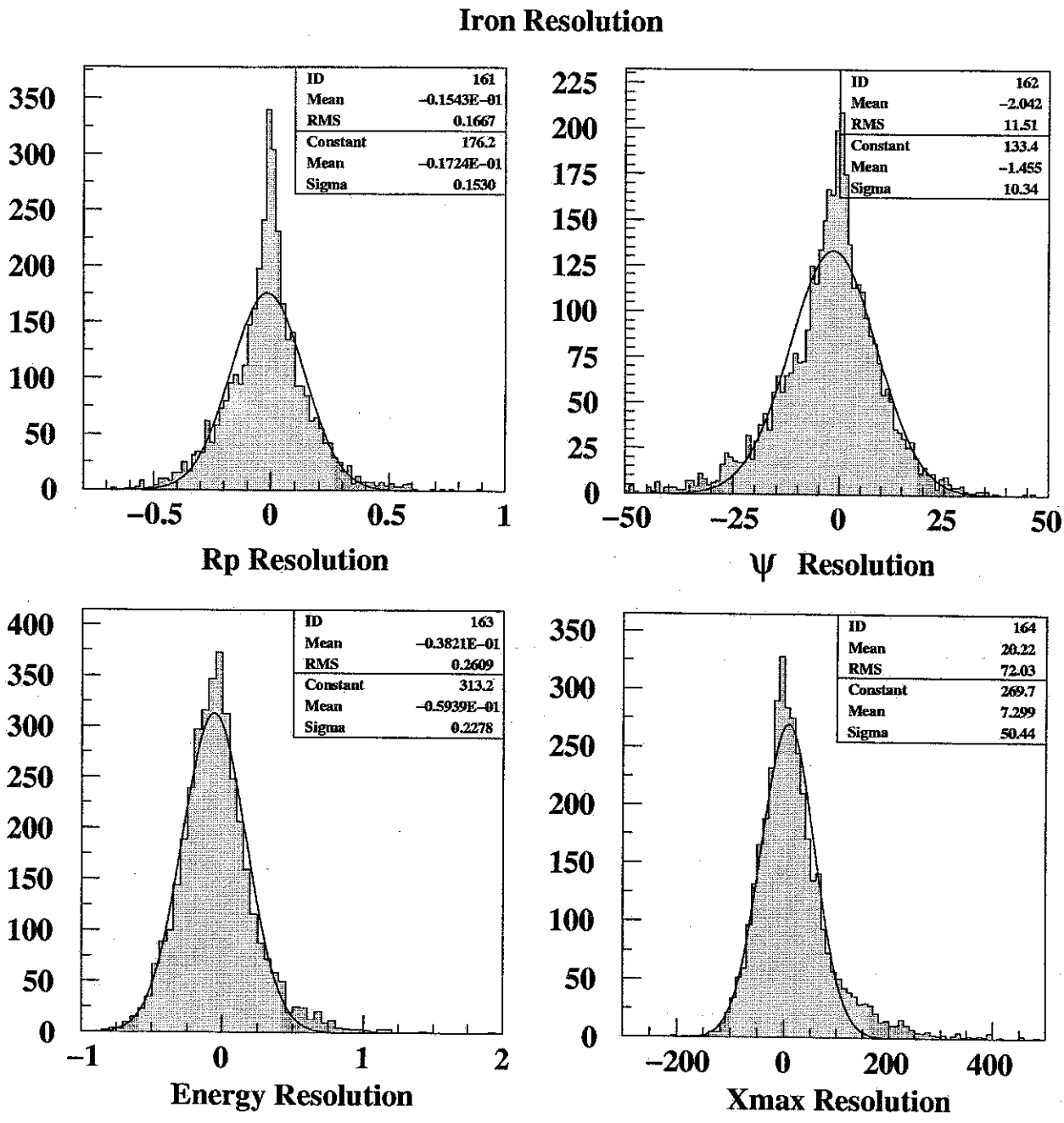

Figure 8.12: *Resolution of proton shower generated with E^{-3} spectrum. The resolution is defined same as in figure 8.7, 8.8, 8.9, 8.10.*

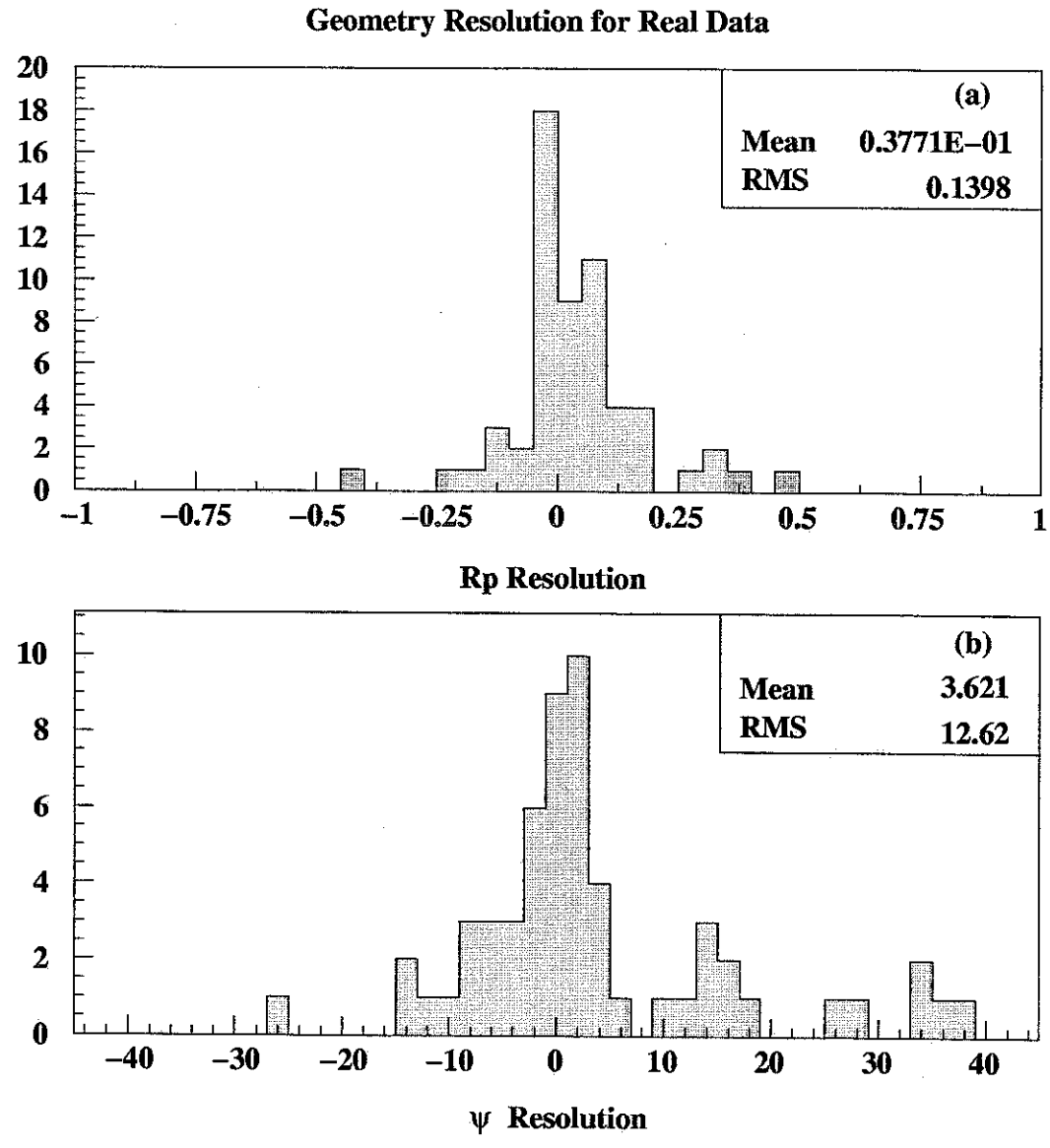

Figure 8.13: *The geometry resolution of the Monocular Global Fitting Method with prototype stereo data. (a) is R_p resolution, (b) is ψ resolution. The resolution is defined as the difference between the monocular geometry to stereo geometry and divided by stereo geometry by assume the stereo geometry as the real geometry.*

Chapter 9

Data Analysis & Comparison between MC and Real Data

HiRes-I detector was running from June 1997 to May 2000 at moon-less nights, the trigger rate is set at 200HZ, which corresponds to 5σ of the sky noise background. The atmosphere monitoring laser shots and vertical flashers are also running every night. So we have a very big dataset. In this dataset, we are interested in two sets of information, one is cosmic ray events, the other is steerable laser shots.

The data analysis of this dataset includes two basic steps. The first is to process the basic events and to extract cosmic ray candidates and the second is to reconstruction EAS as described in Chapter 8. In this chapter, I will also give the comparison between real dataset to MC dataset.

Similar to cosmic ray event analysis, we also analyze steerable laser shots to retrieval atmosphere condition night by night. To do so, we need to extract out the steerable laser shots, match the events recorded by HiRes-I to the information

recorded by HR2SLS, and then analyze the nightly laser shots to get the aerosol condition of the atmosphere as described in Chapter 7. In this Chapter, I will give the results of the aerosol condition extracted by the steerable laser shots for all the months when the laser shots are available.

9.1 Cosmic Ray Events Building and Extracting

9.1.1 Event Building (PASS0)

The raw data packets from triggered mirrors and the central timing crate are send to the central computer. Mirror event packets are matched with the central timing packets to get the absolute time of the mirror trigger. Then the individual mirror event packets are grouped into one event if the trigger time matches. This process is called *time matching.*

Along with the time matching of events, various reference and monitoring packets are also tracked and stored together with the event. This include the Minute packets containing mirror specifying tube thresholds, count-rates, trigger rates etc. Volts packets containing the read back HV for every tube are also included. Some other information such as GPS clock status, the network status, commands entered by operator and weather code are also stored in the events.

9.1.2 Calibration (PASS1)

After the event building-up, raw data containing QDC and TDC values are calibrated and converted into the number of photo-electrons and correct trigger time in each channel. The detail of the calibration is described in section 4.6.

9.1.3 Track Filtering (PASS2)

After the calibration, the events are scanned to filter track like events by using spatial and temporal information. The filter is called *Rayleigh filter*, which gets rid of the random trigger events. The idea is that noise triggered events are random in time and in space. By comparing the track length with that expected from a random walk for the same number of tubes, we can get ride of the random triggered events.

In practice, all pairs of adjacent triggered tubes are connected by vector in time order, the Rayleigh vector is the sum of all the individual vectors. A noise triggered event should be uncorrelated, the Rayleigh vector length r of a random walk follows Rayleigh probability distribution:

$$p(r) = \frac{r}{\sigma^2} exp(-\frac{r^2}{2\sigma^2}) \tag{9.1}$$

with $\sigma^2 = N/2$, N is the number of vectors. Average length of the Rayleigh vector of random walk has the length $r \sim \sqrt{N}$. For a genuine track the individual vector should point more long the track, such that $r \sim N$. In the real dataset, we used 1% Rayleigh probability cut to cut away the noise events.

After the Rayleigh filter cut, majority of the events are up-going flashers or lasers, so the events are further separated into three subsets: downward-going, horizontal, and upward-going according to the Rayleigh vector direction. Only downward going dataset pass through EAS reconstruction in the following. We will lose few percent of real cosmic ray sitting in the horizontal dataset, but in the aperture calculation, the same loss will be included in.

9.2 EAS Reconstruction

EAS reconstruction is applied to the candidate cosmic ray events. Even after the Rayleigh filter, there are still noise trigger events, Cherenkov blast events, or airplane flasher etc in the dataset. Along with the reconstruction, events are also filtered out in this step based on quality cuts.

9.2.1 Amplitude Weighted Plane Fitting (PASS3)

The First step in the EAS reconstruction is the shower-Detector(SD) Plane fitting. Here we only use the amplitude weighted plane fitting to find the SD plane by noting that the triggered tubes pointing directions lie approximately in the SD plane. The method is described in section 8.2.1.

The noise triggered tubes are also rejected in this fitting based on assumption that the noise tube should not correlated spatially or temporally to the real track. So bad tubes are rejected either if it is too far away from the fitted SD plane spatially, or by quadratic fitting the tube trigger times vs. tube direction χ_i, which is the angle the tube's direction projected in the SD plane, the bad tubes are far from this fitted lines temporally.

After the plane fitting, some basic cut are applied to the dataset in order to get good reconstruction in the following:

plane fit failure: if the good tube number in a track is less than 3, then plane fit fails and this event is rejected.

track-length cut: A minimum track-length of 6^o is required for a good event.

brightness cut: the fluctuation of sky-noise for a tube is about 14 photo-electrons, in order to get good signal to noise racial, the average number of photo-electrons seen by good tubes in a event is required at least 55. This cut also cut away the very nearby low energy showers which are very difficult to reconstruct.

track width cut: broad tracks are rejected as noise, Cherenkov blasts or nearby events. A RMS of 1^o is the maximum value.

angular speed cut. Cosmic ray has high flux at low energy, these low energy cosmic rays are very nearby. Near-by track cross the mirror fast than distant tracks. a maximum angular speed of $3.33^o/\mu s$ corresponding to a track 5 km away perpendicular to the mirror axis is allowed.

weather condition cut: about half of the running time is cloudy, which will makes the data difficult to understand, and also for the aperture calculation. To avoid this problem, only good weather dataset, which means very little cloud or no cloud dataset based on the operator's investigation are used.

9.2.2 Ray Tracing Plane Fitting (PASS4)

In order to improve the SD plane fitting, the events survive PASS3 pass through the ray tracing plane fitting. This method is trying to use the real optical response of the HiRes detector to predicted the triggered tube signal corresponding to the SD plane. The detail is described in section 8.2.2.

Pass Step	Function	Program
PASS0	Event Build	hma
PASS1	Calibration	hpass1
PASS2	Rayleigh Filtering	hpass2
PASS3	Plane fitting/Event Selection	hpln/ps3a_to_ps3b
PASS4	Ray Tracing Plane Fitting	hplntim
PASS5	Global EAS Reconstruction/Event Selection	glbft/cut1

Table 9.1: *HiRes-I monocular data analysis stages and corresponding functions. The program used is also shown.*

9.2.3 Global EAS reconstruction (PASS5)

HiRes-I detector has only one ring setup, by using time information only, the shower geometry can not be reconstructed successfully because the track length is too small. The global EAS reconstruction is trying to reconstruct the EAS geometry and profile information in one step. The detail of this method is described in section 8.3. And the resolution is given in section 8.4.

After the global EAS reconstruction, a quality cut is applied to all the successfully reconstructed events as described in section 8.4.1. Only the events pass through the quality cut is used in the MC comparison and physics study.

In summarize, the Data analysis procedure for HiRes-I monocular detector is shown in Table . In this table, the function of each step and the program used is also given.

9.3 Pull Quantity Study

The global EAS reconstruction by using minimizing χ^2 method to find the best fitting point is described in section 8.3. The success of this method strongly depends on the correct evaluation of error, in our case it is tube signal and trig time error. In order to see how well the errors are evaluated, we will study the Pull quantity and normalized χ^2 distribution for the real data.

The pull quantity is defined as:

$$P_X = \frac{X_{measure} - X_{fit}}{\sigma_X} \tag{9.2}$$

where $X_{measure}$ is the real measurement, X_{fit} is the best fitting result, σ_X is the error of measurement X.

In the global EAS fitting method, there are two measurements, one is the tube puls area, the other is the tube trig time. The pull quantity is shown in figure 9.1.

In this figure I also shows the normalized χ^2 distribution. From this figure we case see the pull quantities fit very well to standard distribution. The normalized χ^2 distribution is also peaked around 1.0. These results means that we have correctly evaluated errors in tube pulse area and trigger time. Then the minimizing χ^2 method is success.

9.4 Real Data and MC Comparison

As described in other chapters, Mont Carlo is very important in the HiRes data analysis, not only in the aperture calculation, but also in the resolution study. So

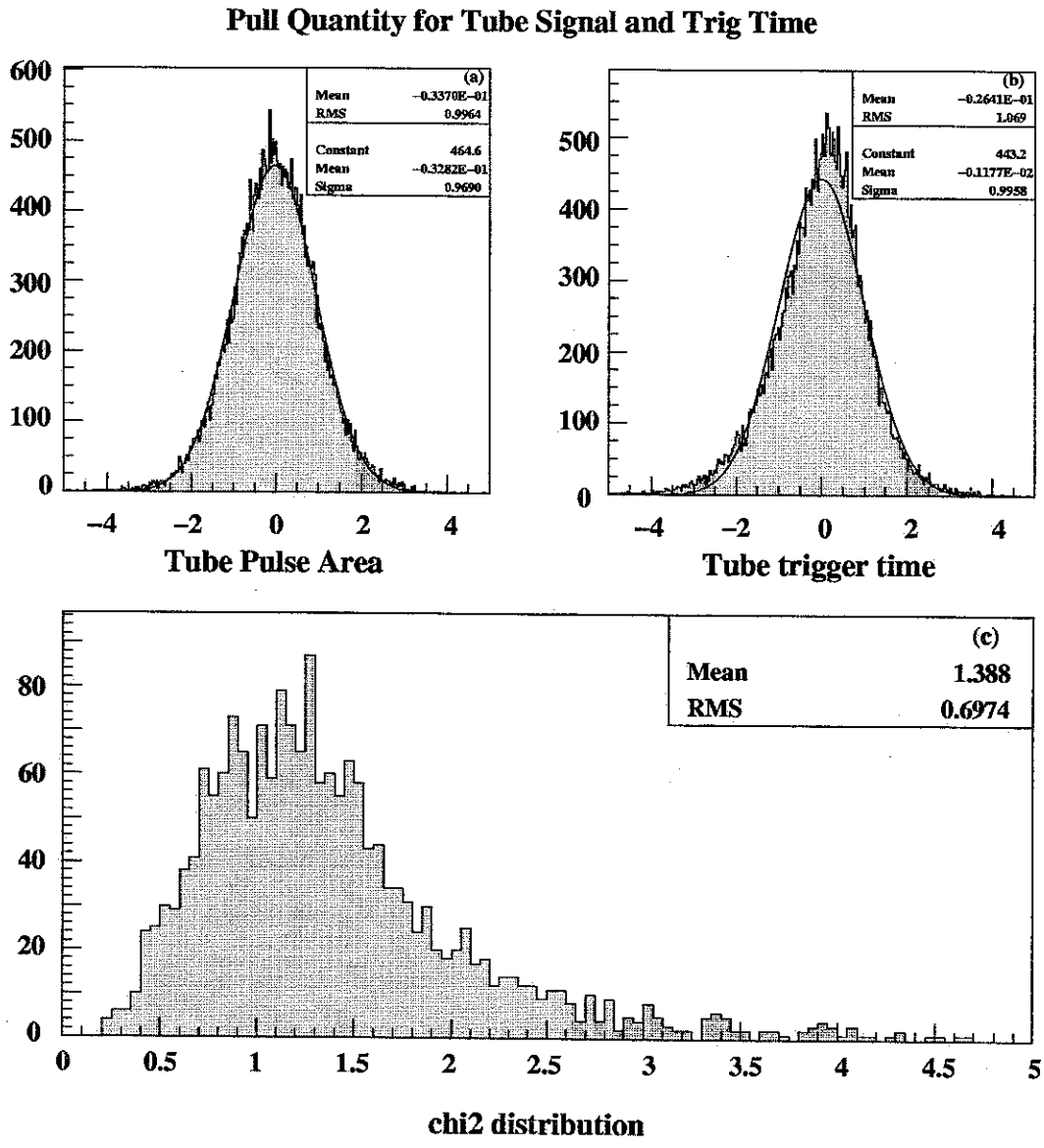

Figure 9.1: *The pull quantities and normalized χ^2 distribution for real dataset. (a) is the pull quantity distribution for tube signal; (b) is for tube trigger time; (c) is normalized χ^2 distribution.*

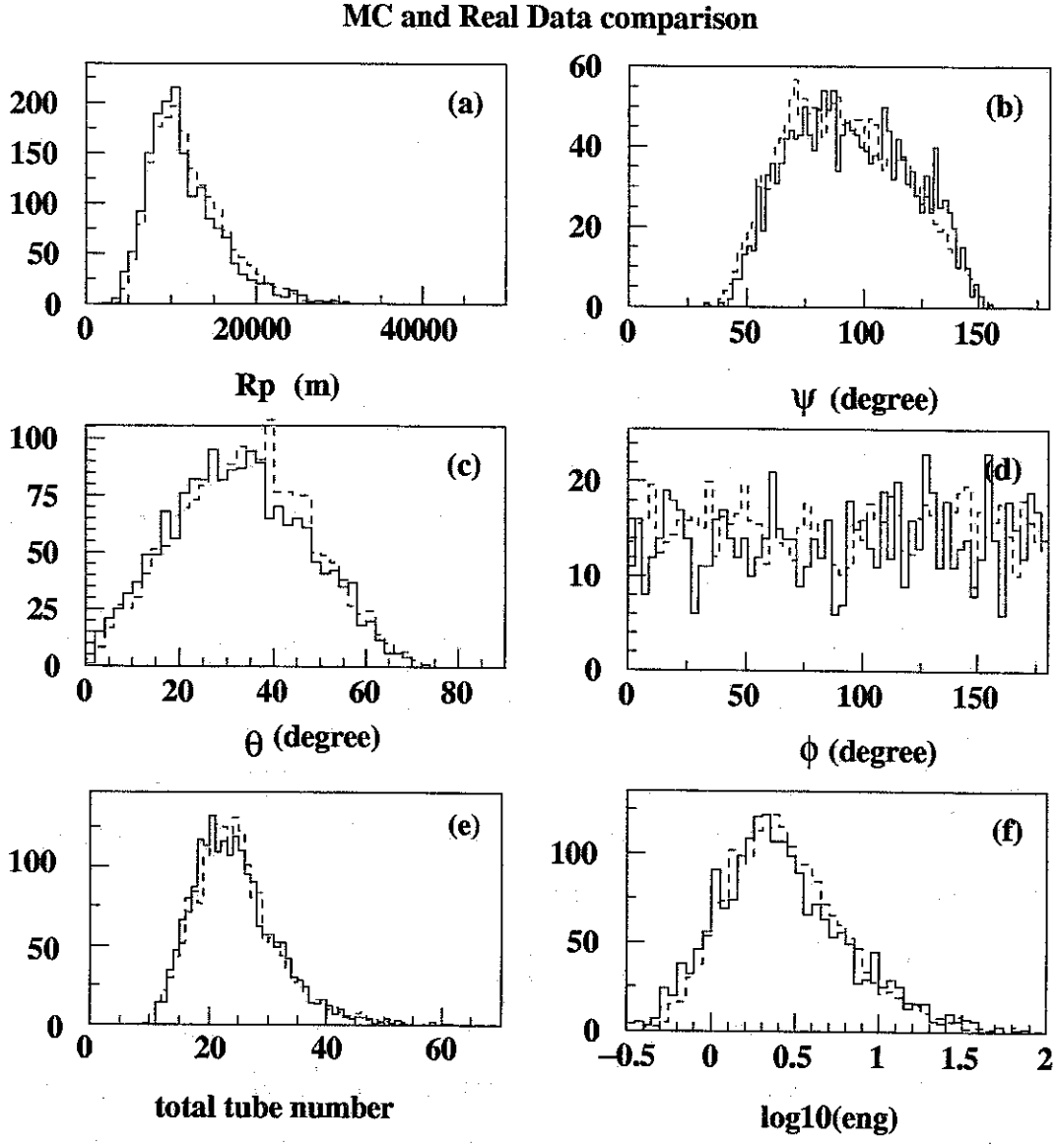

Figure 9.2: *MC and real HiRes data comparison.(a) is R_p distribution; (b) is ψ distribution; (c) is zenith angleθ distribution; (d) is azimuth angle ϕ distribution; (e) is the distribution of good PMT number of every HiRes track; (f) is the distribution of shower energy in log10(eng). Solid line is the real data, dot line is MC data.*

the data analysis of real HiRes events depends on how well we really understand the detector, which in turn in described in the Detector Mont Carlo and atmosphere modeling. In order to see how well we understand HiRes detector as described in chapter 5, and the atmosphere in chapter 7, we will do Mont Carlo and real data comparison in this section.

Based on the previously available results, the cosmic ray spectrum above 1 EeV varies approximately to E^{-3} (see figure 2.2 and 2.3).Based on the composition study of Fly's Eye experiment and HiRes prototype experiment (section 2.2), the composition of Cosmic Rays above 10EeV is almost pure proton, in between 1 EeV to 10 EeV, there is some mixing, but still most of the composition is proton. So the MC data we will study here were only proton shower generated based on a E^{-3} spectrum, which we assume is very close to the real cosmic ray. The atmosphere model we used here is the average atmosphere result we got from chapter 7.

The MC data were pass through all the data analysis procedures as the real data starting from PASS2. After the quality cut in section 8.4.1, we then compare all kinds of distribution between MC data and real data. The results are shown in figure 9.2.

Figure 9.2(a) is R_p distribution; (b) is ψ distribution; (c) is zenith angle θ distribution; (d) is azimuth angle ϕ distribution; (e) is the distribution of good PMT number of every HiRes track; (f) is the distribution of shower energy in log10(eng). Solid line is the real data, dot line is MC data. The MC data is normalized to have the same number of total events as the real data. From these figures, we can see that the Mont Carlo data matches very well with real data in all these distributions from shower geometry distribution, track shape seen in HiRes detector to the total energy distribution.

These results are very important for the confidence of the data analysis. we can

say that as we understand, the detector and atmosphere model in the data analysis is very close to the real situation.

9.5 Atmosphere Calibration Laser Analysis

Parallel to the cosmic ray candidate events analysis, the steerable laser shots installed at HiRes-II site (HR2SLS) as described in section 4.5 is also analyzed to retrieval the real atmosphere condition every night. To accomplish this, events recored by HiRes-I and laser shots recorded by HR2SLS are timing-matched to separate laser events from other measurements.

Data used in this study was collected from September 1999 when the HR2SLS is available. The Laser shots are then analyzed by the method described in Chapter 7. As discussed in Chapter 7, in order to minimize the multiply scattering effects of the atmosphere, of the laser shots fired nightly by HR2SLS, only two sets of shots not far away from HiRes-I detector is used in this analysis. The first set shot is close to horizontal with 2 degree azimuth from HiRes-I detector: Azimuth 32 degree, Zenith of 0.6 degree (32, 0.6) shots and Azimuth 36 degree, Zenith 0.6 degree (36, 0.6) shots; The second set is (19,4.0) and (49, 4.0) which are 15 degree azimuth away from HiRes-I detector (see figure 4.8).

The result is shown in figure 7.15, which gives the average atmosphere condition. Ideally the real atmosphere condition should be plugged in for every cosmic ray event analysis, but unfortunately the laser shots cover only a small part of the HiRes running time. So in the cosmic ray analysis, only the average atmosphere condition is used. the fluctuation of the atmosphere condition is put in as systematics, which will give error in the primary energy measurement of the cosmic ray.

9.6 Systematics of HiRes experiment

Systematics of HiRes experiment is complicated, since there is no absolute calibration of the detector. And only monocular detector is used in this report, when stereo result is available, this question can be answered easier.

So here I will only list the possible systematic errors for the energy reconstruction. In chapter 8, I give a step by step approach for the reconstruction of EAS. I here give a step by step systematics here.

a. From cosmic ray to EAS

In this step, the primary energy of cosmic ray is reconstructed from EAS longitudinal profile, so the results will be model dependent, in this report, CORSIKA package is used to get the result in section 3.4 the systematics is 5% if we assume GESJET is correct.

b. EAS scintillation light generation

The scintillation light generation efficiency is based on experiment [58]. The systematics of this experiment is about 10%. This will be directly transfered to the final energy estimation.

c. EAS light propagation

Because the atmosphere condition is not calibration event by event, so averaged atmosphere condition is used in the reconstruction. After study the different atmosphere models with one sigma away from the average, which will be shown in Chapter 10, the energy error transfered from this systematics is about 20%.

d. Reconstruction resolution

The energy resolution due to reconstruction is studied in chapter 8. For cosmic ray with energy of 10^{20} eV, the resolution is about 15%.

e. PMT calibration systematics

With the experience of the last 20 years scintillation detector by HiRes collaborators, the PMT systematics should be less than 10%, this can be improved when absolute PMT calibration method is employed.

If we assume all the above factors are independent, then the overall systematics is around 30%.

Chapter 10

The Cosmic Ray Energy Spectrum Measurement

In this chapter, I present the high energy cosmic ray energy spectrum for energy greater than 1 EeV by using HiRes-I monocular data. Before that I will explain how to calculate the energy spectrum, discuss the detector aperture calculation, and summarize the HiRes detector exposure time.

10.1 Introduction

The cosmic ray energy spectrum is defined as number of cosmic rays observed per unit area, per unit solid angle, per unit time, and per unit energy, or called differential flux, $j(E)[m^{-2}sr^{-1}s^{-1}eV^{-1}]$. The differential flux is calculated by equation:

$$j(E) = \frac{dN}{dE} \cdot \frac{1}{[A\Omega(E)]T} \tag{10.1}$$

where $[A\Omega(E)]$ is the energy dependent detector aperture, T is the detector exposure time, dN is the number of cosmic rays with energy in between E to $E+dE$.

10.2 Detector Aperture Calculation

HiRes detector configuration has been changed during the running time and the aperture also changes with particle energy. A detector Mont Carlo program has been used to calculate the detector aperture. The detail of the detector Mont Carlo is given in chapter 5. The Mont Carlo was tested for accuracy by comparing with real data distributions like R_p, ϕ, θ, etc. This is given in section 9.4. The simulated distributions agree well with actual distributions.

Using the Mont Carlo program, a set of Mont Carlo events is generated in an trial aperture of:

$$[A\Omega]_0 = \pi r_0^2 \int_0^{2\pi} d\phi \int_0^1 cos\theta d(cos\theta) \qquad (10.2)$$

r_0 is the distance from the detector to the maximum trial core position and it is large enough to contain all possible events that would trigger the detector. The magnitude of r_0 varied from 60 km at 10^{18} eV to 200km for 10^{20} eV.

Then the detector aperture can be calculated as:

$$[A\Omega] = [A\Omega]_0 \cdot \frac{\#\ success\ events}{\#\ trial\ events} \qquad (10.3)$$

The Mont Carlo events pass through same data analysis as real data described in chapter 9. For Proton MC showers, the summary of the trial aperture and the

$4\pi r^2$

Energy(eV)	$R_0(km)$	$[A\Omega(E)]_0(km^2sr)$	Energy(eV)	$R_0(km)$	$[A\Omega(E)]_0(km^2sr)$
1.00×10^{18}	60	4.52×10^4	1.00×10^{19}	120	1.81×10^5
1.58×10^{18}	100	1.26×10^5	1.58×10^{19}	150	2.83×10^5
2.51×10^{18}	120	1.81×10^5	2.51×10^{19}	160	3.22×10^5
3.98×10^{18}	120	1.81×10^5	3.98×10^{19}	170	3.63×10^5
6.31×10^{18}	120	1.81×10^5	6.31×10^{19}	180	4.07×10^5
			1.00×10^{20}	200	5.03×10^5
			1.58×10^{20}	200	5.03×10^5

Table 10.1: *Trial aperture for Mont Carlo mono-energetic proton showers.*

number of trial events and the number of success events pass each analysis is given in table 10.1 and table 10.2. From these tables, by using the equation 10.3, we can calculate the detector aperture at each stage, the results is shown in figure 10.1.

The detector aperture depends on composition of the cosmic ray. The iron shower develops higher in the atmosphere than proton shower with same energy. This results in different reconstructible aperture. Based on the composition study as in Fly's Eye stereo experiment and HiRes-Mia Hybrid experiment (see section 2.2), cosmic rays above $10^{19}eV$ are dominated by protons, below this, the composition are mixed. so in the aperture calculation here, we will simply assume from $10^{18}eV$ to $10^{19}eV$, the cosmic ray compositions are average of proton and iron, above $10^{19}eV$ the composition is pure proton.

The atmospheric condition can also affect the reconstructible aperture calculation. Based on the atmosphere study in chapter 7, we use aerosol horizontal extinction length $L_A = 18km$ and scale height $H_S = 1.0km$ as the average aerosol model,

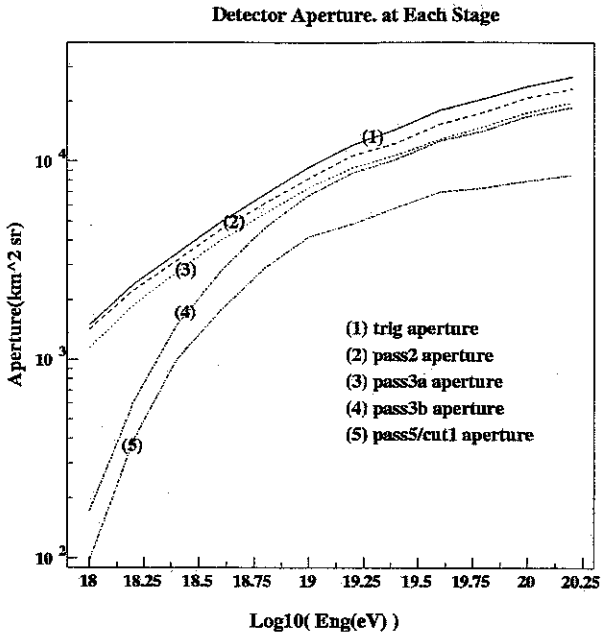

Figure 10.1: *Detector aperture at each reconstruction stage for Proton MC shower.*

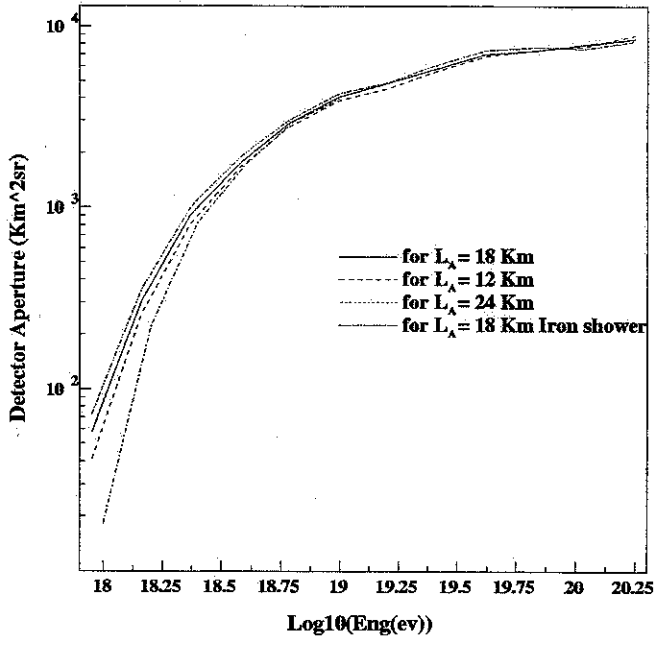

Figure 10.2: *Composition averaged detector aperture for different atmospheric condition. Aperture calculation based on pure Iron is also shown in dot-dash line for comparison.*

Energy(eV)	# gen.	# trig.	# ps2d	# ps3a	# ps3b	# cut1
1.00×10^{18}	121497	4000	3803	3053	463	262
1.58×10^{18}	105059	2000	1872	1569	507	326
2.51×10^{18}	105950	2000	1843	1614	867	584
3.98×10^{18}	73219	2000	1833	1621	1127	718
6.31×10^{18}	53316	2000	1803	1602	1359	851
1.00×10^{19}	19498	1000	878	788	721	446
1.58×10^{19}	23404	1000	885	765	723	400
2.51×10^{19}	22172	1000	851	742	704	402
3.98×10^{19}	20079	1000	850	713	700	387
6.31×10^{19}	19755	1000	855	723	689	356
1.00×10^{20}	21098	1000	874	738	705	333
1.58×10^{20}	18864	1000	869	740	701	320

Table 10.2: *Number of Mont Carlo mono-energetic proton events at different stage of reconstruction.*

$L_A = 12km$ and $L_A = 24km$ are the up and low limit for the aerosol condition.

Figure 10.2 shows the composition averaged reconstructible aperture depending on different aerosol model. The aperture for aerosol condition $L_A = 18km$ is also given in table 10.3.

We will use the averaged atmosphere and composition in the aperture calculation, and put the unknown of the atmosphere condition as one of the systematic errors.

$log_{10}(E(eV))$	$aperture(km^2sr)$	$log_{10}(E(eV))$	$aperture(km^2sr)$
18.0	57.90	19.3	5310
18.1	133.0	19.4	5830
18.2	307.0	19.5	6390
18.3	529.0	19.6	7000
18.4	911.0	19.7	7170
18.5	1260	19.8	7340
18.6	1740	19.9	7630
18.7	2250	20.0	7930
18.8	2910	20.1	8220
18.9	3440	20.2	8530
19.0	4060	20.3	8650
19.1	4430	20.4	8830
19.2	4830	20.5	8980

Table 10.3: *Composition averaged reconstructible aperture for average atmospheric model* $L_A = 18km$.

10.3 Detector Exposure Time

HiRes-I detector started data taking from May 1997 with 14 mirror configuration. Then three more mirrors were employed in June 1997. The final 4 new mirrors were installed in April 1998. Unfortunately, these four new mirrors were not calibrated when the analysis was done in this report. So all the real data set used in this analysis and the exposure time calculated is based on the calibrated mirrors only.

The HiRes detector exposure time is calculated based on the mirror trigger on

mirror	hours	mirror	hours	mirror	hours
1	1738.3	9	1791.7	17*	1142.1
2	1622.5	10	1794.2	18	0.0
3	1757.6	11	1786.1	19*	1278.2
4	1753.9	12	1795.2	20	1777.8
5	1743.8	13	1799.0	21*	1318.0
6	1718.9	14	1788.3	22*	1274.7
7	1786.4	15	1743.8		
8	1795.0	16	1757.0		

Table 10.4: *Detector exposure time for each mirror with good weather condition. Data from mirrors marked with an asterisk is not used because the detectors are not calibrated.*

time. After running of each month, the mirror trigger on time is added up for every mirror. The data used in this analysis includes only good weather data. The weather condition is estimated hourly by the operator. Good weather means very little or no clouds and good visibility.

In Mont Carlo aperture calculation, 22 mirror detector configuration with no cloud weather condition was assumed. To match with this condition, the real detector running time is added up for good weather only mirror by mirror. The result is shown for the running period from May 1997 to February 2000 in table 10.4. The detector exposure time is the average of 22 mirrors exposure time in table 10.4(excluding the marked mirrors, which are not calibrated yet). The total detector exposure time is 1361.34 hours.

$log_{10}(E(eV))$	$\#events$	$log_{10}(E(eV))$	$\#events$
18.0	129	19.1	54
18.1	133	19.2	29
18.2	204	19.3	22
18.3	229	19.4	15
18.4	211	19.5	13
18.5	187	19.6	6
18.6	137	19.7	4
18.7	115	19.8	1
18.8	103	19.9	0
18.9	56	20.0	1
19.0	70	20.1	0

Table 10.5: *Number of good Hires-I Monocular events in each energy bin.*

10.4 Energy Spectrum Measurement

In the analysis we include only those data taken on cloudless weather conditions. The number of events successfully pass through the full analysis and quality cut is shown in table 10.5 for energy above $10^{17.95}eV$. The full data analysis and all quality cuts are given in chapter 9.

The energy spectrum multiplied by E^3 is shown in figure 10.3(a). In this figure, we show three different spectra corresponding to three different aerosol conditions: L_A being 12 Km, 18 Km, and 24 Km respectively (different aperture are calculated and used for different aerosol condition). According to the weather condition study which is described in chapter 7, the average weather condition in our experiemtn is

L_A being 18 Km; $L_A = 12Km$ and $L_A = 24Km$ are for weather condition with one sigma away from average. The different spectrum due to different weather condition gives the systematic error of the result due to weather condition uncertainty. the error shown in the figure is pure statistical error.

The dotted line in the figure represents the spectrum expected by GZK hypothesis for extra-galactic sources distributed uniformly in the universe. The curve is calculated by Berezinsky et. al.[78] with evolutionary parameters of $m = 4$ and $\gamma_g = 2.45$. Here the evolution of the sources enhanced by factor $(1+z)^m$ and γ_g is the power-law generation spectrum. Although the original figure was fitted to AGASA spectrum, we show the same figure rescaled to our spectrum, but it is very impressive that the theoretical curve fits our spectrum very well.

There are two events with energy around or above 10^{20} eV which were not included in the figure 10.3 because these events had normalized χ^2 above the cut of 5 used in the quality cuts (see χ^2 distribution in figure 9.1). In figure 10.4 we change the χ^2 cut to 10, same theoretical curve was also plotted. We do not see any significant difference from figure 10.3.

A MC data set was generated according to Fly's Eye stereo spectrum, by assuming half Proton and half Iron from 10^{18} eV to 10^{19} eV, and pure Proton for energy higher than 10^{19} eV, which is same assumption as in the aperture calculation. The MC data was reconstructed and normalized to the same total number of good event as the real data. The result is shown in figure 10.5. From this figure we can see if the spectrum is as given by Fly's Eye stereo, we should see many events above 10^{20} eV if these are from nearby sources. With a cut off at 10^{20} eV, one event with energy above 10^{20} eV left after reconstruction, this is because of the tail of the reconstruction resolution.

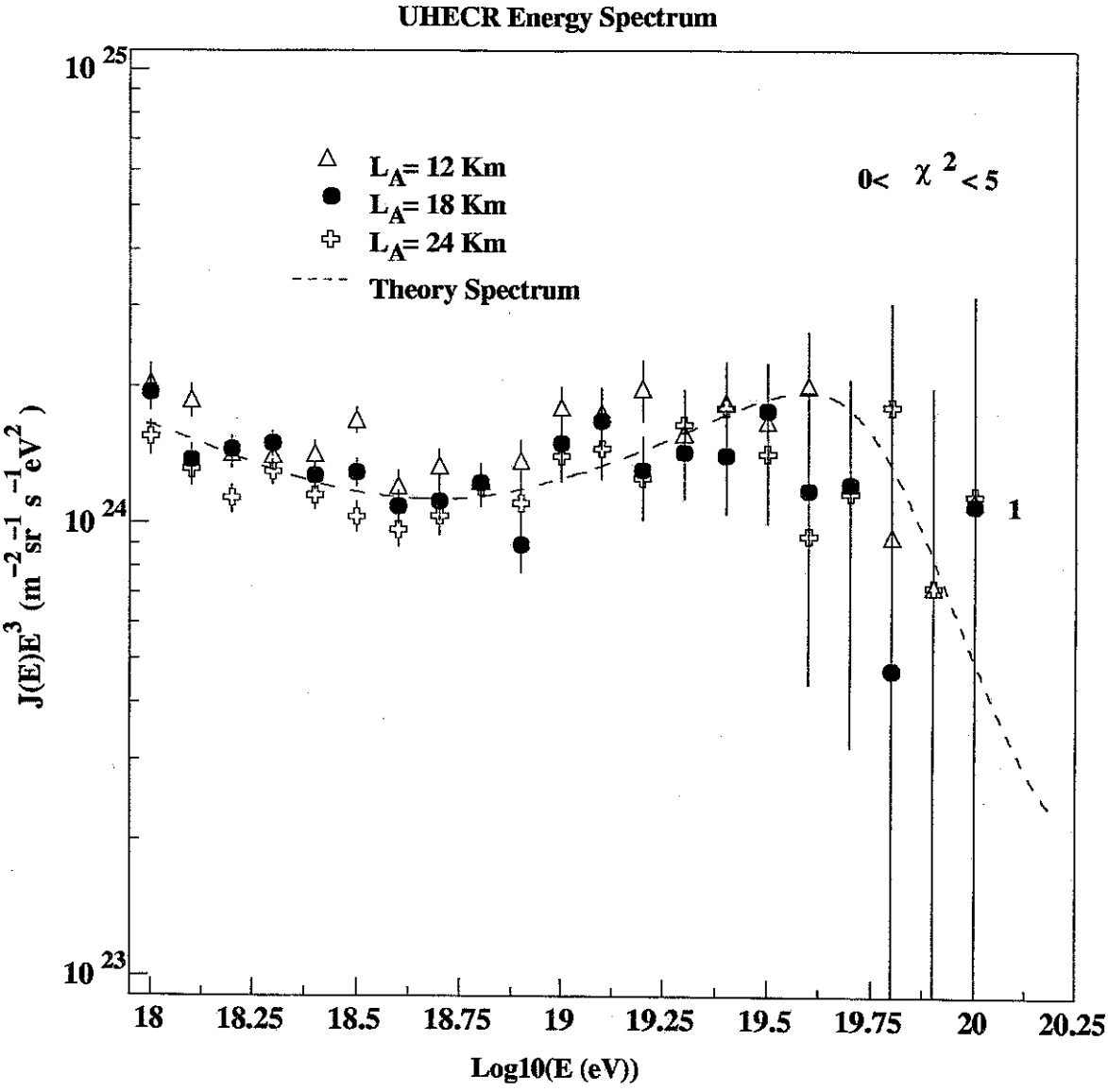

Figure 10.3: *Cosmic ray spectrum measured by HiRes-I monocular detector. Three different spectra are showing for different aerosol conditions:* $L_A = 12km$, $L_A = 18km$, *and* $L_A = 24km$. *The averaged atmosphere condition is* $L_A = 18km$ *as discussed in Chapter 7. Spectra from top to bottom shows the systematic error due to weather condition uncertainty in HiRes experiment. Only statistic error is included in the error bar. The dot line represents the spectrum expected with GZK hypothesis for extragalactic sources distributed uniformly in the universe. Here quality cut* $0 < \chi^2 < 5$ *is used for the data analysis.*

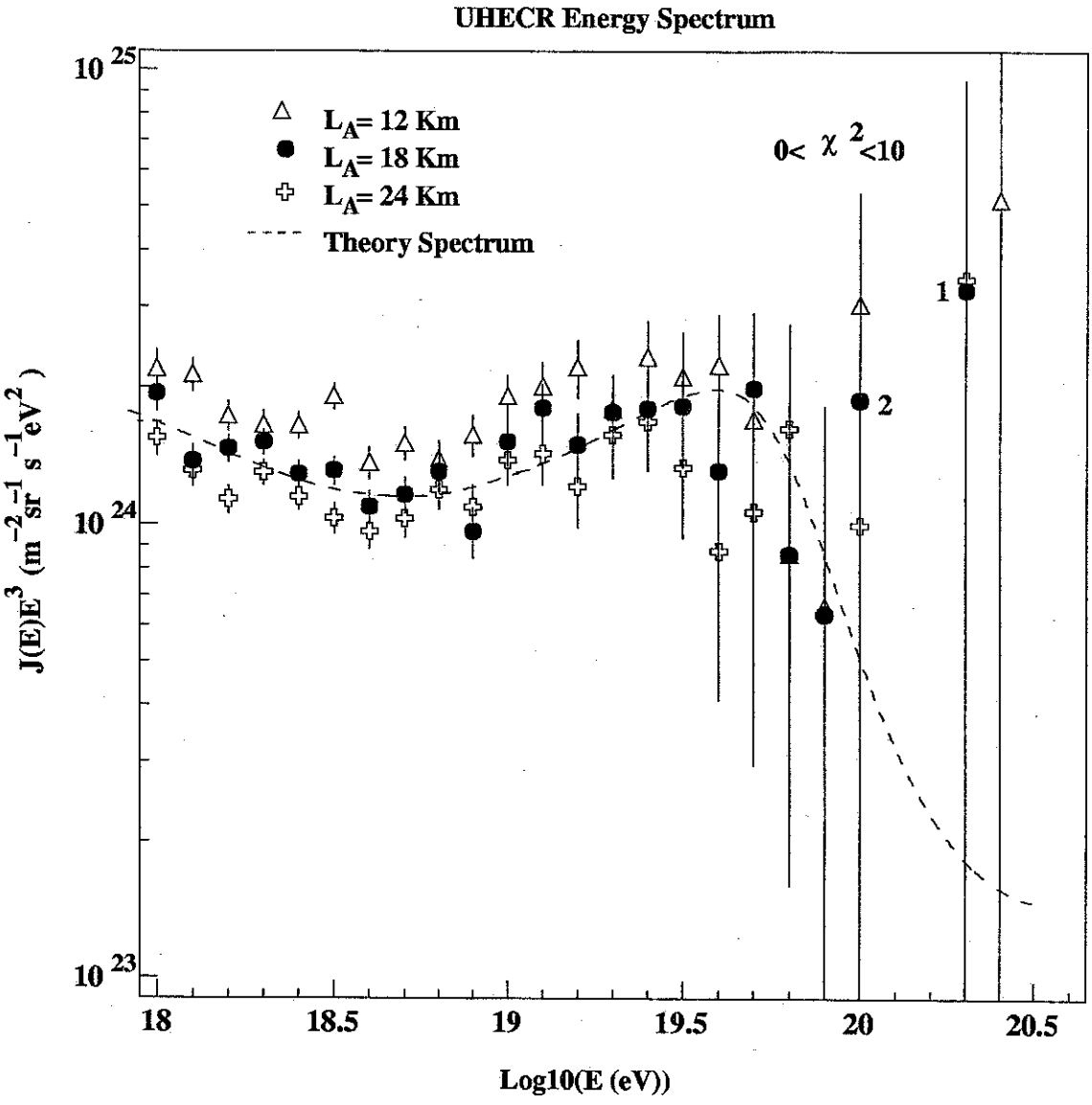

Figure 10.4: *Cosmic ray spectrum measured by HiRes-I monocular detector. Same as figure 10.3 except that quality cut* $0 < \chi^2 < 10$ *is used here. The number shown on the plot means the number of events in that energy bin.*

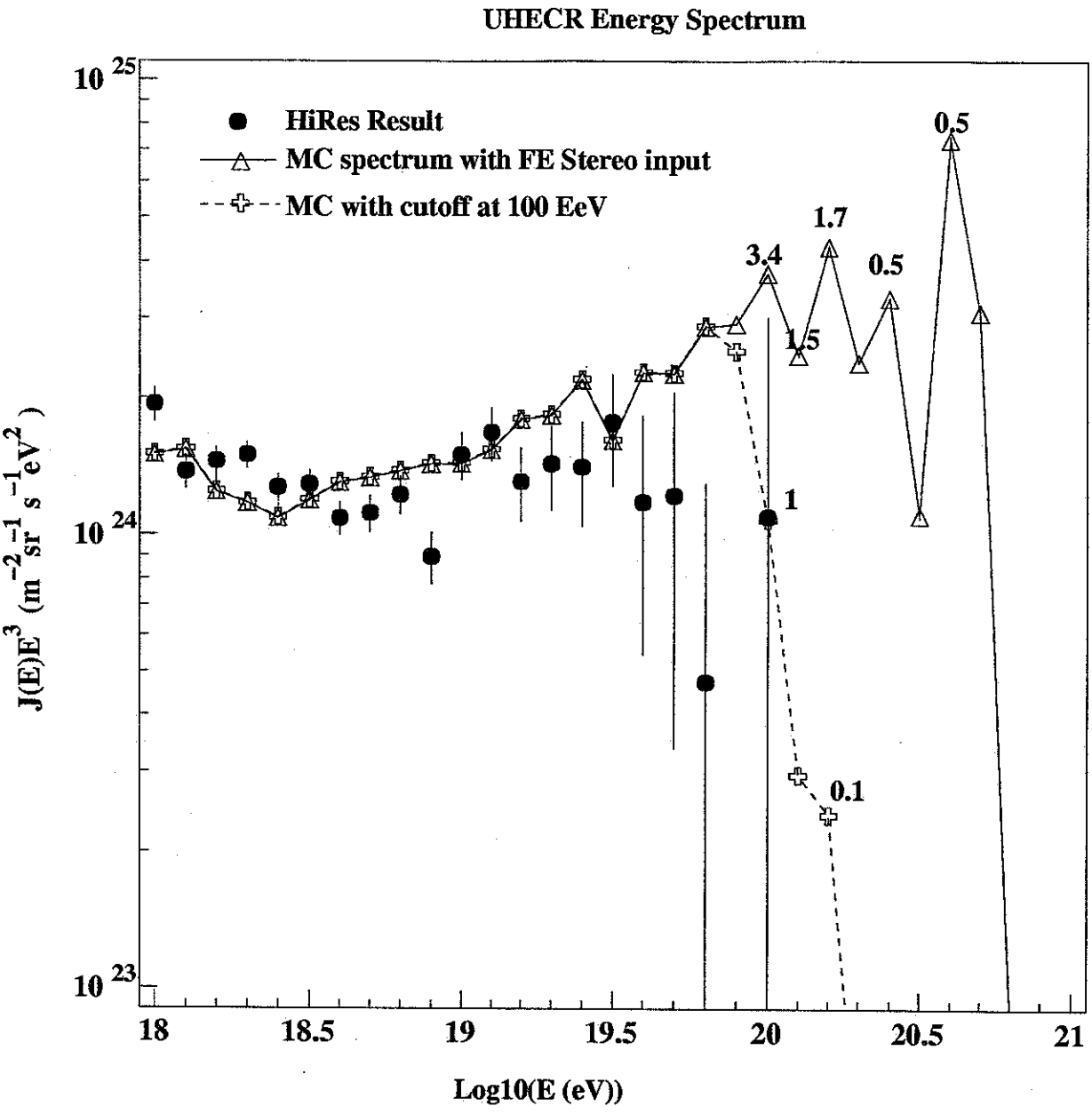

Figure 10.5: *Comparison of HiRes monocular spectrum to reconstructed MC spectrum. MC sets were generated by using Fly's Eye stereo spectrum [3] as input. Solid line is the reconstructed MC spectrum by assuming Fly's Eye spectrum goes beyond* 10^{20} *eV. Dash line is the reconstructed MC spectrum with a cut off at* 10^{20} *eV. The number attached is expected number of events in each bin.*

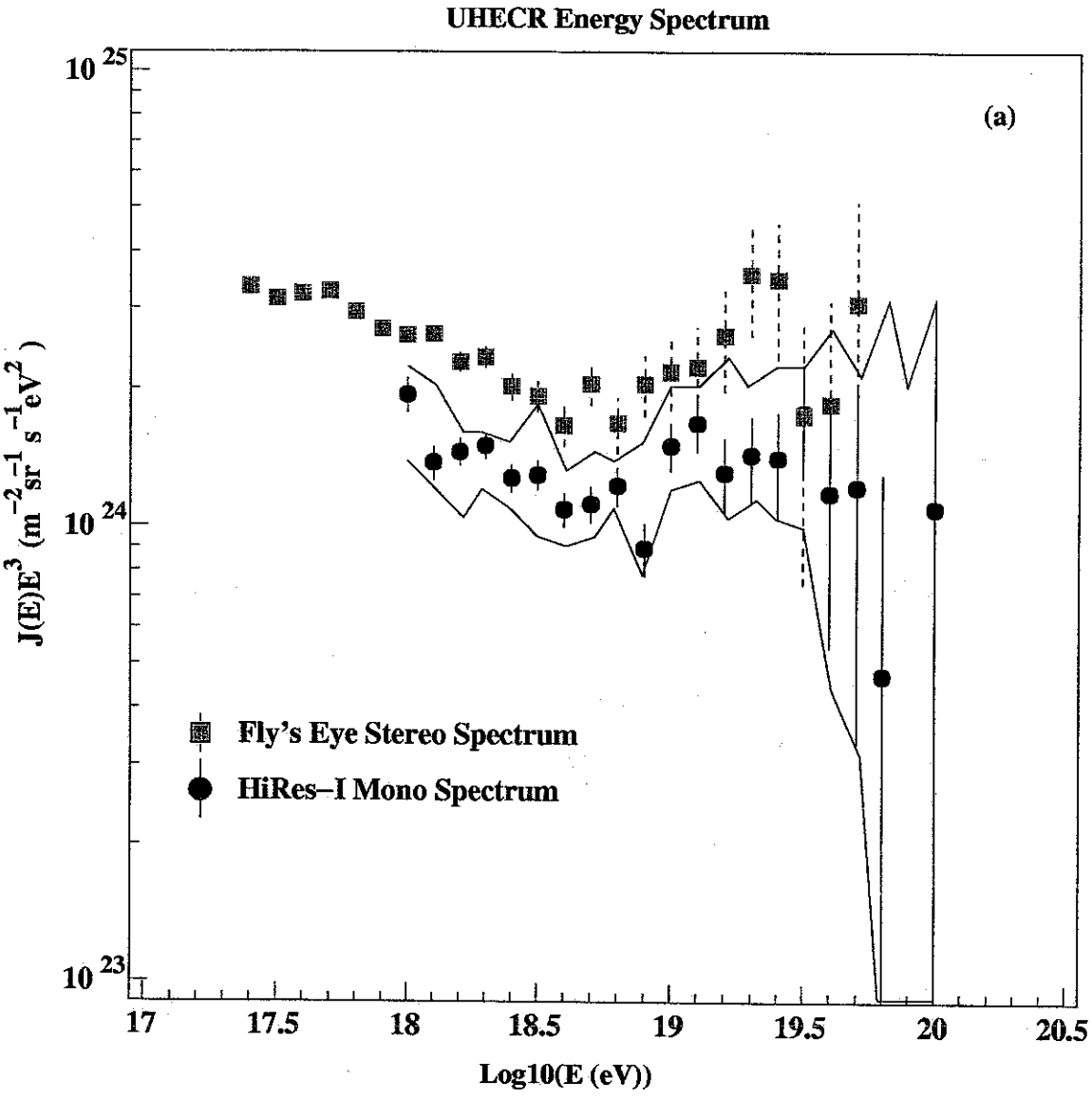

Figure 10.6: *Comparison of HiRes Monocular spectrum with the measurement of Fly's Eye stereo experiment [3]. Solid envelop is the statistic error plus weather condition systematic error shown in figure 10.3.*

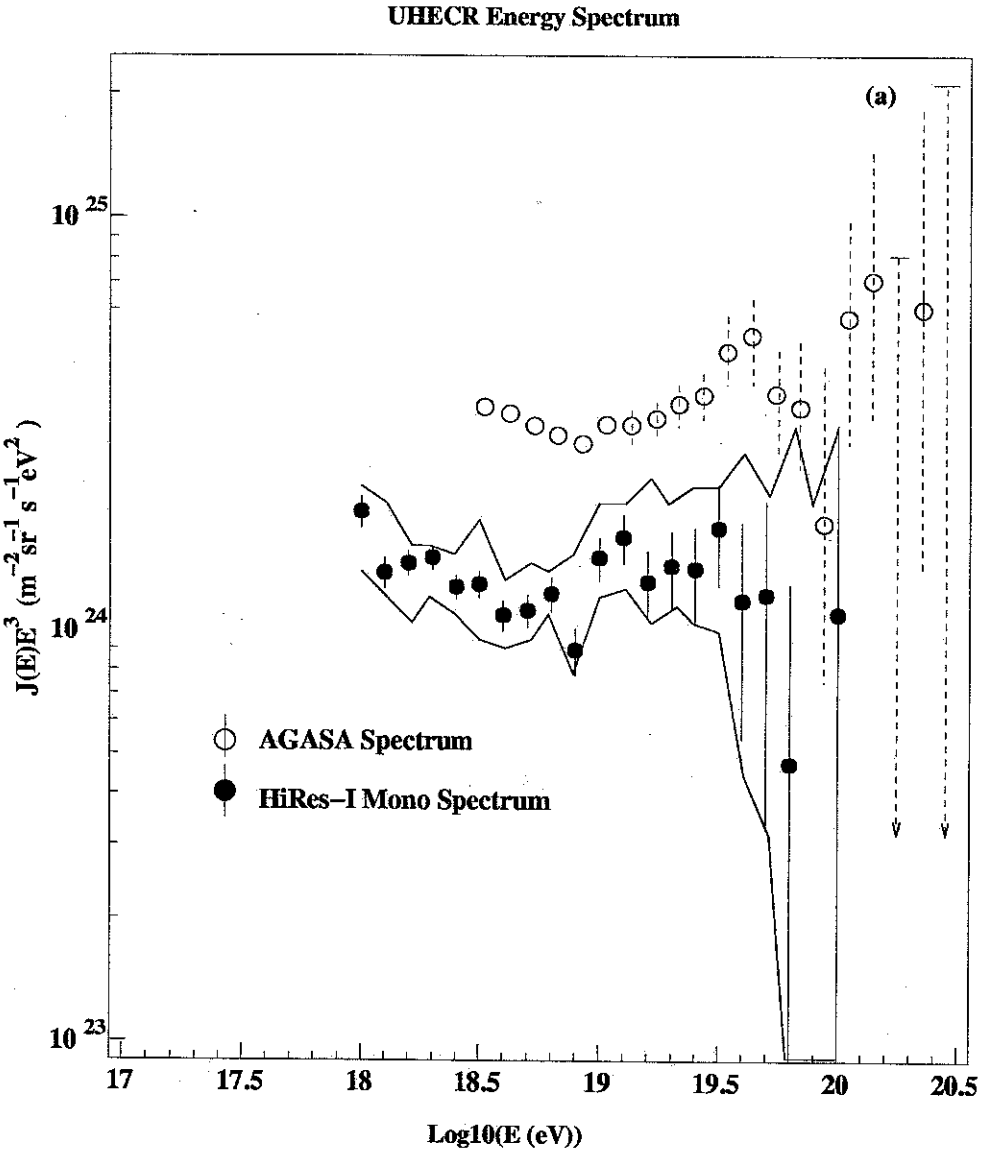

Figure 10.7: *Comparison of HiRes Monocular spectrum with the measurement of AGASA experiment [4]. Solid envelop is the statistic error plus weather condition systematic error shown in figure 10.3.*

In figure 10.6 we compare our results with Fly's Eye stereo measurement. The statistic error and systematic error due to weather uncertainty is shown as a solid lined envelop. Base on the energy resolution study, if we assume the reconstructed energy has 10% uncertainty, this systematic error plus the systematic error in solid envelop is shown as a dot line envelop.

Within errors, two distributions agree well(Remember Fly's Eye experiment used $L_A = 12Km$ in the data analysis). In both spectrum we see indication of a dip at energy 4×10^{18} eV. Note that the calculated theoretical curve in figure 10.3 also shows a dip in the energy region. The first a few bin of HiRes spectrum is lower than Fly's Eye result even for $L_A = 12Km$ model. This fact is also support by HiRes-Prototype data [79].

In figure 10.7 we compare our results with that of AGASA measurement. We can say clearly that they do not agree. The difference between two spectrum is a factor of 2. This factor is outsaide of statistical and systematic errors. As the spectrum is the product of J and E^3, the difference can come from either J or E, or both. It is worth noting that the difference of 30% in absolute energy calibration results in factor of 2 in the plot. There are 8 events above 10^{20} eV in AGASA data. if we extrapolate this number to our experiment by considering the difference in aperture and exposure time. we expected to see around 13 events in our experiment, while we observed only one event instead. We clearly do not agree with AGASA.

10.5 GZK cut off events

The dataset has one event above 10^{20} eV. In order to understand the events above 10^{20} eV, this event is shown in figure 10.8. The top of the figure (a) shows the trigger

pattern on HiRes mirror and the shower-detector plane. The bottom figures show the bin signal vs. slant depth along the track. The upper window (b) shows different the light contribution from scintillation and scattered Cherenkov light. The lower window (c) shows the bin signal and the best fitted shower profile.

Because the exact atmosphere condition of this event is not well know, and the reconstruction resolution of a monocular detector has systematic errors and long tails. clear GZK cutoff is not yet established. But within the current understand of the systematics of HiRes detector, the conclusion we can draw is that this event could be due to tail of the distribution.

In the full dataset there are two more events has reconstructed energy very close to or higher than 10^{20} eV. They can not pass the quality cut: normalized $\chi^2 > 5$, but with normalized $\chi^2 < 10$. These events are shown in figure 10.9 and figure 10.10.

10.6 Summary and Conclusion

Cosmic ray spectrum based on HiRes-I monocular data is presented. Our spectrum is consistent with the theoretical calculation which is based on the GZK hypothesis. The hypothesis is that the extra-galactic sources are distributed uniformly in the universe and these hadrons will collid with 2.7 K microwave as they traverse the universe before reaching to us. The one event with energy above 10^{20} eV is consistant with being a tail of the energy distribution with cut-off at 10^{20} eV.

The flux and shape of our spectrum is consistent with Fly's Eye stereo measurement within errors, but it does not agree with that of AGASA (see figure 10.7). Our spectrum is a factor of 2 lower than that of AGASA. This difference is significant.

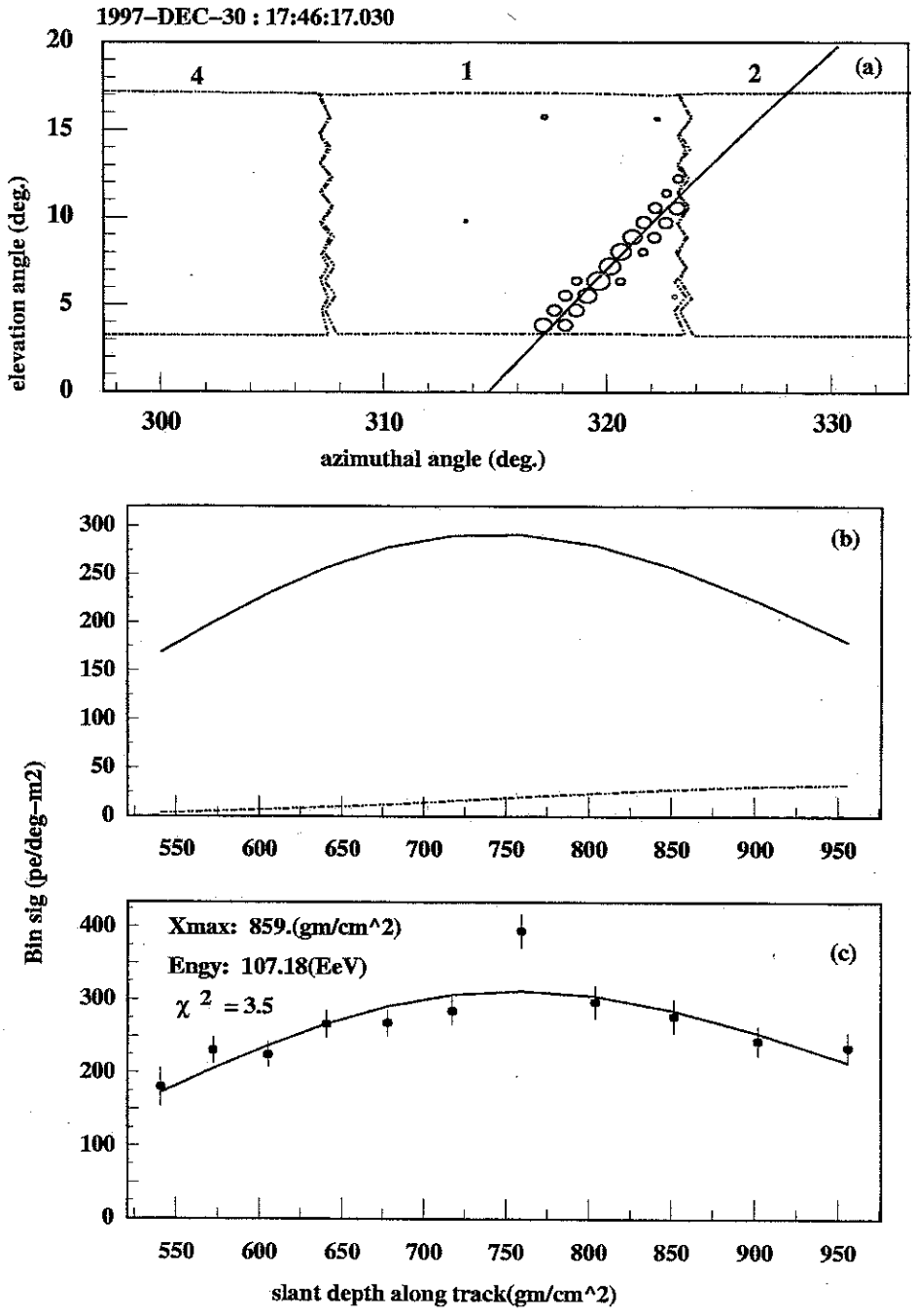

Figure 10.8: *HiRes event recorded on 12/30/1997.*

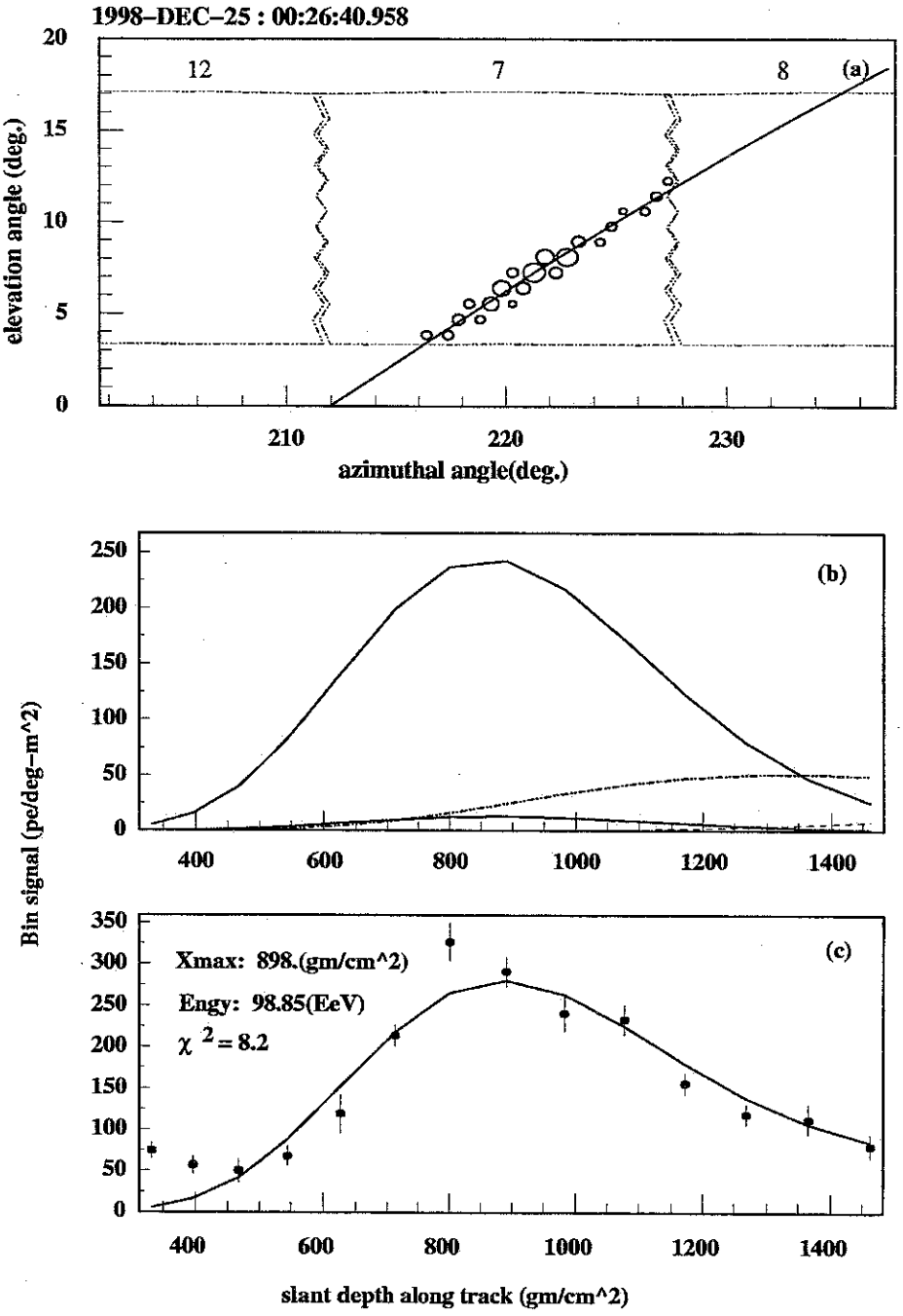

Figure 10.9: *HiRes event recorded on 12/25/1998.*

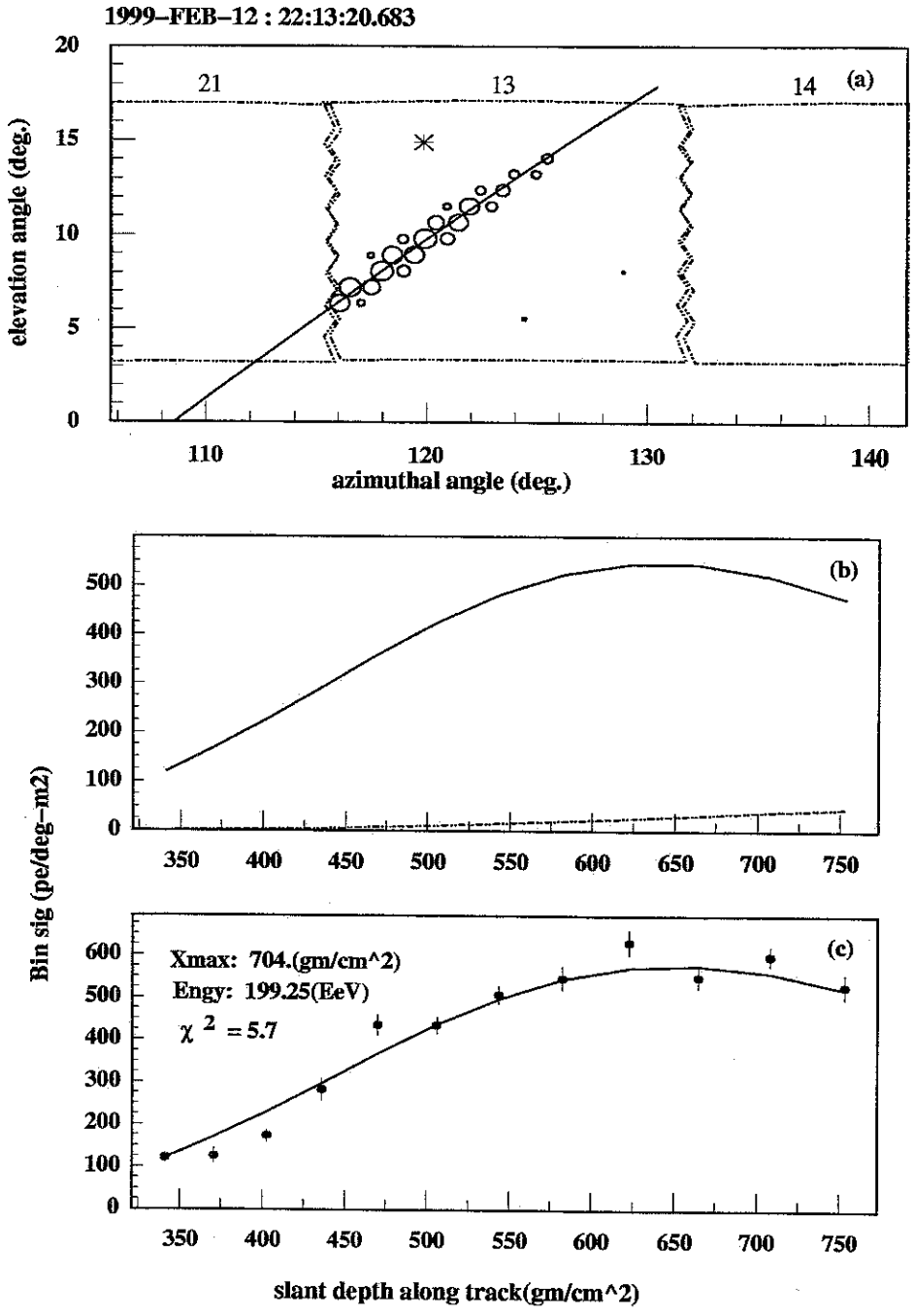

Figure 10.10: *HiRes event recorded on 02/12/1999.*

We also expect to see 13 events in energy greater than 10^{20} eV in our data if 8 events in AGASA data above 10^{20} eV is correct, but we only see one event instead.

Bibliography

[1] K. Greisen, Phys. Rev. Lett. **16**, 748 (1966); G. T. Zatsepin and V. A. Kuzmin, Pis'ma Zh. Eksp. Teor. Fiz. **4**, 114 (1966) [JETP Lett. **4**, 78 (1966)].

[2] http://www-akeno.icrr.u-tokyo.ac.jp/AGASA/

[3] D. J. Bird *et al*, Astrophys J. **441**, 144(1995).

[4] M. Takeda *et al*, Phys. Rev. Lett. **81**, 1163(1998).

[5] J. W. Cronin, in *Unsolved Problems In Astrophysics*, ed. J. N. Bahcall & J. P. Ostriker (Princeton: Princeton Univ. Press), 343 (1996); A. M. Hillas, Nature **395**, 15 (1998).

[6] J. N. Bahcall and E. Waxman, hep-ph/9912326;

[7] G. R. Farrar and T. Piran, Phys. Rev. Lett. **84**, 3527(2000).

[8] P. Auger, R. Maze, and J. Robley, Comptes Rendus de 1'Academie des Sciences(Paris), **208**, 1641 (1938).

[9] Hillas, Proc. 17th ICRC(Paris) **13**, 69(1981).

[10] Hillas, Proc. 16th ICRC(Kyoto) **8**, 7(1979).

[11] D. J. Bird *et al*, Astrophys J. **424**, 491(1994).

[12] M. S. Longair, *High Energy Astrophysics*, 2nd ed. (Cambridge University, Cambridge, 1992)

[13] C. M. Hoffman *et al*, Rev. Mod. Phys. **71**, 897(1999).

[14] L. D. Landau and I. Ya. Pomeranchuk, Dokl. Akad. Nauk SSSR **92**,535&735 (1953); A. B. Migdal, Phys. Rev. **103**, 1811(1956)

[15] K. Shinozaki, N. Inoue and H. P. Vankov unpublished.

[16] D. Heck *et al*, Report FZKA 6019 (1998), Forschungszentrum Karlsruhe.

[17] N. Hayashida. *et al*, J. Phys. G. **21**, 1101 (1995).

[18] T. K. Gaisser *et al*, Phys. Rev. D **47**, 1919(1993)

[19] B. R. Dawson *et al*, Astropart. Phys. **9**, 331(1998).

[20] T. Abu-Zayyad *et al*, Phys. Rev. Lett. **84**, 4276(2000).

[21] M. Teshima, in *Proceeding of the 23rd ICRC*: eds. D. A. Leahy *et al*, 257 (World Scientific Pub. Co. Pte. Ltd., Singapore 1994).

[22] M. H. A. Huang, *Anisotropy of Extremely High Energy Cosmic Rays*, thesis, University of Utah, 1996.

[23] http://www.auger.org/

[24] E. Fermi, Phys. Rev. **75**, 1169 (1949).

[25] A. B. Bell, Mon. Not. R. Astron. Soc. **182**, 147(1978); R. D. Blandford and J. P. Ostriker, Astrophys. J. **221**, L29(1978).

[26] R. O. Legage and C. J. Cesarsky, Astron. Astrophys. **125**, 249(1983).

[27] T. K. Gaisser, *Cosmic Rays and Particle Physics*, (Cambridge University Press, 1990).

[28] P. Sokolsky *et al*, Phys. Rep. **217**, 225(1992).

[29] J. R. Jokipii and G. E. Morfill, Astrophys. J. Lett. **290**, L1(1981).

[30] A. M. Hillas, Can. J. Phys. **46** s623(1968); C. T. Hill *et al*, Phys. Rev. D **36** 1007(1987); V. S. Berezinsky and S. I. Grigor'eva, Astron. Astrophys. **199**, 1(1988).

[31] A. M. Hillas, Ann. Rev. Astr. Astrophys. **22**, 425(1984).

[32] P. Sokolsky, *Introduction to ultrahigh Energy Cosmic Ray physics* (Addison Wesley, New York 1989).

[33] W. Heitler, *Quantum Theory of Radiation* 2ed. (Oxford University Press, 1944).

[34] K. Werner, Phys. Rep. **232**, 87(1993).

[35] J. Ranft, Phys. Rev. D **51**, 64(1995).

[36] R. S. Fletcher *et al*, Phys. Rev. D **50**, 5710(1994).

[37] N. N. Kalmykov and S. S. Ostapchenko, Yad. Fiz. **56**, 105(1993); phys. At. Nucl. **56**(3) 346(1993); N. N. Kalmykov *et al*, Bull. Russ. Acad. Sci. (physics) **58**, 1966(1994).

[38] K. Greisen, *Progess in Elementary Particle and Cosmic Ray Physics*, **3**, 1(1956); Ann. Rev. Nuc. Sci. **10**, 63(1960);

[39] the hires profile paper.

[40] K. Kamata and J. Nishimura, Prog. Theor. Phys. (Kyoto) suppl. **6**, 93(1958); K. Greisen, *Progess in Elementary Particle and Cosmic Ray Physics*, **3**, 1(1956).

[41] M. J. Kidd, *Properties of Extensive Air Showers around* 10^{17} *eV*, Ph. D. Thesis, University of Illinois ,1997.

[42] A. Wolfendale, *Cosmic Rays*, George Newnes Limited, London, 1963.

[43] A. N. Bunner, Ph. D. Thesis, Cornell University, 1964.

[44] H. Hillas, J. Phys. G, **8**, 1461(1982)

[45] R.M.Baltrusaitis *et al*, NIM **A240**, 410(1985).

[46]

[47] R. W. Nicholls *et al*, Proc. Phys. Soc. **74**, 87(1959); R. H. Hughes *et al*, Phys. Rev. **123**, 2084(1961).

[48] Massey and Burhop, *Electronic and ionic Impact Phenomena*,1952; D. T. Stewart and E. Gabathuler, Proc. Phys. Soc. **72**, 287(1958).

[49] J. Linsley, Proc. 19th ICRC, La Jolla, **9**, 475(1985).

[50] A. M. Hillas et al, Acta. Physica, Hung(Proc 11th ICRC), 29 Suppl **3**, 533(1970); Proc 12th ICRC, Hobart, **3**, 1001(1971).

[51] B. N. Afanasiev *et al*, *Proceeding of the International Symposium on Extremely High Energy Cosmic Ray: Astrophysics and Future Observatories*, ed M. Nagano, ICRR Universiy of Tokyo p32-49(1996).

[52] H. Y. Dai *et al*, J. Phys. G. **14**, 793(1988).

[53] J. Delvaille *et al*, J. Phys. Soc. Japan, **17**, Suppl. A-III, 76(1962).

[54] K. Suga, Proc. 5th Interamerican Seminar on Cosmic Rays, La Paz, Bolivia, **II**, XLIX(1962).

[55] A. E. Chudakov, Proc. 5th Ineramerican Seminar on Cosmic Rays, La Paz, Bolivia, **II**, XLIX(1962).

[56] L. G. Porter *et al*, NIM, **87**, 87(1970).

[57] C. Song *et al*, Astropart.Phys. **14**, 7(2000).

[58] F. Kakimoto *et al*, NIM **A372**, 527(1996).

[59] J. Linsley, Proc 19th ICRC, La Jolla, UAS, **7**, 193(1985).

[60] C. R. Wilkinson, Ph. D. Thesis, University of Adelaide, 1998.

[61] T. Abu-Zayyad, Ph. D. Thesis, Iniversity of Utah, 2000.

[62] J. N. Matthews *et al*, ICRC 1999 (Salt Lake City 1999).

[63] J. R. Mumford *et al* , ICRC 1999 (Salt Lake City 1999).

[64] L. R. Wiencke *et al*, NIM A **428**, 593(1999).

[65] D. J. Bird *et al*, NIM A **349**, 592(1994).

[66] E. H. Bellamy *et al*, NIM A **339**,468(1994); D. Bird *et al*, in *Proceeding od the Tokyo Workshop on Techniques for the study of Extremely High Energy Cosmic Rays*. Tokyo, 269(1993).

[67] S. Thomas, privite communication, unpublished.

[68] J. D. Jackson, *Classical Electrodynamics*, Wiley, N, Y. (1962).

[69] D. R. Longtin, *A Wind Dependent Desert Aerosol Model: Radiative Properties*, Air Force Geophysical Laboratory, AFGL-TR-88-0112,1988.

[70] J. D. Spinhirne, J Appl. Meteo. **19**, 4 (1980).

[71] A. S. Zachor, Appl. Opt. **17**, 1911 (1978).

[72] F. Riewe and A. E. S. Green, Appl. Opt. **17**, 1923(1978).

[73] C. Lavigne *et al.*, Appl. Opt. **38**, 6237(1999). and references within.

[74] L. B. Stotts, Appl. Opt. **17**, 504(1978); K. Furutsu, J. Opt. Soc. Am. **70**, 360 (1980); G. C. Mooradian and M. Geller, Appl. Opt. **21**, 1572(1982).

[75] D. M. Reilly and C. Warde, J. Opt. Soc. Am. **69**, 464(1979).

[76] E. Trakhovsky and U. P. Oppenheim, Appl. Opt. **22**, 1633 (1983).

[77] J. A. Matthews *et al*, ICRC 1999 (Salt Lake City 1999).

[78] V.Berezinsky *et al*, ICRC 2001 (Hamburg 2001); hep-ph/0107306.

[79] C. Song, Ph. D. Thesis, Columbia University, 2001.